SHEAR REPAIR METHODS FOR CONVENTIONALLY REINFORCED CONCRETE GIRDERS AND BENT CAPS

Final Report

SPR 636

SHEAR REPAIR METHODS FOR CONVENTIONALLY REINFORCED CONCRETE GIRDERS AND BENT CAPS

Final Report

SPR 636

by

Christopher Higgins, Professor
Daniel A. Howell, Former Graduate Research Assistant
Matthew T. Smith, Former Graduate Research Assistant
A. Ekin Senturk, Post-doctoral Faculty Research Associate

School of Civil and Construction Engineering
Oregon State University
Corvallis, OR 97331

for

Oregon Department of Transportation
Research Section
200 Hawthorne Ave. SE, Suite B-240
Salem OR 97301-5192

and

Federal Highway Administration
400 Seventh Street, SW
Washington, DC 20590-0003

December 2009

Technical Report Documentation Page

1. Report No.	2. Government Accession No.	3. Recipient's Catalog No.
FHWA OR-RD-10-09		

4. Title and Subtitle	5. Report Date
Shear Repair Methods for Conventionally Reinforced Concrete Girders and Bent Caps	December 2009
	6. Performing Organization Code

7. Author(s)	8. Performing Organization Report No.
Christopher Higgins, Professor; Daniel A. Howell, Former Graduate Research Assistant; Matthew T. Smith, Former Graduate Research Assistant; A. Ekin Senturk, Post-doctoral Faculty Research Associate School of Civil and Construction Engineering Oregon State University, Corvallis, OR 97331	

9. Performing Organization Name and Address	10. Work Unit No. (TRAIS)
School of Civil and Construction Engineering Oregon State University Corvallis, OR 97331	11. Contract or Grant No. SPR 636

12. Sponsoring Agency Name and Address	13. Type of Report and Period Covered
Oregon Department of Transportation Research Section and Federal Highway Administration 200 Hawthorne Ave. SE, Suite B-240 400 Seventh Street, SW Salem, OR 97301-5192 Washington, DC 20590-0003	Final Report
	14. Sponsoring Agency Code

15. Supplementary Notes

16. Abstract

Thirteen large-scale girders and two bent caps that replicated as close as possible bridge components from the 1950s were cast and loaded to cause initial cracking similar to that observed in the field. The girders were repaired with epoxy crack injection, internal steel bars, external steel bars, surface bonded CFRP, and near-surface mount CFRP. The bent caps were repaired with surface-bonded CFRP and post-tensioning. The beams were loaded to failure while sensors recorded how the beams deformed. In addition, two bridges, one with surface-bonded CFRP strengthening and one with internal steel strengthening, were instrumented before and after strengthening to assess changes in behavior. The test results were used in conjunction with previous research to compare the repair methods based on ten attributes such as shear capacity improvement, aesthetics, durability, and installation requirements.

Surface bonded CFRP, external stirrups, and internal stirrups were all effective in increasing shear capacity of girders. Epoxy injection had minimal impact on capacity, and there were not enough data to make a conclusion for near-surface mounted CFRP. Considering surface bonded CFRP, external bars, and internal bars, no method was clearly superior, but internal stirrups did offer many advantages across the attributes considered.

The surface bonded CFRP and post-tensioning repairs for the bent caps did not provide as much capacity improvement as expected. However, there was only one bent cap specimen for each of the two repair methods tested; therefore, the results from these tests are considered a basis for further investigation.

17. Key Words	18. Distribution Statement
SHEAR, REPAIR, STRENGTHEN, CRACK, CONCRETE, GIRDER, BENT CAP, BEAM, EPOXY INJECTION, INTERNAL STEEL, EXTERNAL STEEL, COMPOSITE, FRP, NSM, NEAR-SURFACE MOUNT, POST-TENSION	Copies available from NTIS, and online at http://www.oregon.gov/ODOT/TD/TP_RES/

19. Security Classification (of this report)	20. Security Classification (of this page)	21. No. of Pages	22. Price
Unclassified	Unclassified	258 + appendices	

Technical Report Form DOT F 1700.7 (8-72) Reproduction of completed page authorized Printed on recycled paper

SI* (MODERN METRIC) CONVERSION FACTORS

APPROXIMATE CONVERSIONS TO SI UNITS

Symbol	When You Know	Multiply By	To Find	Symbol
		LENGTH		
in	inches	25.4	millimeters	mm
ft	feet	0.305	meters	m
yd	yards	0.914	meters	m
mi	miles	1.61	kilometers	km
		AREA		
in^2	square inches	645.2	millimeters squared	mm^2
ft^2	square feet	0.093	meters squared	m^2
yd^2	square yards	0.836	meters squared	m^2
ac	acres	0.405	hectares	ha
mi^2	square miles	2.59	kilometers squared	km^2
		VOLUME		
fl oz	fluid ounces	29.57	milliliters	ml
gal	gallons	3.785	liters	L
ft^3	cubic feet	0.028	meters cubed	m^3
yd^3	cubic yards	0.765	meters cubed	m^3
NOTE: Volumes greater than 1000 L shall be shown in m^3.				
		MASS		
oz	ounces	28.35	grams	g
lb	pounds	0.454	kilograms	kg
T	short tons (2000 lb)	0.907	megagrams	Mg
		TEMPERATURE (exact)		
°F	Fahrenheit	(F-32)/1.8	Celsius	°C

APPROXIMATE CONVERSIONS FROM SI UNITS

Symbol	When You Know	Multiply By	To Find	Symbol
		LENGTH		
mm	millimeters	0.039	inches	in
m	meters	3.28	feet	ft
m	meters	1.09	yards	yd
km	kilometers	0.621	miles	mi
		AREA		
mm^2	millimeters squared	0.0016	square inches	in^2
m^2	meters squared	10.764	square feet	ft^2
m^2	meters squared	1.196	square yards	yd^2
ha	hectares	2.47	acres	ac
km^2	kilometers squared	0.386	square miles	mi^2
		VOLUME		
ml	milliliters	0.034	fluid ounces	fl oz
L	liters	0.264	gallons	gal
m^3	meters cubed	35.315	cubic feet	ft^3
m^3	meters cubed	1.308	cubic yards	yd^3
		MASS		
g	grams	0.035	ounces	oz
kg	kilograms	2.205	pounds	lb
Mg	megagrams	1.102	short tons (2000 lb)	T
		TEMPERATURE (exact)		
°C	Celsius	1.8C+32	Fahrenheit	°F

*SI is the symbol for the International System of Measurement

ACKNOWLEDGEMENTS

This research was funded by the Oregon Department of Transportation (ODOT). Mr. Steven Soltesz of ODOT coordinated the research project, and his assistance is gratefully acknowledged.

DISCLAIMER

This document is disseminated under the sponsorship of the Oregon Department of Transportation and the United States Department of Transportation in the interest of information exchange. The State of Oregon and the United States Government assume no liability of its contents or use thereof.

The contents of this report reflect the view of the authors who are solely responsible for the facts and accuracy of the material presented. The contents do not necessarily reflect the official views of the Oregon Department of Transportation or the United States Department of Transportation.

The State of Oregon and the United States Government do not endorse products of manufacturers. Trademarks or manufacturers' names appear herein only because they are considered essential to the object of this document.

This report does not constitute a standard, specification, or regulation.

SHEAR REPAIR METHODS FOR CONVENTIONALLY REINFORCED CONCRETE GIRDERS AND BENT CAPS

TABLE OF CONTENTS

1.0 INTRODUCTION....1

1.1 BACKGROUND....1
1.2 RESEARCH OBJECTIVES....1

2.0 LITERATURE REVIEW....3

2.1 CODE PROVISIONS....3
2.1.1 American Concrete Institute 318-05 American Building Code Requirements for Structural Concrete....3
2.1.1.1 ACI 318-05 traditional beam capacity....4
2.1.1.2 ACI 318-05 deep beam capacity....5
2.1.2 American Concrete Institute Committee 440....5
2.1.3 American Association of State Highway and Transportation Officials LRFD Bridge Design Specifications (2005)....8
2.1.3.1 AASHTO LRFD 2005 traditional beam capacity....9
2.1.3.2 AASHTO LRFD 2005 deep beam capacity....14
2.1.3.3 Deep beam comparison: remaining codes....17
2.1.4 Canadian Highway Bridge Design Code....18
2.1.4.1 Canadian Bridge Code traditional beam capacity....20
2.1.4.2 Canadian Bridge Code: deep beam capacity....22
2.1.5 Eurocode 2: Design of Concrete Structures....22
2.1.5.1 Eurocode 2 traditional beam capacity....22
2.1.5.2 Eurocode 2: deep beam capacity....25
2.1.6 Euro-International Committee for Concrete Publications....25
2.1.6.1 CEB-FIP Model Code 1990: traditional beam design....25
2.1.6.2 CEB-FIP Model Code 1990: deep beam analysis....28
2.2 EARLIER WORK....28
2.2.1 Epoxy injection repair....28
2.2.2 External steel stirrup repair....29
2.2.3 Internal supplemental steel stirrup repair....33
2.2.4 Surface bonded Carbon Fiber Reinforced Plastic (CFRP) repair....39
2.2.5 CRFP tape as a Near Surface Mount (NSM) repair....42
2.2.6 Zararis Method (bent cap specimen only)....48
2.2.7 Post-tensioning (bent cap specimen only)....49

3.0 FIELD TESTING OF REPAIRED BRIDGES....53

3.1 CLARKS BRANCH OVERCROSSING....53
3.1.1 Description....53
3.1.2 Inspection and instrumentation....59

3.1.3 Testing method 62
3.1.3.1 Controlled truck tests *62*
3.1.3.2 Ambient traffic induced stirrup stress *68*
3.2 WILLAMETTE RIVER BRIDGE 71
3.2.1 Description 71
3.2.2 Inspection and instrumentation 74
3.2.3 Testing method 76
3.2.3.1 Controlled truck tests *76*
3.2.3.2 Ambient traffic-induced CFRP strains *81*

4.0 EXPERIMENTAL MATERIALS AND METHODS 85

4.1 SPECIMEN IDENTIFICATION 85
4.2 SPECIMEN DESIGN 86
4.2.1 Beam specimen design 86
4.2.2 Bent cap specimen design 89
4.3 MATERIALS AND REPAIR SCHEMES 93
4.3.1 Concrete 93
4.3.2 Mild steel 95
4.4 SPECIMEN CONSTRUCTION AND INSTRUMENTATION 96
4.4.1 Beam specimen construction and instrumentation 96
4.4.2 Bent cap specimen construction and instrumentation 100
4.5 TESTING PROTOCOL 104
4.5.1 Beam specimen testing 104
4.5.2 Bent cap specimen testing 104

5.0 REPAIR METHODS 105

5.1 EPOXY INJECTION FOR GIRDERS 105
5.1.1 Material and application details 105
5.1.2 Experimental results 106
5.1.3 Analytical methods 116
5.1.4 Discussion and design recommendations 116
5.2 EXTERNAL SUPPLEMENTAL STIRRUP REPAIR FOR GIRDERS 119
5.2.1 Material and application details 119
5.2.2 Experimental results 123
5.2.2.1 Investigation on repair scheme efficiency for IT beams *123*
5.2.2.2 Investigation on repair scheme efficiency for the T beam *138*
5.2.2.3 Experimental results *143*
5.2.3 Analytical methods 148
5.2.3.1 External stirrup repair: comparison with literature *148*
5.2.3.2 External stirrup repair: comparison with national/international codes *150*
5.2.3.3 External stirrup repair: comparison with R2K *153*
5.2.3.4 External stirrup repair: comparison with VecTor2 ..... *153*
5.2.4 Discussion and design recommendations 157
5.3 INTERNAL SUPPLEMENTAL STIRRUP REPAIR FOR GIRDERS 158
5.3.1 Material and application details 158
5.3.2 Experimental results 164

5.3.3 Analytical methods 173
5.3.3.1 Internal stirrup repair: comparison with national codes 173
5.3.3.2 Internal stirrup repair: comparison with R2K 176
5.3.3.3 Internal stirrup repair: comparison with VecTor2 176
5.3.4 Discussion and design recommendations 179
5.4 SURFACE BONDED CFRP REPAIR FOR GIRDERS 180
5.4.1 Material and application details 180
5.4.2 Experimental results 185
5.4.3 Analytical methods 188
5.4.3.1 CFRP stirrup repair: comparison with literature review 188
5.4.3.2 CFRP stirrup repair: comparison with international codes 189
5.4.3.3 CFRP stirrup repair: comparison with R2K 189
5.4.3.4 CFRP stirrup repair: comparison with VecTor2 189
5.4.3.5 CFRP stirrup repair: design recommendations 192
5.4.4 Discussion and design recommendations 192
5.5 NEAR SURFACE MOUNT (NSM) REPAIR FOR GIRDERS 192
5.5.1 Material and application details 192
5.5.2 Experimental results 198
5.5.3 Analytical methods 201
5.5.3.1 NSM stirrup repair: comparison with literature review 201
5.5.3.2 NSM stirrup repair: comparison with codes 201
5.5.3.3 NSM stirrup repair: comparison with R2K 202
5.5.3.4 NSM stirrup repair: comparison with VecTor2 202
5.5.4 Discussion and design recommendations 203
5.6 REPAIR METHODS FOR BENT CAPS: CFRP AND LONGITUDINAL POST-TENSIONING 204
5.6.1 Material and application details 204
5.6.2 Experimental results 208
5.6.3 Analytical methods 217
5.6.3.1 Bent cap comparison: literature review 217
5.6.3.2 Bent cap modeling: ACI 440 217
5.6.3.3 Bent cap modeling: strut-and-tie method 218
5.6.3.4 Bent cap modeling: Zararis Method 224
5.6.3.5 Bent cap modeling: VecTor2 226
5.6.4 Discussion and design recommendations 228
5.7 LONGEVITY, RELATIVE COMPARISONS, AND SELECTION OF APPROPRIATE SHEAR STRENGTHENING METHOD 229
5.7.1 Longevity of repairs 229
5.7.2 Relative comparisons of repair alternatives 230
5.7.3 Recommendation of design alternatives 230
6.0 CONCLUSIONS 233
6.1 SUMMARY AND CONCLUSIONS 233
6.2 RECOMMENDATIONS 237
6.3 FUTURE WORK CONSIDERATIONS 237
7.0 REFERENCES 239

List of Figures

Figure 2.1: AASHTO LRFD general approach for determining β and θ values 12
Figure 2.2: AASHTO LRFD Strut-and-Tie component identification 14
Figure 2.3: AASHTO LRFD effective area of concrete strut anchored by reinforcement 15
Figure 2.4: AASHTO LRFD effective area of concrete for strut anchored by bearing and reinforcement 16
Figure 2.5: AASHTO LRFD effective area of concrete for strut anchored by bearing and struts 16
Figure 2.6: Canadian code reliability index against failure 18
Figure 2.7: Eurocode 2 ultimate limit state truss model analogy 24
Figure 2.8: External stirrup repair scheme from Altin, et al. 31
Figure 2.9: External stirrup repair scheme from Kim, et al. 32
Figure 2.10: External stirrup repair scheme from Shamsai, et al. 33
Figure 2.11: Bond model variations based on tests compiled by Cook, et al. 36
Figure 2.12: Test setup for post installed anchors taken from Hammad, et al. 38
Figure 2.13: Force diagram for post installed anchors taken from Hammad, et al. 39
Figure 2.14: Near Surface Mount beam type pullout test setup taken from Cruz and Barros 45
Figure 2.15: Instrumentation of CFRP taken from Cruz and Barros 48
Figure 2.16: Deep beam specimen #1 details taken from Aravinthan and Suntharavadivel 49
Figure 2.17: Deep beam specimen #2 details taken from Aravinthan and Suntharavadivel 50
Figure 3.1a: 1955 design drawings for Clarks Branch Overcrossing 54
Figure 3.1b: 1955 design drawings for Clarks Branch Overcrossing 55
Figure 3.1c: 1955 design drawings for Clarks Branch Overcrossing 56
Figure 3.2a: 1995 design drawings for Clarks Branch Overcrossing with supplemental exterior girder 57
Figure 3.2b: 1995 design drawings for Clarks Branch Overcrossing with supplemental exterior girder 58
Figure 3.3a: Observed diagonal crack and stirrup locations in main girders 59
Figure 3.3b: Observed diagonal crack and stirrup locations in bent caps 60
Figure 3.4: Example installation of strain gage on stirrup at diagonal crack location 61
Figure 3.5: Schematic of locations instrumented stirrups on Clarks Branch Overcrossing 62
Figure 3.6: Test truck configuration and axle loads 63
Figure 3.7: Test Run #1 (truck straddling the driving lane fog line): (a) unrepaired, and (b) after supplemental internal stirrups. Note vertical scales are different. 66
Figure 3.8: Test Run #4 (truck over the centerline): (a) unrepaired, and (b) after supplemental internal stirrups. Note vertical scales are different. 67
Figure 3.9: Cast-in-place stirrup stress range-number of cycles (a) before repair (CH10 not working) and (b) after installation of supplemental internal stirrups (CH5 was noisy during ambient traffic monitoring; CH6 not working) 69
Figure 3.10: Cast-in-place stirrup equivalent stress ranges after discarding lowest bin stress range data (a) before and (b) after installation of supplemental internal stirrups 70
Figure 3.11: Willamette River Bridge overall plan and elevation and main girder details 72
Figure 3.12: CFRP repairs to (a) main girders and (b) bent caps 73
Figure 3.13: Field measured cracking, embedded stirrups, and externally bonded CFRP on exterior girder 74
Figure 3.14: Schematic of instrumentation locations 75
Figure 3.15: Example diagonal cracks observed 75
Figure 3.16: Example loss of surface protective coating 76
Figure 3.17: Controlled test truck configurations (a) 2004 and (b) 2008 76
Figure 3.18: Example of measured CFRP strip strains from controlled test trucks located northbound driving over the center stripe (a) 2004 and (b) 2008 80
Figure 3.19: Strain range-number of cycles measured under ambient traffic conditions at all CFRP instrumented locations measured in (a) 2004 and (b) 2008 82
Figure 3.20: Equivalent constant amplitude strain ranges for all instrumented locations with fatigue exponent of 10 and minimum strain of 3 microstrain (a) 2004 and (b) 2008 83
Figure 4.1: T and IT beam elevations 87

Figure 4.2: T and IT beam typical sections for (a) epoxy injection specimens, (b) other repair specimens 88
Figure 4.3: Typical beam loading setup (IT section shown) 89
Figure 4.4: Bent cap elevation view of reinforcing details and geometry 90
Figure 4.5: Bent cap section at midspan and at stub girder 91
Figure 4.6: Bent cap indirect loading at stub girder location 92
Figure 4.7: Typical strain gage locations along flexural steel 96
Figure 4.8: Typical strain gage locations along stirrups 97
Figure 4.9: Assembly of completed reinforcing cage adjacent to formwork (IT specimen shown) 98
Figure 4.10: Schematic view of sensors for IT and T beams 99
Figure 4.11: Typical bent cap stirrup assembly 101
Figure 4.12: Typical bent cap stub girder assembly 102
Figure 4.13: Schematic view of sensors for bent cap 103
Figure 5.1: Shear-midspan displacement response 107
Figure 5.2: Shear-axial load variability of specimen 5-EA 108
Figure 5.3: Shear-diagonal displacement response. Values were recorded near centerline of specimens on north side. 110
Figure 5.4: Crack pattern locations on east face of specimens. Figure includes precracking, epoxy injected cracks, post-injection cracks, and final failure crack. 111
Figure 5.5: Applied shear-stirrup strain behavior for specimen 3-ED. Strain gages located near (a) injected diagonal cracks and (b) un-injected diagonal cracks. 112
Figure 5.6: Stirrup strains at maximum service level shear (311 kN (70 kip)) before and after injection. (Solid symbol: sensor located near injected diagonal crack; hollow symbol: sensor located far from injected diagonal crack.) 113
Figure 5.7: Applied shear at diagonal cracking initiation before and after injection. (Solid symbol: sensor located near injected diagonal crack; hollow symbol: sensor located far from injected diagonal crack.) 114
Figure 5.8: Diagonal deformation range during curing of specimen B.IT.NC.EL 115
Figure 5.9: Stirrup strain during curing of specimen B.IT.NC.EL 115
Figure 5.10: Photographs of cores taken from specimens 3-ED and 4-EL: (a) core taken from specimen 3-ED; (b) core taken from specimen 5-EA with small voids 118
Figure 5.11: External stirrup typical section: channel repair 120
Figure 5.12: External stirrup typical section: W Beam repair 120
Figure 5.13: External stirrup typical section: strengthened W Beam repair 121
Figure 5.14: Specimen B.IT.NC.ES repair 122
Figure 5.15: Specimen B.IT.C.ES repair 122
Figure 5.16: Specimen B.T.NC.ES repair 122
Figure 5.17: External stirrup installation 123
Figure 5.18: External stirrup repair: (a) channel section; (b) W Beam; (c) Strengthened W Beam 125
Figure 5.19: Maximum shear force versus centerline displacement 126
Figure 5.20: Mohr's circle for strain 127
Figure 5.21: Diagonal displacement geometry 127
Figure 5.22: Average vertical strain comparison between different dead load and external stirrup support conditions at installation of external stirrups due to post-tensioning condition 129
Figure 5.23: Best fit curve of shear versus average vertical strain for panel 2S: beam self weight 130
Figure 5.24: Integrally cast stirrup absolute strain reduction due to post-tensioning 131
Figure 5.25: Exposure of integrally cast stirrup leg to replace failed strain gage 131
Figure 5.26: Shear force versus internal stirrup 3N strain range for three reaction sections: service loading 132
Figure 5.27: External stirrup 3S strain range for various initial conditions at service level loading 133
Figure 5.28: Shear versus external stirrup 3S and average vertical strain in panel 2S (a) with dead load, and (b) without dead load 134
Figure 5.29: External stirrup and supports idealized as springs 135
Figure 5.30: Repair section efficiency versus repair section stiffness 135
Figure 5.31: Weak axis bending of reaction section 136
Figure 5.32: B.T.NC.ES revised test setup B 138
Figure 5.33: B.T.NC.ES revised test setup C 139

Figure 5.34: Specimen B.T.NC.ES integrally cast stirrup strain: (a) before and after post-tensioning; (b) strain reduction due to post-tensioning. Note: asterisk denotes chipped in stirrups. 140
Figure 5.35: Comparison of specimens B.IT.NC.ES, B.IT.C.ES, and B.T.NC.ES integrally cast stirrup absolute strain reduction due to post-tensioning 141
Figure 5.36: B.T.NC.ES shear force versus centerline displacement for tests A, B, and C 141
Figure 5.37: B.T.NC.ES shear versus internal stirrup 1N strain range for tests A, B, and C 142
Figure 5.38: B.T.NC.ES shear versus external stirrup 5N strain for tests A, B, and C 142
Figure 5.39: Specimen B.T.NC.ES shear versus external stirrup 5N and average vertical strain in panel 2N for tests A, B, and C, offset for clarity 143
Figure 5.40: External stirrup repair specimens shear force versus centerline displacement 144
Figure 5.41: External stirrup repair specimens shear force versus diagonal displacement 144
Figure 5.42: External stirrup repair specimens shear force versus average vertical strain 145
Figure 5.43: External stirrup repair specimens shear force versus typical internal stirrup strain 145
Figure 5.44: External stirrup repair specimens crack maps: individual load steps indicated 146
Figure 5.45: External stirrup repair specimens crack maps: precrack versus repair 147
Figure 5.46: Specimen B.IT.C.ES shear force versus external stirrup and average vertical strain 147
Figure 5.47: Predicted Minh, et al. shear interaction diagram using Response 2000™ 148
Figure 5.48: Predicted Altin, et al. shear interaction diagram using Response 2000™ 149
Figure 5.49: Code Comparison for (a) B.IT.NC.ES, (b) B.IT.C.ES, & (c) B.T.NC.ES 152
Figure 5.50: VecTor2 meshing schemes for (a) B.IT.NC.ES, (b) B.IT.C.ES, and (c) B.T.NC.ES 155
Figure 5.51: VecTor2 external stirrup load deflection estimates for (a) B.IT.NC.ES, (b) B.IT.C.ES, (c) B.T.NC.ES 156
Figure 5.52: Internal stirrup typical section 159
Figure 5.53: Specimen B.IT.NC.IS repair 159
Figure 5.54: Specimen B.IT.C.IS repair 160
Figure 5.55: Specimen B.T.NC.IS repair 160
Figure 5.56: Internal stirrup pullout test setup 161
Figure 5.57: Internal stirrup 627 MPa (91 ksi): bar stress versus displacement 162
Figure 5.58: Internal stirrup 413 MPa (60 ksi): bar stress versus displacement 162
Figure 5.59: Internal stirrup installation 164
Figure 5.60: Internal stirrup repair specimens shear force versus centerline displacement 165
Figure 5.61: Internal stirrup repair specimens shear force versus diagonal displacement 166
Figure 5.62: Internal stirrup repair specimens shear force versus average vertical strain 167
Figure 5.63: Internal stirrup repair specimens shear force versus typical internal stirrup strain 168
Figure 5.64: Internal supplemental stirrup repair specimens crack maps: individual load steps indicated 169
Figure 5.65: Internal supplemental stirrup repair specimens crack maps: precrack versus repair 170
Figure 5.66: B.IT.NC.IS shear force versus internal and supplemental internal stirrup strain: strength loading 170
Figure 5.67: B.IT.C.IS flange damage: (a) top of flange and (b) side of flange 172
Figure 5.68: B.IT.C.IS revised repair 173
Figure 5.69: Code Comparison for (a) B.IT.NC.IS, (b) B.IT.C.IS, and (c) B.T.NC.IS 175
Figure 5.70: VecTor2 meshing schemes for (a) B.IT.NC.IS, (b) B.IT.C.IS, and (c) B.T.NC.IS 176
Figure 5.71: VecTor2 internal stirrup load deflection estimate for (a) B.IT.NC.IS, (b) B.IT.C.IS, and (c) B.T.NC.IS 178
Figure 5.72: CFRP beam typical section 180
Figure 5.73: Specimen B.IT.NC.CF repair 181
Figure 5.74: CFRP beam installation: epoxy injection 184
Figure 5.75: CFRP installation: ground surface (left) and primer application (right) 184
Figure 5.76: CFRP girder repair specimen shear force versus centerline displacement 185
Figure 5.77: CFRP girder repair specimens shear force versus diagonal displacement 186
Figure 5.78: CFRP girder repair specimens shear force versus average vertical strain 186
Figure 5.79: CFRP girder repair specimens shear force versus typical internal stirrup strain 186
Figure 5.80: CFRP repair specimen crack map: individual load steps indicated 187
Figure 5.81: CFRP repair specimen crack map: precrack versus repair 187
Figure 5.82: Specimen B.IT.NC.CF shear force - average vertical strain and CFRP strain 188
Figure 5.83: B.IT.NC.CF shear force - integral stirrup strain and CFRP strain 188

Figure 5.84: VecTor2 meshing scheme for B.IT.NC.CF 190
Figure 5.85: Bond-slip relationship for VecTor2 modeling of CFRP sheets 190
Figure 5.86: VecTor2 load-deflection response for B.IT.NC.CF 192
Figure 5.87: NSM FRP typical section 193
Figure 5.88: Specimen B.IT.NC.NS repair 193
Figure 5.89: NSM pullout test setup 195
Figure 5.90: Specimen B.IT.NC.NS repair 196
Figure 5.91: NSM installation: cut grooves (left) and initial epoxy application (right) 197
Figure 5.92: NSM installation: final product 197
Figure 5.93: NSM repair specimen shear force versus centerline displacement 198
Figure 5.94: NSM repair specimen shear force versus diagonal displacement 198
Figure 5.95: NSM repair specimen shear force versus average vertical strain 199
Figure 5.96: NSM repair specimen shear force versus typical internal stirrup strain 199
Figure 5.97: NSM specimens crack maps: individual load steps indicated 199
Figure 5.98: NSM repair specimens crack maps: precrack versus repair 200
Figure 5.99: B.IT.NC.NS shear force versus NSM strain: strength loading 200
Figure 5.100: B.IT.NC.NS shear force versus NSM and integrally cast stirrup strain 201
Figure 5.101: VecTor2 meshing scheme for B.IT.NC.NS 202
Figure 5.102: VecTor2 load-deformation response for B.IT.NC.NS 203
Figure 5.103: B.IT.NC.NS restraint of cracks under load 204
Figure 5.104: CFRP bent cap installation: epoxy injection 205
Figure 5.105: CFRP bent cap installation: primer (left) and putty (right) 205
Figure 5.106: CFRP bent cap installation: strip installation 206
Figure 5.107: Specimen D.IT.C.PT repair elevation 206
Figure 5.108: Specimen D.IT.C.PT repair top view 207
Figure 5.109: Post-tensioned bent cap installation 207
Figure 5.110: Post-tensioned bent cap installation: adjacent reaction beam 207
Figure 5.111: Baseline and strength loading crack maps for bent cap specimens 209
Figure 5.112: Bent cap shear force versus centerline displacement: ultimate loading condition 210
Figure 5.113: Bent cap shear force versus south stub girder displacement: ultimate loading condition 211
Figure 5.114: Bent cap shear force versus north stub girder displacement: ultimate loading condition 212
Figure 5.115: Bent cap shear force versus north tension diagonal: ultimate loading condition 213
Figure 5.116: Bent cap shear force versus south average vertical strain: ultimate loading condition 213
Figure 5.117: Bent cap shear force versus south tension diagonal: ultimate loading condition 214
Figure 5.118: Bent cap shear force versus typical north internal stirrup: ultimate loading condition 215
Figure 5.119: Bent cap shear force versus typical south internal stirrup: ultimate loading condition 215
Figure 5.120: Bent cap D.T.C.CF shear force versus CFRP and average vertical strain: strength loading condition 216
Figure 5.121: Bent cap D.T.C.CF shear force versus CFRP and integrally cast stirrup strain: strength loading condition 216
Figure 5.122: CAST STM model base specimen: member and node assignments 219
Figure 5.123: CAST STM model base specimen governing member/load 221
Figure 5.124: D.T.C.CF failure load – CAST STM model 222
Figure 5.125: D.T.C.PT failure load – CAST STM model 222
Figure 5.126: STM efficiency factors from international codes 223
Figure 5.127: VecTor2 meshing scheme for D.T.C.PT 226
Figure 5.128: VecTor2 load-deformation response for D.T.C.PT 227
Figure 5.129: VecTor2 D.T.C.CF meshing scheme for D.T.C.CF 227
Figure 5.130: VecTor2 load-deformation response for D.T.C.CF 228

List of Tables

Table 2.1: AASHTO LRFD β and θ values for sections meeting minimum transverse steel requirements 11
Table 2.2: AASHTO LRFD β and θ values for sections with transverse steel, not meeting minimum transverse steel requirements 12
Table 2.3: Comparison of international codes for strut-and-tie model 19
Table 3.1: Stirrup strain peaks during controlled test truck loading before repair of Clarks Branch Overcrossing 64
Table 3.2: Stirrup strain peaks during controlled test truck loading after repair of Clarks Branch Overcrossing 65
Table 3.3: CFRP strip strain peaks during controlled test truck loading in 2004 of Willamette River Bridge near Newberg 78
Table 3.4: CFRP strip strain peaks during controlled test truck loading in 2008 of Willamette River Bridge near Newberg 79
Table 4.1: Specimen test matrix 86
Table 4.2: Concrete properties 94
Table 4.3: Reinforcing steel properties 95
Table 5.1: Specimen experimental summary 116
Table 5.2: External stirrup reinforcing steel properties from tensile tests 121
Table 5.3: External stirrup specimen B.IT.NC.ES testing matrix 125
Table 5.4: External stirrup reaction section efficiency 150
Table 5.5: External stirrup strength estimates based on international codes 151
Table 5.6: R2K shear pressure comparison for different repair methods 153
Table 5.7: External stirrup VecTor2 comparison 154
Table 5.8: Internal stirrup reinforcing steel properties 160
Table 5.9: Internal stirrup pullout tests data 163
Table 5.10: Supplemental internal stirrup strength estimates based on national codes 174
Table 5.11: Internal stirrup VecTor2 comparison 177
Table 5.12: CFRP tensile test data 182
Table 5.13: CFRP pull-off test results 182
Table 5.14: Curing temperatures for B.IT.NC.CF and D.IT.C.CF 185
Table 5.15: CFRP beam code comparison 189
Table 5.16: CFRP beam VecTor2 comparison 191
Table 5.17: NSM tensile test data 194
Table 5.18: NSM pull-off and pull-out test results 196
Table 5.19: NSM beam code comparison 202
Table 5.20: NSM VecTor2 comparison 203
Table 5.20: Bent cap specimen failure shear including specimen self-weight 209
Table 5.21: Bent cap capacity predictions 218
Table 5.22: STM strength reduction factors for various elements 223
Table 5.23: Relative comparisons between girder strengthening methods 232

1.0 INTRODUCTION

1.1 BACKGROUND

Large numbers of conventionally reinforced concrete deck girder (RCDG) bridges were built during the Eisenhower interstate era of the late 1940s to the mid 1960s. These bridges were designed following AASHO national standards of the time (*AASHO 1953*). The shear design requirements of this period were less stringent than those in modern AASHTO specifications (*AASHTO 2004*). Higher demands have been placed on the bridge members during their service lives with increasing load magnitudes, millions of load cycles, and environmental exposure such as temperature gradients, freeze-thaw, and/or wet-dry cycles. These conditions may result in diagonal-tension cracks in the main girders and supporting bent caps. As an example, in Oregon, a large number of RCDG bridges in the inventory are from the 1950's, and state inspectors have identified diagonal cracks in the girders and supporting bent caps on over 500 of these bridges, including 200 such bridges on the state's dominant truck routes (*Zaintz and Long 2007*).

Wholesale replacement of the large inventory of aging RCDG bridges may not be practicable due to economic constraints. However, a management approach that could apply effective repair methods in conjunction with replacement for bridges with insufficient live load ratings would be able to maintain freight mobility and operational safety. Several possible repair alternatives are available for diagonally cracked RCDG members including epoxy injection, internal supplemental stirrups, external supplemental stirrups-threaded steel rod, carbon fiber reinforced plastic (CFRP) sheets, near surface mounted (NSM) fiber reinforced plastic strips, and post-tensioning. Comparisons between the alternatives, however, that can quantify available capacity increases, installation sensitivity, and service-level performance for large lightly reinforced concrete members, are not available. Thus research is needed to provide this information.

1.2 RESEARCH OBJECTIVES

Currently, the structural performance of large lightly reinforced RCDG girders and bent caps with diagonal cracks, and repaired with different materials and techniques, is uncertain. No general comparisons are available among the various alternatives, and there is no guidance for assessing the costs and benefits of the various methods. Furthermore, design and analysis methods have not been validated, and inspection protocols of post-repaired specimens have not been established.

The objectives of this research were to quantify the structural performance of repair techniques for reinforced concrete bridge girders and bent caps lightly reinforced for shear: 1) at service level (before and after repair); and 2) at ultimate load. Several available and emerging repair methods were investigated in the laboratory, including epoxy injection, internal and external supplemental steel stirrups, surface-bonded carbon fiber composites (CFRP), near surface

mounted composite tape (NSM), and external post-tensioning. The laboratory results were compared with current national and international code and/or applicable archival literature design approaches. Where appropriate, modifications were made for design. Based on the laboratory tests, recommendations were made for detailing and inspection of repaired girders.

2.0 LITERATURE REVIEW

2.1 CODE PROVISIONS

The current code provisions from the United States, Canada, and Europe are included for comparison. The North American codes include the American Building Code Requirements for Structural Concrete, referred to as ACI 318-05 (*ACI 2005*), the American Association of State Highway and Transportation Officials LRFD Bridge Design Specifications, referred to as AASHTO LRFD (*AASHTO 2004*), and the Canadian Highway Bridge Design Code (*CSA 2000*). The European codes include Eurocode 2: Design of Concrete Structures (*CEN 2004*), the Euro-International Committee for Concrete & International Federation for Prestressing Model Code (*CEB 1993*), and the International Federation for Prestressing Recommendations on Practical Design of Structural Concrete (*FIP-Commision 1999*). Each code was reviewed with respect to the shear strength of unrepaired specimens as well as any additional strength gain provided by supplemental strengthening schemes for slender and deep beam specimens.

2.1.1 American Concrete Institute 318-05 American Building Code Requirements for Structural Concrete

ACI 318-05 provides the minimum requirements for design and construction of both traditionally reinforced and prestressed concrete structures (*ACI 2005*). Member failure is minimized utilizing strength reduction factors such that the reduced nominal strength of a section is greater than the required strength, as denoted in Equation 2-1 below.

$$\phi R_n \geq U \tag{2-1}$$

where ϕ is a resistance factor, typically less than 1.0, intended to reduce the nominal strength of a section, R_n, based on the applied forces; and U is the required strength, as outlined in Article 9.2, based on several possible load combinations and associated factors.

The requirements for shear and torsion of a concrete section are addressed in Chapter 11. For shear, Equation 2-2 is modified as:

$$\phi V_n \geq V_u \qquad \text{ACI 318-05 (11-1)} \tag{2-2}$$

where V_u (kips) is the factored shear demand and the nominal shear strength, V_n (kips), is computed as a superposition of the contributions from both concrete and steel as:

$$V_n = V_c + V_s \qquad \text{ACI 318-05 (11-2)} \tag{2-3}$$

where V_c (kips) is the nominal shear strength carried by the concrete, and V_s (kips) is the nominal shear strength provided by the transverse reinforcement.

2.1.1.1 ACI 318-05 traditional beam capacity

Prior to calculation of the shear capacity of a section, ACI 318 requires a check to ensure minimum transverse steel area and spacing. Also, Article 11.1.2 limits the value of $\sqrt{f_c'}$ to 100 psi, unless the section of interest contains at least minimum web reinforcement. Minimum shear reinforcement is required, as outlined in Article 11.5.6.1 where the factored shear force V_u exceeds ½ the factored nominal concrete shear strength. Once met, the minimum area of steel is denoted in Article 11.5.6.3 and determined as:

$$A_{v,\min} = 0.75\sqrt{f_c'}\frac{b_w s}{f_{yt}} > \frac{(50 b_w s)}{f_{yt}} \qquad \text{ACI 318-05 11-13} \qquad \textbf{(2-4)}$$

where $A_{v,min}$ ($in.^2$) is the minimum area of shear reinforcement within spacing s (in.); f_c' (psi) is the specified compressive strength of concrete; b_w (in.) is the web width, s (in.) is the center-to-center spacing of the shear reinforcement; and f_{yt} (psi) is the specified yield strength of the transverse reinforcement.

In addition to minimum area requirements, Article 11.5.5 limits spacing of the transverse reinforcement to the lesser of half the effective depth, d/2, or 24 in. for nonprestressed members, except where V_s exceeds $4\sqrt{f_c'}b_w d.$ In this case, the above spacing limits must be reduced by one half. The variable d (in.) is defined as the distance from the extreme compression fiber to the centroid of the tension reinforcement.

Once minimum area and spacing requirements are satisfied, the nominal shear resistance resulting from the contributions of steel and concrete can be determined. The concrete contribution to shear strength is outlined in Article 11.3 and utilizes two design equations. The first, denoted in Equation 2-5 below, is intended for members subjected to shear and flexure only; it is recommended unless a more detailed calculation is required:

$$V_c = 2\sqrt{f_c'}b_w d \qquad \text{ACI 318-05 (11-3)} \qquad \textbf{(2-5)}$$

The more detailed equation is given as:

$$V_c = \left(1.9\sqrt{f_c'} + 2500\rho_w \frac{V_u d}{M_u}\right) b_w d < 3.5\sqrt{f_c'}b_w d \qquad \text{ACI 318-05 (11-5)} \qquad \textbf{(2-6)}$$

where $\rho_w = \frac{A_s}{b_w d}$ is the flexural reinforcement ratio; V_u (kips) and M_u (kip-ft) are the factored shear and moment at the section of interest – with the stipulation that the value $\frac{V_u}{M_u}$ not exceed 1.0.

The shear strength provided by the transverse steel (stirrups) is documented in Article 11.5.7 and calculated as:

$$V_s = \frac{A_v f_{yt} d}{s} \qquad \text{ACI 318-05 (11-15)} \tag{2-7}$$

2.1.1.2 ACI 318-05 deep beam capacity

Deep beam specimens are described in ACI 318 Section 11.7. The design of deep beams uses strut and tie modeling (STM). The ACI and AASHTO LRFD STM provisions are similar, and for the present work, AASHTO-LRFD is used for STM in Section 2.1.3.2 with comparisons to other remaining codes as described later.

2.1.2 American Concrete Institute Committee 440

The 2005 American Concrete Institute Manual for Concrete Practice includes the recommendations of Committee 440 regarding the design and construction of externally bonded fiber reinforced plastic systems for strengthening concrete structures (*ACI 2006*). As the guideline is enveloped by ACI, the governing principles regarding load and resistance factors are the same as outlined under ACI 318-05. The scope of the document encompasses the latest technical information based on a twenty-year period of experimental research, field studies, and analytical work. Within this context, the committee recommendations form a lower bound so as to provide a conservative repair methodology. The application of the repair scheme on the surface of the beams requires significant surface preparation and quality control of materials, plus attention to environmental factors such as temperature, humidity, and moisture concerns. The installation procedures, including curing time, temperature, and humidity, are included in Chapter 3.

The design requirements for ACI 440 are included in Chapter 8 of ACI 440.2R-02 (*ACI 2002*). Two limit states are considered for design. The service limit state limits excessive deflections, cracking, vibrations, etc., while the strength limit state limits failure of the member, stress rupture, and fatigue. Consideration of the virgin specimen strength without FRP is a concern, as indicated by the strengthening limits proposed in Equation 2-8 below:

$$\left(\varphi R_n\right)_{existing} \geq \left(1.25 S_{DL} + 0.85 S_{LL}\right)_{new} \qquad \text{ACI 440.2R (8-1)} \tag{2-8}$$

Equation 2-8 indicates that the existing structure must be capable of sustaining its own dead load plus a portion of the live load. The requirement is intended to safeguard the structure in the event the repaired FRP is removed or rendered ineffective by a fire event.

Environmental factors may affect the long-term strength of FRP systems. As such, the committee recommends the use of an environmental reduction factor C_E as shown below in Equation 2-9.

$$f_{fu} = C_E f_{fu}^{*} \qquad \text{ACI 440.2R (8-3)} \tag{2-9}$$

The design rupture strain is also reduced as indicated in Equation 2-10 below.

$$\varepsilon_{fu} = C_E \varepsilon_{fu}^{*} \qquad \text{ACI 440.2R (8-4)} \tag{2-10}$$

Strengthening for shear is covered in Chapter 10 of the guide. The first consideration for strengthening pertains to the wrapping scheme used; either a full wrap, a 3-sided U-wrap, or a 2-sided wrap are covered. For beam strengthening, the use of a full wrap is prohibited due to geometric constraints of the deck superstructure between adjacent beams. Of the two remaining repair schemes, the 3-sided U-wrap is preferred.

The additional strength gain from the FRP repair is analogous to the shear strength contribution from steel and concrete respectively. In this respect, the FRP repair is simply added to the previous two shear contributions, resulting in a nominal resistance as shown below in Equation 2-11.

$$\phi V_n = \phi(V_c + V_s + \Psi_f V_f) \qquad \text{ACI 440.2R (10-2)} \tag{2-11}$$

where ϕ is 0.90 for shear design; and V_c (kips) and V_s (kips) are as determined in ACI 318-05 in Equations 2-5 or 2-6 and 2-7 respectively. The ψ_f term is an additional reduction factor for the shear contribution from FRP which varies from 0.85 for the three-sided U-wrap or bonded face plies to 0.95 for completely wrapped members. The V_f (kips) term is the strength gain from the FRP.

The FRP contribution to shear strength is described in Section 10.4. Once a repair scheme has been selected, the fiber orientation to the estimated failure crack is determined. The shear strength provided by the FRP is then calculated from the force resulting from the stress in the FRP across the failure crack, as shown below in Equation 2-12.

$$V_f = \frac{A_{fv} f_{fe} (\sin\alpha + \cos\alpha) d_f}{s_f} \qquad \text{ACI 440.2R (10-3)} \tag{2-12}$$

where A_{fv} (in.^{2}) is defined below in Equation 2-13; f_{fe} (psi) is the effective stress in the FRP at failure; α is the inclination of the reinforcement to the longitudinal axis of the member; d_f (in.) is the depth of the FRP; and s_f (in.) is the spacing of the FRP strips.

$$A_{fv} = 2nt_f w_f \qquad \text{ACI 440.2R (10-4)} \tag{2-13}$$

where n is the number of plies of reinforcement; t_f (in.) is the nominal thickness of one ply of reinforcement; and w_f (in.) is the width of the FRP plies. FRP remains linear until fracture; thus the effective stress f_{fe} in Equation 2-12 is proportional to the modulus and the failure strain, as denoted in Equation 2-14 below.

$$f_{fe} = \varepsilon_{fe} E_f \qquad \text{ACI 440.2R (10-5)} \tag{2-14}$$

where ε_{fe} (in./in.) is the effective strain in the FRP at failure; and E_f (psi) is the modulus of elasticity of the FRP.

The guide provides further information for calculating the effective strain at failure depending on the repair scheme. For the current investigation, utilizing a 3-sided wrap, the code directs the user to Section 10.4.1.2. The failure mode of this repair scheme is governed by the bond strength between the FRP and the concrete. Thus, the effective strain is calculated using a reduction coefficient as denoted in Equation 2-15 as:

$$\varepsilon_{fe} = \kappa_v \varepsilon_{fu} \le 0.004 \qquad \text{ACI 440.2R (10-6(b))} \tag{2-15}$$

The reduction factor is calculated based on the concrete strength, the wrapping scheme, and the stiffness of the laminate, as denoted in English units in Equation 2-16 below.

$$\kappa_v = \frac{k_1 k_2 L_e}{468\varepsilon_{fu}} \le 0.75 \qquad \text{ACI 440.2R (10-7) U.S.} \tag{2-16}$$

The corresponding SI factor is shown in Equation 2-17.

$$\kappa_v = \frac{k_1 k_2 L_e}{11900\varepsilon_{fu}} \le 0.75 \qquad \text{ACI 440.2R (10-7) SI} \tag{2-17}$$

where k_1 is a factor relating to the concrete strength denoted in Equations 2-18 (U.S. Units) and 2-19 (SI Units) as:

$$k_1 = \left(\frac{f_c'}{4000}\right)^{\frac{2}{3}} \qquad \text{ACI 440.2R (10-9) U.S.} \tag{2-18}$$

$$k_1 = \left(\frac{f_c'}{27}\right)^{\frac{2}{3}} \qquad \text{ACI 440.2R (10-9) SI} \tag{2-19}$$

where f_c' is the concrete strength in psi (Equation 2-18) and MPa (Equation 2-19). The term k_2 relates to the wrapping type as shown in Equation 2-20:

$$k_2 = \begin{cases} \dfrac{d_f - L_e}{d_f} \text{ for U-wraps} \\ \dfrac{d_f - 2L_e}{d_f} \text{ for two sides bonded} \end{cases} \qquad \text{ACI 440.2R (10-10)} \tag{2-20}$$

where d_f has previously been defined; and L_e is the active bond length as shown below in Equations 2-21 (U.S. Units) and 2-22 (SI Units).

$$L_e = \frac{2500}{\left(nt_f E_f\right)^{0.58}} \qquad \text{ACI 440.2R (10-8) U.S.} \tag{2-21}$$

$$L_e = \frac{23300}{\left(nt_f E_f\right)^{0.58}} \qquad \text{ACI 440.2R (10-8) SI} \tag{2-22}$$

The variables used in the above equations have been previously defined.

2.1.3 American Association of State Highway and Transportation Officials LRFD Bridge Design Specifications (2004)

The 2005 AASHTO LRFD provisions "apply to design, evaluation, and rehabilitation of both fixed and moveable highway bridges" (*AASHTO 2004*). The specifications provide load and resistance factors based on reliability theory with appropriate load and resistance modifiers based on the current state of knowledge concerning their individual distributions. A general approach is described as:

$$\sum \eta_i \gamma_i Q_i \le \phi R_n \qquad \text{AASHTO LRFD } \left(1.3.2.1-1\right) \tag{2-23}$$

where η_i is a load modifier which accounts for ductility, redundancy, and operational importance; γ_i is a load factor; Q_i is the nominal force effect; φ is a resistance factor; and R_n is the nominal resistance.

Both load and resistance are assumed to follow a normal distribution with a higher degree of uncertainty associated with the applied loads. The provisions define four limit states which encompass design loads, ultimate loading, fatigue, and extreme force effects. The first, denoted as the service limit state, places restrictions on stress, deformation, and crack width under traffic loads. The second, identified as the strength limit state, is used to ensure global structural stability with the designed load combinations, modified by accompanying load factor(s). The third, denoted as the fatigue and fracture limit state, relates to stress range limitations and material toughness requirements for fatigue and fracture, respectively. The last, denoted as the extreme event limit state, provides structural survival based on a major earthquake, flood, vessel collision, scour, or ice flow. The scope of the current research project will include service and

strength limit states. For the service limit state, the load modifiers, load factors, and resistance factors are set to 1.0.

2.1.3.1 AASHTO LRFD 2005 traditional beam capacity

Beams having a span-to-depth ratio greater than 2.0 conform to traditional Bernoulli beam theory in which plane sections remain plane. The design of traditionally reinforced as well as prestressed concrete members is covered under Chapter 5 within AASHTO. As with the ACI code, the minimum transverse steel reinforcing and spacing is checked prior to capacity calculations. The first condition that is checked for the shear design of a member relates to the use of minimum transverse steel reinforcement defined as:

$$V_u > 0.5\phi\left(V_c + V_p\right) \qquad \text{AASHTO LRFD 5.8.2.4-1} \tag{2-24}$$

where V_u (kips) is the factored shear force; V_c (kips) is the nominal shear resistance of the concrete; V_p (kips) is the component of the prestressing force in the direction of the shear force (equal to zero in the current investigation); and φ is the resistance factor specified in Section 5.5.4.2. For shear the value is 0.90. The corresponding nominal shear resistance of the concrete is determined as:

$$V_c = 0.0316\beta\sqrt{f_c'}\,b_v d_v \qquad \text{AASHTO LRFD 5.8.3.3-3} \tag{2-25}$$

where V_c (kips) is the nominal shear resistance from the concrete; β is a factor indicating the ability of the diagonally cracked concrete to transmit tension as specified in Article 5.8.3.4; f_c' (ksi) is the compressive strength of the concrete; b_v (in.) is the effective web width, taken as the minimum web width within the depth d_v (in.) as determined in Article 5.8.2.9; and d_v (in.) is the effective shear depth as determined in Article 5.8.2.9.

Article 5.8.2.9 defines the shear stress on a concrete section as:

$$v_u = \frac{V_u - \phi V_p}{\phi b_v d_v} \qquad \text{AASHTO LRFD 5.8.2.9-1} \tag{2-26}$$

where b_v (in.) is defined as the effective web width taken as the minimum web width, measured parallel to the neutral axis, between the resultants of the tensile and compressive forces due to flexure; and d_v (in.) is defined as the effective shear depth taken as the distance, measured perpendicular to the neutral axis, between the resultants of the tensile and compressive forces due to flexure; it need not be taken to be less than the greater of $0.9d_e$ or 0.72h. From Article 5.7.3.3.1, d_e (in.) is as shown below in Equation 2-27.

$$d_e = \frac{A_{ps} f_{ps} d_p + A_s f_y d_s}{A_{ps} f_{ps} + A_s f_y} \qquad \text{AASHTO LRFD 5.7.3.3.1-2} \tag{2-27}$$

With no prestressing present, this formula reduces down to:

$$d_e = d_s \qquad \text{AASHTO LRFD 5.7.3.3.1-2} \tag{2-28}$$

where d_s (in.), as denoted in Article 5.7.3.2.2, is defined as the distance from the extreme compression fiber to the centroid of nonprestressed tensile reinforcement. The procedure for determining β, as defined in Article 5.8.3.4, provides a simplified approach which defaults to a value of 2.0, as well as a general procedure in Article 5.8.3.4.2. For the purpose of the initial check, as indicated in Equation 2-25, the simplified assumption is sufficient; the general procedure is investigated in detail at a later section.

The experimental specimens in the current investigation meet the requirements of Equation 2-24; therefore, the minimum steel reinforcing required for design is determined. Article 5.8.2.5 provides the requirements for the minimum steel reinforcing:

$$A_v \geq 0.0316\sqrt{f_c'}\,\frac{b_v s}{f_y} \qquad \text{AASHTO LRFD 5.8.2.5-1} \tag{2-29}$$

where A_v (in.^{2}) is the area of transverse reinforcement within a distance s (in.); f_c'(ksi) is the compressive strength of the concrete; f_y (ksi) is the tensile strength of the transverse reinforcement; s (in.) is the spacing of the transverse reinforcement; and b_v (in.) is the minimum web width, previously defined under Equation 2-26. A further requirement within AASHTO relates to the maximum spacing of transverse reinforcement as documented in Article 5.8.2.7 and in Equations 2-30 and 2-31 below.

If $v_u < 0.125 f_c'$, then:

$$s_{max} = 0.8 d_v \leq 24.0 in \qquad \text{AASHTO LRFD 5.8.2.7-1} \tag{2-30}$$

If $v_u \geq 0.125 f_c'$, then:

$$s_{max} = 0.4 d_v \leq 12.0 in \qquad \text{AASHTO LRFD 5.8.2.7-2} \tag{2-31}$$

where v_u (ksi) is the shear stress on the section as determined in Equation 2-26. If the requirements regarding minimum shear reinforcement and spacing are satisfied, the nominal shear resistance is defined in Article 5.8.3.3 as the lesser of Equations 2-32 and 2-33 as shown below.

$$V_n = V_c + V_s + V_p \qquad \text{AASHTO LRFD 5.8.3.3-1} \tag{2-32}$$

$$V_n = 0.25 f_c' b_v d_v + V_p \qquad \text{AASHTO LRFD 5.8.3.3-2} \tag{2-33}$$

where the V_p component applies only to prestressed sections. Also, V_c was previously defined in Equation 2-25. The remaining V_s term is defined in Equation 2-34 below:

$$V_s = \frac{A_v f_y d_v \left(\cot\theta + \cot\alpha\right)\sin\alpha}{s} \qquad \text{AASHTO LRFD 5.8.3.3-4} \qquad \textbf{(2-34)}$$

where A_v (in.^{2}) is the area of transverse reinforcement within a distance s (in.); and α is the angle of inclination of transverse reinforcement to the longitudinal axis. The remaining terms have previously been defined.

The general procedures for determining β and θ, based on Modified Compression Field Theory (MCFT), are outlined in Article 5.8.3.4.2. The values are found from two tables denoted within this text as Table 2.1 and 2.2, respectively. Table 2.1 is reserved for specimens that have at least minimum transverse steel, as denoted in Equation 2-29. Table 2.2 is reserved for specimens which have less than the minimum transverse steel requirement. As a general approach, both tables are covered as indicated below.

Table 2.1: AASHTO LRFD β and θ values for sections meeting minimum transverse steel requirements

$\frac{v_u}{f'_c}$	$\varepsilon_x \times 1{,}000$								
	≤−0.20	≤−0.10	≤−0.05	≤0	≤0.125	≤0.25	≤0.50	≤0.75	≤1.00
≤0.075	22.3 6.32	20.4 4.75	21.0 4.10	21.8 3.75	24.3 3.24	26.6 2.94	30.5 2.59	33.7 2.38	36.4 2.23
≤0.100	18.1 3.79	20.4 3.38	21.4 3.24	22.5 3.14	24.9 2.91	27.1 2.75	30.8 2.50	34.0 2.32	36.7 2.18
≤0.125	19.9 3.18	21.9 2.99	22.8 2.94	23.7 2.87	25.9 2.74	27.9 2.62	31.4 2.42	34.4 2.26	37.0 2.13
≤0.150	21.6 2.88	23.3 2.79	24.2 2.78	25.0 2.72	26.9 2.60	28.8 2.52	32.1 2.36	34.9 2.21	37.3 2.08
≤0.175	23.2 2.73	24.7 2.66	25.5 2.65	26.2 2.60	28.0 2.52	29.7 2.44	32.7 2.28	35.2 2.14	36.8 1.96
≤0.200	24.7 2.63	26.1 2.59	26.7 2.52	27.4 2.51	29.0 2.43	30.6 2.37	32.8 2.14	34.5 1.94	36.1 1.79
≤0.225	26.1 2.53	27.3 2.45	27.9 2.42	28.5 2.40	30.0 2.34	30.8 2.14	32.3 1.86	34.0 1.73	35.7 1.64
≤0.250	27.5 2.39	28.6 2.39	29.1 2.33	29.7 2.33	30.6 2.12	31.3 1.93	32.8 1.70	34.3 1.58	35.8 1.50

Table 2.2: AASHTO LRFD β and θ values for sections with transverse steel, not meeting minimum transverse steel requirements

s_{xe} (in.)	$\varepsilon_x \times 1000$										
	≤–0.20	≤–0.10	≤–0.05	≤0	≤0.125	≤0.25	≤0.50	≤0.75	≤1.00	≤1.50	≤2.00
≤5	25.4 6.36	25.5 6.06	25.9 5.56	26.4 5.15	27.7 4.41	28.9 3.91	30.9 3.26	32.4 2.86	33.7 2.58	35.6 2.21	37.2 1.96
≤10	27.6 5.78	27.6 5.78	28.3 5.38	29.3 4.89	31.6 4.05	33.5 3.52	36.3 2.88	38.4 2.50	40.1 2.23	42.7 1.88	44.7 1.65
≤15	29.5 5.34	29.5 5.34	29.7 5.27	31.1 4.73	34.1 3.82	36.5 3.28	39.9 2.64	42.4 2.26	44.4 2.01	47.4 1.68	49.7 1.46
≤20	31.2 4.99	31.2 4.99	31.2 4.99	32.3 4.61	36.0 3.65	38.8 3.09	42.7 2.46	45.5 2.09	47.6 1.85	50.9 1.52	53.4 1.31
≤30	34.1 4.46	34.1 4.46	34.1 4.46	34.2 4.43	38.9 3.39	42.3 2.82	46.9 2.19	50.1 1.84	52.6 1.60	56.3 1.30	59.0 1.10
≤40	36.6 4.06	36.6 4.06	36.6 4.06	36.6 4.06	41.2 3.20	45.0 2.62	50.2 2.00	53.7 1.66	56.3 1.43	60.2 1.14	63.0 0.95
≤60	40.8 3.50	40.8 3.50	40.8 3.50	40.8 3.50	44.5 2.92	49.2 2.32	55.1 1.72	58.9 1.40	61.8 1.18	65.8 0.92	68.6 0.75
≤80	44.3 3.10	44.3 3.10	44.3 3.10	44.3 3.10	47.1 2.71	52.3 2.11	58.7 1.52	62.8 1.21	65.7 1.01	69.7 0.76	72.4 0.62

For Table 2.1 – specimens meeting the minimum transverse steel requirement – the table requires three values: ε_x, v_u, and f_c', where ε_x is defined as the calculated longitudinal strain at the middepth of the member; v_u (ksi) is the average factored shear stress on the concrete previously defined in Equation 2-26; and f_c' (ksi) is the specified compressive strength of the concrete. In lieu of more accurate calculations, ε_x is determined by Equation 2-35 below, with an initial value not be taken greater than 0.001. It is noted that Figure 2.1 identifies the parameters used in Equations 2-35 through 2-37 and should be used in conjunction with the described text. Equations 2-35 through 2-37 have been modified to negate the effects of prestressing.

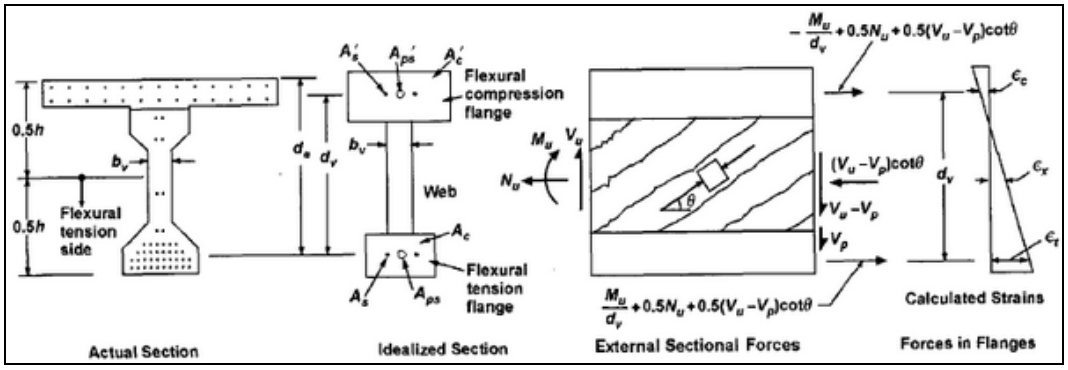


Figure 2.1: AASHTO LRFD general approach for determining β and θ values

$$\varepsilon_x = \frac{\frac{M_u}{d_v} + 0.5N_u + 0.5V_u \cot\theta}{2E_s A_s} \qquad \text{AASHTO LRFD 5.8.3.4.2-1} \qquad \textbf{(2-35)}$$

In Equation 2-35, M_u (kip-in.) is the factored moment taken as a positive value, but not less than $V_u d_v$, where d_v was previously defined in Equation 2-26 as the effective shear depth taken as the distance, measured perpendicular to the neutral axis, between the resultants of the tensile and compressive forces due to flexure, which need not be taken to be less than the greater of $0.9d_e$ or $0.72h$. N_u (kip) is the factored axial force taken as positive if tensile and negative is compressive; V_u (kip) is the factored shear force taken as a positive quantity; E_s (ksi) is the modulus of elasticity of the steel reinforcing; and A_s ($in.^2$) is the area of nonprestressed steel on the flexural tension side of the member. (For bars terminating less than the full development length at the section of interest, they shall be ignored.)

For the second table, ε_x is defined as the largest calculated longitudinal strain which occurs in the web of the member; it is determined as shown below in Equation 2-36, with the initial value not taken greater than 0.002.

$$\varepsilon_x = \frac{\frac{M_u}{d_v} + 0.5N_u + 0.5V_u \cot\theta}{E_s A_s} \qquad \text{AASHTO LRFD 5.8.3.4.2-2} \qquad \textbf{(2-36)}$$

where the variables are as defined for Equation 2-35.

If the value of ε_x is negative for either Equation 2-35 or 2-36, then ε_x should be as defined below in Equation 2-37.

$$\varepsilon_x = \frac{\frac{M_u}{d_v} + 0.5N + 0.5V \cot\theta}{2\left(E_c A_c + E_s A_s\right)} \qquad \text{AASHTO LRFD 5.8.3.4.2-3} \qquad \textbf{(2-37)}$$

where the variables are as defined for Equation 2-35 with the exception of A_c ($in.^2$), which is defined as the area of concrete on the flexural tension side of the member; (refer to Figure 2.1 for additional clarity). E_c (ksi) is defined as the modulus of elasticity of the concrete as denoted under Section 5.4.2.4 and Equation 2-38 below.

$$E_c = 33{,}000 w_c^{1.5} \sqrt{f_c'} \qquad \text{AASHTO LRFD 5.4.2.4-1} \qquad \textbf{(2-38)}$$

where w_c (kip/cubic foot) is the unit weight of the concrete and f_c' (ksi) is the compressive strength of the concrete.

2.1.3.2 AASHTO LRFD 2005 deep beam capacity

The Traditional Bernoulli Beam Theory assumption of plane sections remaining plane does not hold true for deep beam specimens. Among the active international codes covered in the current study, the method of choice for dealing with deep beam analysis is the strut-and-tie (STM) method. The procedure is outlined below, focusing on the AASHTO interpretation, due to the specificity to the bridge community, with comparisons to the remaining codes.

The STM method uses an idealized truss model consisting of upper and lower chords, vertical ties, and diagonal elements to transmit concentrated loads through a member. The concrete component is idealized as a diagonal strut in compression; shear reinforcement is idealized as vertical ties; and longitudinal reinforcement at the limits of the cross section is denoted as chord members, as shown in Figure 2.2. The intersection of these elements is denoted as a Node, and the concrete adjacent to the node is referred to as a Nodal Region; the concrete in this area is assumed to distribute the resulting nodal forces to adjacent regions or bearings. Force equilibrium of the truss model is required, subject to truss geometry and complexity. The method provides a lower bound for capacity, such that modifying the truss geometry and/or complexity is permitted to obtain the highest capacity.

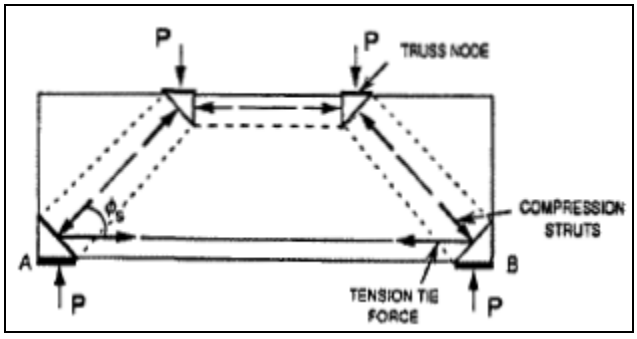


Figure 2.2: AASHTO LRFD Strut-and-Tie component identification

AASHTO defines a deep component as one in which 1) the distance from the point of zero shear to the face of the support is less than 2 times the member height; or 2) structural components in which a load is causing more than one-third of the shear at a support are closer than 2 times the member height from the face of the support. The STM model is documented under section 5.6.3. The capacity of the strut and ties are defined under section 5.6.3.2 and in Equation 2-39 below.

$$P_r = \phi P_n \qquad \text{AASHTO LRFD 5.6.3.2-1} \tag{2-39}$$

where P_r (kip) is the factored resistance and P_n (kip) is the nominal resistance.

The ϕ resistance factor is based on sign convention of the component. From Article 5.5.4.2, ϕ equals 0.70 for STM compression members, 0.90 for tension members, and 0.80 for compression members in anchorage zones. Once the general equation is presented, the nominal strength of the strut and ties must be determined. For a compressive strut, the nominal strength is defined in Article 5.6.3.3.1 and in Equation 2-40 below.

$$P_n = f_{cu} A_{cs} \qquad \text{AASHTO LRFD 5.6.3.3.1-1} \qquad \textbf{(2-40)}$$

where P_n (kip) is the nominal strength of the strut; f_{cu} (ksi) is the limiting compressive strength as defined in Article 5.6.3.3.3; and A_{cs} (in.^{2}) is the effective cross sectional area of the strut as defined in Article 5.6.3.3.2, based on the anchorage conditions at the end of the strut.

For a strut which is anchored by reinforcement, the effective concrete area may extend a distance up to six bar diameters from the anchored bar, as shown in Figure 2.3. For struts anchored by bearing and reinforcement or bearing and struts, the effective concrete area is as shown in Figures 2.4 and 2.5, respectively. The limiting compressive stress in a strut is defined in Article 5.6.3.3.3 and in Equation 2-41 below.

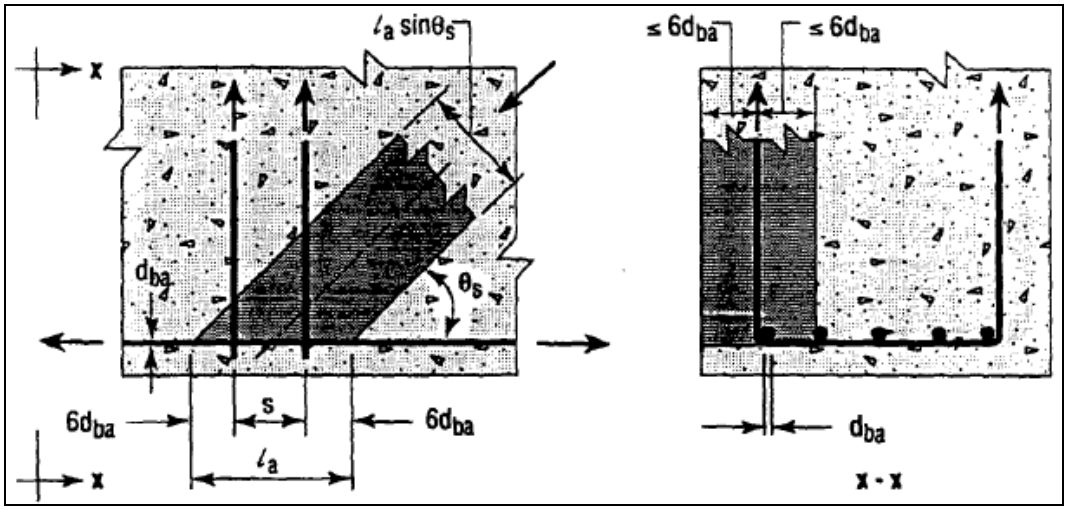


Figure 2.3: AASHTO LRFD effective area of concrete strut anchored by reinforcement

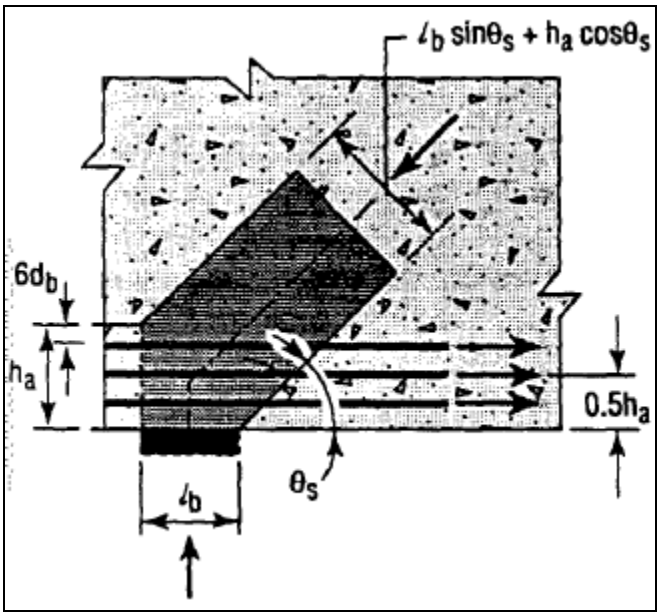


Figure 2.4: AASHTO LRFD effective area of concrete for strut anchored by bearing and reinforcement

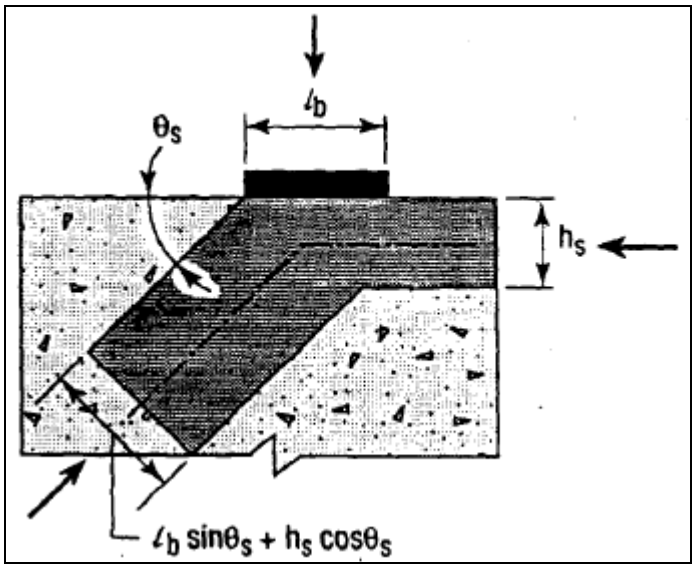


Figure 2.5: AASHTO LRFD effective area of concrete for strut anchored by bearing and struts

$$f_{cu} = \frac{f_c^{'}}{0.8 + 170\varepsilon_1} \leq 0.85 f_c^{'} \qquad \text{AASHTO LRFD 5.6.3.3.3-1} \qquad \textbf{(2-41)}$$

where ε_1 is defined below in Equation 2-42 as:

$$\varepsilon_1 = \varepsilon_s + (\varepsilon_s + 0.002)\cot^2 \alpha_s \qquad \text{AASHTO LRFD 5.6.3.3.3-2} \tag{2-42}$$

where α_s is the smallest angle between the compressive strut and adjoining tension ties; ε_s (in./in.) is the tensile strain in the concrete; and f_c' (ksi) is the compressive strength of the concrete.

If the compressive strut includes reinforcement that is parallel to the strut and detailed to develop its yield strength in compression, the nominal resistance is defined in Article 5.6.3.3.4 and in Equation 2-43 below.

$$P_n = f_{cu} A_{cs} + f_y A_{ss} \qquad \text{AASHTO LRFD 5.6.3.3.4-1} \tag{2-43}$$

where f_y (ksi) is the yield strength of the reinforcement; and A_{ss} (in.^{2}) is the area of the reinforcement in the strut.

Turning toward the tension ties, the nominal resistance is denoted under Article 5.6.4.3.1 and in Equation 2-44 below.

$$P_n = f_y A_{st} + A_{ps}\left[f_{pe} + f_y \right] \qquad \text{AASHTO LRFD 5.6.3.4.1-1} \tag{2-44}$$

where f_y (ksi) is the yield strength of the mild steel; A_{st} (in.^{2}) is the area of the mild steel; A_{ps} (in.^{2}) is the area of prestressed steel; and f_{pe} (ksi) is the stress in the prestressing steel after all losses.

The anchorage of the tensile reinforcement in the nodal regions is required for this method. If confinement is not provided for the compressive strut at the nodal zone, the code requires a reduction in the available strength according to the following anchorage types: for node regions bounded by compressive struts and bearing areas, the reduction shall be $0.85\phi f_c'$. For node regions anchoring a one-direction tension tie, the reduction shall be $0.75\phi f_c'$. For node regions anchoring tension ties in more than one direction, the reduction shall be $0.65\phi f_c'$. The tension tie reinforcement shall be distributed over an area equal to the tension tie force divided by the stress reductions just mentioned. In addition, crack control measures are required on the face of the section, with a maximum spacing of 12 in. The ratio of reinforcement to gross concrete area shall not be less than 0.003 in each direction.

2.1.3.3 Deep beam comparison: remaining codes

As mentioned previously, the remaining international codes rely on the STM for analysis of deep beams. Each of the different codes has requirements dealing with serviceability of crack control in terms of maximum spacing of vertical and horizontal reinforcement as well as reduction factors for the compression strut – in most cases based on either a rectangular stress distribution of a typical beam or a bottle shaped strut as in a diagonal compression element. Also, the compressive concrete contribution at the nodal regions is

typically reduced based on the anchorage conditions and/or stress condition at the node (i.e., one compression strut is treated differently than a node with two compression struts and one tension tie). The differences of the various codes are outlined in Table 2.3.

2.1.4 Canadian Highway Bridge Design Code

The design philosophy which underlies the Canadian Highway Bridge Design Code (CBC) is based on three limit states: the Service Limit State (SLS), Ultimate Limit State (ULS), and the Fatigue Limit State (FLS) (*CSA International 2000*). The first limit state is in place to ensure deflection requirements are met, and crack control and excess vibrations are minimized. The second limit state is the failure load for the structure, while the third limit state deals with material fatigue. Safety for the Ultimate Limit State is based on the structural reliability index β, which is defined as the ratio of the mean to the standard deviation of a random variable X. In this case, X is taken as the natural logarithm of Resistance over Load Effect (refer to Figure 2.6 for the reliability index against failure). For the Service Limit State, the variable X is taken as the safety margin, or the difference between Resistance and Load. For an intended design life of 75 years, the reliability index β is equal to 3.5.

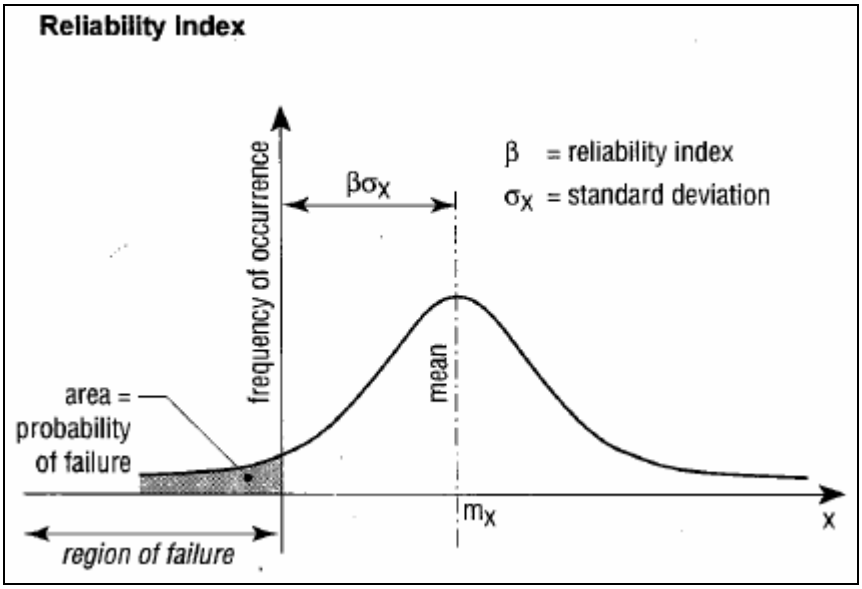


Figure 2.6: Canadian code reliability index against failure

Table 2.3: Comparison of international codes for strut-and-tie model

Code:	$V_{n\,max}$	Min A_{trans}	S_{max}	Min A_{vert}	Strut		Tension Tie	Nodal Region
					Compression		Tension	
					Rectangular	Other Shape		
ACI 318-05 (US)	$10\sqrt{f_c'}bd$	0.0025bs	$d/5 \geq 12"$	0.0015bs	$0.6375f_c'A_c$	$0.478f_c'A_c$	$0.3825f_c'A_{ct}$	$0.75A_sf_y$	$0.75[0.85\beta_n{}^{*4}f_c']A_{node}$
AASHTO LRFD 2005 (US)	-	$.0316\sqrt{f_c'}\frac{bs}{f_y}$	12" or $0.003A_g$	-	$0.70\left[\frac{f_c'}{0.8+170\varepsilon_1{}^{*1}} \leq 0.85f_c'\right]A_c$		-	$0.90[A_sf_y+A_{ps}(f_{ps}+f_y)]$	$\beta^{*7}0.70f_c'A_{node}$
CEB-FIP 1990 (metric)	-	$0.2\%A_g$	-	$0.2\%A_g$	Uncracked Section: $A_c0.85[1-f_{cl}/250]f_{cd}{}^{*2}$	Cracked Section: $A_c0.60[1-f_{cl}/250]f_{cd}{}^{*2}$	-	$f_{yd}/\gamma_s{}^{*5}$	$f_{cd}A_{node}{}^{*8}$ or $f_{cd}A_{node}{}^{*9}$
CEB-FIP 1999 (metric)	-	$0.2\%A_g$	-	$0.2\%A_g$	$A_c(1-f_{cl}/250)f_{1cd}$	$A_c\nu_2{}^{*4}f_{1cd}$	-	$f_{yd}/\gamma_s{}^{*5}$	$1.20f_{cd}A_{node}{}^{*10}$ or $3.88f_{cd}A_{node}{}^{*11}$
Eurocode 2 (metric)	-	$0.1\%A_g \geq 150$ mm^2/m	-	$0.1\%A_g \geq$ 150 mm^2/m	$A_cf_{cd}/\gamma_c{}^{*3}$	$A_c0.6(1-f_{cl}/250)f_{cd}{}^{*2}$	-	$f_{yd}/\gamma_s{}^{*5}$	$1.0[1-f_{cl}/250]f_{cd}{}^{*12}$ or $0.85[1-f_{cl}/250]f_{cd}{}^{*13}$ or $0.75[1-fck/250]fcd^{*14}$
Canadian Bridge Code (US)	-	$0.3\%A_g$ or 300 mm	-	$0.3\%A_g$ or 300 mm	$0.75\left[\frac{f_c'}{0.8+170\varepsilon_1{}^{*1}} \leq 0.85f_c'\right]A_c$		-	$0.90A_sf_y+0.95A_{ps}f_{py}$	$\beta^{*7}0.70f_c'A_{node}$

*1 $\varepsilon_1 = \varepsilon_s + (\varepsilon_s+0.002)\cot^2\alpha_s$

*2 $f_{cd} = f_{cl} / \gamma_c{}^{*3}$

*3 For persistent/transient loading, $\gamma_c = 1.5$; for accidental loading $\gamma_c = 1.2$

*4 $\nu_2 = 0.80$ for struts with cracks parallel to strut and transverse reinforcement, $\nu_2 = 0.60$ for struts transferring compression across cracks with normal crack widths such as in the webs of a beam, or $\nu_2 = 0.45$ for struts transferring compression across large cracks (members with axial tension or sections with flanges in tension)

*5 For persistent/transient loading, $\gamma_s = 1.15$; for accidental loading $\gamma_s = 1.0$

*6 $\beta_n = 0.80$ for a nodal region with 1 tie, $\beta_n = 0.60$ for a nodal region with 2 ties

*7 $\beta = 0.85$ for a nodal area with a compressive strut and bearing area, $\beta = 0.75$ for a nodal area anchoring a 1-D tension tie, and $\beta = 0.65$ for a nodal area with a tension ties in more than 1 dimension

*8 For compression only and other nodes where inclusive angle between struts is > 55 degrees and the reinforcement at the node is designated "with special care"

*9 Required at a node where main tensile bars are anchored

*10 For nodes subjected to biaxial compression only

*11 For nodes subjected to triaxial compression only; for nodes with tensile forces, the node is checked for anchorage length and bearing stresses

*12 For compression only nodes

*13 For nodes with anchored ties in one direction

*14 For nodes with anchored ties in two directions

2.1.4.1 Canadian Bridge Code traditional beam capacity

Traditional beam design is outlined in Chapter 8 for the CBC. The Canadian code uses a sectional analysis which applies shear, moment, and torsion at the section of interest, with no regard to the flow of forces through the member; the section is simply checked for the calculated loads at the section of interest. CBC Article 8.9.2.2 sets the requirements for sections requiring transverse reinforcement, as denoted below in Equation 2-45.

$$V_f > 0.20\phi_c f_{cr} b_v d_v + 0.5\phi_p V_p \qquad \text{Canadian Bridge Code} \tag{2-45}$$

where ϕ_c is a material resistance factor equal to 0.75 for concrete from CBC Table 8.4.6; f_{cr} (MPa) is the cracking strength of the concrete; b_v (mm) is the minimum web width within a the effective depth; d_v (mm) is the effective shear depth of the section – taken as the perpendicular distance from the resultant tensile and compression forces from flexure – it shall not be less than 0.9d for non-prestressed section, where d is measured from the extreme fiber in compression to the centroid of the tension reinforcement; ϕ_p is a material resistance factor equal to 0.90 for high strength bars from CBC Table 8.4.6; and V_p (N) is the portion of any prestressing force in the direction of the applied force, taken as positive if resisting the applied shear force.

Once the section is shown to require transverse reinforcement, then the minimum required area of steel is denoted in CBC Article 8.9.2.3 and in Equation 2-46 below.

$$A_v > 0.15 f_{cr} \left(\frac{b_v s}{f_y} \right) \qquad \text{Canadian Bridge Code} \tag{2-46}$$

where A_v (mm^2) is the area of transverse steel; f_y (MPa) is the yield strength of the reinforcing steel; and s (mm) is the spacing of the transverse steel. Previous variables have been defined under Equation 2-45.

In addition to minimum area requirements, the code places a limit on the amount of vertical prestressing force on the section of interest under CBC Clause 8.9.2.4 as 400 MPa plus the effective prestress force, but not more than the yield strength of the prestressing steel. The total factored shear resistance is calculated under CBC Article 8.9.3.3. The shear resistance is taken as the individual contributions from concrete, mild steel, and prestressing tendons, as shown in Equation 2-47.

$$V_r = V_c + V_s + \phi_p V_p \qquad \text{Canadian Bridge Code} \tag{2-47}$$

where V_c (N) is the concrete contribution; V_s (N) is the mild steel contribution; and V_p (N) is the prestressed steel contribution.

The determination of the concrete contribution to shear strength is covered under CBC Clause 8.9.3.5 based on the Modified Compression Theory work of Collins and Mitchell (*1986*) Vecchio and Collins (*1986*). The code provides a simplified approach that assumes a 45º angle for the internal compressive stress. It is outlined under CBC Clause 8.9.3.4.2 and is divided between sections that meet the minimum steel requirements of CBC Clause 8.9.2.3 – shown below in Equation 2-48 – and the sections that have less than or no transverse steel – shown in Equation 2-49.

$$V_c = 0.46\phi_c f_{cr} b_v d_v \qquad \text{Canadian Bridge Code} \tag{2-48}$$

$$V_c = \left(\frac{600}{1000 + d_v}\right)\phi_c f_{cr} b_v d_v \geq 0.23\phi_c f_{cr} b_v d_v \qquad \text{Canadian Bridge Code} \tag{2-49}$$

The code also permits a general approach to the concrete contribution, shown below in Equation 2-50, which is similar to the AASHTO specifications.

$$V_c = 2.5\beta\phi_c f_{cr} b_v d_v \qquad \text{Canadian Bridge Code} \tag{2-50}$$

The β and corresponding θ terms used in Equation 2-50 are located in two tables based on two conditions: sections meeting the minimum transverse steel requirements of CBC Clause 8.9.2.3 (CBC Table 8.9.3.4.1(a)); and sections with less than or no transverse steel (CBC Table 8.9.3.4.1(b)). The commentary of CBC Clause 8.9.3.5 provides the iterative procedure for determining β and θ. First, the shear stress ratio is calculated from CBC Clause 8.9.3.5, as shown below in Equation 2-51.

$$\frac{\left(\frac{V_f - \phi_p V_p}{b_v d_v}\right)}{\phi_c f_c'} \qquad \text{Canadian Bridge Code} \tag{2-51}$$

Next, an iterative process is followed to determine the appropriate angle and corresponding value of ε_x. CBC Clause 8.9.3.6 illustrates the equation for determining ε_x as shown below in Equation 2-52.

$$\varepsilon_x = \frac{0.5N_f + 0.5\left(V_f - \phi_p V_c\right)\cot\theta + \frac{M_f}{d_v} - A_{ps} f_{po}}{E_s A_s + E_p A_{ps}} \leq 0.002 \text{ CBC} \tag{2-52}$$

where N_f (N) is the factored load acting perpendicular to the cross section acting simultaneously with V_f, including the effects of creep and shrinkage; M_f (N-mm) is the factored moment at the section of interest; A_{ps} (mm^2) is the area of prestressed steel; f_{po} (MPa) is the stress in the prestressing steel when the stress in the surrounding concrete is zero – which may be taken as 110% of f_{se} (MPa), the effective stress in the prestressing after all losses have occurred.

Leaving cot θ as an unknown, the possible values for θ are determined based on the shear stress ratio (Equation 2-51) from Table 8.9.3.4.1(a). Choose a value of θ and the corresponding value of ε_x from the table. Now, calculate the value of ε_x from Equation 2-52. Using this value of ε_x, determine the corresponding θ value from CBC Table 8.9.3.4.1(a). Check the assumed value of θ; if the value is less than the second θ, then ε_x is a conservative value. If the converse is true, repeat the steps until the initial θ value is less than the second θ. Once a satisfactory result is reached, β can be found from CBC Table 8.9.3.4.1(a).

The steel contribution to shear strength is outlined in CBC Clause 8.9.3.8 and in Equation 2-53 below.

$$V_s = \frac{\phi_s f_y A_v d_v \cot\theta}{s} \qquad \text{Canadian Bridge Code} \tag{2-53}$$

where ϕ_s is a material resistance factor equal to 0.90 for mild steel from CBC Table 8.4.6; θ is the angle of the principal diagonal compressive stresses to the longitudinal axis of the member – taken as 45 for the simplified method, or from CBC Tables 8.9.3.4.1(a) or 8.9.3.4.1(b) for sections containing the minimum transverse steel and less than or no transverse steel respectively; all other parameters have previously been introduced.

2.1.4.2 Canadian Bridge Code: deep beam capacity

As indicated previously, the deep beam analysis for all codes utilize the STM method. It was discussed in detail under the AASHTO LRFD specifications, with special attention to the differences among the active international codes.

2.1.5 Eurocode 2: Design of Concrete Structures

The European Standard EN 1992-1-1:2004 denoted as the Eurocode is the British Standard for design (*CEN 2004*). The design guide encompasses many nations and is subject to variability in terms of various factors used throughout the document. However, the code provides recommended design values in lieu of country-specific values. For the current investigation, the recommended design values were followed as opposed to country-specific values. The rationale for the code relies on a service condition and ultimate strength condition denoted as Serviceability Limit State (SLS) and Ultimate Limit State (ULS) respectively.

2.1.5.1 Eurocode 2 traditional beam capacity

Prior to application of design equations, detailing requirements for shear reinforcement must be satisfied, as outlined in Chapter 9. The first requirement, under Section 9.2.2, requires the orientation of the shear reinforcement to form an angle α between 45 and 90 degrees with the longitudinal axis of the bridge. Once orientation has been established, the requirement for the combination of closed stirrups and open stirrups – denoted in this context as links and bent up bars – are defined. The specifications require the closed stirrups (links) to encompass the longitudinal tension reinforcement and the compression

zone, with half of the stirrups to be closed. The code also requires the shear reinforcement ratio – a measurement of the shear reinforcement per unit length – to be greater than minimum value. The shear reinforcement ratio is defined in Article 9.4 and in Equation 2-54 below.

$$\rho_w = \frac{A_{sw}}{sb_w \sin\alpha} \qquad \text{Eurocode 2; 9.4} \tag{2-54}$$

where A_{sw} (mm^2) is the area of shear reinforcement within a distance s (mm); s (mm) is the spacing of the shear reinforcement measured along the longitudinal axis of the member; b_w (mm) is the web width; and α is the angle between the shear reinforcement and the longitudinal axis of the member.

The minimum shear reinforcement ratio is given in Equation 2-55 below.

$$\rho_{w_\min} = \frac{0.08\sqrt{f_{ck}}}{f_{yk}} \qquad \text{Eurocode 2; 9.5N} \tag{2-55}$$

where f_{ck} (MPa) is the 28-day compressive cylinder strength of the concrete; and f_{yk} (MPa) is the yield strength of the transverse steel.

The final condition relates to the spacing of the shear steel – both in terms of the links and bent up bars about the longitudinal axis of the member and in terms of the lateral spacing among the links and bent up bars. The maximum spacing of the link elements is shown below in Equation 2-56.

$$s_{l_\max} = 0.75d(1+\cot\alpha) \qquad \text{Eurocode 2; 9.6N} \tag{2-56}$$

where d (mm) is the effective depth of the cross section; and α has previously been defined as the angle the shear reinforcement makes with the longitudinal axis of the member.

The maximum spacing of the bent up bars is as shown in Equation 2-57.

$$s_{b_\max} = 0.6d(1+\cot\alpha) \qquad \text{Eurocode 2; 9.7N} \tag{2-57}$$

The requirement for the lateral spacing of the link and bent up bars are as shown in Equation 2-58.

$$s_{t_\max} = 0.75d \le 600mm \qquad \text{Eurocode 2; 9.8N} \tag{2-58}$$

The requirements for strength at the Ultimate Limit State is covered under Section 6.2.3 based on a truss analogy, as shown in Figure 2.7.

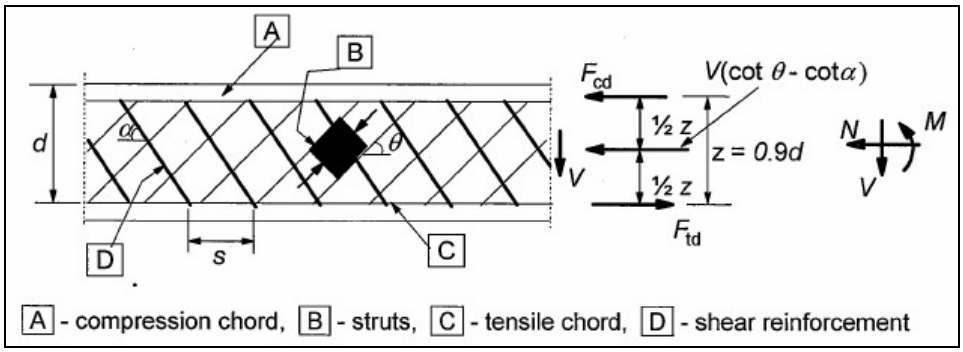


Figure 2.7: Eurocode 2 ultimate limit state truss model analogy

The shear strength is the lesser of Equations 2-59 and 2-60.

$$V_{Rd,s} = \frac{A_{sw}}{s} z f_{ywd} \cot\theta \qquad \text{Eurocode 2; 6.8} \tag{2-59}$$

$$V_{Rd,\max} = \frac{\alpha_{cw} b_w z v_1 f_{cd}}{\cot\theta + \tan\theta} \qquad \text{Eurocode 2; 6.9} \tag{2-60}$$

where A_{sw} (mm^2) is the cross sectional area of the shear reinforcement; s (mm) is the spacing of the shear reinforcement along the longitudinal axis of the bridge; z (mm) is the internal lever arm denoted in Figure 2.7; f_{ywd} (MPa) is the design yield strength of the shear reinforcement; θ is the angle of the concrete compressive strut and beam axis, perpendicular to the shear force; α_{cw} is a coefficient taking into account the state of stress in the tension chord (taken as 1.0 for non-prestressed members); b_w (mm) is the width of the web; v_1 is a strength reduction factor for concrete cracking in shear; and f_{cd} (MPa) is the design cylinder compressive strength.

The code includes several additional notes regarding the use of these equations. The first limits the value of cot θ as shown below in Equation 2-61.

$$1 \le \cot\theta \le 2.5 \qquad \text{Eurocode 2; 6.7N} \tag{2-61}$$

The recommended value of v_1 is v as described in Article 6.2.2 and shown below in Equation 2-62.

$$v = 0.6\left[1 - \frac{f_{ck}}{250}\right] \qquad \text{Eurocode 2; 6.6N} \tag{2-62}$$

If the design stress in the shear reinforcement is less than 80% of f_{yk} (MPa), then:

$$v_1 = 0.6 \text{ for } f_{ck} \le 60MPa$$

$$v_1 = 0.9 - \frac{f_{ck}}{200} > 0.5 \text{ for } f_{ck} \ge 60MPa$$

The maximum effective cross sectional area of the shear reinforcement for cot θ = 1.0 is defined in Equation 2-63 below.

$$\frac{A_{sw,\max} f_{ywd}}{b_{ws}} < \frac{1}{2}\alpha_{cw} v_1 f_{cd} \qquad \text{Eurocode 2; 6.12} \qquad \textbf{(2-63)}$$

2.1.5.2 Eurocode 2: deep beam capacity

As indicated previously, the deep beam analysis for all codes utilize the STM method. It was discussed in detail under the AASHTO LRFD specifications, with special attention to the differences among the active international codes.

2.1.6 Euro-International Committee for Concrete Publications

The CEB-FIP is a model code that provides general design guidelines for civil engineering structures; it is not specific to building, bridge, or other specialized civil infrastructure components (*CEB 1993*). However, the code does provide interpretation developing such codes within governing entities throughout Europe. As such, several codes, such as the Eurocode, are derived from the CEB-FIP. The code includes a 1990 publication, in addition to a 1999 state-of-the-industry publication denoted as practical design of structural concrete. Together, these documents represent the latest advances from academia in terms of analysis as well as a focus on safety for the analysis and design of concrete structures. The current investigation will focus on the 1990 model code, as the 1999 addition is aimed at clarification for the STM. The code utilizes a limit state approach that seeks to control deflections and vibrations at service loads (service limit state) while ensuring local element and global structural stability under the ultimate loads (ultimate limit state). In addition, the model code utilizes reduction factors for load and resistance denoted as partial safety factors. As such, the factors for specific loading combinations are increased while material strength characteristics are reduced.

2.1.6.1 CEB-FIP Model Code 1990: traditional beam design

Traditional beam design is outlined under Chapter 6: verification of the ultimate limit states. The code idealizes a beam for shear and axial loading as a truss member under subsection 6.3.3 consisting of longitudinal steel chords, compressive concrete struts, and steel web reinforcement in one or more directions. The code precludes the effects of torsion, longitudinal shear, and transverse bending within this definition. Subsection 6.3.3 further separates the analysis based on the section type with reinforced or prestressed concrete beams are treated separately than reinforced concrete columns, subject to the conditions of subsection 6.3.3.1. The first condition of subsection 6.3.3.1

relates to the reinforcement ratio of the longitudinal steel such that the section is not over-reinforced, as indicated in Equations 2-64 and 2-65 below.

$$0.0035\frac{d-x}{d} > \frac{f_{yd}}{E_s} \qquad \text{CEB-FIP 6.3-1a} \tag{2-64}$$

$$0.0035\frac{d-x}{d} > \frac{f_{yk}}{E_s\gamma_s} \qquad \text{CEB-FIP 6.3-1b} \tag{2-65}$$

where d (mm) is the effective depth of the section, x (mm) is the height of the compression block, f_{yd} (MPa) is the design yield strength of the longitudinal reinforcement, E_s (MPa) is the modulus of elasticity of the longitudinal reinforcement, f_{yk} (MPa) is the characteristic design yield strength of the longitudinal reinforcement, and γ_s is a partial material factor equal to 1.15 for persistent/transient events and 1.0 for accidental events (taken from Table 1.6.2 for reinforcing steel). The second condition under subsection 6.3.3.1 relates to the area of transverse steel, denoted in the code as the mechanical ratio in Equation 2-66 below.

$$\omega_{sw} = \frac{A_{sw} f_{yk}}{b_w s f_{ctm} \sin\alpha} \geq 0.2 \qquad \text{CEB-FIP 6.3-1b} \tag{2-66}$$

where A_{sw} (mm^2) is the area of transverse reinforcement, f_{yk} (MPa) is the yield strength of the transverse reinforcement, b_w (mm) is the width of the web, s (mm) is the spacing of the transverse reinforcement perpendicular to the longitudinal axis of the member, α is the angle between the transverse reinforcement and the longitudinal axis of the member, and f_{ctm} (MPa) is the mean characteristic tensile strength of the concrete. The mean tensile strength is defined under subsection 2.1.3.3.1 and in Equation 2-67 below.

$$f_{ctm} = f_{ctko,m}\left(\frac{f_{ck}}{f_{cko}}\right)^{\frac{2}{3}} \qquad \text{CEB-FIP 2.1-4} \tag{2-67}$$

where $f_{ctko,m}$ (MPa) is equal to 1.40 MPa, f_{cko} (MPa) is equal to 10 MPa, and f_{ck} (MPa) is the characteristic compressive strength of the concrete. In addition to minimum area requirements, the code requires the inclination of the stirrups to the longitudinal axis be at least 45 degrees and 30 degrees for bent up bars while the spacing of stirrup legs (longitudinal and transverse) shall not exceed the lesser of 0.75d or 800 mm. Finally, the code requires the shear reinforcement to be adequately anchored to the chords.

Once the requirements of subsection 6.3.2 are satisfied, the code identifies the value for the components of the idealized truss. Starting with the tension chord, the maximum force is as indicated in Equation 2-68).

$$F_{st} = \frac{|M_{Sd}|}{z} + N_{Sd}\frac{(z - z_s)}{z} + \frac{V_{Sd}}{2}(\cot\theta - \cot\alpha) \quad \text{CEB-FIP 6.3-4} \tag{2-68}$$

where M_{Sd} (N-mm) is the moment at the section of interest, z (mm) is the internal lever arm between the resultant chord forces, N_{Sd} (N) is the axial load taken positive for tension and negative for compression, z_s (mm) is the distance from the line of action of the axial force N_{Sd} to the centroid of the tension reinforcement, V_{Sd} (N) is the shear force at the section of interest, θ is the angle the compression strut makes with the longitudinal axis of the member, and α is the angle of the transverse reinforcement with the longitudinal axis of the member. If support reactions and/or direct loads are applied to the section as to induce transverse compression along the depth, then the tension force is limited by Equation 2-69.

$$F_{st} \le \frac{|M_{Sd,\max}|}{z} + N_{Sd}\frac{(z - z_s)}{z} \quad \text{CEB-FIP 6.3-5} \tag{2-69}$$

For cases in which the tensile reinforcement is entirely contained in the web of a section, the tension chord force may be determined from Equation 2-70 below.

$$F_{Rt} = A_s f_{yd} \quad \text{CEB-FIP 6.3-6} \tag{2-70}$$

Moving to the compression chord, the allowable force is shown in Equation 2-71 below.

$$F_{Sc} = \frac{|M_{Sd}|}{z} - N_{Sd}\frac{z_s}{z} - \frac{V_{Sd}}{2}(\cot\theta - \cot\alpha) \quad \text{CEB-FIP 6.3-7} \tag{2-71}$$

Equation 2-71 governs except in the case of direct loading at the location of maximum moment, in which case Equations 2-72 and 2-73 govern.

$$F_{Sc} = \frac{|M_{Sd,\max}|}{z} - N_{Sd}\frac{z_s}{z} \quad \text{CEB-FIP 6.3-8} \tag{2-72}$$

$$F_{Rc} = f_{cd1}A_c + f_{ycd}A_{sc} \quad \text{CEB-FIP 6.3-9} \tag{2-73}$$

where f_{cdl} (MPa) is the design strength of the concrete in the compression chord, A_c (mm^2) is the area of the compression chord, f_{ycd} (MPa) is the yield strength of the transverse steel, A_{sc} (mm^2) is the area of transverse steel within the compression chord. The compressive concrete strut force is limited to Equations 2-74 and 2-75 below.

$$F_{Scw} = \frac{V_{Sd}}{\sin\theta}\left(\frac{\cot\theta}{\cot\theta + \cot\alpha}\right) \quad \text{CEB-FIP 6.3-10} \tag{2-74}$$

$$F_{Rcw} = f_{cd2}b_w z\cos\theta \quad \text{CEB-FIP 6.3-11} \tag{2-75}$$

where V_{Sd} (N) is the design value the acting design shear force and f_{cd2} (MPa) is the design yield strength of the concrete in the compressive strut; the remaining parameters have previously been defined. The final component, the tension of the web steel, is denoted in Equations 2-76 and 2-77 below.

$$F_{Stw} = \frac{V_{Sd}}{\sin\alpha} \qquad \text{CEB-FIP 6.3-12} \tag{2-76}$$

$$F_{Rtw} = \left[\frac{A_{sw} f_{yd}}{s}\right] z\left(\cot\theta + \cot\alpha\right) \qquad \text{CEB-FIP 6.3-13} \tag{2-77}$$

where A_{sw} (mm^2) is the area of the transverse steel, f_{yd} (MPa) is the yield strength of the transverse steel, and the remaining parameters have previously been defined.

2.1.6.2 CEB-FIP Model Code 1990: deep beam analysis

As noted previously, the deep beam analysis among the active international codes rely on the STM method for analysis. The STM is described in detail under the AASHTO LRFD section, with special attention given to the differences of the method among the active international codes.

2.2 EARLIER WORK

2.2.1 Epoxy injection repair

The application of epoxy resin for highway maintenance began during the early 1950's. At the forefront of epoxy material testing was the California Division of Highways Materials and Research Department (*Rooney 1963*). Studies utilizing small-sized plain concrete prisms demonstrated that the bond strength of properly applied epoxy was greater than that of the concrete tensile strength (*Tremper 1960*). Rupture occurred in the concrete and not in the adhesive bond layer irrespective of the loading conditions (shear, flexure, or tension). Some of the first uses for epoxy in highway maintenance were patching of damaged roadways and securing reflective traffic markers. Early applications of epoxy injection were performed with a grease gun and were found through observation to improve plate bonding for expansion joints.

As epoxy materials became more widely used, researchers began to investigate the effects of epoxy injection on reinforced concrete members. Early tests to evaluate the performance of epoxy-injected reinforced concrete beams were performed by Chung (*1975*). Each of the three beam specimens in this study measured 125 x 200 mm (5 x 8 in.) with a clear span of 2754 mm (9 ft). Longitudinal and transverse reinforcement were provided, and each specimen was loaded to failure and then injected with epoxy resin. Chung observed that epoxy restored the capacity and integrity of the failed specimens.

Another study conducted by Popov and Bertero examined the behavior of full-scale and half-scale reinforced concrete specimens injected with epoxy and exposed to reversed cyclic loading

(*Popov and Bertero 1975*). The steel detailing and member proportions were typical of large-sized, short-span cantilevers and beam-column sub-assemblages for buildings. Complete hysteretic loops were recorded for each of the three specimens in the study, which characterized the cyclic behavior of the injected specimens. They observed that epoxy injection improved the original strength of the specimens but exhibited reduced overall stiffness. At locations where severe rebar-concrete bond degradation occurred, the epoxy did not perform as well. Additional research by Chung (*1981*) noted that epoxy injection of small 200 x 300 x 2000 mm (7.9 x 11.8 x 78.7 in.) reinforced concrete beams was not an effective means to restore or improve rebar-concrete bond performance.

Basunbul, et al. compared several repair methods for reinforced concrete beams, one of which was epoxy injection (*Basunbul, et al. 1990*). Nine epoxy-injected specimens measuring 150 x 150 mm (5.9 x 5.9 in.) in cross section and 1250 mm (49.2 in.) long, with longitudinal and transverse reinforcement, were loaded to induce varying degrees of flexural damage. Cracks were injected with epoxy resin and allowed to cure before each specimen was loaded to failure. The loads required to re-initiate cracking were observed to be higher for the injected specimens compared to the original member response.

In more recent years, the effects of environment and fatigue have been included in studies of epoxy-injected specimens. Abu-Tair, et al. investigated concrete beams reinforced with transverse and longitudinal steel and measuring 205 x 140 mm (8 x 5.5 in.) in cross section with a 2300 mm (90.6 in.) span (*Abu-Tair, et al. 1991*). Seven specimens were loaded in flexure to failure and then injected with epoxy resin. Upon reloading, several of the specimens were tested statically, while others were fatigue loaded with varying magnitudes. Additionally, two of the specimens were soaked in 38 ºC (100 ºF) water to investigate the effect of water absorption on durability and performance. The results of the study indicated that epoxy injection restored the original strength and stiffness of the beams regardless of the loading conditions, and the four months of water immersion had insignificant effects.

Only a small fraction of the research performed to date on epoxy injection has incorporated full-scale specimens with realistic steel reinforcing details. No data are available for shear response of epoxy injected CRC girders, and few researchers have investigated loading conditions on the curing and bonding of epoxy resin. Furthermore, reduced-sized specimens may not accurately replicate strain fields and behavior of large reinforced concrete members. Other important issues to consider are in-service loading responses and localized behavioral effects, incorporation of service-induced diagonal cracks, and effects of load and shrinkage strains on epoxy-injected member performance.

2.2.2 External steel stirrup repair

Mihn, et al. produced the earliest publication utilizing external steel stirrups as one of five different repair methods for traditionally reinforced concrete beams (*Minh, et al. 2001*). The experimental program included six half-scale square beams, including one control specimen, with identical longitudinal reinforcement ratios, no integrally cast steel stirrups, and a shear span-to-depth ratio of 3.85. Dimensions of the beams were 300 mm (11.81 in.) in height/width including a shear span of 1000 mm (39.37 in.). The components of the repair included two-10

mm (0.39 in.) diameter steel rods attached to a steel angle section (L50 x 50 x 8) about the top and bottom of the beam. The experimental program did not include initial loading of the specimens prior to application of the repair materials. Of the five repair specimens, only the external stirrup specimen failed in flexure. A corresponding Finite Element Model (FEM) for the external stirrup specimen indicated a shear failure at a load slightly lower than the experimental results. The authors attributed the difference in the failure mode to an unreported prestress force applied to the external stirrups that was not accounted for in the FEM. The article did not give guidance as to strength gain from the external stirrups with respect to governing codes or recommendations for future research needs of the repair method.

Altin, et al. utilized external steel stirrups on traditionally reinforced concrete T beams (*Altin, et al. 2003*). The experimental program included 13 half-scale beams with two different shear span to effective depth (a/d) ratios (3.3 and 4.5) and identical longitudinal reinforcement. The beam dimensions were 360 mm (14.17 in.) deep, with a flange width of 360 mm (14.17 in.), a web width of 120 mm (4.72 in.), and a flange thickness of 75 mm (2.95 in.). The repair media included 60 mm (2.36 in.) square by 10 mm (0.39 in.) thick steel plate washers on the top of the flange with two-500 mm (19.68 in.) long partially threaded steel rods extending through holes in the flange terminating at a 40 mm (1.57 in.) by 40 mm (1.57 in.) by 10 mm (0.39 in.) thick steel tube section at the base of the stem secured with 40 mm (1.57 in.) square by 10 mm (0.39 in.) thick steel plate washers and high strength nuts. Details of the specimens and their repair method are shown in Figure 2.8.

Within each group of a/d ratios, both the integrally cast and externally applied stirrup spacing was varied. Of the 13 specimens, three were designated as control and one specimen was strengthened with external stirrups but devoid of integrally cast stirrups. The remaining nine specimens consisted of two distinct repair types. The first group included seven beams with varying a/d ratios which were strengthened with external stirrups prior to application of load and consequently loaded to failure; the second group of two beams included one from each a/d ratio which were loaded up to 60% of the estimated base capacity of the section, unloaded, repaired, then loaded to failure. All repair specimens were designed to be under strength for shear, with an anticipated flexural failure mode after strengthening.

The research program produced several noteworthy results. The calculated capacities, based on ACI 318, were 20% to 30% higher than the experimental results for the specimens strengthened prior to application of load, but 6% to 7% lower than the experimental results for the specimens strengthened after cracking was achieved. The article gave recommendations for future work, including the need to identify load sharing among internal and external stirrups in terms of strain compatibility. The article did not investigate losses due to deformations of the tube section or compare results with design codes other than ACI 318.

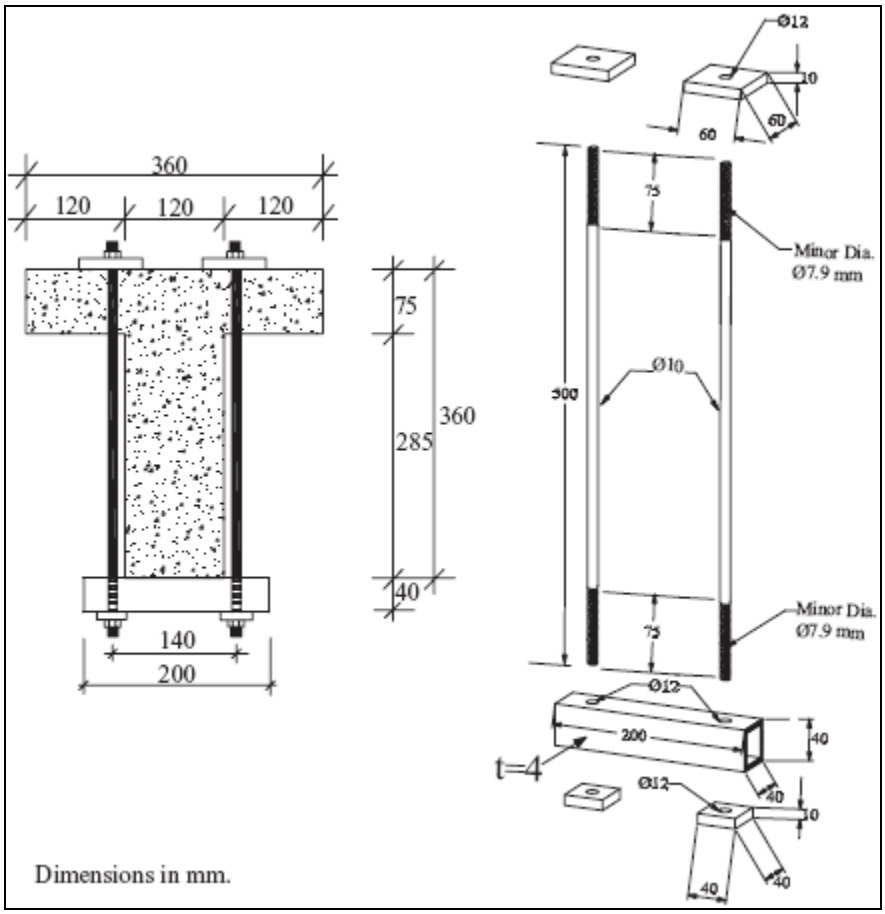


Figure 2.8: External stirrup repair scheme from Altin, et al.

Kim, et al. utilized wire rope as an external strengthening method (*Kim, et al. 2007*). While this is not a direct comparison to the method utilized in the current study, the common goal of applying a post-tensioning force about the transverse axis of the beam is achieved. The experimental study included 15 quarter-scale beams with three differing shear span to effective depth (a/d) ratios of 1.5, 2.5, and 3.25 to encompass deep beam specimens. Beam specimens were 400 mm (15.75 in) deep and 200 mm (7.87 in.) wide. The beams were devoid of integrally cast stirrups, relying on the rope units and concrete contribution to shear capacity. The repair apparatus included a wire rope that formed a U shape about the bottom of the beam; it was attached to a 20 mm (0.79 in.) thick steel plate at the top of the beam via two I-bolts with corresponding nuts and washers. An angle section at the lower corner of the web completed the repair method in order to minimize local crushing of the concrete. Details of the repair scheme are shown in Figure 2.9.

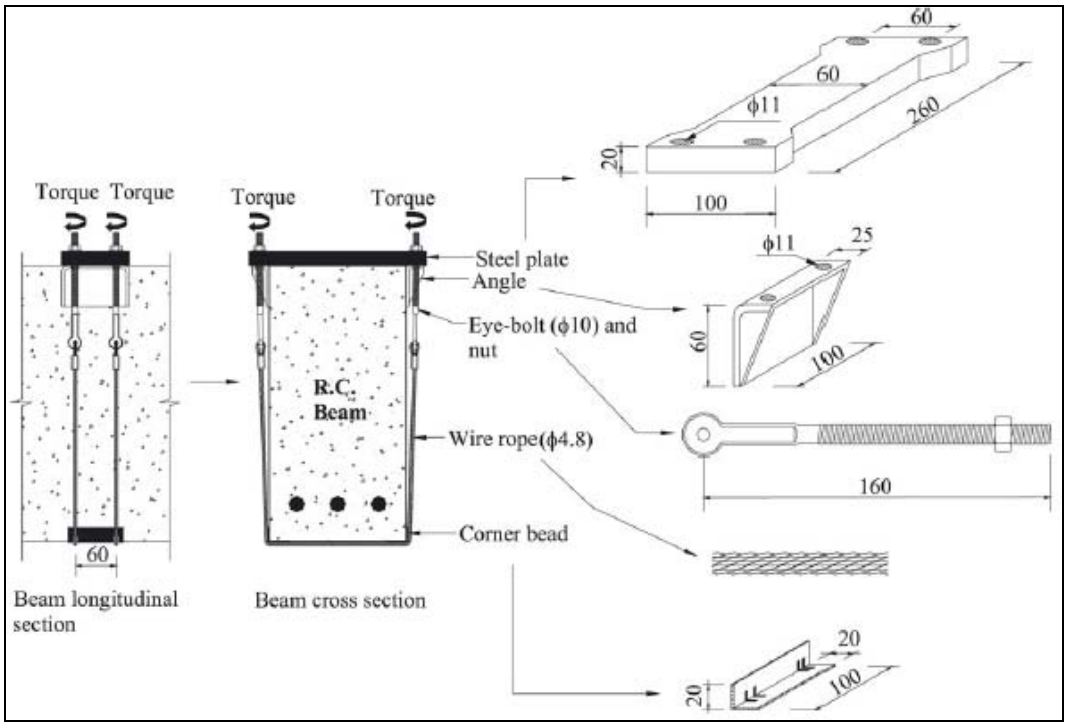


Figure 2.9: External stirrup repair scheme from Kim, et al.

The experimental program considered the effect of epoxy injection as a standalone repair, the inclination of the wire rope units to the longitudinal axis of the beam, prestress force applied to the wire rope units, and the spacing of the wire rope units for a fixed prestressing force for each a/d ratio. Within this framework, all the beams were incrementally loaded to failure (defined in the article as formation of a single shear crack due to a lack of integrally cast stirrups), unloaded, then repaired with epoxy injection. One beam for each a/d ratio was tested to failure with epoxy injection as the only repair. The remaining beams in each group were repaired with the wire rope units at 45 and 90 degrees to the longitudinal axis of the beam, with the prestress force kept at a constant 46 kN (10.43 Kip). However, for beams with an a/d ratio of 2.5, the prestressing force was varied from 33.2 kN (7.46 Kip) to 60 kN (13.49 Kip) for both the orthogonal and inclined repair.

Results from the tests were compared to ACI 318-05 (including a STM comparison for the deep beam specimens) and Eurocode 2. Due to the lack of internal stirrups, the capacity equations simply used the area of the wire rope units for the steel contribution to shear strength. All test specimens failed in shear after repair. Conclusions from the experimental program indicated that the use of inclined wire rope units provided higher shear capacity when compared to the orthogonal wire rope units, due to a closer alignment to the principle axis stress in the concrete. Higher shear capacity was achieved within the 2.5 a/d ratio group by increasing the post-tensioned force in the wire rope units. Comparisons with the two codes indicate that the ACI 318-05 analysis method is conservative for a shear-to-depth ratio below 2.5, while the Eurocode is unconservative for shear-to-depth ratio of 3.25.

Shamsai, et al. published an article that dealt with remedial strengthening of traditionally reinforced concrete girders for earthquake loading (*Shamsai, et al. 2007*). The research plan included 24 quarter-scale rectangular beams, including three control specimens, with longitudinal reinforcement ratios of ½ ρmax and ⅔ ρmax as defined by ACI 318-95 corresponding to two different shear spans. Beam dimensions were 150 mm (4.72 in.) deep, 80 mm (3.15 in.) wide, with shear spans of 420 mm (16.53 in.) and 275 mm (10.83 in.), representing a/d ratios of 3.5 and 2.3 respectively. The beams were subjected to four point loading such that integrally cast steel stirrups were included only in the middle section of the beam. The repair apparatus consisted of unequal leg steel angles, placed such that the longer end was in bearing with the beam, a steel plate and elastomeric pad just below the angles along the top and bottom of the beam intended to distribute the vertical force over the entire shear span, and two connecting rods and associated hardware. Specimen details and repair apparatus are shown in Figure 2.10.

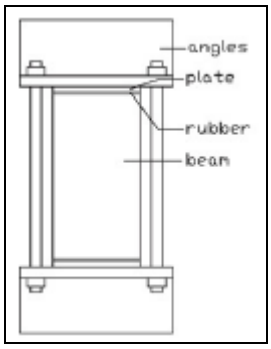


Figure 2.10: External stirrup repair scheme from Shamsai, et al.

The testing protocol included seven beams which were loaded until a shear crack propagated in the shear span, unloaded, repaired, then loaded to failure; it also include beams repaired prior to application of load. The experimental program also included two post-tensioning forces within the shear span equal to $0.04f_c'$ and $0.075f_c'$. Capacity of the section reflected the traditional approach from ACI by including the contribution from the concrete and steel separately, with the addition of a third term to compensate for the external stirrups. Results from the experimental work indicated that increasing the shear capacity regardless of the presence of integrally cast stirrups or shear cracks resulted in a traditional flexural failure. Thus, due to the failure mechanism, it was not possible to identify the amount of shear contributed by the external stirrups. Also, due to the small scale of the specimens, large angle sections, and plate section used between the angle and concrete surface, the effective bearing area of the reaction sections produced a post-tensioning force distributed evenly over the shear span. At full scale, the use of a similar setup may be cost/weight prohibitive.

2.2.3 Internal supplemental steel stirrup repair

The earliest and most complete account of utilizing internal supplemental steel stirrups to strengthen traditionally reinforced concrete specimens was provided by Kansas Department of

Transportation (KDOT) from 1976 to 1984 (*Stratton, et al. 1977; 1978; 1982*). Kansas' bridge inventory at that time included several hundred adjacent two-girder cast-in-place deck girder bridges, a majority of which were multi-span bridges continuous over intermediate supports. The bridges were lightly reinforced for shear, having been designed with the AASHO code coincident with construction (1955-1965) (*AASHO 1953*). Consequently, the bridges began to exhibit shear cracks primarily near the interior supports. Originally, the problem was thought to be simply a maintenance issue, with the objective to seal the cracks that formed as a preventative measure against corrosion. The initial remedy was to seal the cracks with a two-part epoxy injected under low pressure. However, this method was abandoned because over time, the crack would reopen. Due to this observation, KDOT looked at a method which involved temporary shoring of the beam at the interior support, removal of the cracked concrete, placing additional mild steel in the location, and finally restoring the beam to its original shape with additional scab concrete. The method was effective, but it was expensive and resulted in temporary closure of the bridge for an extended period of time.

A third solution was implemented – as reported by Stratton, et al. – that required the insertion of mild steel within the center of the beam, utilizing a drill rig and vacuum system capable of drilling a hole at any angle in a matter of minutes from the top of the deck (*Stratton, et al. 1977*). After trial and error with existing machinery within the maintenance department, a rig was developed capable of drilling a 19 mm (0.75 in.) diameter hole a distance of 2.1 m (7 ft) to 2.4 m (8 ft) in a time of 22 minutes. After drilling, half of the drilled hole was filled with a two-part epoxy, and a grade 420 MPa (60 ksi), 15.8 mm (0.625 in.) diameter bar was inserted in the hole. Gravity leakage of the epoxy to the outer limits of the girders during the initial test was rectified in subsequent applications.

Two additional reports by Stratton, et al. outlined the progress of the program and future plans (*Stratton, et al. 1978, 1982*). The development of an industrial drilling rig was required due to the harsh conditions of drilling a small diameter hole a relatively long distance. Upon completion of the new drill rig, additional repairs were completed. Also, a method to seal the outer crack surface in a quick efficient manner was proposed. At the completion of the year, 19 girders were repaired, at an estimated savings of over $1 million (1978 dollars) for the comparable repair noted earlier. Thus, the initial investment in equipment and training proved cost effective. The two reports also documented a computer analysis program used to determine the additional shear strength gain, utilizing the additional area of steel from the 1981 AASHTO shear equations.

Engineering calculations at the time estimated the use of supplemental internal stirrups used in Kansas provided a shear strength increase 10% above the 1981 AASHTO standard. However, no laboratory tests were concluded to determine the actual strength gain for the specimens. The assumption of using an additional area of steel consistent with the shear equations in AASHTO has not been confirmed. On the other hand, many of the repaired bridges still remain within Kansas' bridge inventory; the durability of the epoxy and overall repair method has stood the test of time. Recent contact with KDOT's maintenance engineers indicate that the bridges repaired with this method have shown no additional signs of shear distress over a period of roughly 30 years. Thus, while the actual strength gain for this repair methodology has not been validated by conventional laboratory tests, serviceability and crack control over a large population of different

span lengths and varying concrete strengths over an extended period of time attest to the durability of the repair.

The primary concern regarding supplemental internal stirrups is with regard to the shear strength of the epoxy matrix to the steel reinforcing bar and surrounding concrete. A comprehensive study by Cook, et al. proposed a simplified model for concrete anchors which included a review of 2,929 bond tests with varying embedment depths, concrete strengths, number of anchors, cracked or uncracked concrete, different epoxy manufacturers, confined and unconfined concrete, and loading near or away from the free edge of the specimen (*Cook, et al. 1998*). The number of tests was reduced to include only unconfined tension tests of threaded rod and reinforcing bar anchors tested at least a distance equal to the embedment length away from the free edge and where the cored/drilled hole was clean, dry, and free of dust. The reduction also excluded steel failures, which reduced the number of tests to 888. The effects of hole diameter d, embedment depth h_{ef}, and concrete strength f_c were determined according to a least squares approach. The variations of parameters are shown below in Figure 2.11. From hundreds of tests, the main variation appears to come from the concrete strength (while the comparable variation for hole diameter and embedment depth can be essentially taken as 1.00 with a 0.25 coefficient of variation), indicating that for some epoxy manufacturers, a variation in concrete strength has a great effect on the resulting capacity of the anchor system.

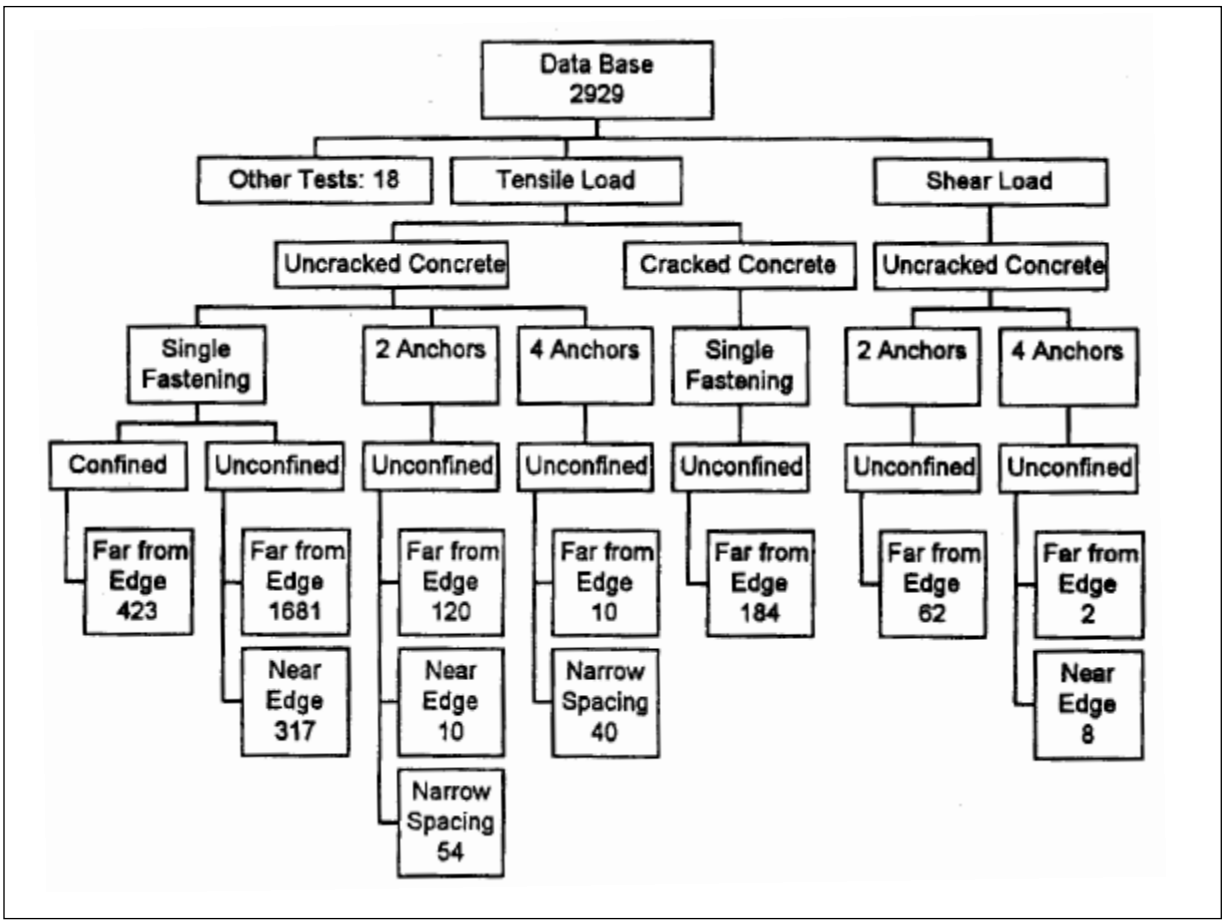


Figure 2.11: Bond model variations based on tests compiled by Cook, et al.

Throughout the literature review of bond models for concrete anchors, Cook, et al. determined six primary failure models:

- The first model identifies failure primarily from a cone shaped pullout, such that the capacity of the system is a function of the square root of the concrete compressive strength and the embedment depth; no dependency on the diameter of the anchor is required.

- The second model identifies a bond failure of the epoxy matrix at the interface of the reinforcing bar or anchor with no mention of a cone failure. In this case, failure is defined as a function of the bond strength of the surrounding epoxy, the diameter of the bar, and the embedment depth.

- The third model is also based on bond failure, but it takes into account a shallow cone pullout by reducing the effective depth of the anchor if such a failure occurs.

- The fourth model assigns failure from a cone model for shallow depths and a bond failure for deeper embedment.

- The fifth model looks at a cone failure for shallow depths, with a combined cone/bond failure for deeper embedment depths.

- The sixth failure model accounts for the interface stresses between the adhesive/steel and the adhesive/concrete locations.

After introducing the six design models in the literature, the authors compare the design equations for the six methods to a uniform bond stress model. Comparisons of the uniform bond model to the database of 888 tests indicate a good fit when compared to the models which differentiate between shallow cone failure and/or a mixture of shallow cone and bond failure. However, the sixth model, which accounts for the interface stresses between the adhesive and concrete/steel, produced the best fit.

An experimental program by Colak looked at the influence of embedment length, adhesive thickness, percentage of filler material, and type of two-part epoxy used on simple direct pull-out tests of deformed mild steel reinforcing bars (*Colak 2001*). Two types of epoxy were used, denoted as EP1 and EP3, with the same resin, reactive diluents, but differing curing agents. Each epoxy also had a varying level of filler content, denoted as EP2 and EP4 relating to EP1 and EP3 respectively, in order to identify what effect the filler had on the shear modulus of the epoxy.

The investigation looked at three different embedment lengths – 50 mm (1.97 in.), 75 mm (2.95 in.), and 100 mm (3.94 in.) – as well as adhesive thickness varying from 1 mm (0.04 in.) to 4 mm (0.16 in.) for epoxies EP1 and EP3. The effect of increasing the embedment length indicated a linear bond stress relationship for the 50 mm (1.97 in.) embedment, turning toward a higher order curve as the embedment length crossed the 75 mm (2.95 in.) plateau for both epoxies.

Results for filler up to 46% indicated a similar shear strength between the epoxies, decreasing and diverging (with EP2 having a higher modulus) as the filler neared 74%. Epoxies EP1 and EP3 (with no fillers) were used in determining the effect of epoxy thickness with shear modulus. Results indicated that the shear strength for EP1 increased as the epoxy thickness increased from 1 mm (0.04 in.) to 2 mm (0.08 in.), but decreased at 3 mm (0.12 in.) and finally became static from 3 mm (0.12 in.) to 4 mm (0.16 in.). On the other hand, epoxy EP3 was consistent through the range of thicknesses. It is noteworthy that the results of each thickness were based on a series of three tests, indicating it was not likely that the increase for EP1 at a thickness of 2 mm (0.08 in.) was due to experimental error.

Another investigation by Hammad, et al. compared the bond capacity of integrally cast straight and 90 degree hooked bars meeting the minimum embedment depths provided by ACI 318-05 with post-inserted straight bars secured with two commercially available epoxies (*Hammad, et al. 2006*). The authors proposed that steel reinforcing bars meeting minimum spacing requirements and/or having confining steel to prevent a splitting failure anchored with epoxy should provide a bond greater than or equal to that of an integrally cast bar. The authors investigated the termination detail of a floor slab into a wall. Due to space limitations, bars extending from a girder or floor slab into a wall are typically bent utilizing a 90 or 180 degree hook, as recommended by Section 12 of ACI 318-05 to reach the yield strength of the bar. The scope of work included two bar sizes, three development lengths, two concrete strengths, and

two epoxies; all reinforcing steel for the project met the deformation requirements of ASTM 615, Grade 420 (60 ksi).

As the purpose of the experimental program was to investigate additions or use changes resulting in structural detailing of buildings, the authors modeled the connection of a floor slab to a column as the location of a possible tie-in point, as shown in Figure 2.12, with two cantilever vertical sections anchored to a horizontal section. As such, the specimens were modeled using the STM method which requires equilibrium at the location of the joint or node. Based on the geometry of the node, the value of the resultant inclined compressive force C_0 and the angle θ formed between the vertical tensile force from the post installed anchor and the resultant compressive force from the vertical member, as shown in Figure 2.13, were determined.

The results of the experiment showed that variations in concrete strength and bar diameter had little effect on the failure modes of the post-installed bars compared to the integrally cast bars. The failure loads indicate the integrally cast hooked bars provided the greatest anchorage, followed by bars secured with epoxy No. 2, epoxy No. 1, and finally the integrally cast straight bars. All but the shallowest embedment lengths resulted in yielding of the reinforcement just prior to failure of the concrete cover and subsequent pullout of the bars. The shortest embedment depths resulted in a cone type failure which is indicative of a direct tension failure mode.

Another interesting aspect of the research relates to the failures with respect to the angle of the inclined strut C_0 and the horizontal direction, defined by θ. For angles of θ less than 30 degrees, the ACI method for embedment overestimated the capacity of the connection, but for values between 35 and 50 degrees, the method quite accurately predicts the ultimate strength of the connection.

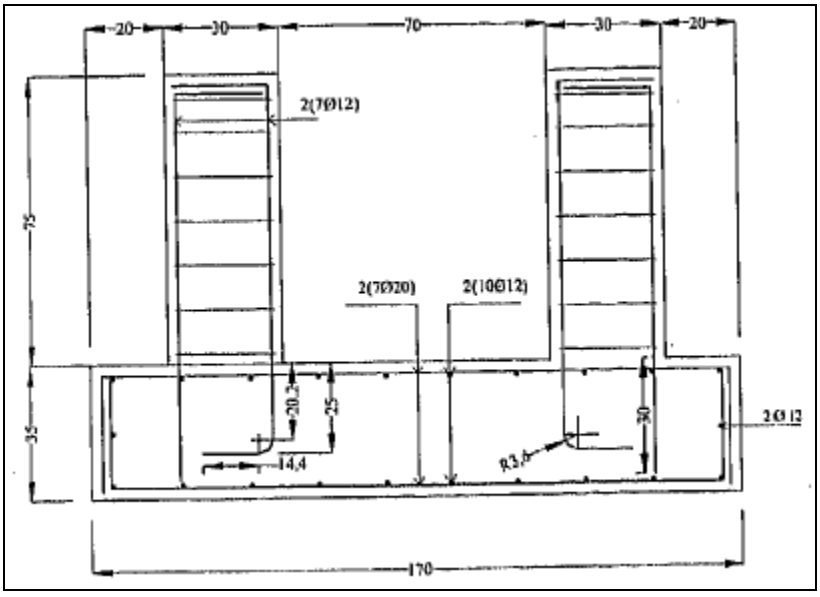


Figure 2.12: Test setup for post installed anchors taken from Hammad, et al.

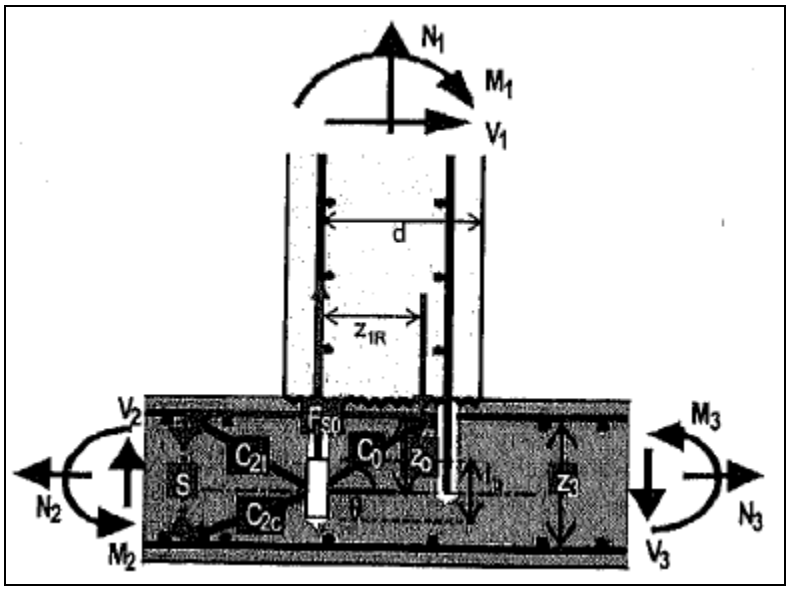


Figure 2.13: Force diagram for post installed anchors taken from Hammad, et al.

2.2.4 Surface bonded Carbon Fiber Reinforced Plastic (CFRP) repair

Carbon Fiber Reinforced Plastic (CFRP) has been used with great success in the aerospace industry, but has only gained attention for use in civil infrastructure applications over the past two decades. Historically, the early use of CFRP for flexural repair is well documented within the available literature. However, a shift toward shear repair methods for CFRP began in the early 1990s. Moreover, many of the recommendations from the influx of articles by researchers since that time have been incorporated into the current ACI 440 recommendations. Thus, the bulk of the literature review in this area will account for the major articles that have contributed to the ACI 440 recommendations; in this light, the review is not intended to be an exhaustive list on the subject.

One of the first papers to investigate repair of concrete beams by way of CFRP sheets was undertaken by Chajes, et al. (*1995*). The experimental program included 12 quarter-scale T beams devoid of integrally cast stirrups which included four control specimens and three different woven fabric configurations: aramid, E-glass, and graphite. The beam dimensions were 1219 mm (48 in.) long, 191 mm (7.5 in.) deep, with a flange width of 140 mm (5.5 in.), a web width of 64mm (2.5 in.), and a shear span of 406 mm (16 in.) (a/d ratio of 2.67). The composite materials were applied prior to loading of the specimens utilizing the three-sided U-wrap and designed to fail in shear even with the anticipated increase in capacity from the composite materials.

In order to determine the bond characteristics of the two-component epoxy with respect to the three composite materials, single shear pull-off tests were performed on a 1 in. width of each material. The anchorage lengths varied from 25 mm (1 in.) to 76 mm (3 in.) and indicate that the development length for the E-glass and graphite fabric required to reach fracture of the material

was 25 mm (1 in.), while the aramid fabric required 76 mm (3 in.). Failure modes for the graphite and E-glass beams were due to rupture of the composite material at the location of the shear failure crack, while the aramid woven fabric failed by bond. Failure strains indicated that the full capacities of the composite materials were not obtained. In spite of this, the shear contribution of the composite materials were back-calculated by subtracting the concrete contribution (as determined from ACI 318-89) from the total shear load. A corresponding design equation for the composite material contribution was presented. The contribution of the composite material was limited by strain equal to 0.005 in/in based on experimental work.

The results of the initial study lead to a second investigation by Chajes, et al. to investigate bond and force transfer between the epoxy and composite material as they pertain to concrete surface preparation, type of adhesive, and concrete strength (*Chajes, et al. 1996*). The test setup was as previously described, with a constant development length of 76 mm (3 in.), which corresponded to the longest length for rupture of the aramid fiber in the previous study. The investigation looked at four commercially available epoxies: Sikadur 32 Hi-Mod, Sikadur 31 Hi Mod gel, and two manufactured by the Lord Corporation – Tyrite 7500 and Fusor 320/322.

Results of the surface preparation indicated that mechanical abrasion resulted in the highest average bond stress when compared to grinding and the as-formed surface. Failure of the bond tests for all but the Tyrite epoxy exhibited concrete shear failure, while the Tyrite sample failed within the epoxy matrix. The tests also indicated average bond stress increased with increasing concrete compressive strength. The experimental program investigated the strain distribution of the composite materials along the bonded length. General trends for lengths of 51, 102, 152, and 203 mm (2, 4, 6, and 8 in.) indicated the distribution was highest at the start of the bonded length, decreasing to zero strain at the free end.

Sato, et al. conducted an experimental program using six quarter-scale rectangular beams including one control specimen (*Sato, et al. 1996*). Beam dimensions were 200 mm (7.87 in.) in width, 300 mm (11.81 in.) in depth, with a shear span of 700 mm (27.56 in.), tested under four point loading. The shear span of all but one of the CFRP repaired beams were cast devoid of stirrups. The beams were repaired with both side and U-wrap orientation schemes, with discrete and continuous strips over the length of the shear span; no load was applied prior to application of the FRP. Failure modes for the beams without integrally cast stirrups resulted from diagonal tension failure after delamination and peeling of the FRP, while the specimen that included integrally cast stirrups in the shear span failed in a flexural mode. The authors provided general equations for calculating the FRP contribution to shear, but they did not include the effect of bond stress in their simplified equations. The paper did provide the first experimental data that validates the use of a three-sided U-wrap compared to a side wrap that terminates at the base of the web.

Norris, et al. tested six quarter-scale rectangular beams, including one control specimen (*Norris, et al. 1997*). Beam dimensions were 127 mm (5 in.) wide, 203 mm (8 in.) deep, with a 457 mm (18 in.) shear span (a/d ratio of 2.69). The specimens were repaired with a three-sided U-wrap both prior to application of load and after application of a precrack load. The investigation also included unidirectional and 45 degree strand orientations within the FRP. By applying the two FRP fabrics in the same U-shaped repair scheme, the principle tensile strength of the FRP was

changed based on the fiber orientation. Results indicated no significant difference in strength gain for precracked versus virgin specimens. Also, the beams with the fiber oriented at 45 degrees achieved higher load than the corresponding unidirectional fiber orientation – based on the fact that the 45 degree fibers were aligned closer to the principle tensile stresses in the concrete. The authors also provided strength contribution equations similar to Sato, et al., only noting that the effect of limited bond stress may reduce the contribution from FRP and that further work is needed in this area.

Kachlakev and McCurry investigated the flexural and shear repair of an existing historic structure slated for rehabilitation (*Kachlakev and McCurry 2000*). Due to the age of the structure, changing the physical appearance was prohibited; thus FRP was chosen as the repair material. The in-service rectangular beams were replicated by four full-scale specimens, including one control specimen, in the laboratory. Beam dimensions were 305 mm (12 in.) wide, 762 mm (30 in.) deep, with a shear span of 1829 mm (72 in.) and a corresponding a/d ratio of 2.60. The replicated beams were cast without internal steel stirrups to reflect the condition of the in-service beams. The remaining specimens were repaired for shear, flexure and a combination of the two with no load applied prior to the carbon fiber application. The beam repaired for shear included unidirectional GFRP sheets attached in a three-sided U-wrap about the tension side of the beam. Failure of the beam was via yielding of the tension steel followed by crushing of the compression concrete. The beam repaired for both flexure and shear did not have a definitive failure mode, although from the strain data at the maximum load, it appeared that an over-reinforced failure due to excessive deflection and strain hardening of the flexural steel would have occurred.

While previous work has focused on the contribution from FRP based on the tensile capacity of the strips, the focus on limiting the strain in the FRP based on bond failure was introduced by several articles, the first of which were published by Triantafillou and by Khalifa, et al. (*Triantafillou 1998; Khalifa, et al. 1998*). The paper by Triantafillou is especially beneficial, as it reviews the pertinent models in the literature at that time (including Berset, Dolan, Al-Sulaiman, Uji, Ohuchi, et al., Chajes, et al., Malvar, Vielhaber and Limberger, and Sato, et al.), many of which contradict each other in their recommendations for determining the shear contribution from FRP (*Triantafillou 1998*). The author described two failure modes that dominate the literature in terms of a debonding failure originating at the free edge or rupture of the FRP, both of which lead to an abrupt nonductile failure mode. Triantafillou proposed that limiting the effective strain in the FRP would produce a lower bound for the contribution and provide an equation for determining the shear contribution from FRP.

In order to add to the existing database of shear repaired specimens, the author included a series of eleven rectangular beams without integrally cast stirrups and side wrapping utilizing CFRP at 90, 45, and 56 degrees to the longitudinal axis of the beam. Dimensions of the beams were 70 mm (2.75 in.) wide, 110 mm (4.33 in.) deep, with a shear span of 320 mm (12.60 in.), resulting in an a/d ratio of 3.2. All beams in the test matrix failed in shear, and the corresponding contribution from CFRP was back calculated by subtracting the concrete contribution from the total experimental shear stress. Then the corresponding effective strain the CFRP was determined and compared to the test data of seven of the nine other investigators, resulting in a total of 42 shear tests for comparison. Triantafillou produced a plot of the effective strain in the

FRP at failure versus the FRP reinforcement ratio times the material modulus. The plot indicated a similar trend regardless of the wrapping scheme. In addition, a best fit curve to the data indicated a decreasing second order polynomial for $\rho_{frp}E_{frp}$ less than 1, but a linear decreasing fit for values greater than 1.

The relative shortcomings of Tiantafillou's 1998 paper, including the effect of concrete strength on bond and the various repair wrapping schemes were noted in the publication by Khalifa, et al. (*1998*). The article also presented an equation for the FRP contribution in terms of an ACI format. The problem related to the bond model was based on the work of Maeda, et al. in 1997, which documented the effective bond length for FRP based on a series of direct tension tests, but was limited to a single design concrete strength (*Maeda, et al. 1997*). Utilizing the work of Horiguchi and Saeki in 1997, Khalifa, et al. modified the bond model to include the effect of varying concrete strength (*Horiguchi and Saeki 1997*). Khalifa, et al. also modified the capacity equation to include an effective width of the FRP, based on the wrapping scheme and the distance of the FRP strip to the failure crack. Utilizing the modified effective bond length, the contribution to shear strength based on proximity to the failure crack and the anchoring scheme/wrapping type was proposed. The authors also included a reduction factor for FRP equal to 0.7, in order to produce a lower bound failure mode in design, which could be modified as more data populated the existing database. The value proposed by ACI 440 is currently equal to 0.765.

Triantafillou and Antonopoulos published an article in 2000 to address the concerns pointed out by Khalifa, et al. to include the effect of concrete strength on the bond model and to differentiate failure based on the wrapping scheme (*Triantafillou and Antonopoulos 2000*). The governing equation for FRP contribution was modified to follow the Madea, et al. bond model (modified for varying concrete strengths). Thus, from the early series of investigators, the contribution of FRP was presented, based on the wrapping scheme. For a side- or U-wrapped specimen, the failure occurred from bond, which resulted in a limiting of the effective strain in the FRP, based on a maximum value of 0.004 or a value related to the active bond length and concrete strength.

2.2.5 CRFP tape as a Near Surface Mount (NSM) repair

The use of carbon fiber in a near surface mount application gained attention as of early 2001, with a bulk of the initial work completed at the University of Missouri-Rolla by De Lorenzis and Nanni. They published several papers, the first two in 2001, which outlined a research program that included both bond and beam tests (*De Lorenzis and Nanni 2001a; 2001b*). For the bond tests, a beam-type pull-out specimen was used to determine the local bond-slip characteristics of the FRP-to-epoxy system in order to quantify the effect of development length and minimum cover requirements. The beam tests included eight full-scale T beams, including two control specimens. The beam dimensions were 406 mm (16 in.) deep, with a flange width of 381 mm (15 in.), a web width of 152 mm (6 in.), a flange thickness of 102 mm (4 in.), and a shear span of 107 mm (42 in.), resulting in an a/d ratio of 3.0. Only two of the eight beams were cast with internal steel stirrups, including one control specimen. The research program included parameters such as NSM spacing, orientation (orthogonal to the tension steel or oriented at 45 degrees to the tension steel), and anchorage (into the flange or termination of the rod at the junction of the web and flange). Failure was due to either lack of confining stirrups at the base

of the stem, resulting in a splitting of the concrete cover along the bottom flexural steel or insufficient epoxy cover to the FRP bar.

Results from the research program indicated higher shear strength was gained (in order of least to most important) by: decreasing the spacing of the FRP, orienting the rods closer to the principle tensile stress in the shear span, and increasing the anchorage length of the rods into the flange. A design method was presented that determined the total shear capacity based on the contributions from steel, concrete, and FRP.

The contribution from the NSM was presented as the lesser of two equations; the first is related to the bond of the NSM with respect to the surrounding concrete while the second limits the strain in the NSM to 4000 με. The first equation related to bond failure is based on three assumptions: the formation of shear cracks occur at 45 degrees to the longitudinal axis of the member, the distribution of bond stresses along the effective lengths of the FRP is uniform, and the ultimate bond strength is reached in all rods intersecting the failure crack at the same time. The total shear force from NSM is taken as the summation of each individual rod that crosses the failure crack.

A second paper by De Lorenzis and Nanni, also published in 2001, investigated bond characteristics of the FRP and included two full-scale repaired beams and one control specimen that were included in the previous paper and are not reviewed a second time (*De Lorenzis and Nanni 2001b*). For the bond tests, a beam type pull-out test was performed in lieu of a traditional direct tension pull-out test with the objective of determining the effect of the bonded length to bar diameter with three different ratios – 6, 12, and 18. For the ratio of 12, the width and corresponding depth of the groove were varied from ½ in., ¾ in., to 1 in. Results from the test indicated a splitting failure of the epoxy cover in all but one of the tests – the bonded length to bar diameter of 12 with the 1 in. groove indicated a failure due to cracking of the concrete. The effect of the bonded length indicated a higher ultimate tensile load with increasing bonded length; however, strain gage data along the bonded length indicated a nearly uniform distribution of strain over this length at failure.

A third paper by De Lorenzis and Nanni extended the objectives of the previous bond paper (*De Lorenzis and Nanni 2002*). In this paper, the same beam type pull-out tests were used but the investigation included two bar diameters (9.5 mm (0.375 in) and 12.7 mm (0.5 in)), two different bar types (CFRP and GFRP rod), four bonded length to diameter ratios (6, 12, 18, and 24), and four groove sizes (12.7 mm (0.5 in.), 15.9 mm (0.625 in.), 19 mm (0.75 in.), and 25.4 mm (1 in.)). For the GFRP rods, two surface treatments were investigated – sand blasted and traditionally deformed bars. Across all test variables, the maximum load, as a percentage of the ultimate tensile capacity of the FRP rod, turned out to be 60% for the 12.7 mm (0.5 in) diameter bar with a 25.4 mm (1 in.) groove size and a bonded length equal to 24 bar diameters.

Failure modes varied based on the specific test configurations, although general trends were evident. For a majority of the specimens, a splitting failure in the epoxy matrix led to failure; however, stress cracking in the concrete at the interface with the epoxy was also noted in several of the longer embedment lengths. For the GFRP sand blasted specimens, the lack of rib geometry resulted in a small circumferential stress field surrounding the bar. Consequently, the sand blasted GFRP bars experienced a pullout failure due to lack of mechanical anchorage that is

typical of a deformed bar once the chemical adhesive bond limit is reached and bar slip initiates. The authors provide a solution for the embedment length of the bars assuming the stress in the bars is limited to a value on the ascending portion of the bond-slip relationship.

A final paper published by De Lorenzis in 2004 attempted to provide a governing explanation of the bond model from two additional papers (published in 2002 and 2004 respectively), which looked at the experimental bond model of ribbed CFRP rods in both epoxy and mortar, GFRP ribbed and spiral bars in epoxy and cement paste, and GFRP sandblasted rods in epoxy (*De Lorenzis 2004*). Combining the latest experiments with the previous work on bond, De Lorenzis used an analytical approach to the bond modeling based on the experimental work. As such, the bond models were divided into three different curves. The first dealt exclusively with deformed CFRP rods with failure at the interface of the concrete and the groove filler (for smooth grooves only), splitting failure of the epoxy, and all bars in cement paste. The second curve dealt with splitting failure of GFRP deformed and spiral bars in epoxy or pull-out type failure of spiral bars in cement paste. The last curve dealt with sand blasted bars in epoxy which result in a pull-out failure mode.

Once the bond stress-slip relationship was measured experimentally, an analytical model was chosen to describe the behavior. The Bertero-Popov-Eligenhausen (BPE) relationship was used for the ascending branch of the curve with post peak responses modeled based on experimental data. For each bond test, the maximum bond stress at failure and the slip corresponding to this maximum bond stress were recorded. These values were used to determine the shape of the ascending and post peak responses, respectively.

For specimens failing at the epoxy to concrete interface, bond stress decreased with increasing groove depth. For the epoxy filled specimens, failure occurred at the interface with the surrounding concrete or within the epoxy matrix; the highest bond stresses were from spirally wound bars, followed by deformed CFRP bars, and finally deformed GFRP bars. The use of sand blasted bars was not recommended due to the low bond stresses attributed to lack of deformations.

An article by Cruz and Barros looked at analytical modeling of the bond for NSM and concrete via an epoxy matrix (*Cruz and Barros 2004*). The research program looked at a beam type pullout test setup similar to that of De Lorenzis, as shown in Figure 2.14. The strain in the FRP was measured as a relative slip value compared to the surrounding epoxy and concrete, with the assumption that the strain in the epoxy and concrete are quite small in comparison. Thus, the strain in the FRP can be measured experimentally at both the free and loaded end. Results indicated that the analytical bond stress parameter was modeled accurately. The authors also performed FEM testing to find the total pullout force and loaded end slip with results comparable to the analytical and experimental work. The authors proposed a development length equation. The relationship is highly susceptible to the geometry of the grooves, the concrete strength, and the epoxy used; thus the equation is excluded from the current discussion.

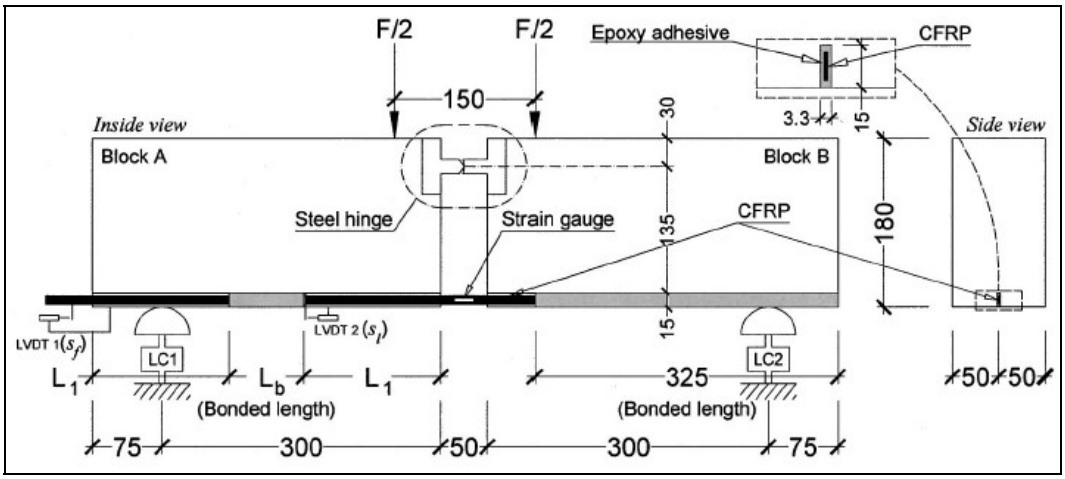


Figure 2.14: Near Surface Mount beam type pullout test setup taken from Cruz and Barros

The suite of articles published by De Lorenzis and other colleagues presented the initial investigation of an analytical bond model for round FRP bars used in a NSM application. However, the current study utilizes rectangular FRP tape as opposed to a circular FRP rod. This decision was based on the work of Shield and French, utilizing the same rectangular tape with various epoxy manufacturers in direct pull-out tests to determine the best pairing of epoxy to FRP tape since most repair systems for FRP do not couple the FRP with the epoxy (*Shield, et al. 2005*).

Shield and French's experimental program was twofold: 1) initial testing on scaled specimens included seven different epoxies with six specimens per adhesive; and 2) upon results of the small scaled testing, two epoxies were used on larger scaled specimens. Material specifications were as follows: the FRP was Aslan 500 CFRP tape, manufactured by Hughes Brothers with dimensions of 2 mm (0.079 in.) by 16 mm (0.63 in.) and a cross sectional area of (32.3 mm^2 (0.05 $in.^2$). The guaranteed ultimate strength of the tape was reported as 2,068 MPa (300 ksi), although test results by Shield and French achieved an ultimate strength closer to 2,482 MPa (360 ksi) with a 4.5% Coefficient of Variation. Epoxies included Sikadur AnchorFix-3, Master Builders/Chemrex Concresive 1420, 3M DP600NS, 3M DP460NS, Sonneborn Epofil, Sikadur 35 Hi-Mod LV, and Sikadur 32 Hi-Mod.

Scaled specimens were 152 mm (6 in.) by 152 mm (6 in.) by 203 mm (8 in.) in length. A groove measuring 6.4 mm (0.25 in.) wide by 19 mm (0.75 in.) deep was cut along one of the 152 mm (6 in.) sides of the specimens. Once the groove was cut, it was cleaned out with compressed air to remove any trace amounts of cement that may interfere with the bond. Some of the epoxy manufacturers did not provide a mixing applicator, thus mixing was accomplished in a separate container prior to application. For the remaining epoxies, an applicator gun with a static mixing nozzle was provided, thus ensuring the correct proportions prior to application. The NSM tape was anchored in the groove and allowed to cure for 24 hours prior to testing. The anchor block was placed in compression at the bottom of a universal testing machine via a reaction section placed on top of the concrete block. The free end of the NSM tape extended upward, with two

aluminum tabs inserted into the grips of the machine. Once secured, the NSM tape was pulled out of the testing block.

Results from the small-scale tests indicated a mixed failure mode across the seven manufacturers. For Sikadur AnchorFix-3, Master Builder/Chemrex Concresive 1420, Sikadur 32 Hi-Mod, Sikadur 35 Hi-Mod LV, and Sonneborn Epofil, the failure occurred between the tape and the adhesive, indicating a poor bond between the epoxy and NSM surface. 3M DP600NS failed between the adhesive and the concrete, while 3M DP460NS exhibited several failure modes including bond between the tape and adhesive, within the adhesive matrix, failure within the concrete surrounding the adhesive, and failure of the FRP – in which case the failure was progressive, as each individual strand within the tape failed, until the entire specimen failed. However, the 3M DP460NS achieved the highest average and maximum load for the small-scale tests, indicating a stress up to 98% of the experimental capacity of the FRP tape.

The authors attempted to correlate the manufacturer's adhesive properties with respect to the small-scale specimens with poor results. Among the manufacturers investigated, the adhesive tensile strength and shear strength had a correlation (r^2 value) of 0.07 and 0.02, respectively. The results were better for the tension modulus and elongation at failure at 0.053 and 0.42 respectively, but still less than half of what was reported by the manufacturer. The authors conclude that choosing an FRP system and corresponding epoxy system is not based solely on manufacturers' reported test values.

From the results of the small-scale tests, Sikadur AnchorFix-3 and 3M DP460NS were chosen for the larger scaled test. The test consisted of two reinforced concrete blocks to simulate a crack between two pieces of concrete. A 76 mm (3 in.) groove oriented perpendicular to the "crack" was cut on both sides of each block resulting in two NSM tapes per test. In addition to the orthogonal test, grooves cut at 45 degrees to the crack were included in the test to simulate a shear repair. The blocks were situated in a Universal testing machine with LVDT sensors at all four corners to ensure linear loading of the specimen (to eliminate any eccentric loading or rotation).

Results from the large-scale tests indicate the 3M 460NS was superior both in total load and post investigation of the failure plane. The 3M product consistently anchored the NSM, with failure occurring in the surrounding concrete; no failure between the tape and epoxy or epoxy and concrete was found. The authors theorized that the 3M 460NS has a higher ductility compared with the other materials, thus allowing higher strains than are permitted in the adjoining concrete.

An article published by Barros and Dias looked at the shear strength contribution from traditional steel stirrups, CFRP fiber wrap, and NSM rectangular FRP laminates (*Barros and Dias 2006*). The investigation included 20 quarter-scale beams with several design parameters. The breakdown of the 20 beams were as follows: four sets of five beams included one control specimen devoid of integrally cast stirrups; one beam with integrally cast stirrups; one beam devoid of integrally cast stirrups utilizing CFRP U-wrapping as the shear reinforcement; and the last two beams were cast devoid of integral stirrups reinforced with rectangular FRP laminates at 90 and 45 degrees to the axis of the beam. Within this general architecture, the four groups varied in specimen depth, shear span, and longitudinal reinforcement ratio. The first two sets

each had a rectangular cross section of 300 mm (11.8 in.) by 150 mm (5.9 in.) with differing longitudinal reinforcement and a 600 mm (23.6 in.) shear span; the second two sets had a 150 mm (5.9 in.) square cross section with differing longitudinal reinforcement. In both cases the shear span was equal to twice the depth, resulting in a/d ratios of 2.2 and 2.4 respectively.

In order to test the shear contribution from each specimen, the concrete contribution was determined from the Portuguese code, which is modeled after the CEB-FIP. The steel contribution was also taken from the Portuguese code, but it did not take into account the dowel action, which is outlined in the CEB-FIP model code. The shear contribution from CFRP wrapping was taken from ACI 440 and *FIP* provisions. As there are no specific guidelines for implementation of NSM as a shear repair, the authors chose the recommendations of Parretti and Nanni (*2004*). From these provisions, all the specimens were designed to fail in shear. Also, due the lack of internal stirrups, the FRP beams were not loaded prior to application of the appropriate system.

Results from the test indicated that the prediction models for the CFRP wrapping were quite accurate with a slight underestimation of 2% and 8% respectively for the ACI 440 and *fib* methods. However, using the design method by Parretti and Nanni (*2004*) with a maximum bond stress in the FRP equal to 0.59% of the tensile capacity of the section (taken from the beam type pullout tests previously performed by Cruz and Barros), resulted in a strength prediction equal to 79% of the experimental work. This may provide a usable lower bound for design, but it could also be higher as more tests confirm or refine the method proposed by Parretti and Nanni.

A paper by Dias and Barros investigated the effect of rectangular NSM as a shear repair on 12 quarter-scale T beams (*Dias and Barros 2008*). The beam dimensions were 400 mm (15.7 in.) deep, with a flange width of 450 mm (17.7 in.), a web width of 180 mm (7.1 in.), a flange thickness of 100 mm (3.9 in), and shear span of 900 mm (35.4 in.), resulting in an a/d ratio of 2.5. The study looked at several parameters including the NSM shear reinforcement ratio (in terms of spacing of the strips) and orientation of the NSM with respect to the longitudinal axis of the beam (90, 60, and 45 degrees were used). The beams were subjected to three point loading, eccentric to the centerline of the beam. In order to force a shear failure in the shorter shear span, the longer shear span was over-reinforced. The authors also chose to limit the stress in the laminate equal to a strain of 0.5% as a compromise that is higher than the 0.4% recommended from ACI 440 for externally applied CFRP and pullout bending tests from Cruz and Barros of 0.59% (*Cruz and Barros 2004*).

The experimental setup included three control beams. One was devoid of integrally cast stirrups within the shorter shear span, while the remaining two had two and six 6 mm diameter stirrups within the 900 mm shear span. The remaining nine beams had varying NSM and internal stirrup spacing as well as varied NSM orientation to the longitudinal axis of the beam. Within the test matrix, one integrally cast stirrup and one CFRP laminate near the same location were instrumented to compare the relative strain measurements. The stirrups were instrumented at three locations, whereas the CFRP were instrumented at 1/5 points, as shown in Figure 2.15. The beams were not subjected to any previous load prior to installation of the NSM; the beams were tested to failure after the NSM was applied.

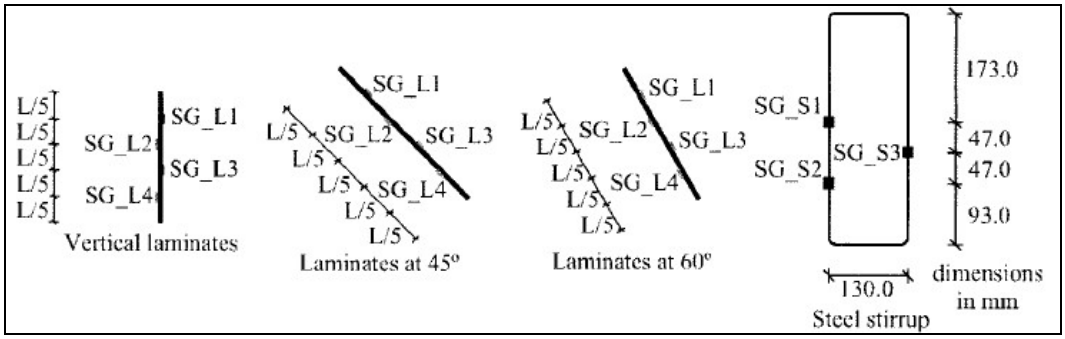


Figure 2.15: Instrumentation of CFRP taken from Cruz and Barros

The control specimen with no integrally cast stirrups in the shear span failed at a 45 degree crack relative to the longitudinal axis, whereas the two remaining control beams failed at an approximately 55 degree angle to the longitudinal axis of the beam. As such, the efficiency of the NSM material for the beams with integrally cast stirrups in the shear span was highest for the 60 degree specimen, then the 45 degree specimen and finally the 90 degree specimen. The spacing of the NSM also played a role in the increased capacity of the section, based on the shear cracks that formed. For the widest spacing of NSM, only one or two shear cracks formed, resulting in a longer development length of the NSM from the crack to the terminating end of the strip. For the narrowest spacing, several shear cracks formed along the shear span, thus reducing the developed lengths between cracks or from one crack to the terminating end of a strip. This resulted in the lowest strain distribution of the FRP, indicating the efficiency of the repair as a whole was compromised. The authors indicated this may result in a maximum spacing requirement to fully utilize the strength of individual NSM strips. In addition, once a diagonal crack formed within the shear span, the stiffness of the beam increased with the addition of the NSM reinforcement.

2.2.6 Zararis Method (bent cap specimen only)

The STM method can lead to overly conservative ratings for deep beams; this finding is based on previous work on full scale bent cap specimens at Oregon State University (*Senturk and Higgins in press*). However, within the review of academic research in this area, the work of Zararis stood out as a reasonable estimate of the capacity of deep beam specimens encompassing several parameters including stirrup grade and spacing, flexural cutoffs, and beam depth (*Zararis 2003*). The method provides a fundamental theory on the behavior of deep beams having a shear span-to-depth ratio (a/d) of 1.0 to 2.5 with and without transverse steel. It assumes an ultimate shear force on a section, based on a reduced compression zone and moment equilibrium with the vertical and flexural steel.

The method assumes at a crack location, strain is perpendicular to the crack; no aggregate interlock or shear transfer along the interface is assumed. In this respect, the only stresses that are formed at the crack are in the longitudinal and transverse steel. In addition to pure tensile stresses, Zararis assumes the reinforcement also undergoes shear deformations. By orienting the

stresses at the crack location from those perpendicular to the crack to a vertical and horizontal direction, the stresses can be determined. After the formation of the critical shear crack, Zararis uses moment equilibrium to calculate the depth of the compression zone above the crack. The sequence of failure of a deep beam with transverse reinforcement proposed by Zararis assumes the transverse steel yields, which causes an increased shear force which must be compensated by the flexural steel. Once the flexural steel is exhausted, a horizontal crack will form at the location of the flexural steel, and the increased shear force will begin to decrease. At this point the forces in the compression zone become too great and crushing of the concrete in this area begins. By taking a free body of the forces acting on the top and bottom half of the wedge shape, the ultimate shear strength of the section is determined.

2.2.7 Post-tensioning (bent cap specimen only)

The use of post-tensioning for repair of concrete structures is limited in the literature mainly toward flexural repair. However, Aravinthan and Suntharavadivel published a paper regarding the post-tensioning of bent cap specimens as a shear repair method (*Aravinthan and Suntharavadivel 2007*). The paper was divided into two sections – the first focused on the testing of a quarter-scale single column cantilever bent cap, while the second investigated a quarter-scale model for the repair of an existing two column bent cap. Both portions of the experimental work included a control specimen loaded to failure without repair and two additional specimens loaded to what the authors denoted as failure, although no qualifying criteria was given for the definition. After preloading, the force was removed from the specimen, a post-tensioning force was applied, and the specimens were loaded to failure. The tapered bent cap had dimensions 250 mm (9.8 in.) wide with a varying depth of 400 mm (15.7 in.) at the heel tapering to 350 mm (13.8 in.) at the toe and a shear span of 750 mm (29.5 in.), resulting in an a/d value of 2.2. The two-column bent cap had dimensions 220 mm (8.6 in.) wide, 420 mm (16.5 in.) deep, and a 395 mm (15.5 in.) shear span, resulting in an a/d value of 1.0. Details of the two specimens are shown in Figure 2.16 and 2.17, respectively.

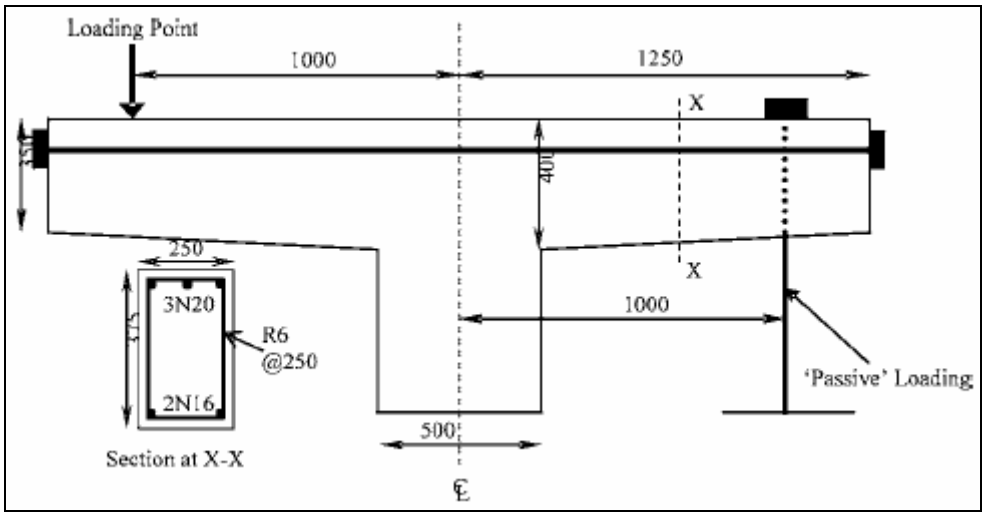


Figure 2.16: Deep beam specimen #1 details taken from Aravinthan and Suntharavadivel

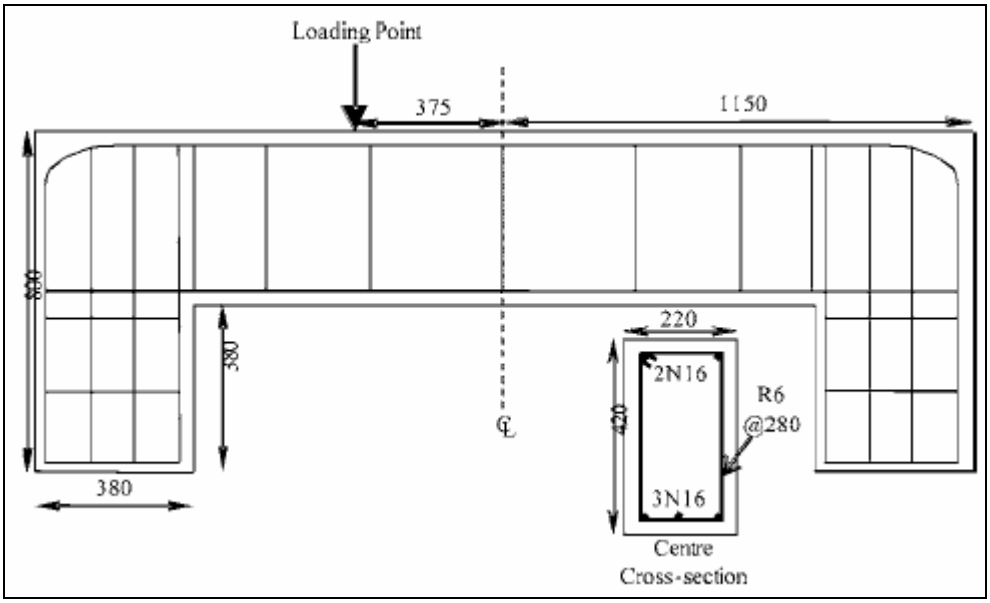


Figure 2.17: Deep beam specimen #2 details taken from Aravinthan and Suntharavadivel

For the tapered rectangular cantilever bent cap, the test setup included an active load cell placed on one end of the cantilever with a passive constraint consisting of two channel sections anchoring the adjacent cantilever end. The control specimen failed at a load of 149 kN (33.5 kip). The second specimen was preloaded to 135 kN (30.3 kip), experiencing a maximum shear crack width of 2 mm (0.08 in.), then unloaded; a post-tensioning force of 150 kN (33.7 kip) was applied, reducing the crack width to 0.5 mm (0.02 in.); and the specimen failed at a load of 180 kN (40.5 kip). For the third specimen, it was again preloaded to 135 kN (30.3 kip), experiencing the same 2 mm (0.08 in.) shear crack width, then unloaded; a post-tensioning force of 300 kN (67.4 kip) was applied, although the maximum crack width reduced to 1mm (0.04 in); and the specimen failed at a load of 105 kN (23.6 kip), or 30 kN (6.7 kip) less than the preload force.

The authors attribute the lack of strength gain to the crack inclination and width. According to their analysis, the shear capacity of a section is governed by aggregate interlock and the ability of the concrete along the interface to prevent sliding of the two rigid bodies along the crack. As the angle of the crack decreases and the crack width increases, the shear capacity is reduced. For the third specimen, the crack width was only reduced to 1 mm (0.04 in.) during post-tensioning, even though the post-tensioning force was doubled. In order to further test the third specimen, the failure crack was injected with a two part epoxy and permitted to cure; then the specimen was retested to a failure load of 201 kN (45.2 kip).

The second part of the experimental study included the quarter-scale testing of the Tenthill Creek Bridge, which was slated for external post-tensioning as the repair method. The bridge consists of two columns at each end of the rectangular bent with four girders resting on bearing pads on top of the cap. The first interior girder was modeled in the laboratory, thus creating two unequal shear spans with 1.2 and 2.9 shear span-to-depth (a/d) ratios respectively. As in the first

investigation, the control specimen was loaded until a shear crack formed in the shorter span with loading continuing until failure, at a load of 366 kN (82.3 kip). The control specimen failed in the larger shear span by diagonal tension. The second specimen was preloaded to 250 kN (56.2 kip), then unloaded; a post-tensioning force of 239 kN (53.7 kip) was applied; and failure occurred from diagonal tension in the shorter shear span at a load of 333 kN (74.9 kip). The ultimate load was lower than the control specimen, but this was attributed to a lower concrete strength. The second specimen was further tested after epoxy injection and the same post-tensioned force, resulting in a shear compression failure within the shorter shear span at a load of 420 kN (94.4 kip). The third specimen was preloaded to 423 kN (95 kip), then unloaded; epoxy was injected; a post-tensioning force of 245 kN (55.1 kip) was applied, and failure occurred at a load of 546 kN (122.7 kip) due to shear compression in the shorter shear span. The authors pointed to the different failure modes of the control specimen and the second specimen without epoxy injection as evidence that the use of epoxy injection changes the behavior and ultimately the capacity of the section in shear.

3.0 FIELD TESTING OF REPAIRED BRIDGES

Two bridges were investigated in-situ to assess performance after installation of two different strengthening alternatives. Only two of the four strengthening options were available and accessible during the study period for evaluation. These included supplemental internal stirrups and surface-bonded CFRP strips. The bridges were Clarks Branch Overcrossing, I-5 southbound (Bridge Number 07839) near Roseburg, OR and Willamette River Bridge, OR 219 (Bridge Number 08156) near Newberg, OR. Clarks Branch Overcrossing deployed supplemental internal stirrups, and Willamette River Bridge deployed surface-bonded CFRP. Each of these bridges is described subsequently.

3.1 CLARKS BRANCH OVERCROSSING

3.1.1 Description

The Clarks Branch Overcrossing crosses Clarks Branch Road on Interstate-5 near mile-marker 113.44. The reinforced concrete deck girder bridge consists of 3 spans (Figures 3.1a-c), and the bridge drawings for the original portion of the spans were dated 1955. The span lengths are 14.3 m, (47 ft), 16.5 m (54 ft), and 13.4 m (44 ft) from the north to south, respectively. There is a skew angle of approximately 55 degrees. The spans support a roadway width of 11 m (36 ft), and have a total width of 12.4 m (40 ft, 10 in). There are six girder lines in each of the spans. The original bridge consisted of 5 girder lines; an additional girder line was added to the west exterior face in 1995, as seen in Figures 3.2a and b. Cantilever brackets were also added to the east face during the 1995 expansion. Diaphragms, 203 mm (8 in) x 864 mm (34 in), are located at the quarter points of all spans. The girders are 368 mm (14.5 in) x 914 mm (36 in), uniform and prismatic between the quarter and ¾ points. The girders are haunched near the interior support locations for a quarter of each span and are 1295 mm (51 in) deep at the supporting locations. Bent caps are 368 mm (14.5 in) x 1676 mm (66 in) and supported on three (3) 610 mm (24 in) square columns (caps are three span continuous). The reinforced concrete deck is 152 mm (6 in) thick, and a 51 mm (2 in) thick asphalt wearing surface was assumed for the bridge. The specified concrete compression strength was 22.75 MPa (3300 psi), and the reinforcing steel was specified as ASTM A305-50T intermediate grade deformed round and square bars (nominally 40 ksi yield stress).

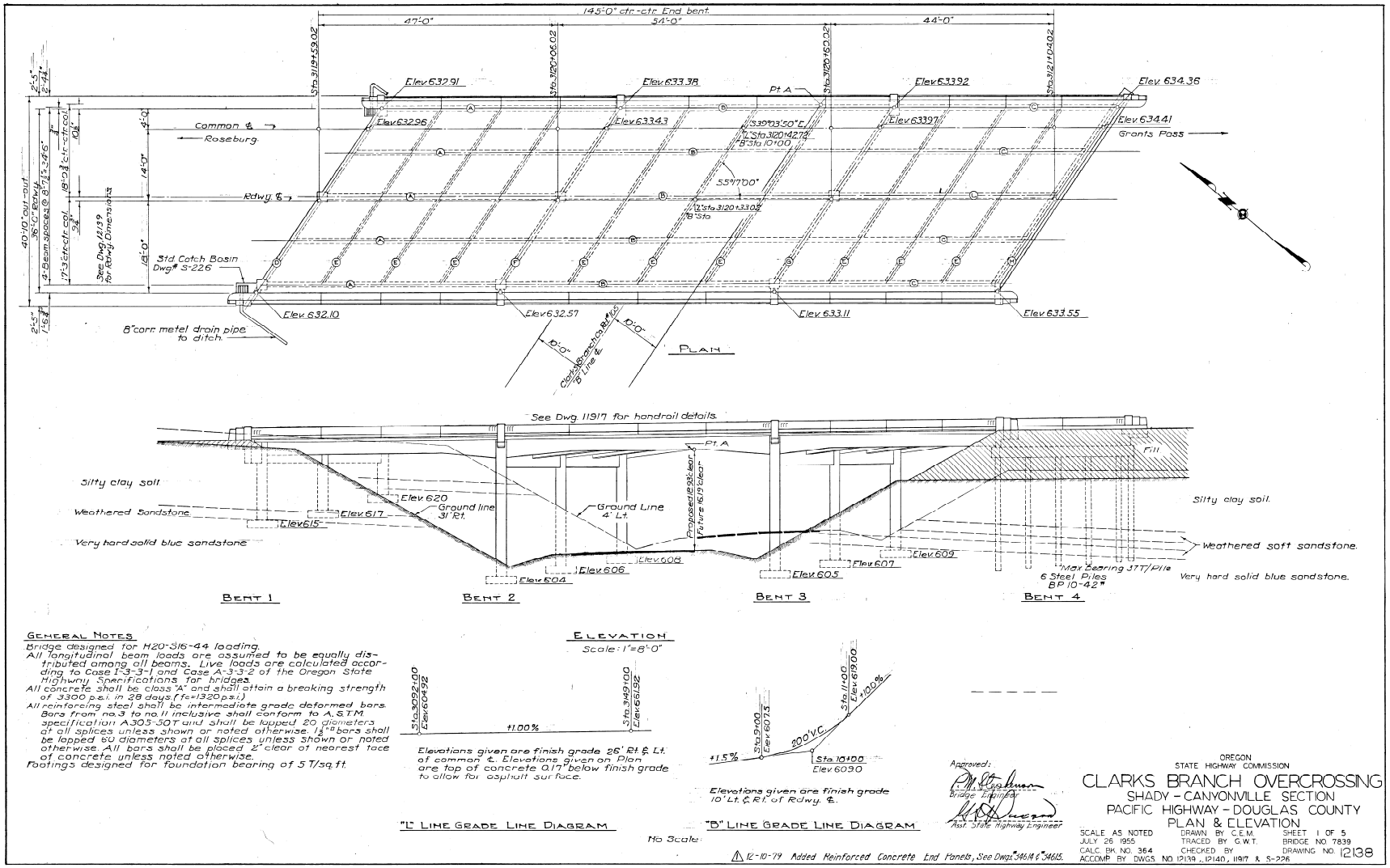


Figure 3.1a: 1955 design drawings for Clarks Branch Overcrossing

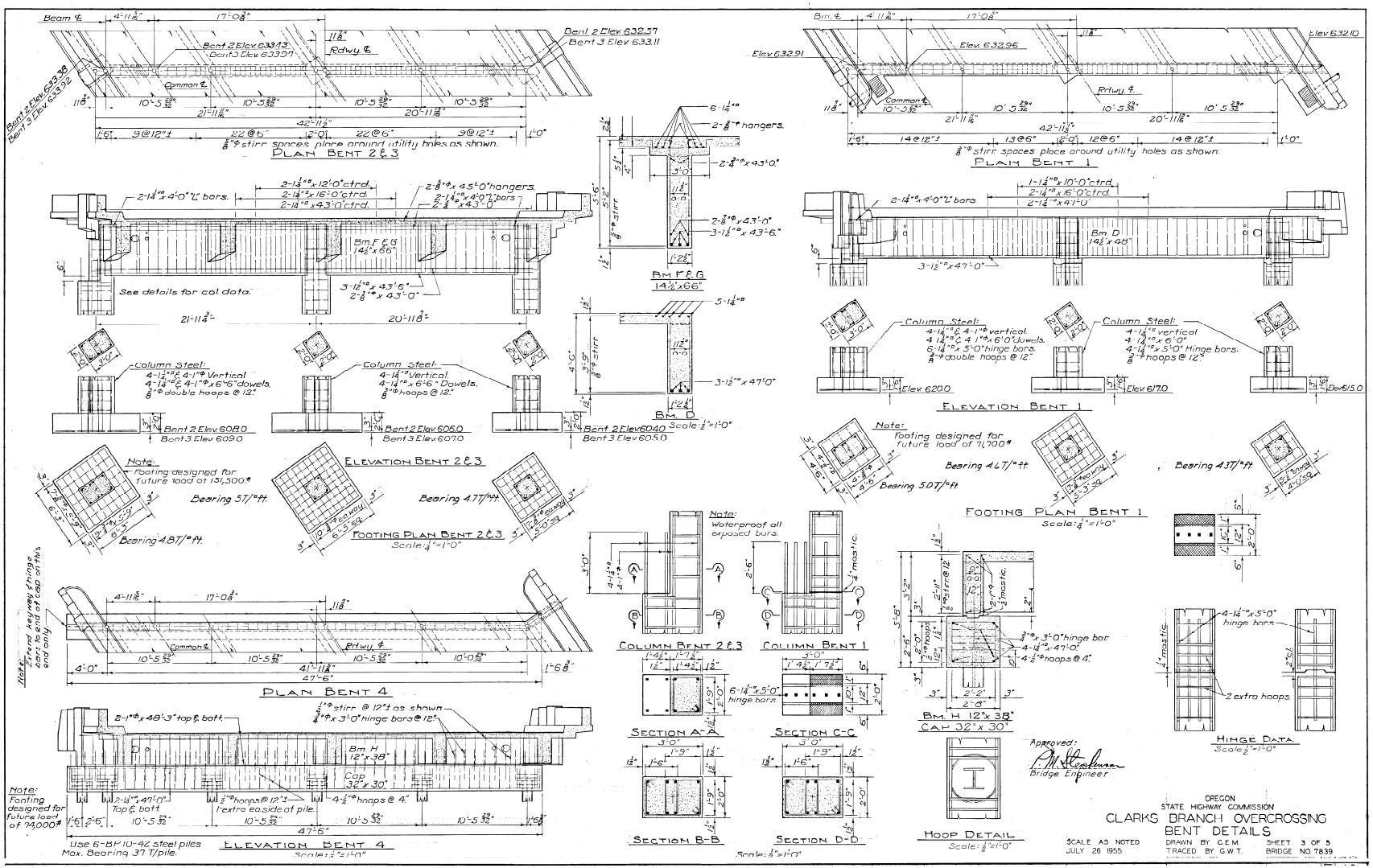


Figure 3.1b: 1955 design drawings for Clarks Branch Overcrossing

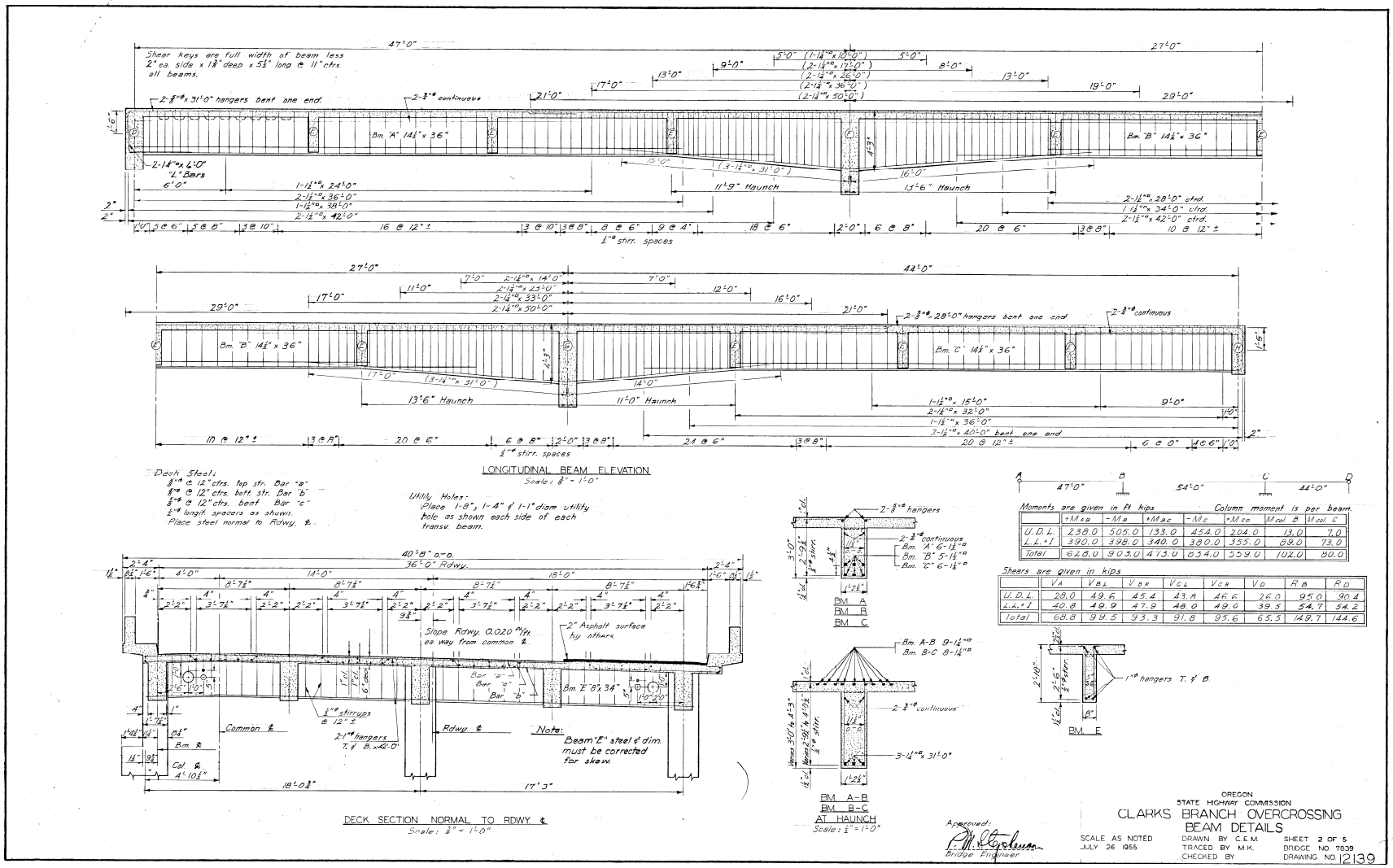


Figure 3.1c: 1955 design drawings for Clarks Branch Overcrossing

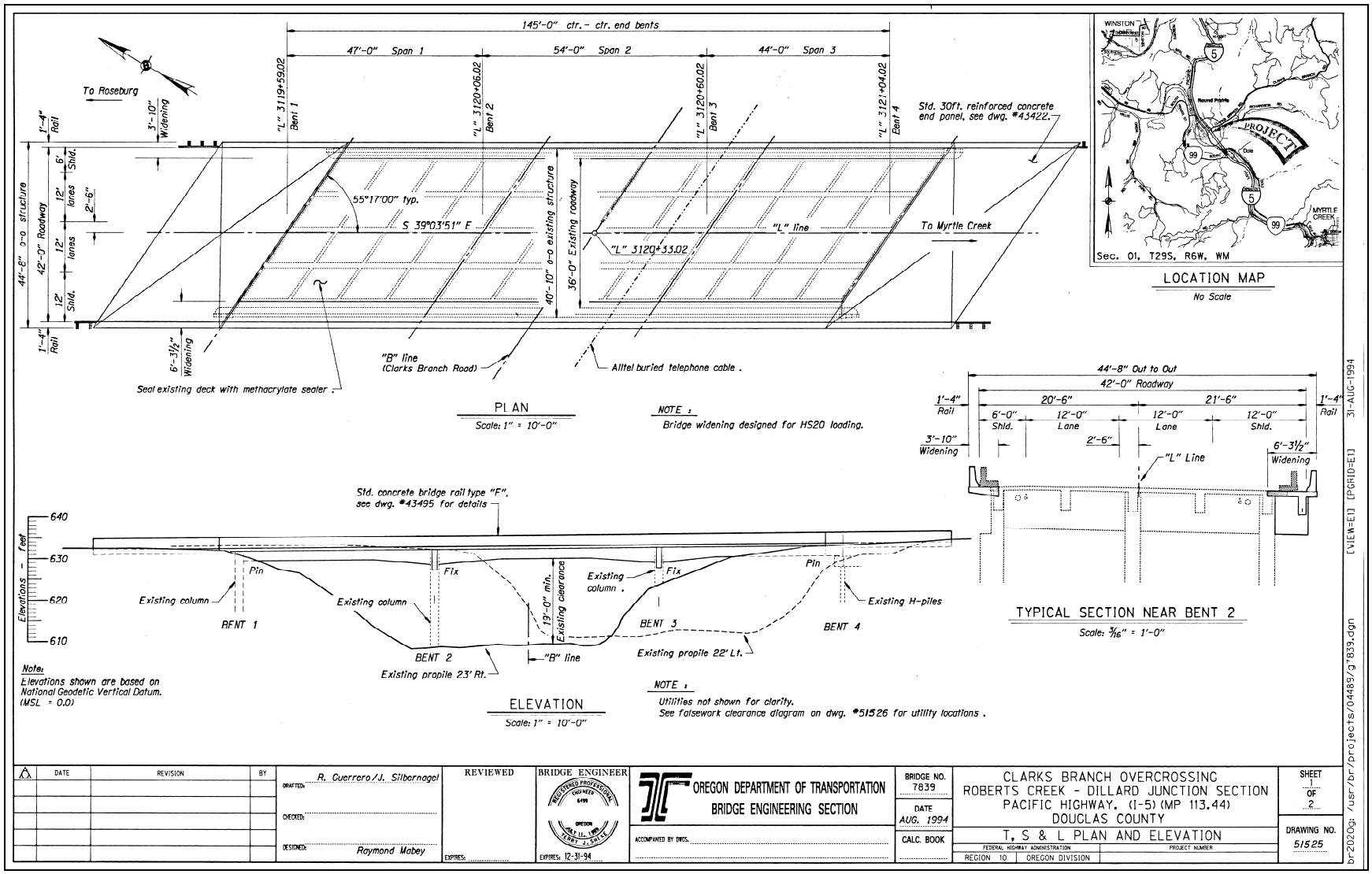


Figure 3.2a: 1995 design drawings for Clarks Branch Overcrossing with supplemental exterior girder

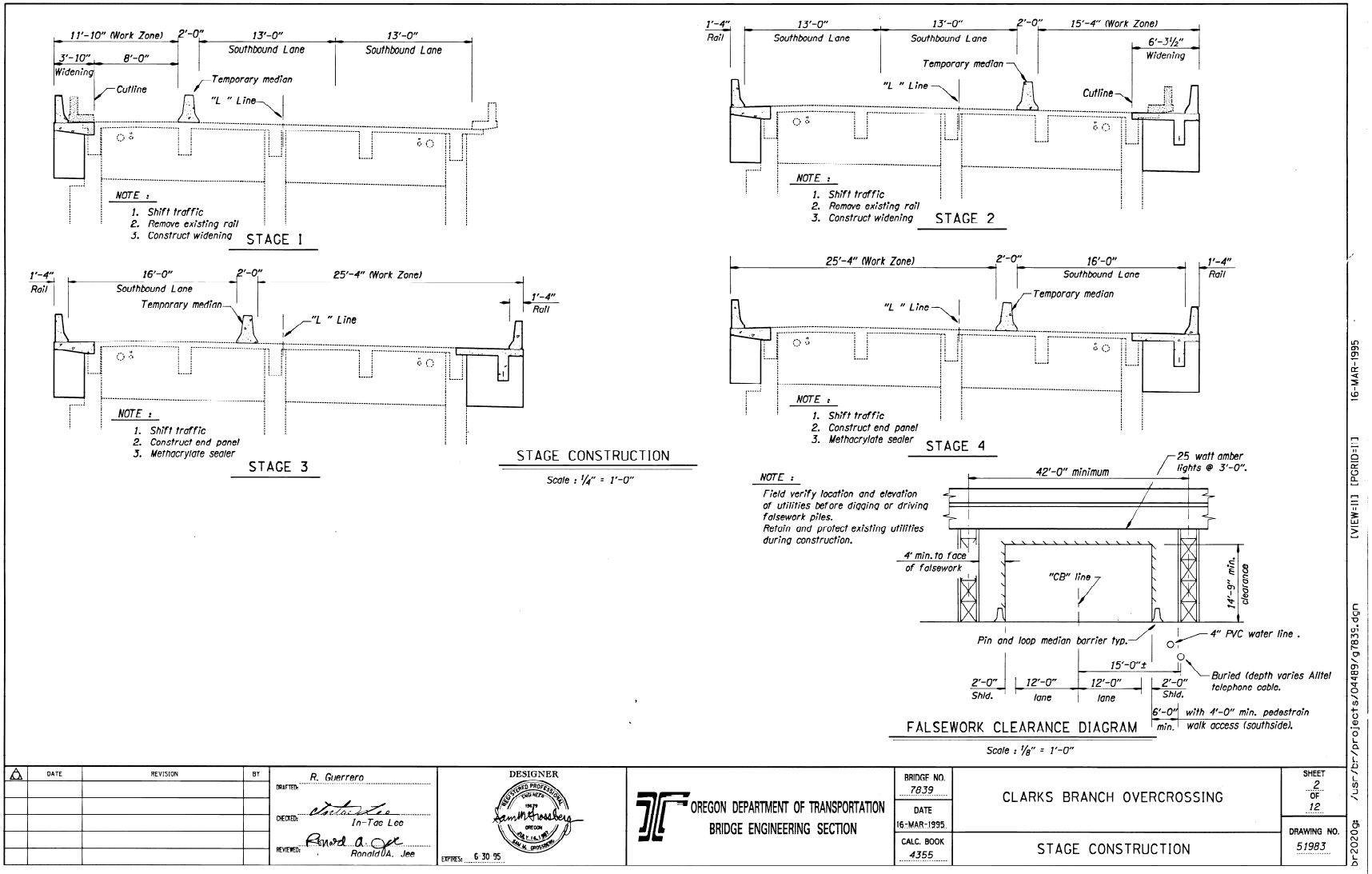


Figure 3.2b: 1995 design drawings for Clarks Branch Overcrossing with supplemental exterior girder

3.1.2 Inspection and instrumentation

Visual inspection of the bent caps and center span was performed to identify diagonal cracks and select instrument locations. Diagonal crack locations of larger diagonal cracks were measured relative to the support faces using a hand-held laser distance meter. Locations of stirrups near the diagonal cracks were identified using a Proceq Profometer 3 rebar locator, and the position measured relative to the support faces using the laser distance meter. Stirrup locations and instrumented existing diagonal cracks on the main girders and bent caps are shown in Figures 3.3a and b. Diagonal tension cracks were observed in bent caps, as well as the interior girders and original exterior girders of the main span. No significant diagonal cracks were observed in the 1995 girder.

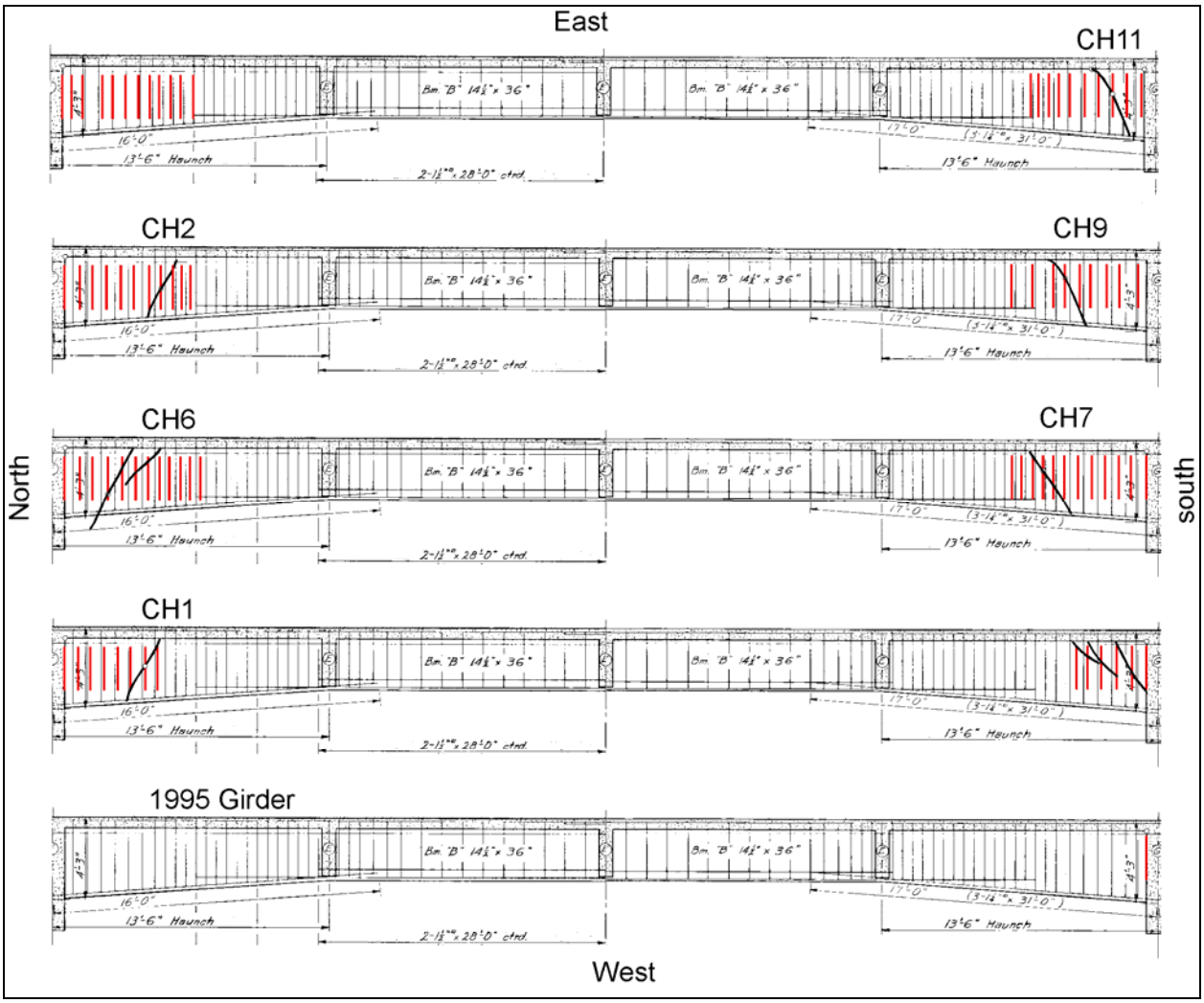


Figure 3.3a: Observed diagonal crack and stirrup locations in main girders

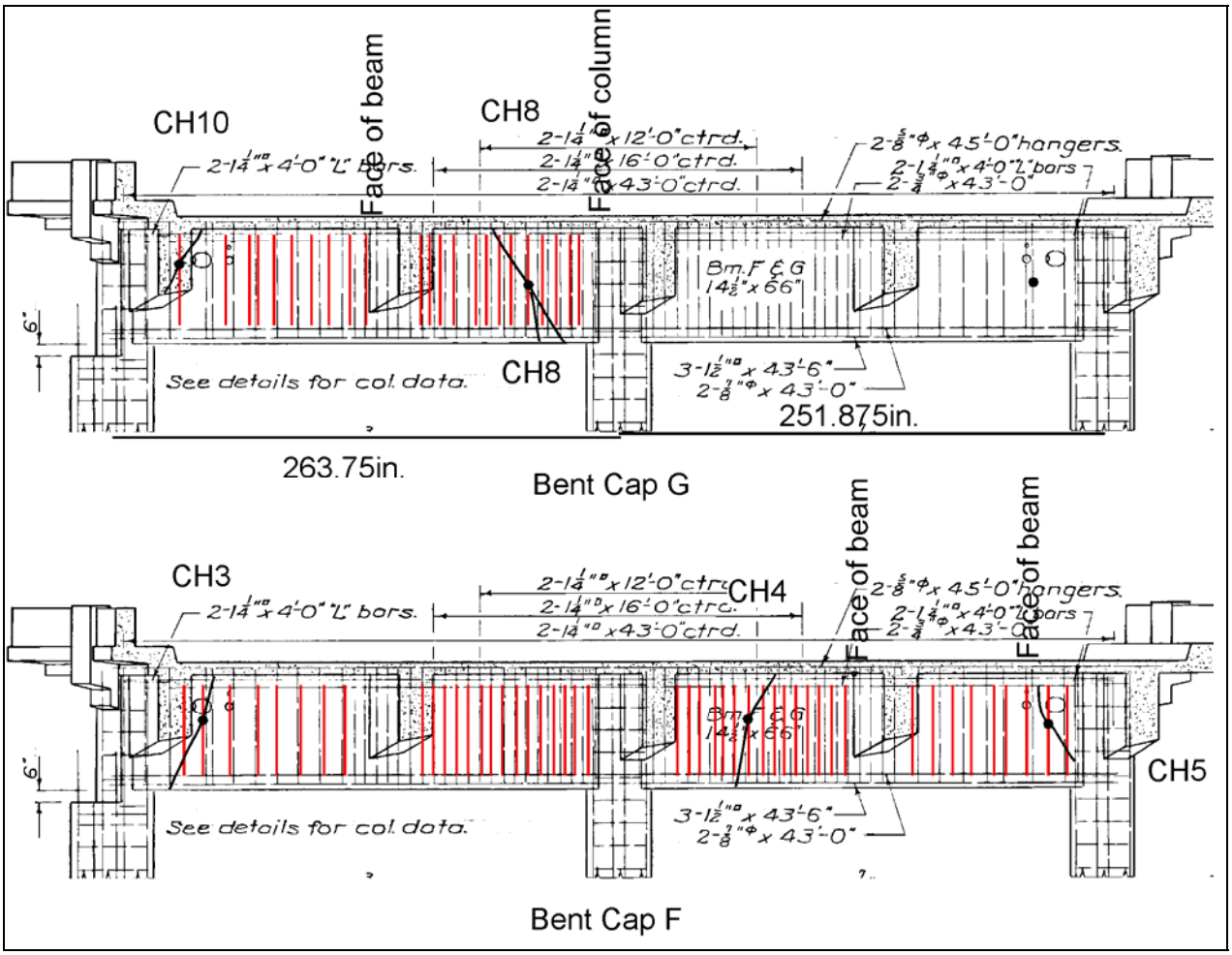


Figure 3.3b: Observed diagonal crack and stirrup locations in bent caps

After inspection, locations were selected for instrumentation. At selected diagonal crack locations, strain gages were installed on stirrups at the crack locations. Diagonal crack locations were selected based on the width and orientation of the cracks and to coincide as well as possible with locations that were of similar distance from the face of the supports. Strain gages were installed to measure stirrup stress at the diagonal cracks during ambient traffic and controlled truck loading. Strain gages were installed by chipping into the concrete and exposing the embedded stirrup at the diagonal crack locations. The actual amount of concrete removed varied, based on the concrete cover, but typical concrete removal provided an exposed stirrup length of approximately 75-100 mm (3-4 in) overall, centered about the crack as seen in Figure 3.4. The width of the excavation was approximately 50-75 mm (2-3 in), permitting preparation of the rebar surface for bonding strain gages on the stirrup leg. The deformation pattern on the stirrup was not removed to install the strain gages, as the strain gage size (Measurements Group strain gage EA-06-062AQ-350, with a gage length of 1.5 mm (1/16 in) and gage factor of 2.105) permitted installation within the deformation pattern. This strain gage was a bondable type gage with a 350-Ohm resistance.

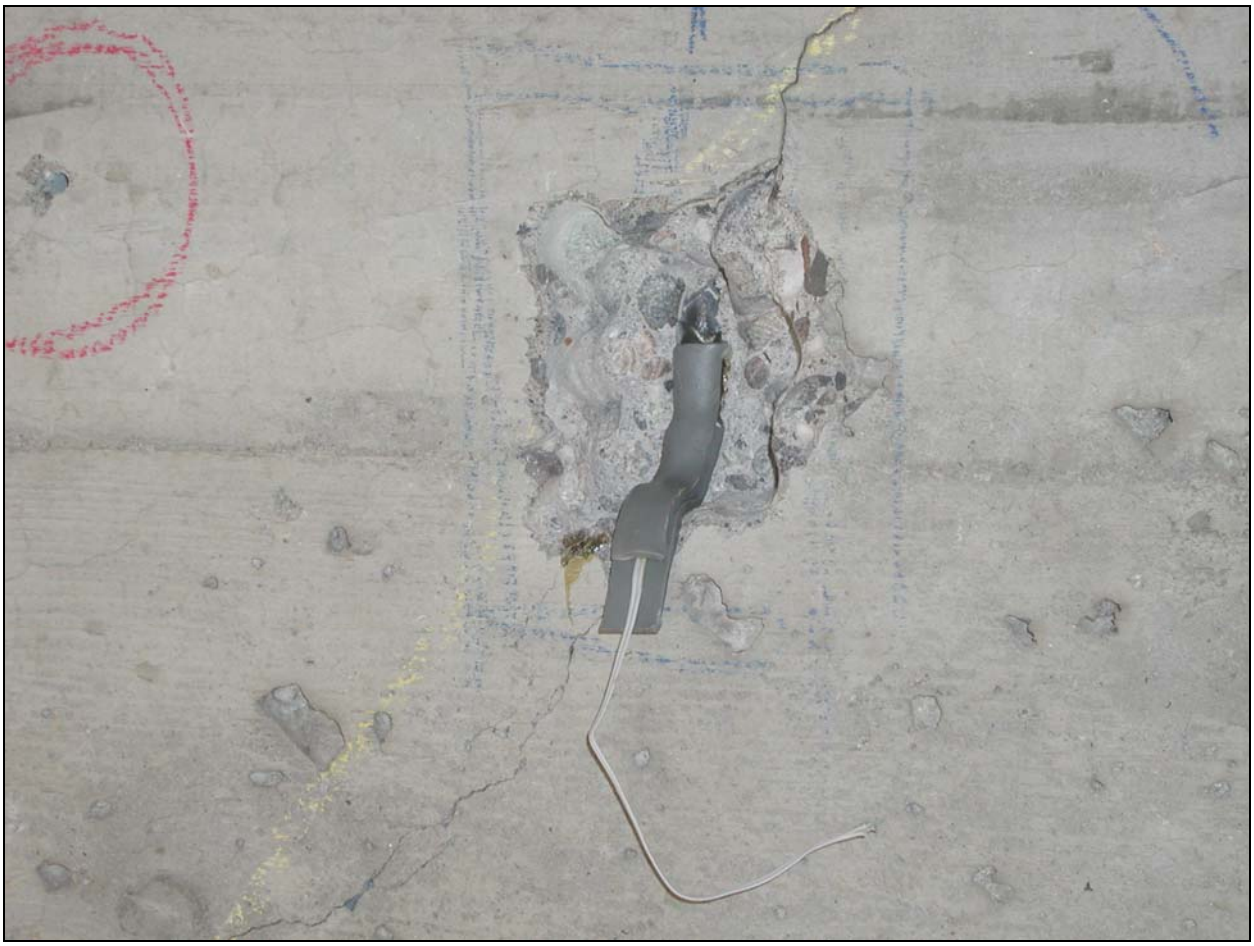


Figure 3.4: Example installation of strain gage on stirrup at diagonal crack location

Strain gages were installed in 11 different locations on the bridge; the locations are illustrated schematically in Figure 3.5. The holes were patched with rapid setting concrete mortar after completion of testing prior to repair installation. At one location, the sensor failed to operate properly during the first phase of testing (sensor #10). After installation of the supplemental stirrups, sensor #6 did not operate properly. The west exterior girder was not instrumented, because no significant diagonal cracking was observed on this girder (this girder was added in 1995).

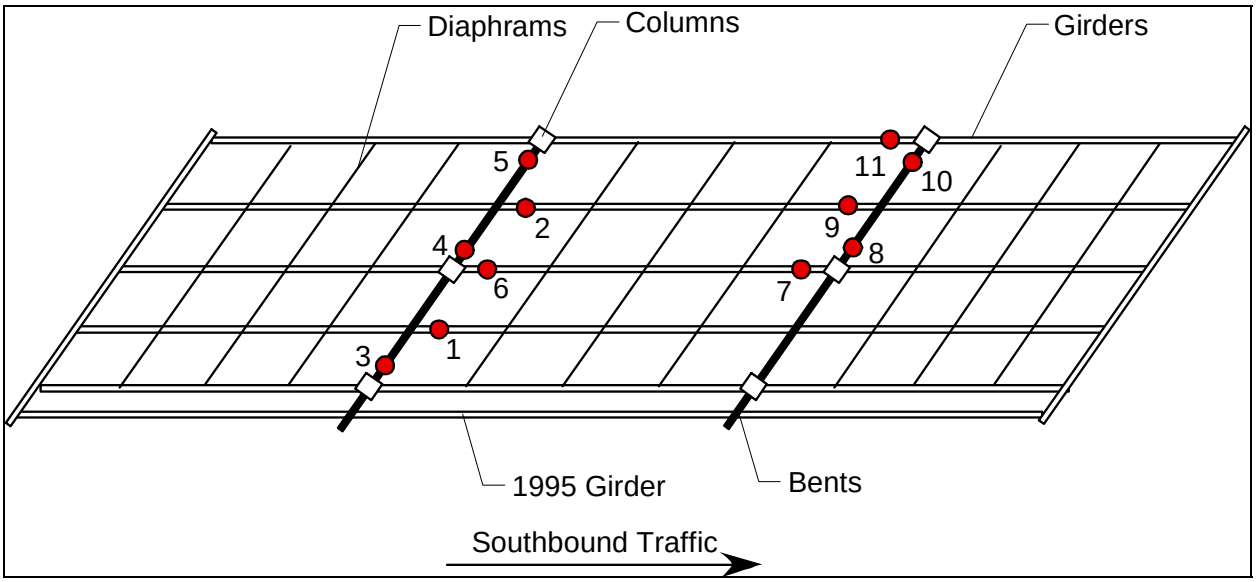


Figure 3.5: Schematic of locations instrumented stirrups on Clarks Branch Overcrossing

The strain gages and position sensors were connected to a Campbell Scientific CR9000 data logger. This is a high-speed, multi-channel, 16-bit digital data acquisition system. Resolution for the strain measurements was 5.84E-7 strain. In order to reduce noise and prevent aliasing in the data, both analog and digital filters were employed. During the ambient monitoring period, data were sampled at 100 Hz. A digital high-pass filter was utilized with a cut-off frequency of 40 Hz. The system recorded sensor readings and converted signals into corresponding rebar stresses. Data from the sensors were archived for retrieval and post-processing.

3.1.3 Testing method

Testing was performed on the bridge in the original condition in December 2006 before any work was done to the bridge. Then in December of 2007, after installation of supplemental internal stirrups, the bridge was retested (using the original sensors installed for the 2006 tests). In this report the 2006 tests are called "before repair," and the 2007 tests are called "after repair." Two different types of live load data were collected: response under ambient traffic loading and response under controlled truck loading.

3.1.3.1 Controlled truck tests

Controlled truck loading tests were conducted using a heavily loaded ODOT maintenance truck with axle weights and spacing shown in Figure 3.6. As seen in this figure, the test truck loads were similar for the tests in 2006 and 2007. Traffic was temporarily slowed with the use two incident response vehicles to create a rolling roadblock, so that the control truck would be the only vehicle on the bridge during data collection. The control truck passed over the bridge at several designated speeds and lane positions. Test speeds varied from 8 to 97 km/h (5 to 60 mph). Lane locations included placing the truck centered over the truck lane fog line, placing the passenger-

side tires on the truck fog line, placing the truck in the truck lane, straddling the truck over the center-line stripe, placing the truck in the passing lane, and placing the driver-side tires on the passing lane fog line.

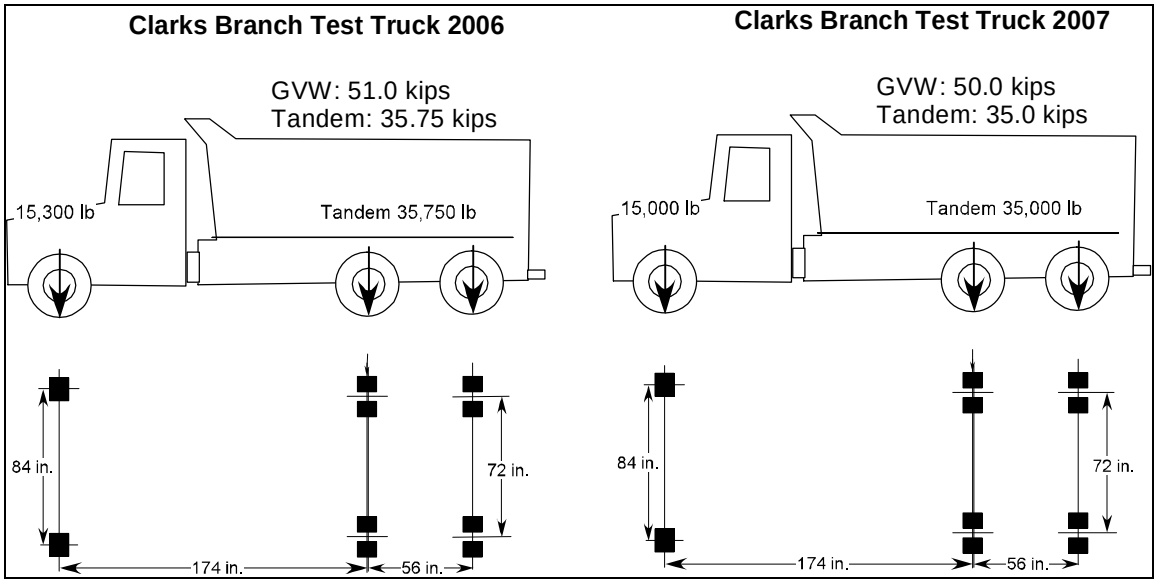


Figure 3.6: Test truck configuration and axle loads

During each pass of the control truck, stirrup stresses were recorded for each of the instrumented locations. For each of the test runs, peak stress values prior to installation of supplemental stirrups are summarized in Table 3.1 and values after installation of supplemental stirrups are summarized in Table 3.2. Example recorded strain histories for two truck positions on the bridge before and after installation of the supplemental stirrups are shown in Figures 3.7 and 3.8. Unfortunately, during the 2006 tests, sensor #10 did not work properly. It was fixed prior to the 2007 tests, but then sensor #6 was damaged during the repair installation. These two locations exhibited the larger strain histories, and changes associated with the repair installation cannot be directly compared for these two locations. For the other nine locations, which operated before and after repair installation (as seen in Figures 3.7 and 3.8 and in Tables 3.1 and 3.2) the measured strains for the cast-in-place stirrups were significantly reduced after installation of the supplemental internal stirrups.

Table 3.1: Stirrup strain peaks during controlled test truck loading before repair of Clarks Branch Overcrossing

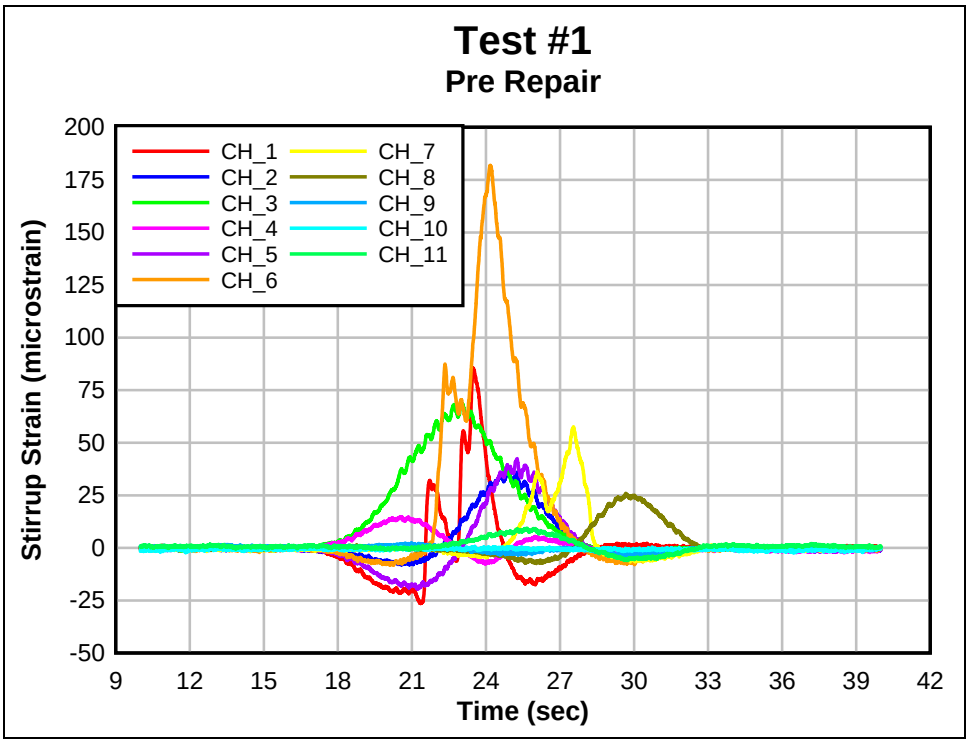
Maximum Strain (microstrain)													
Lane Position	Speed	Test #	Ch_1	Ch_2	Ch_3	Ch_4	Ch_5	Ch_6	Ch_7	Ch_8	Ch_9	Ch_10	Ch_11
Straddle truck Fogline	5 mph	1	88	27	90	13	27	141	23	20	2	2	4
On Truck Fogline	5 mph	2	86	36	69	15	42	182	58	26	2	1	9
In Truck Lane	5 mph	3	44	45	47	18	51	202	81	31	2	1	9
Over Centerline	5 mph	4	3	78	18	53	93	128	105	65	29	1	15
In Passing Lane	5 mph	5	3	81	9	81	107	27	78	82	62	1	22
On Passing Fogline	5 mph	6	1	68	9	73	81	14	54	80	76	1	33
In Truck Lane	53 mph	7	71	47	66	25	61	175	66	31	3	2	11
In Passing Lane	54 mph	8	3	87	8	82	105	26	79	82	51	2	23
In Truck Lane	68 mph	9	101	39	83	28	42	248	57	34	2	2	11
In Passing Lane	65 mph	10	7	95	11	81	106	32	86	78	63	1	24
Minimum Strain (microstrain)													
Lane Position	Speed	Test #	Ch_1	Ch_2	Ch_3	Ch_4	Ch_5	Ch_6	Ch_7	Ch_8	Ch_9	Ch_10	Ch_11
Straddle truck Fogline	5 mph	1	-24	-8	-2	-8	-17	-14	-5	-9	-4	-1	-6
On Truck Fogline	5 mph	2	-26	-8	-3	-8	-20	-8	-7	-7	-4	-2	-6
In Truck Lane	5 mph	3	-19	-7	-3	-5	-20	-7	-7	-5	-5	-2	-9
Over Centerline	5 mph	4	-11	-5	-5	-2	-17	-2	-10	-2	-4	-2	-12
In Passing Lane	5 mph	5	-6	-2	-18	-1	-6	-4	-11	-3	-19	-2	-12
On Passing Fogline	5 mph	6	-4	-3	-17	-2	0	-5	-11	-4	-12	-1	-8
In Truck Lane	55 mph	7	-31	-11	-7	-8	-30	-10	-8	-8	-5	-1	-8
In Passing Lane	55 mph	8	-9	-4	-20	-2	-7	-7	-13	-4	-16	-1	-12
In Truck Lane	61 mph	9	-34	-15	-5	-13	-31	-16	-10	-10	-6	-1	-8
In Passing Lane	63 mph	10	-11	-4	-20	-3	-8	-13	-16	-5	-17	-1	-13

Note: CH 10 bad.

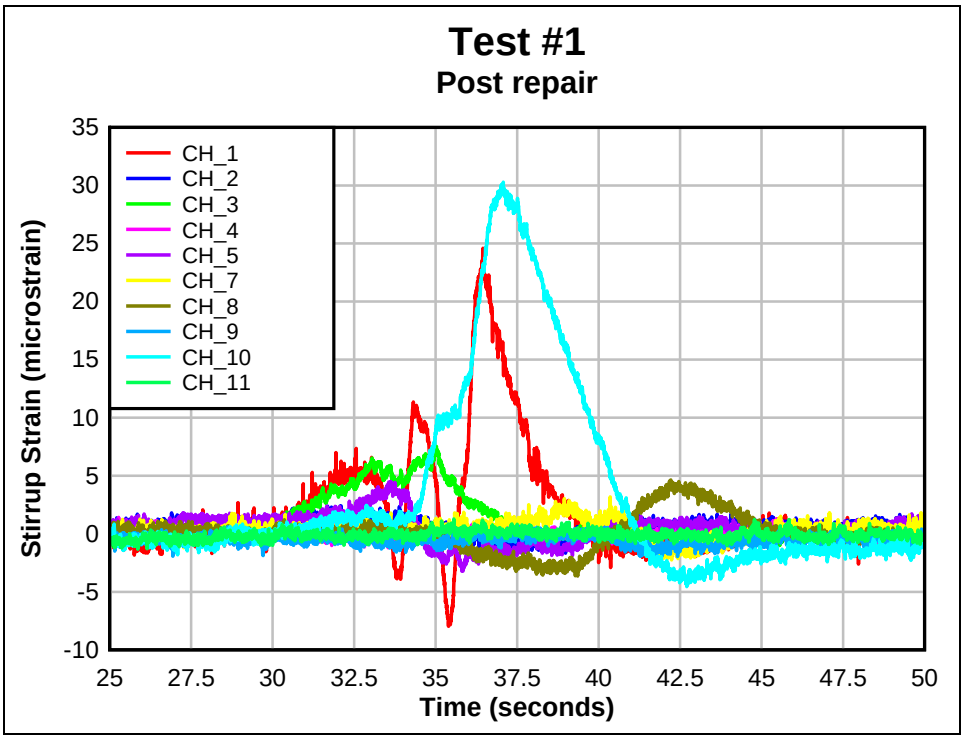
Table 3.2: Stirrup strain peaks during controlled test truck loading after repair of Clarks Branch Overcrossing

Maximum Strain (microstrain)													
Lane Position	Speed	Test #	Ch_1	Ch_2	Ch_3	Ch_4	Ch_5	Ch_6	Ch_7	Ch_8	Ch_9	Ch_10	Ch_11
Straddle truck Fogline	5 mph	1	25	2	8	1	4	0	4	4	1	31	1
On Truck Fogline	5 mph	2	20	2	4	1	4	0	3	5	2	36	1
In Truck Lane	5 mph	3	15	3	5	1	5	0	2	6	1	37	1
Over Centerline	5 mph	4	5	1	2	1	5	0	2	5	4	13	1
In Passing Lane	5 mph	5	6	1	2	2	6	0	2	3	1	8	2
On Passing Fogline	5 mph	6	4	2	2	2	6	0	3	2	1	7	4
In Truck Lane	53 mph	7	12	2	5	1	26	0	3	5	1	44	1
In Passing Lane	54 mph	8	3	1	2	2	44	0	2	3	2	8	3
In Truck Lane	68 mph	9	12	1	4	1	40	0	2	6	1	36	1
In Passing Lane	65 mph	10	2	1	2	2	57	0	2	3	2	9	3
Minimum Strain (microstrain)													
Lane Position	Speed	Test #	Ch_1	Ch_2	Ch_3	Ch_4	Ch_5	Ch_6	Ch_7	Ch_8	Ch_9	Ch_10	Ch_11
Straddle truck Fogline	5 mph	1	-8	-2	-1	-2	-4	0	-2	-5	-2	-4	-1
On Truck Fogline	5 mph	2	-12	-3	-3	-1	-5	0	-2	-5	-1	-6	-1
In Truck Lane	5 mph	3	-1	-3	-1	-2	-6	0	-4	-5	-2	-6	-1
Over Centerline	5 mph	4	-3	-8	-2	-4	-8	0	-13	-7	-2	-5	-2
In Passing Lane	5 mph	5	-2	-5	-2	-5	-10	0	-10	-8	-10	-4	-2
On Passing Fogline	5 mph	6	-4	-5	-2	-4	-10	0	-7	-6	-7	-2	-1
In Truck Lane	55 mph	7	-1	-3	-2	-2	-26	0	-1	-5	-2	-6	-2
In Passing Lane	55 mph	8	-2	-4	-1	-4	-32	0	-8	-7	-8	-4	-1
In Truck Lane	61 mph	9	-2	-4	-2	-2	-41	0	-5	-5	-1	-6	-2
In Passing Lane	63 mph	10	-2	-4	-2	-5	-37	0	-9	-8	-6	-3	-1

Note: CH 6 bad after repair.

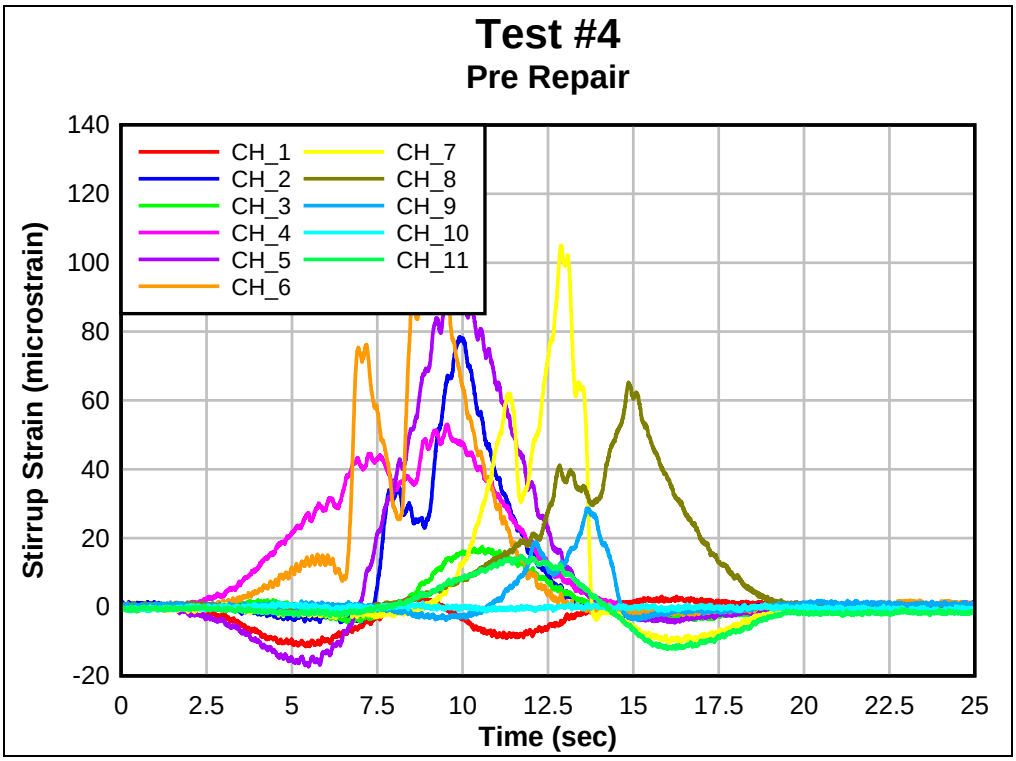


(a)

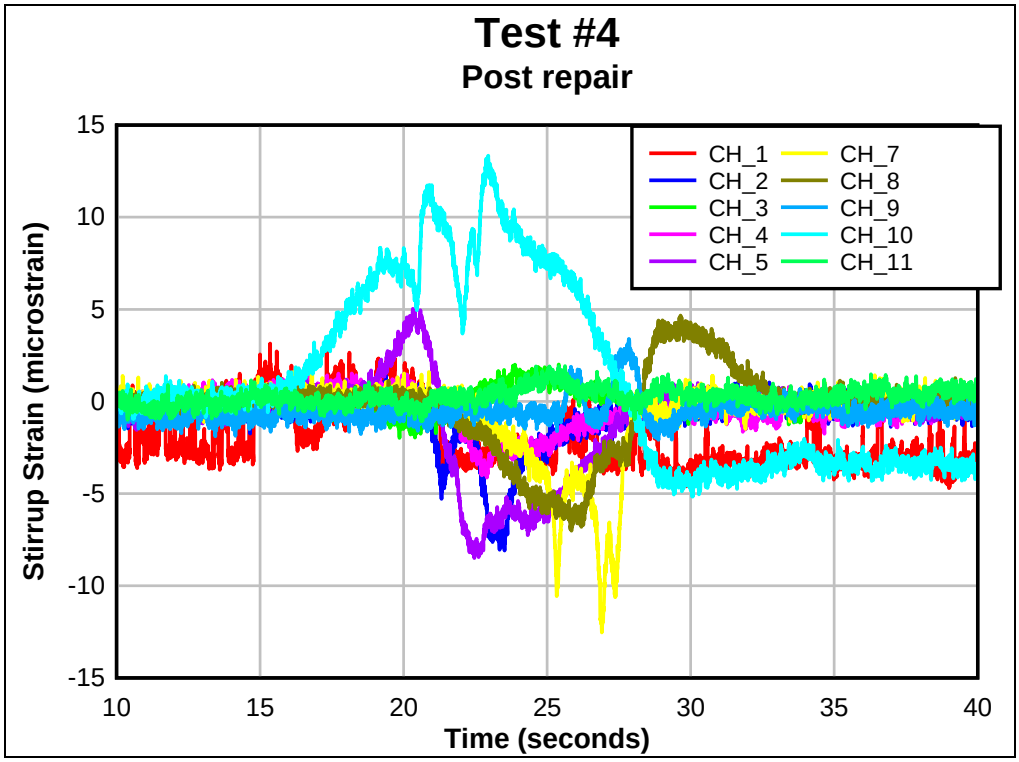


(b)

Figure 3.7: Test Run #1 (truck straddling the driving lane fog line): (a) unrepaired, and (b) after supplemental internal stirrups. Note vertical scales are different.



(a)



(b)

Figure 3.8: Test Run #4 (truck over the centerline): (a) unrepaired, and (b) after supplemental internal stirrups. Note vertical scales are different.

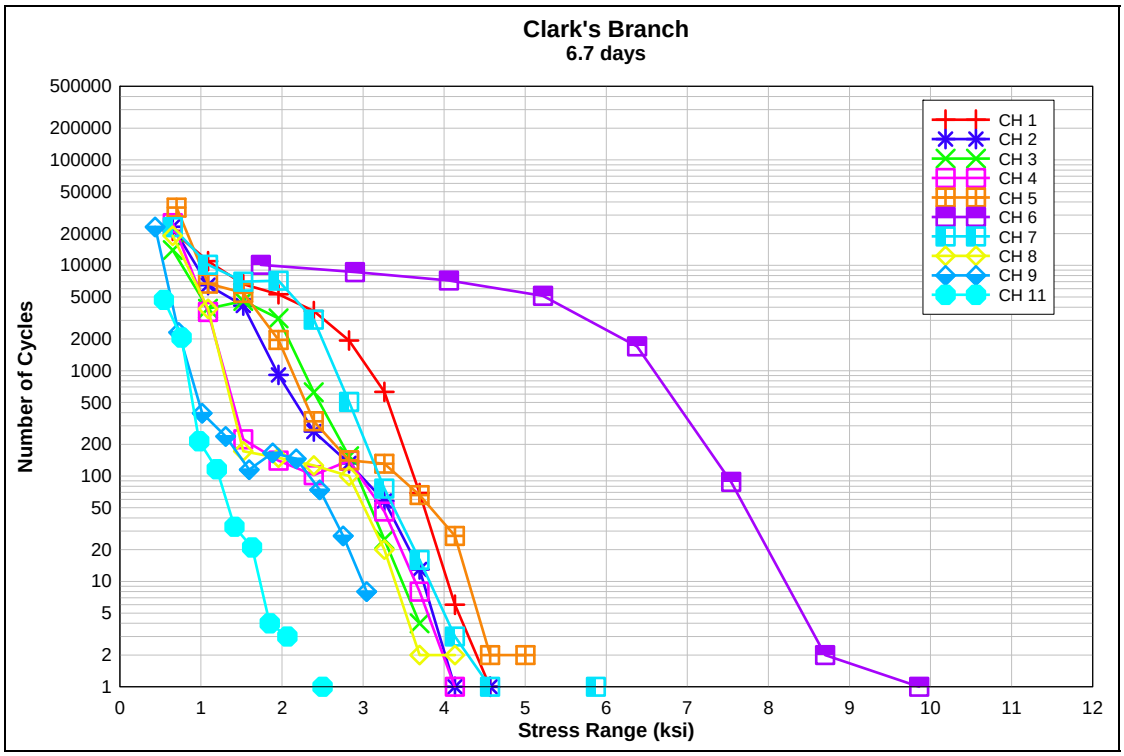
3.1.3.2 Ambient traffic induced stirrup stress

The stirrup reinforcing stresses generated by normal traffic flow were recorded over a period of 6.7 days during the period from December 7 to 18, 2006 and for a period of 2.4 days from November 29 to December 2, 2008. The system also recorded individual event histories to ensure that large strain cycle counts could be verified as load induced rather than due to instrument drift or noise. The stress-ranges and numbers of cycles recorded at the instrumented locations are shown in Figures 3.9a and 3.9b for "before repair" and "after repair," respectively. Stress-ranges below 2.76 MPa (400 psi) were discarded. The largest single strain-range measured at any location was approximately 340 microstrain (corresponding to approximately 10.0 ksi) at location CH_6, the girder near the interior column (see Figure 3.5). Using Miner's Rule (*Miner 1945*), the variable amplitude stresses were described as an equivalent constant amplitude stress-range for each of the instrumented locations:

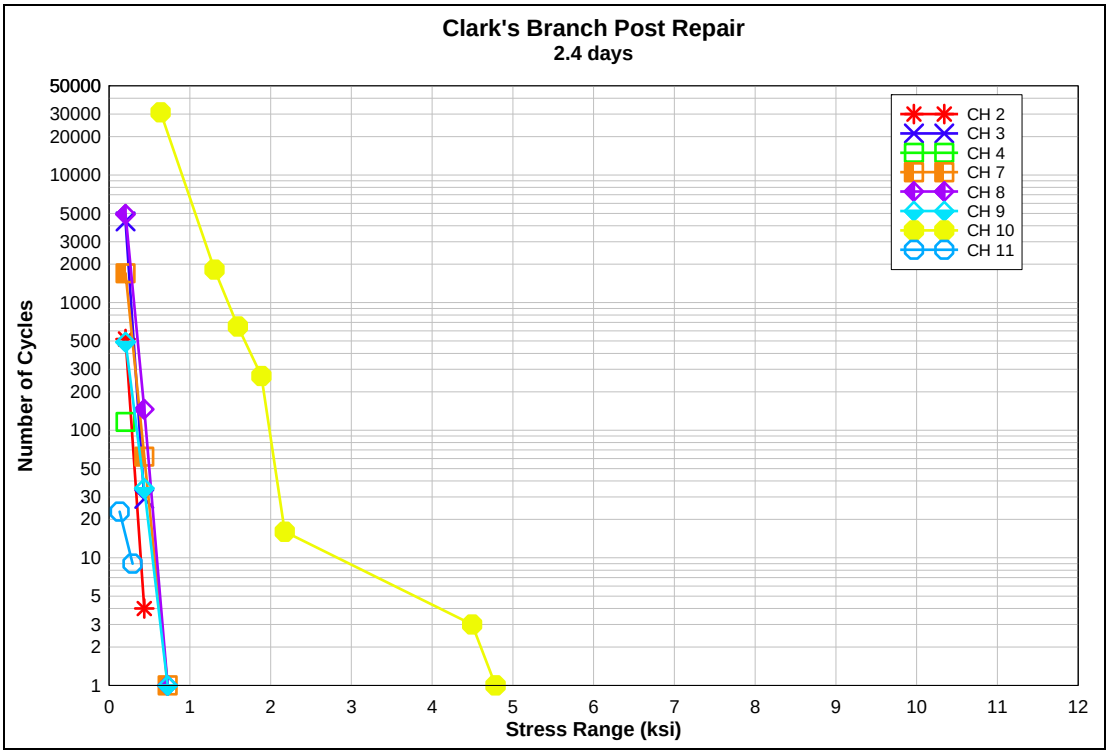
$$SR_{eqv} = \sqrt[3]{\sum \frac{n_i}{N_{tot}} SR_i^3} \qquad \textbf{(3-1)}$$

where SR_i is the i^{th} stress-range; n_i is the number of cycles observed for the i^{th} stress-range; and N_{tot} is the total number of cycles at all stress ranges.

The equivalent constant amplitude stress-ranges were below 4 ksi prior to repair at all locations and below 2 ksi after repair at all locations as seen in Figures 3.10a and 3.10b. These relatively small equivalent constant amplitude stress-ranges are consistent with those measured in previous research on other 1950's vintage RCDG bridges (*Higgins, et al. 2004a*) and indicate that high-cycle fatigue of the embedded stirrups is unlikely. Further installation of the supplemental internal stirrups reduced the demands on the cast-in-place stirrups.

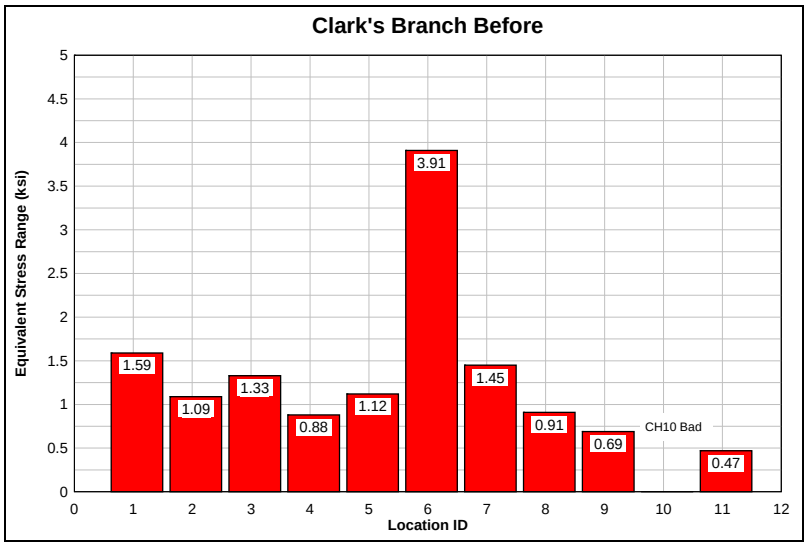


(a)

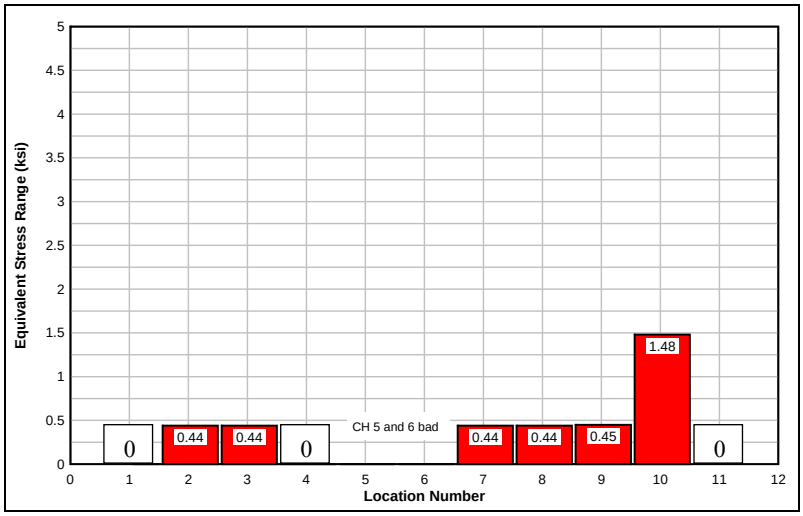


(b)

Figure 3.9: Cast-in-place stirrup stress range-number of cycles (a) before repair (CH10 not working) and (b) after installation of supplemental internal stirrups (CH5 was noisy during ambient traffic monitoring; CH6 not working)



(a)



(b)

Figure 3.10: Cast-in-place stirrup equivalent stress ranges after discarding lowest bin stress range data (a) before and (b) after installation of supplemental internal stirrups

3.2 WILLAMETTE RIVER BRIDGE

3.2.1 Description

The Willamette River Bridge (ODOT Bridge Inventory Number 08156) is located on Oregon Highway 219, near Newberg, OR. The RCDG bridge was designed in 1954 and investigated previously by Oregon State University (*Higgins, et al. 2004a*).[1] The original inspection of the bridge, which occurred in late summer of 2001, indicated significant diagonal cracking in the high-shear regions near the supports. Details of this prior work are reported in Higgins, et al. (*2004a*). The bridge consists of ten spans: four steel plate girder spans over water and three conventionally reinforced concrete approach spans at each end. The bridge has a regular layout with rectangular prismatic girders, and the south approach spans were selected for instrumentation.

The approach spans have three equal span lengths, 16.8 m (55 ft) each, and have a total width of 10.7 m (35 ft) as illustrated in Figure 3.11. The spans are comprised of one simple span having five girders 368 x 1346 mm (14.5 x 53 in) and two continuous spans having four girders 330 x 1346 mm (13 x 53 in). Reinforced concrete diaphragms 229 x 1219 mm (9 x 48 in) are located at quarter points of each span. The approach spans have three simple supports and are continuous over one interior support with a transverse bent cap 419 x 1803 mm (16.5 x 71 in) supported by two columns. The specified concrete compression strength was 22.75 MPa (3300 psi), and reinforcing steel consisted of ASTM A305 intermediate grade deformed square and round bars with nominal yield stress of 276 MPa (40 ksi).

The bridge was repaired primarily for shear with CFRP in the fall of 2001. The material used was CF130 unidirectional high-strength carbon fiber fabric, manufactured by MBrace. Prior to application of the CFRP, the surface was prepared by diamond grinding, and the diagonal and flexural cracks were epoxy-injected. An epoxy primer was then applied, followed by a high viscosity epoxy paste. Individual 305 mm (12 in) wide strips of CFRP laminate were applied in a U-shape to the prepared surface around the girder webs and soffit in varying plies with an epoxy-encapsulated resin saturant. An open space of approximately 51 mm (2 in) was left between strips. Additionally, CFRP strips were placed along the web soffit and along the top of the web to provide supplemental flexural reinforcing. Typical CFRP repair of the main girders and bent caps is shown in Figures 3.12a and b, respectively.

[1] Oregon Department of Transportation, Research Unit, Project SPR 341

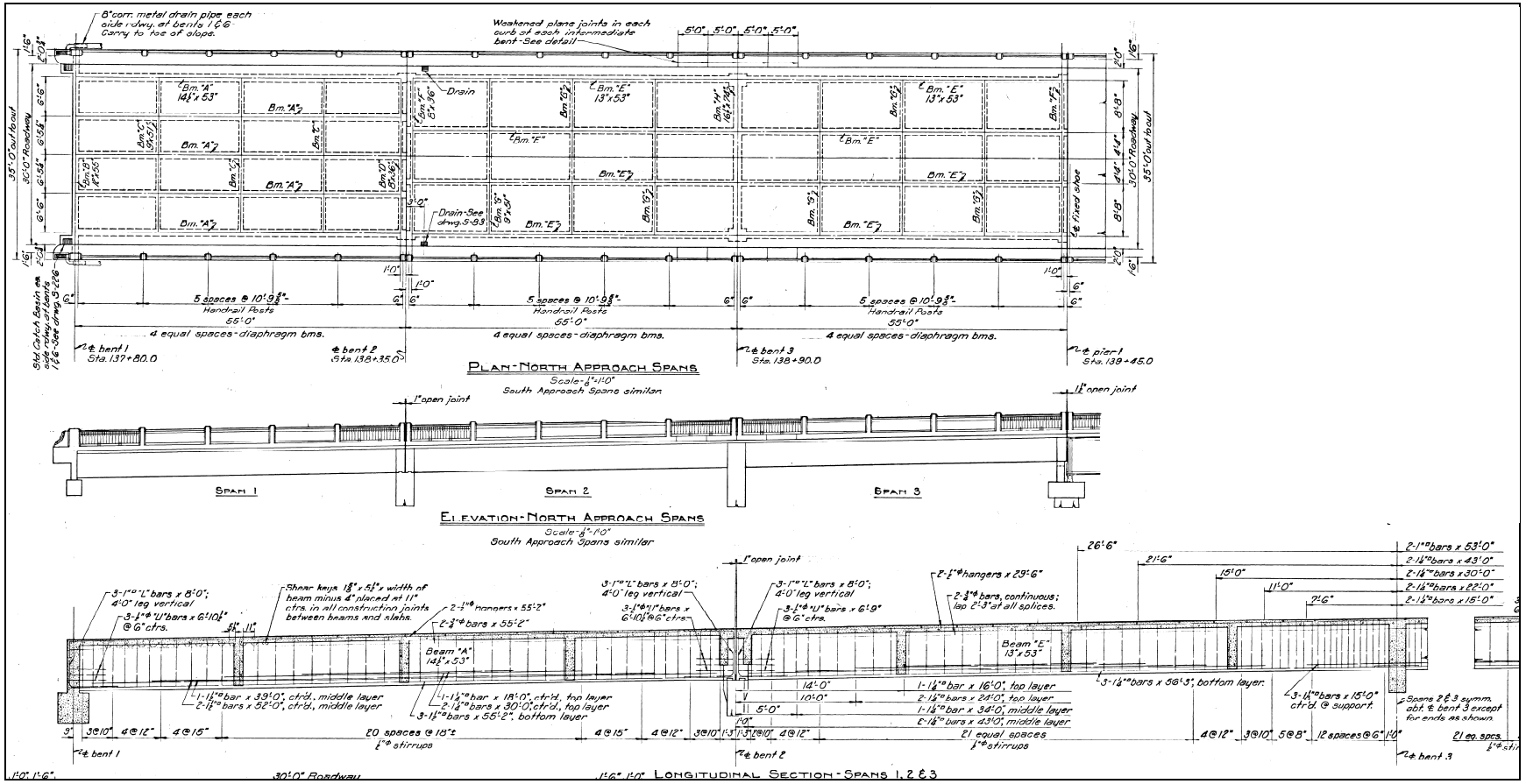
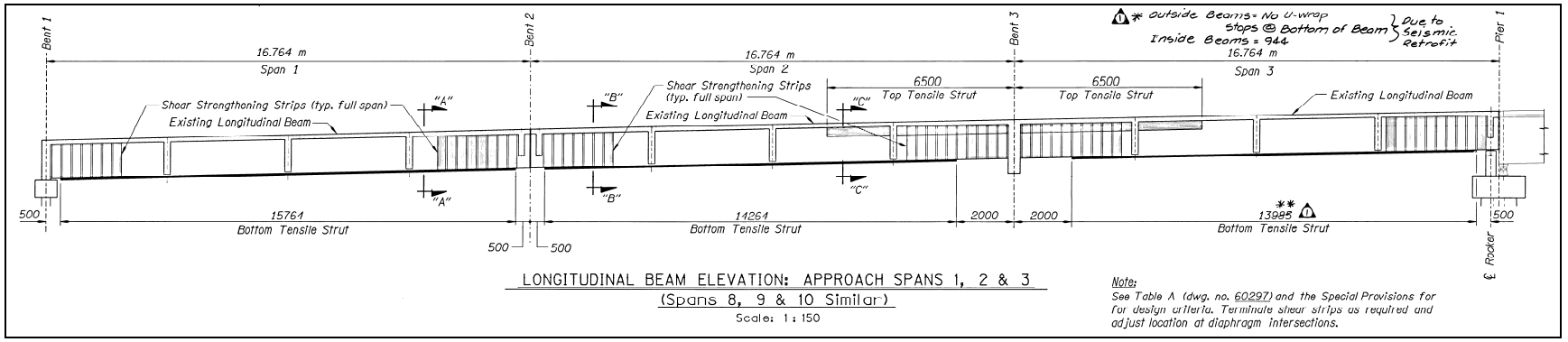
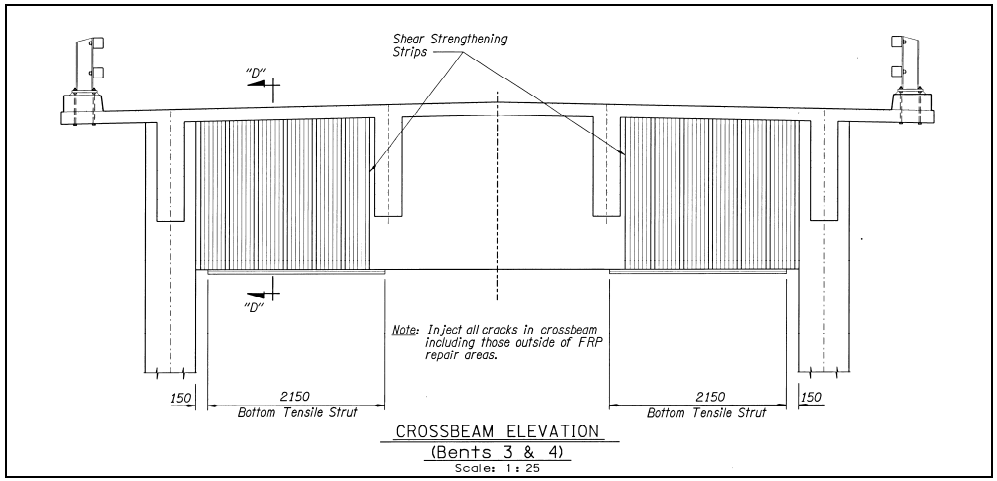


Figure 3.11: Willamette River Bridge overall plan and elevation and main girder details



(a)



(b)

Figure 3.12: CFRP repairs to (a) main girders and (b) bent caps

3.2.2 Inspection and instrumentation

In October 2004, three years after installation of the CFRP repairs, the bridge was re-inspected, instrumented, and monitored under ambient traffic conditions to measure in-situ CFRP strain ranges at high shear locations. The bent caps and longitudinal deck girders were re-inspected to determine if cracking re-occurred and to identify the as-built locations of the CFRP strips. A hand-held laser distance meter was used to rapidly locate cracks and CFRP strips relative to support locations. Examples of stirrup locations, original cracks, and CFRP strips on the exterior girder are shown in Figure 3.13. During the post-repair inspection, no new diagonal cracks were observed in the bent caps or girders. Flexural cracking was observed at only one location near midspan of the exterior girder.

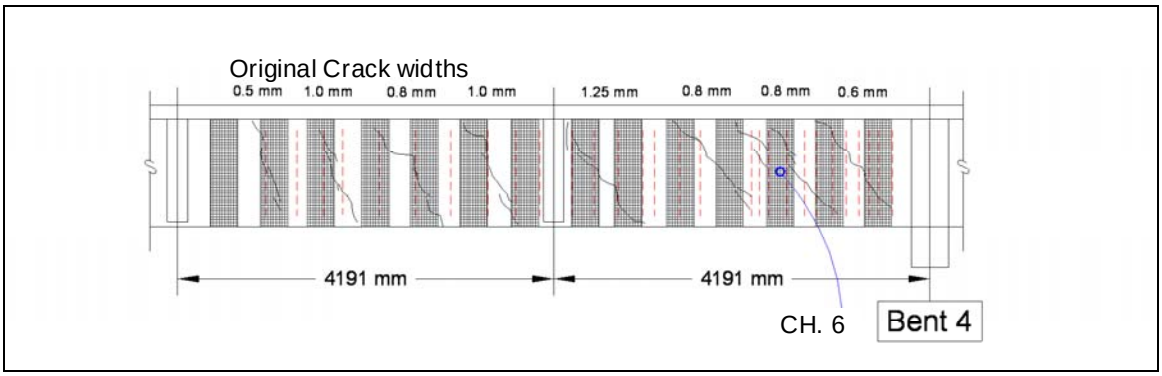


Figure 3.13: Field measured cracking, embedded stirrups, and externally bonded CFRP on exterior girder

After inspection, strain gages were installed on individual CFRP strips at selected high-shear locations. Strain gages were bonded to the surface of the CFRP at mid-depth of the girder and oriented in the vertical (fiber) direction. The chosen strain gage length was 51 mm (2 in.), permitting strain averaging over several transverse weave fibers that were spaced approximately 8 mm (0.31 in.). Instrumented locations are illustrated schematically in Figure 3.14. The strain gages were connected to a high-speed, multi-channel, 16-bit digital data logger. To reduce noise and prevent aliasing in the data, both analog and digital filters were employed. During the ambient monitoring period, data were sampled at 100 Hz. The system recorded sensor readings and converted signals into corresponding CFRP strains. Data from sensors were archived for retrieval and post-processing.

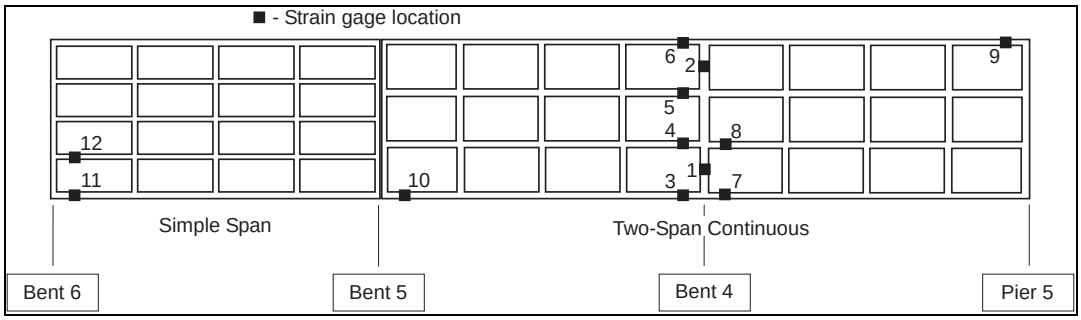


Figure 3.14: Schematic of instrumentation locations

The bridge was re-inspected in 2008, and the original sensors were checked to determine if they were still operational. They were observed to be in good condition without a change in resistance; thus they were wired into the same data logger system described previously, and CFRP strains were collected during field testing using the same sensors at the same locations used in 2004. During this re-inspection, diagonal cracking was observed in the concrete between CFRP strips at a number of locations, with most being located on the exterior girders as seen in Figure 3.15. These cracks appeared to be previous diagonal cracks that had reopened. No stress induced CFRP debonding was observed at strip terminations or at locations adjacent to the newly observed diagonal cracks. Additionally, there were locations that exhibited loss or flaking of the protective coating that covers the CFRP matrix as seen in Figure 3.16.



Figure 3.15: Example diagonal cracks observed



Figure 3.16: Example loss of surface protective coating

3.2.3 Testing method

Testing was performed on the bridge in December 2004[2] after installation of the CFRP (installed in 2001). The bridge was retested as part of the present research study in May 2008. Two different types of live load data were collected in both 2004 and 2008: response under ambient traffic loading and response under controlled truck loading. The same sensors and locations were used in both studies.

3.2.3.1 Controlled truck tests

Controlled truck loading tests were conducted using a heavily loaded ODOT maintenance truck with axle weights and spacing shown in Figure 3.17.

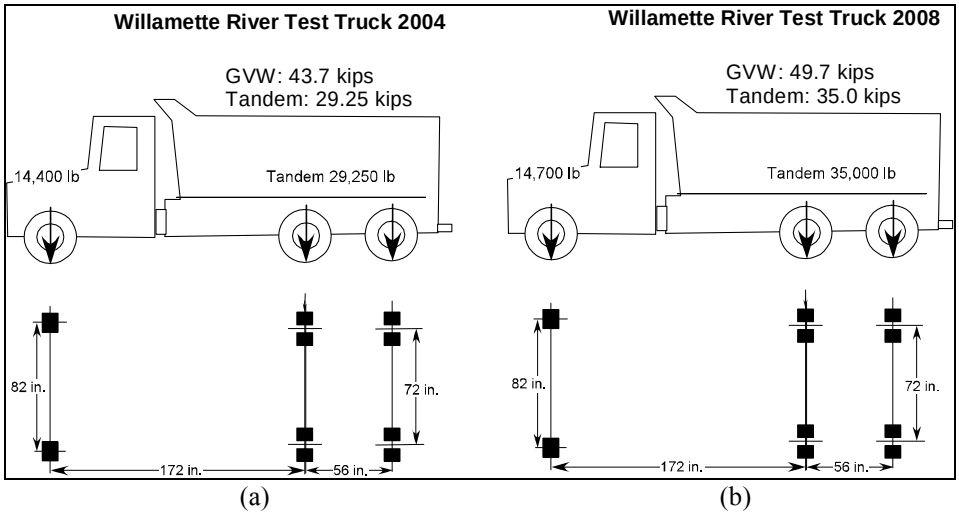


Figure 3.17: Controlled test truck configurations (a) 2004 and (b) 2008

[2] Oregon Department of Transportation, Research Unit, Project SPR 341

As seen in this figure, the test truck loads were similar to the tests of Clarks Branch Overcrossing in 2006 and 2007. Traffic was temporarily stopped using a flagging crew, so that the control truck would be the only vehicle on the bridge during data collection. This allowed the truck to be positioned in lanes that are sometimes opposite to the direction of travel. The control truck passed over the bridge at several designated speeds and lane positions. Test speeds varied from 8 to 97 km/h (5 to 60 mph). Lane locations included placing the truck centered over the truck lane fog line, placing the passenger-side tires on the truck fog line, placing the truck in the truck lane, straddling the truck over the center-line stripe, placing the truck in the passing lane, and placing the driver-side tires on the passing lane fog line.

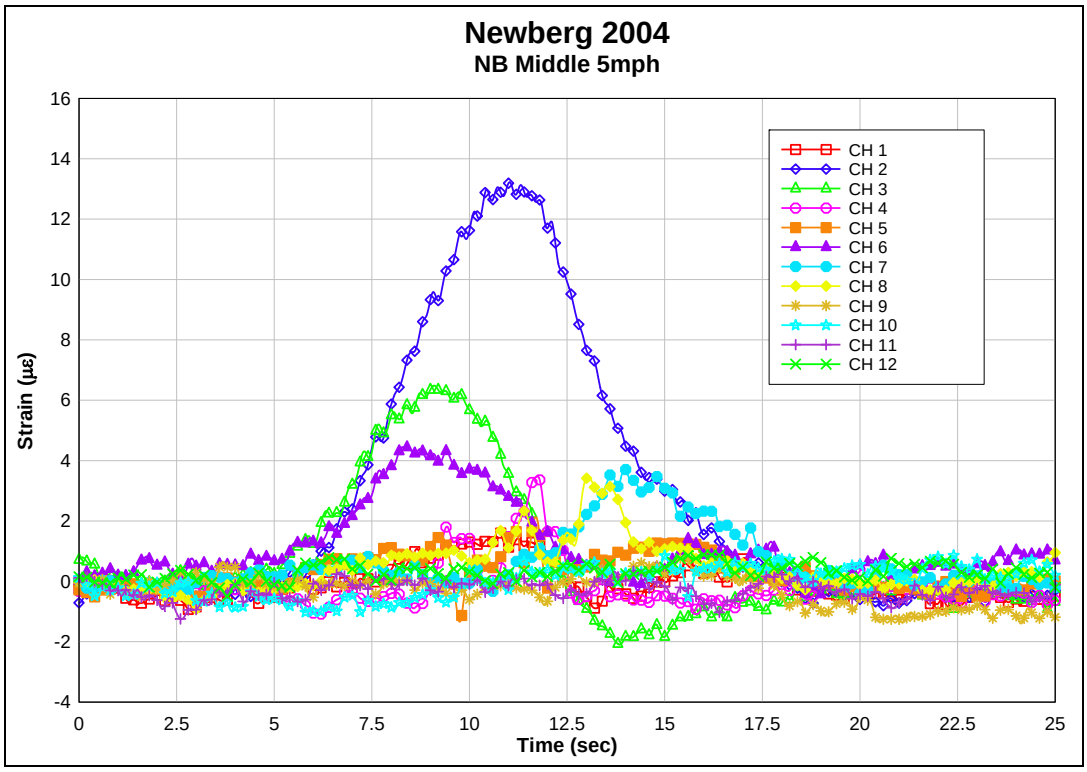
During each pass of the control truck, CFRP strains were recorded for each of the instrumented locations. For each of the test runs, peak stress values are summarized in Table 3.3 for the 2004 tests and in Table 3.4 for the 2008 tests. Example recorded strain histories for the test truck driving northbound over the center stripe at 8 km/h (5 mph) are shown in Figure 3.18a and b for 2004 and 2008, respectively. For all locations, as seen in Figure 3.18 and Tables 3.3 and 3.4, the measured CFRP strains were only slightly larger and effectively similar. On average for all tests and all sensors, the difference between the 2004 and 2008 results were less than 1 microstrain.

Table 3.3: CFRP strip strain peaks during controlled test truck loading in 2004 of Willamette River Bridge near Newberg

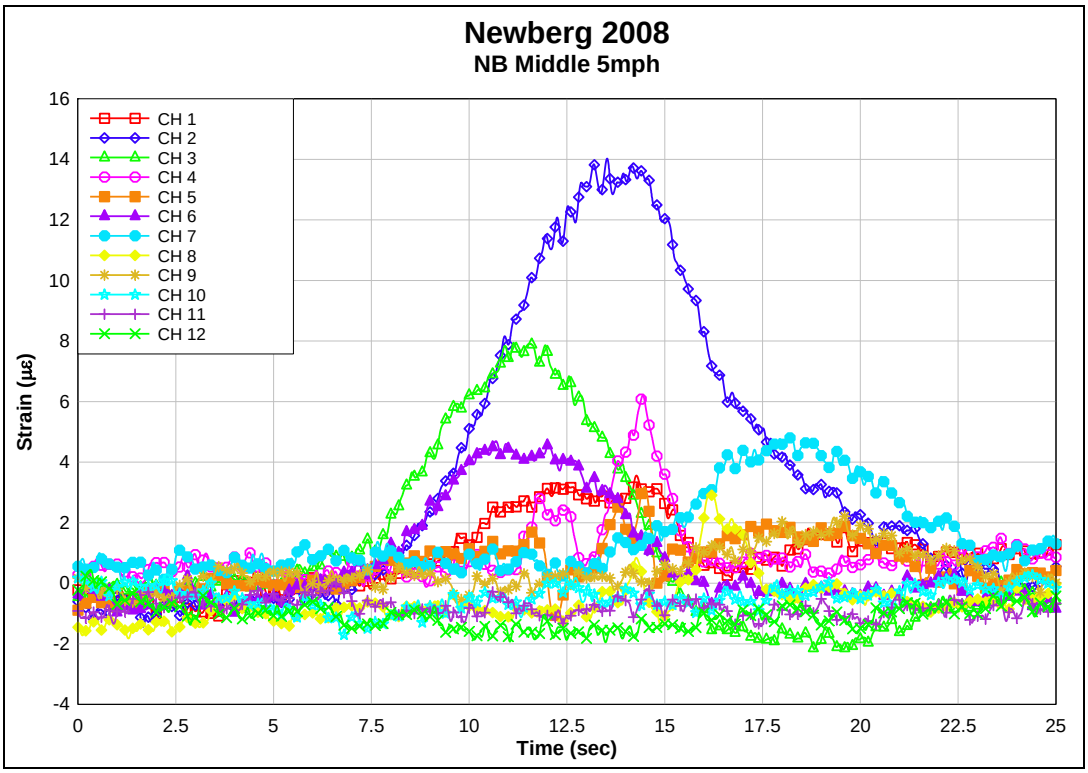
2004														
Maximum Strain														
Lane Position	Speed	Test #	Ch_1	Ch_2	Ch_3	Ch_4	Ch_5	Ch_6	Ch_7	Ch_8	Ch_9	Ch_10	Ch_11	CH_12
NbinNBLane	5	1	5	8	7	0	2	2	4	1	0	1	0	1
NBinSBLane	5	2	2	11	4	1	2	5	3	2	1	1	0	0
NBonNBFogline	5	3	7	8	8	0	0	0	3	1	1	1	1	0
NBonSBFogline	5	4	2	10	3	1	1	5	1	0	2	1	0	0
NBoverCL	5	5	1	13	6	3	2	4	4	3	0	1	0	0
5mphSBinNBLane	5	6	5	10	9	2	2	2	2	3	2	1	1	1
5mphSBinSBLane	5	7	2	10	4	1	2	6	3	2	2	2	1	1
5mphSBonNBFogline	5	8	6	8	10	1	1	1	3	1	1	2	1	1
5mphSBonSBFogline	5	9	4	11	4	1	2	8	3	1	3	0	1	1
5mphSBoverCL	5	10	2	14	6	3	3	3	3	4	1	1	1	1
55mphNBinLane	55	11	5	9	9	1	1	2	4	2	1	0	1	1
55mphSBinLane	55	12	2	11	5	1	2	6	2	1	2	1	1	0
63mphNBinLane	63	13	8	12	12	1	1	2	5	3	1	2	1	1
63mphSBinLane	63	14	3	9	4	1	2	6	3	0	3	2	1	1
Minimum Strain														
Lane Position	Speed	Test #	Ch_1	Ch_2	Ch_3	Ch_4	Ch_5	Ch_6	Ch_7	Ch_8	Ch_9	Ch_10	Ch_11	CH_12
NbinNBLane	5	1	-4	-2	-5	-6	-1	-1	-5	-3	0	-4	-3	-1
NBinSBLane	5	2	-3	-1	-3	-2	0	-1	-4	-1	-1	-4	-2	0
NBonNBFogline	5	3	-1	-1	-2	-1	-1	0	0	0	-1	-1	-1	0
NBonSBFogline	5	4	-2	0	-2	0	-1	-6	-1	1	-7	-1	0	0
NBoverCL	5	5	-2	0	-2	0	-4	-8	-1	-1	-9	-1	0	0
5mphSBinNBLane	5	6	-3	-1	-3	-1	0	-1	-5	-1	0	-4	-2	0
5mphSBinSBLane	5	7	-2	-1	-3	-1	-3	-6	-1	-1	-8	-1	-1	-1
5mphSBonNBFogline	5	8	-5	-1	-4	-4	-1	-1	-6	-4	-1	-5	-3	-1
5mphSBonSBFogline	5	9	-2	-1	-2	-1	-5	-5	-1	-1	-5	-1	-1	-1
5mphSBoverCL	5	10	-2	-1	-2	-1	-1	-1	-1	-1	-1	-1	-1	0
55mphNBinLane	55	11	-3	-1	-3	-2	-1	-1	-4	-1	0	-5	-1	-1
55mphSBinLane	55	12	-2	-1	-2	-1	-1	-5	-2	0	-6	-1	-1	-1
63mphNBinLane	63	13	-4	-2	-3	-2	0	-1	-3	0	-1	-3	-1	-1
63mphSBinLane	63	14	-2	-2	-2	0	-3	-5	-1	-1	-5	-1	-1	-1

Table 3.4: CFRP strip strain peaks during controlled test truck loading in 2008 of Willamette River Bridge near Newberg

2008														
Maximum Strain														
Lane Position	Speed	Test #	Ch_1	Ch_2	Ch_3	Ch_4	Ch_5	Ch_6	Ch_7	Ch_8	Ch_9	Ch_10	Ch_11	CH_12
5mphNBinNBLane	5 mph	1	6	9	9	2	1	3	5	0	0	0	0	4
5mphNBinSBLane	5 mph	2	3	11	5	2	2	6	3	1	2	1	1	1
5mphNBonNBFogline	5 mph	3	8	7	10	0	0	0	4	1	1	0	1	3
5mphNBonSBFogline	5 mph	4	2	10	5	0	2	7	3	1	2	1	1	0
5mphNBoverCL	5 mph	5	3	14	8	6	3	5	5	3	2	1	0	0
5mphSBinNBLane	5 mph	6	5	11	10	1	2	4	5	2	1	1	2	3
5mphSBinSBLane	5 mph	7	2	9	5	1	3	8	4	1	2	1	1	1
5mphSBonNBFogline	5 mph	8	8	8	12	1	1	1	4	1	1	1	1	3
5mphSBonSBFogline	5 mph	9	3	10	4	1	1	9	2	1	2	1	1	1
5mphSBoverCL	5 mph	10	3	13	8	5	4	5	4	3	2	0	1	1
50mphNBinLane	50 mph	11	7	9	10	1	1	2	4	3	2	2	1	4
50mphSBinLane	50 mph	12	3	10	5	0	3	9	3	1	4	1	1	1
59mphNBinLane	59 mph	13	9	9	10	1	1	3	6	1	0	1	0	3
62mphSBinLane	62 mph	14	3	11	6	1	2	9	3	0	3	1	2	1
Minimum Strain														
Lane Position	Speed	Test #	Ch_1	Ch_2	Ch_3	Ch_4	Ch_5	Ch_6	Ch_7	Ch_8	Ch_9	Ch_10	Ch_11	CH_12
5mphNBinNBLane	5 mph	1	-4	-1	-5	-2	-1	-1	-6	-4	-2	-7	-2	-2
5mphNBinSBLane	5 mph	2	-3	-1	-3	-1	-3	-6	-1	-1	-7	-1	-1	0
5mphNBonNBFogline	5 mph	3	-5	-2	-6	-7	-1	-2	-7	-6	-1	-7	-3	-2
5mphNBonSBFogline	5 mph	4	-3	-1	-2	-2	-7	-10	-2	0	-10	-1	0	-1
5mphNBoverCL	5 mph	5	-1	-1	-2	0	-1	-1	0	-2	-1	-2	-1	-2
5mphSBinNBLane	5 mph	6	-3	-1	-4	-1	-1	0	-4	-1	-1	-4	-1	-2
5mphSBinSBLane	5 mph	7	-3	-1	-3	0	-4	-7	-1	-1	-10	-1	-1	-1
5mphSBonNBFogline	5 mph	8	-5	-1	-3	-5	-1	-2	-8	-5	-1	-7	-3	-2
5mphSBonSBFogline	5 mph	9	-2	-4	-3	-1	-8	-7	-2	-1	-8	-1	-1	-1
5mphSBoverCL	5 mph	10	-1	-2	-2	-1	-1	-1	-1	-1	-1	-1	-1	-1
50mphNBinLane	50 mph	11	-4	-1	-4	-3	-2	-1	-7	-2	0	-5	-2	-2
50mphSBinLane	50 mph	12	-3	-2	-3	-2	-5	-7	-2	-1	-9	-1	-1	-1
59mphNBinLane	59 mph	13	-4	-2	-6	-4	-1	-2	-5	-3	-2	-5	-3	-1
62mphSBinLane	62 mph	14	-3	0	-2	-1	-5	-6	-2	-2	-9	-2	0	-1



(a)



(b)

Figure 3.18: Example of measured CFRP strip strains from controlled test trucks located northbound driving over the center stripe (a) 2004 and (b) 2008

3.2.3.2 Ambient traffic-induced CFRP strains

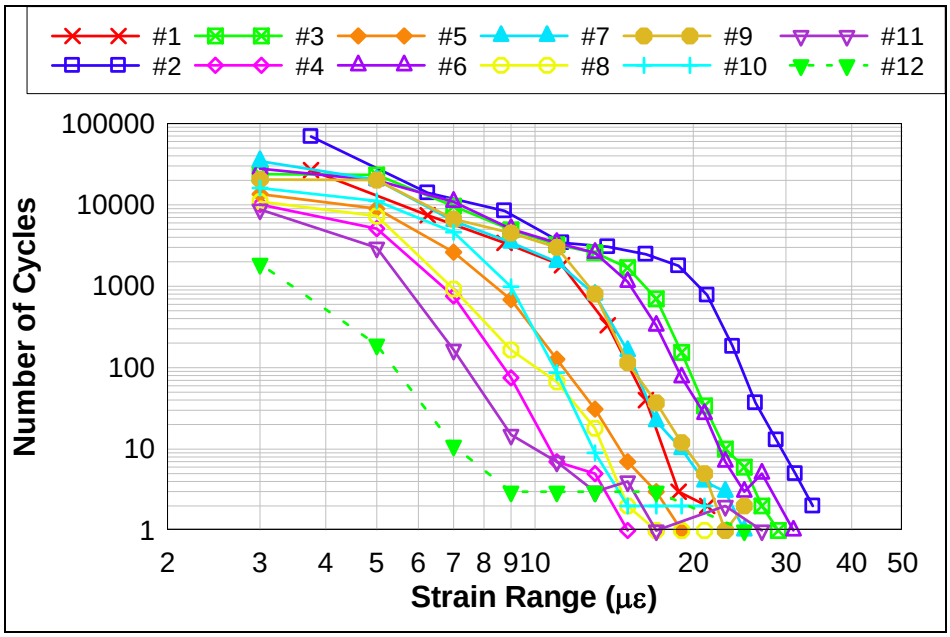
Ambient traffic-induced CFRP strains at mid-depth of the girders and bent cap were monitored over a period of 32.6 days from September 16 to October 19, 2004 and for a period of 6.1 days from May 15 to May 22, 2008. The strain ranges and numbers of cycles recorded at the instrumented locations are shown in Figure 3.19a and b for the 2004 and 2008 monitoring, respectively. The largest single strain range was measured at approximately 34 με in 2004 and 42 με in 2008, both at location #2 on the bent cap. Miner's Rule (*Miner 1945*), was used to express the variable amplitude strains as an equivalent constant amplitude strain range for each of the instrumented locations:

$$SR_{eqv} = \sqrt[k]{\sum \frac{n_i}{N_{tot}} SR_i^k} \qquad \textbf{(3-2)}$$

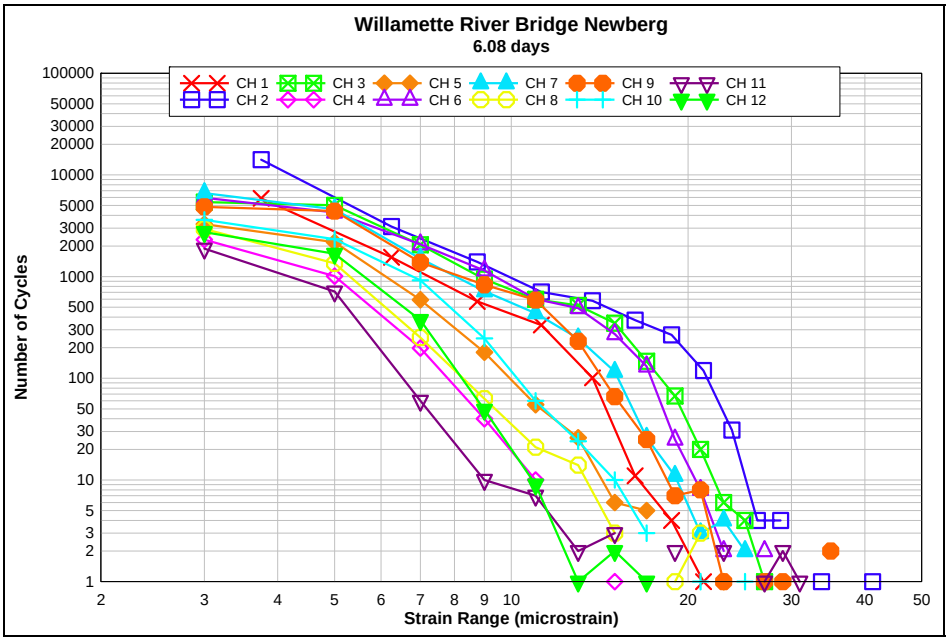
where SR_i is the i^{th} strain range; n_i is the number of cycles observed for the i^{th} strain range; N_{tot} is the total number of cycles at all strain ranges; and k is the fatigue exponent or slope of the S-N curve.

Steel is generally regarded as having a relatively low fatigue exponent of 3 (as used for Clarks Branch Overcrossing previously), compared with composite materials having higher fatigue exponents of 10 or above (*Mandell, et al. 1993*). For materials with higher fatigue exponents, fatigue damage is not particularly sensitive to the low strain-range cycles. However, the few cycles that occur at higher strain ranges contribute disproportionately to fatigue damage as compared with low fatigue exponent materials. Thus, there is a higher degree of uncertainty related to events that occur in the upper tails of the distribution when using short data collection windows.

Considering a high fatigue exponent of 10 and using the field data collected over the relatively long time frame relative to the in-service life of the CFRP installation, equivalent constant amplitude strain ranges were computed at all instrumented locations as shown in Figure 3.20. The single highest equivalent constant amplitude strain range was 15 με for location #2 in 2004 and was 18 με for location #11 in 2008. There were small increases in the equivalent strain ranges, but the general trends for all sensor locations were similar in 2008 and 2004. These observed changes would not significantly reduce the expected fatigue life of the materials or impact results of the laboratory calibrated fatigue tests conducted previously at Oregon State University (*Williams and Higgins 2008*).

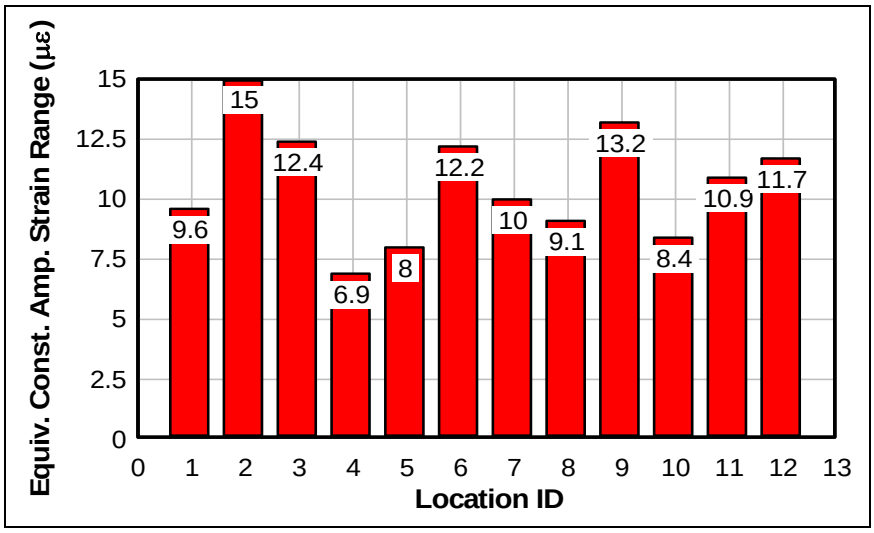


(a)

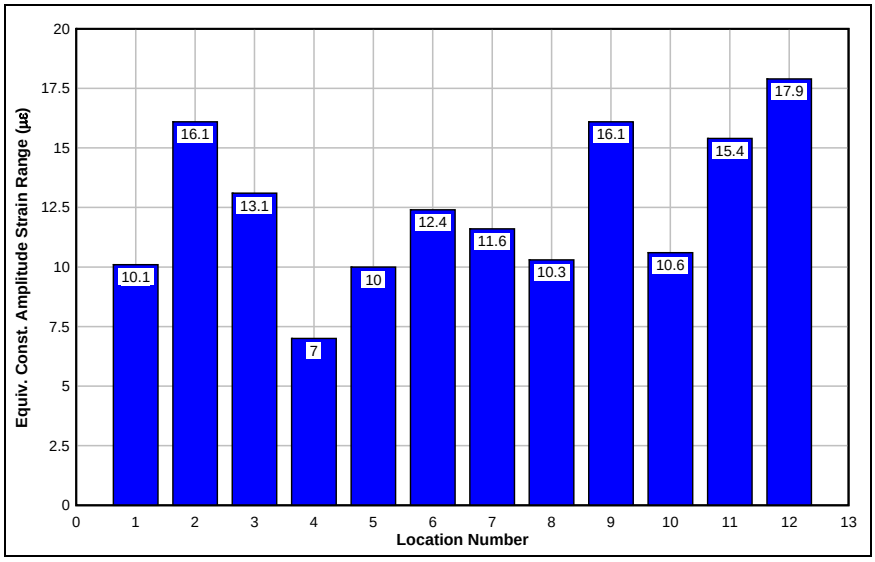


(b)

Figure 3.19: Strain range-number of cycles measured under ambient traffic conditions at all CFRP instrumented locations measured in (a) 2004 and (b) 2008



(a)



(b)

Figure 3.20: Equivalent constant amplitude strain ranges for all instrumented locations with fatigue exponent of 10 and minimum strain of 3 microstrain (a) 2004 and (b) 2008

4.0 EXPERIMENTAL MATERIALS AND METHODS

An experimental research program was implemented which included design of full-scale beam and bent cap specimens, instrumentation, construction, and application of each repair type. Repair for the beam specimens included epoxy injection, surface bonded carbon fiber reinforced polymer (CFRP) strips, external supplemental steel stirrups, internal supplemental steel stirrups, and carbon fiber tape in a near surface mount (NSM) application. The bent cap specimens were repaired with surface bonded CFRP strips and longitudinal post-tensioning. Once cast, both the beam and bent cap specimens were loaded to produce initial diagonal cracking, unloaded, repaired by the previously mentioned methods, and then tested to failure. The specimen descriptions, design, construction, and material property designations for base specimens are presented in this section. Specific details of each repair method – including repair installation procedures, testing protocol, and instrumentation for the test beams and bent caps – are given in Chapter 5.

4.1 SPECIMEN IDENTIFICATION

To readily identify the specimens used in the current study, the following convention is used: the first letter identifies the repair specimen as either a beam (B) (girder) or a deep beam (D) (bent cap). The second term indicates if the specimen is tested such that the deck is placed in flexural compression (T) or in flexural tension (IT). In this notation, T stands for T beam (flange is on top to represent positive moment regions) and IT stands for inverted-T beam (flange is on bottom to represent negative moment regions). Although the bent cap specimens do not include the deck portion, the orientation of these specimens is denoted as "T," since the deck would be in flexural compression if included. The third term differentiates beams that have flexural tension cutoff details located within the shear span (C) from specimens which have fully developed flexural bars within the shear span (NC). The final term designates the repair medium for each specimen, as given in Table 4.1.

Table 4.1: Specimen test matrix

Specimen #	Specimen Identification	Repair Method
1	B.IT.NC.C	No repair, control specimen
2	B.IT.NC.EC	Epoxy injection with no applied loads
3	B.IT.NC.ED	Epoxy injection with simulated dead load
4	B.IT.NC.EL	Epoxy injection with varying live load plus dead load
5	B.IT.NC.EA	Epoxy injection with axial tension
6	B.IT.NC.ES	Supplemental External stirrups
7	B.IT.C.ES	Supplemental External stirrups
8	B.T.NC.ES	Supplemental External stirrups
9	B.IT.NC.IS	Supplemental Internal stirrups
10	B.IT.C.IS	Supplemental Internal stirrups
11	B.T.NC.IS	Supplemental Internal stirrups
12	B.IT.NC.CF	CFRP
13	B.IT.NC.NS	Near Surface Mount
14	D.T.C.CF	CFRP
15	D.T.C.PT	Longitudinal Post-tensioning

4.2 SPECIMEN DESIGN

4.2.1 Beam specimen design

Beam specimens were designed to reflect the anchorage details and relative specimen sizes indicative of 1950s vintage highway bridges (*Higgins, et al. 2004a*). Beams used in the study were full-scale, designed to place the deck in either flexural compression – denoted as a T beam – or in flexural tension – denoted as an inverted T (IT) beam. These conditions replicate shear in the presence of positive moment, typical of a bridge girder near an abutment, or shear in the presence of negative moment, typical of a bridge girder near an interior support. The T beams were designed with stirrups spaced at 607 mm (24 in.), or h/2, while the IT beams were designed with either 305 mm (12 in.) or 457 mm (18 in.) stirrup spacing. In each case, the repaired beams were designed to fail in a shear dominated mode.

Specimens with the NC designation contained fully developed flexural steel within the shear span. Specimens B.IT.C.ES and B.IT.C.IS, representing external and internal supplemental steel stirrup repairs, were cast with two flexural cutoff bars cutoff within the shear span to investigate the performance of the repair method in the presence of an abrupt decrease in flexural steel, as is typically encountered for older bridge girders. The specimens had a 1219 mm (48 in.) overall height, with a flange width of 914 mm (36 in.), a web width of 356 mm (14 in.), and a flange thickness of 152 mm (6 in.). Beam specimens were cast to a total length of 7925 mm (312 in.); the shear span of the T beams was 2896 mm (114 in.), while the IT beams had a shear span of 2997 mm (118 in.), corresponding to a shear span-to-depth (a/d) ratio of 2.5 and 2.6 respectively. Typical T and IT beam elevations are shown in Figure 4.1, with typical sections shown in Figure 4.2.

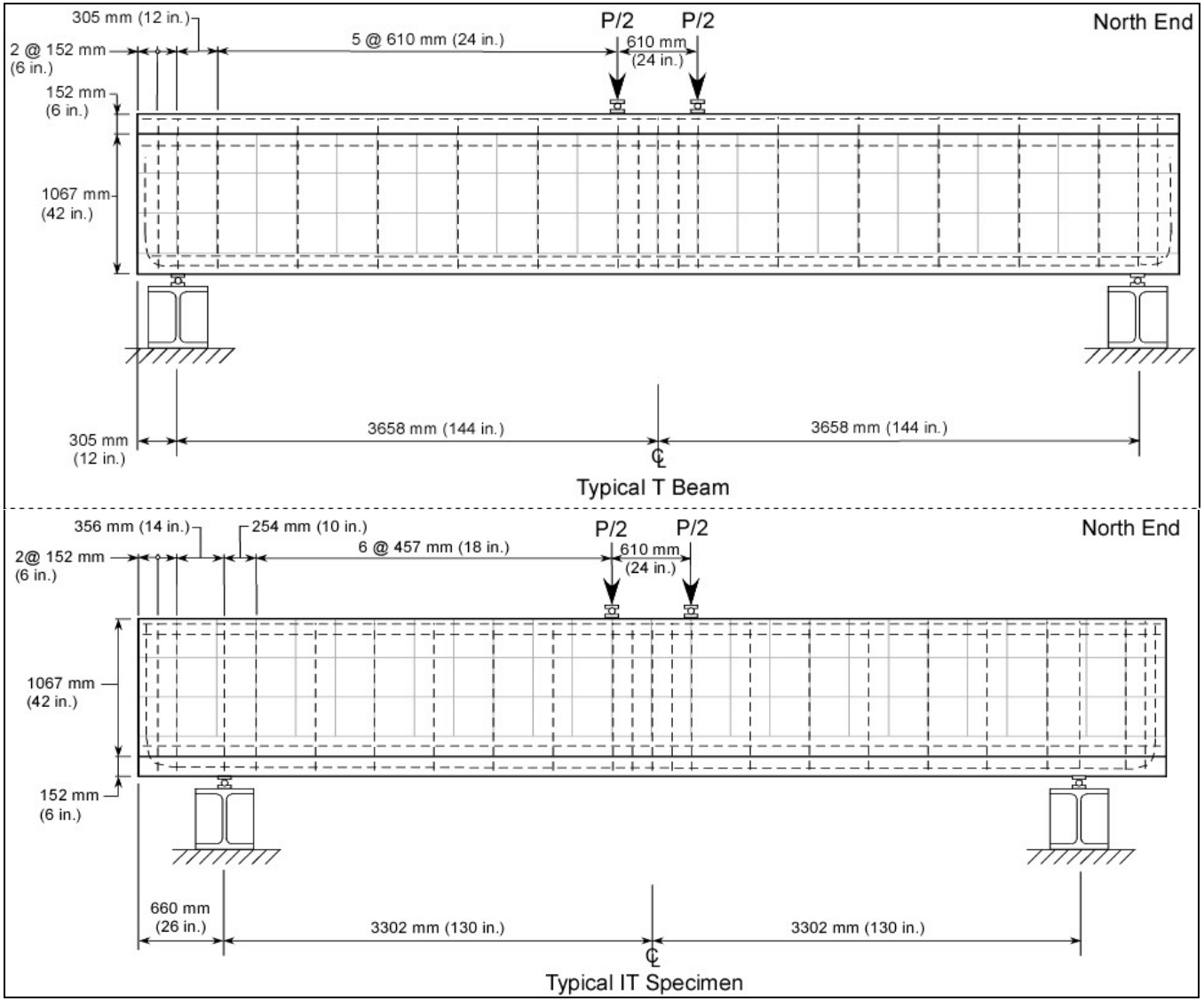
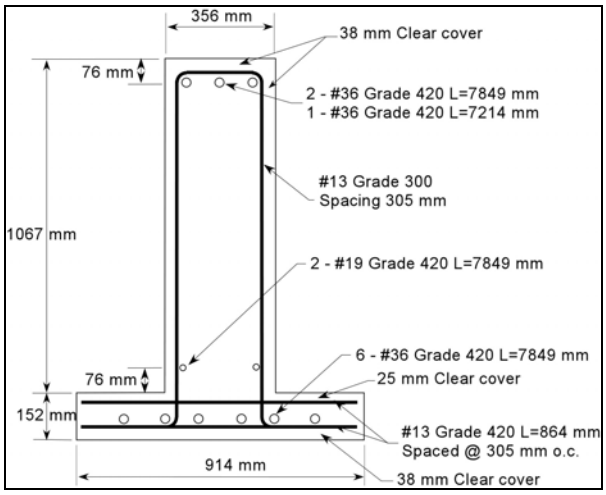
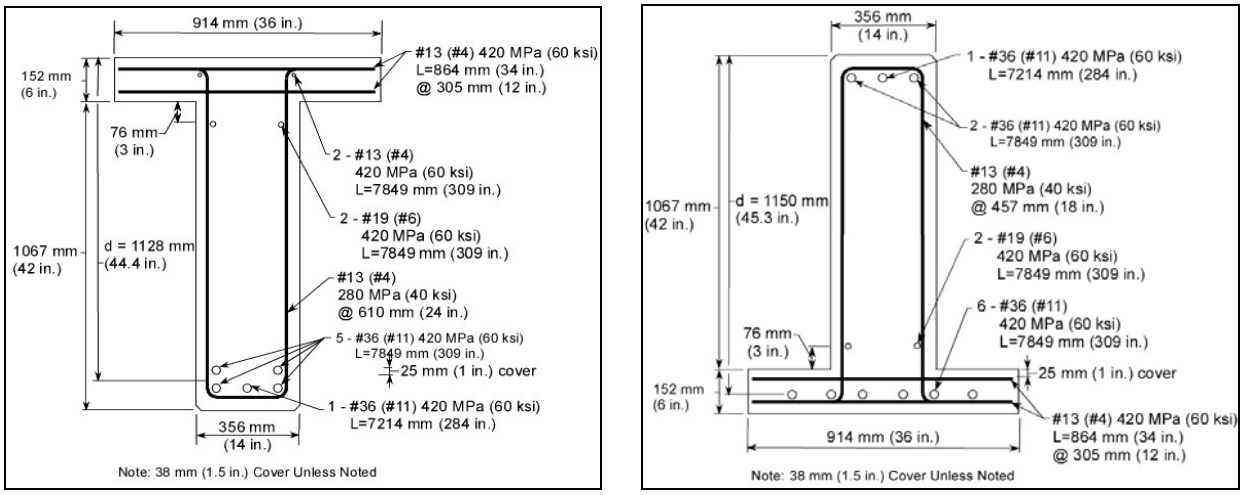


Figure 4.1: T and IT beam elevations



(a)



(b)

Figure 4.2: T and IT beam typical sections for (a) epoxy injection specimens, (b) other repair specimens

Support conditions for the beam specimens were similar for both T and IT specimens. Both specimen types were supported on reaction beams with 102 mm (4 in.) wide plates, 51 mm (2 in.) diameter high strength steel rollers supporting the beams on 25 mm (1 in.) thick by 102 mm (4 in.) wide steel plates extending across the appropriate flange/web width. The T beam specimens were supported laterally at the support locations by steel column sections attached to the reaction beams and rollers that permitted end rotations under positive moment but prevented out of plane movement. Load was applied by a single actuator at midspan, by way of a spreader beam, with loading points offset 305 mm (12 in.) from midspan of the beam. Capture plates were welded to the underside of the spreader beam, which was in turn supported on 51 mm (2 in.) diameter high-strength steel rollers and 102 mm (4 in.) wide steel plates in contact with the specimen. In order to assure a level bearing surface at the junction of the final steel plate and the concrete, Hydrostone – a quick-setting gypsum cement with a dry compressive strength of 69

MPa (10 ksi) – was applied between the concrete surfaces and steel plates. The loading frame and support conditions are shown in Figure 4.3.

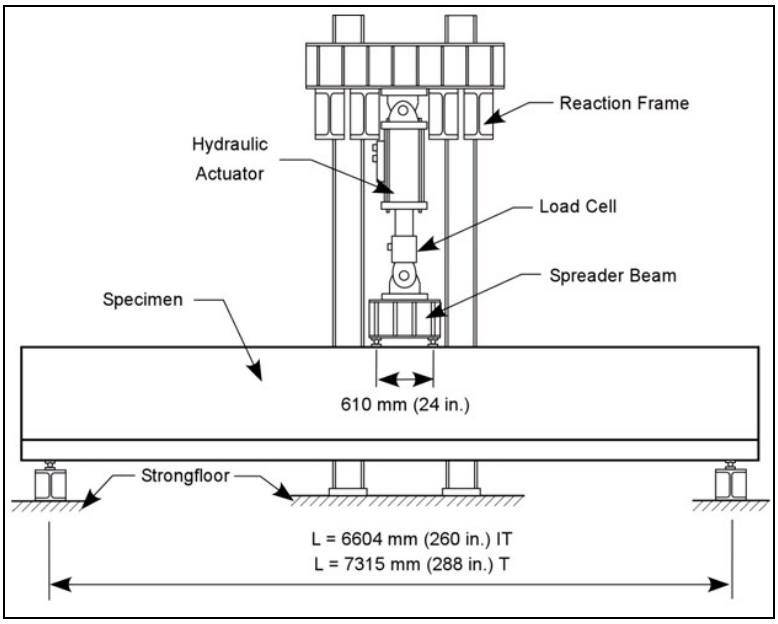


Figure 4.3: Typical beam loading setup (IT section shown)

4.2.2 Bent cap specimen design

Full-scale bent cap specimen design was based on previous work at Oregon State University (OSU); specimen dimensions, span lengths, flexural and transverse steel details, and utility hole opening locations were based on a review of existing bent caps within the Oregon Department of Transportation's (ODOT) bridge inventory. The bent cap specimens were designed as single span beams with four girders framing into the bent. The two exterior girder loads were assumed to be transmitted directly into the columns and were not included in the experimental setup, while the two interior girders provided load into the cap from the adjacent longitudinal spans. Thus, the cap beam was loaded indirectly from the two interior girders in the form of a shortened stub section, not directly loaded on the cap beam itself. The specimen dimensions were as follows, with reference to Figures 4.4 and 4.5: columns were 610 mm (24 in.) square, the cap beam was 1829 mm (72 in.) deep by 406 mm (16 in.) wide, with a span-to-overall height ratio of 1.33. The overall specimen length was 7925 mm (312 in.) with a 6706 mm (264 in.) length excluding the columns. The stub girders were 1219 mm (48 in.) deep with a 357 mm (14 in.) by 406 mm (16 in.) cross sectional area.

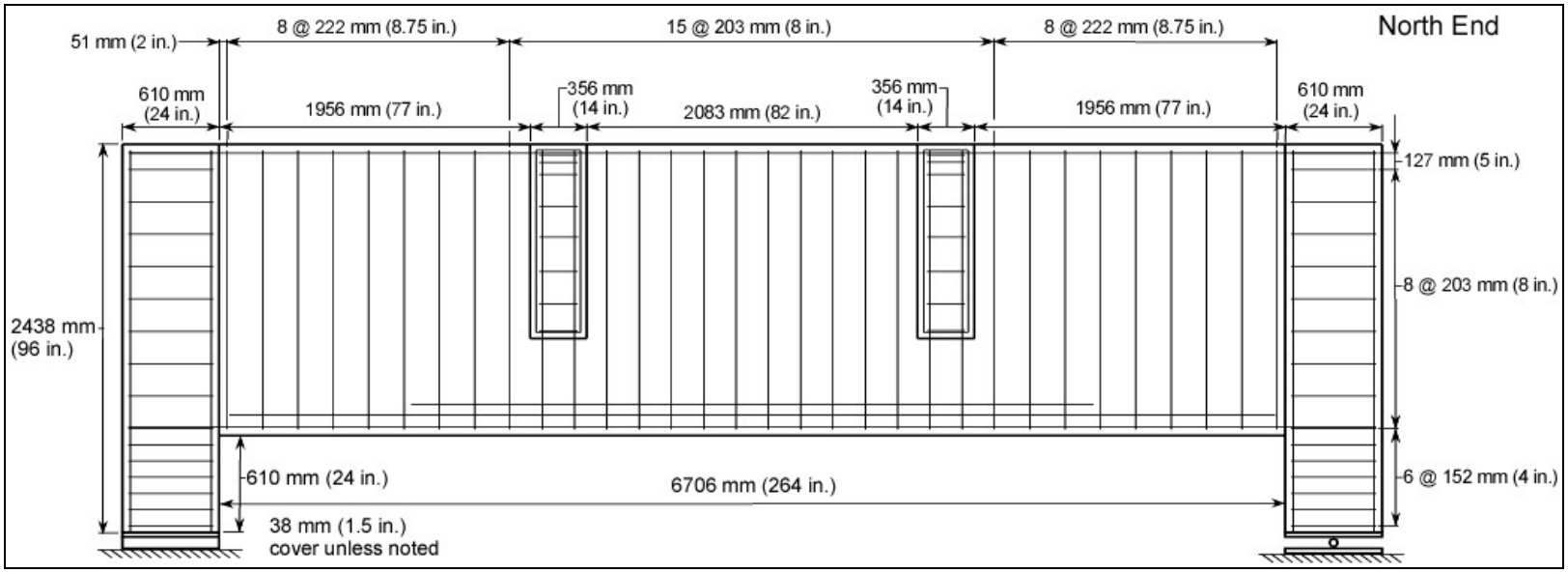


Figure 4.4: Bent cap elevation view of reinforcing details and geometry

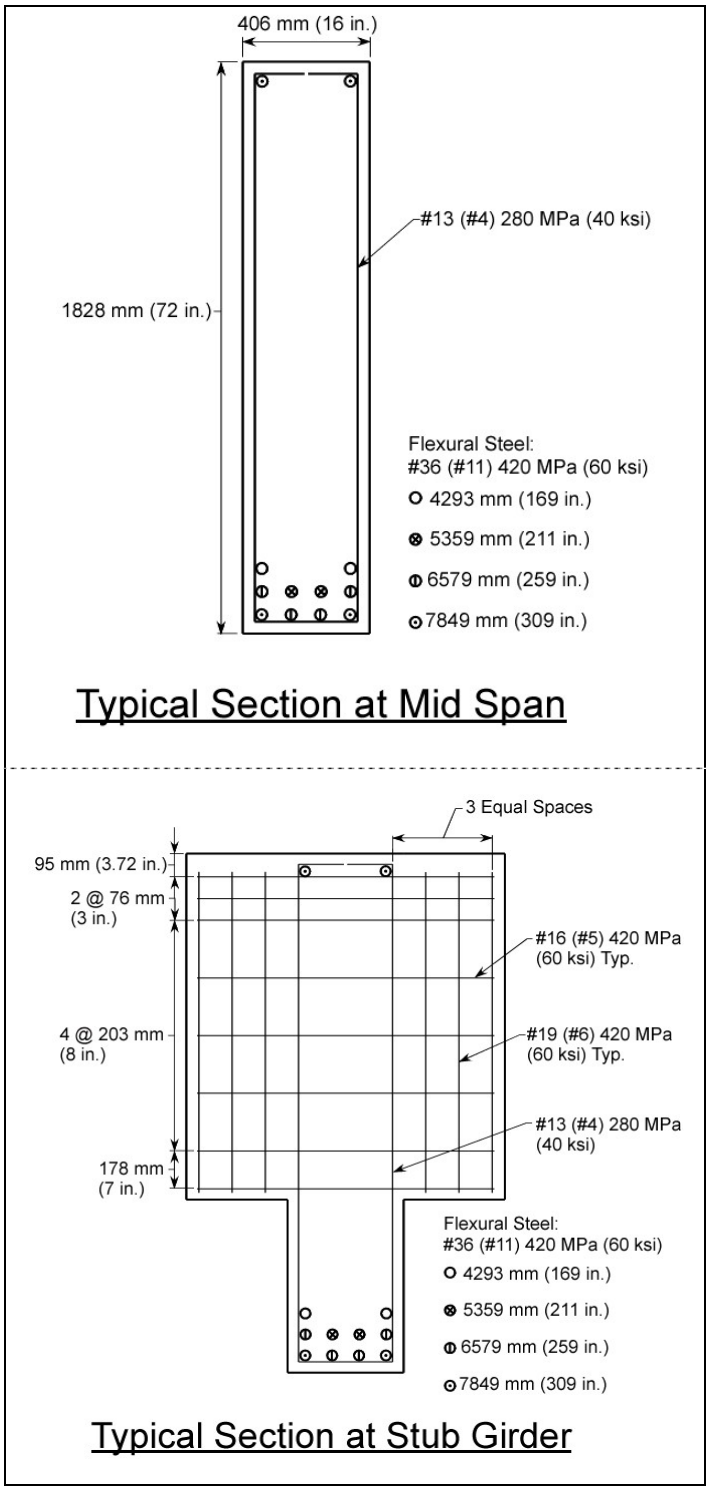


Figure 4.5: Bent cap section at midspan and at stub girder

Support conditions for the bent cap simulated those of an externally determinant rigid frame. The square concrete columns, which extended a distance of 610 mm (24 in.) down from the bottom of the cap beam, were cast onto single 25 mm (1 in.) thick steel plates with identical

cross sectional area. One column was supported by a 51 mm (2 in.) diameter high-strength steel roller placed on a slightly curved 38 mm (1.5 in.) steel plate. The steel plate for the second column was welded to a series of slightly larger perimeter steel plates such that the column bases could translate relative to one another and also rotate. The stub girders were supported laterally with vertical rollers to restrict out of plane motion. The columns were also supported laterally at the same elevation as the stub girders, as shown in Figure 4.6. Also, the loading frame was braced laterally out of plane with steel channel sections anchored to the strong floor.

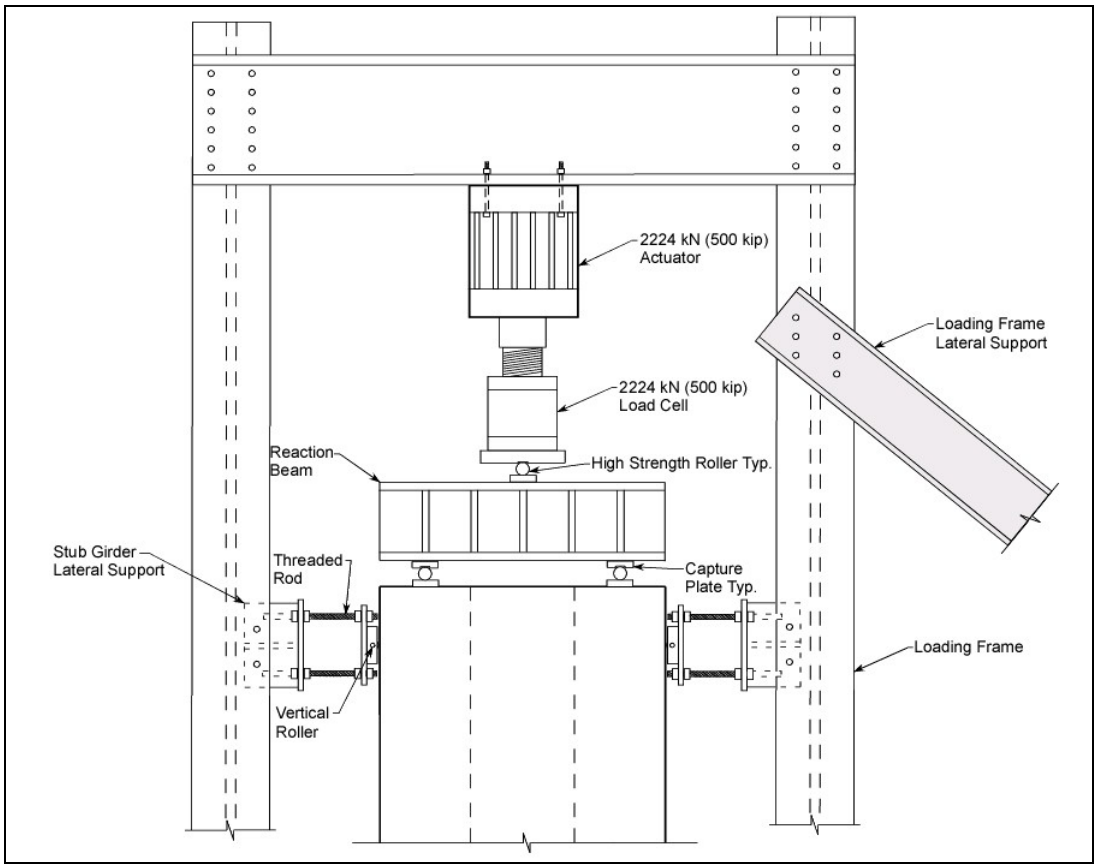


Figure 4.6: Bent cap indirect loading at stub girder location

Since the bent cap was loaded through each individual stub girder, two actuators and associated reaction beams were required. A capture plate mounted to the underside of the actuator was supported by a single 51 mm (2 in.) diameter high-strength steel roller and 102 mm (4 in.) wide by 25 mm (1 in.) thick plate bearing on the top midpoint of the reaction beams. This was to ensure free rotation of the reaction beam within the plane of the stub girders. A second set of capture plates, similar to those used for the beam specimens, was welded to the underside of the reaction beams at the location of the stub girders, supported on 51 mm (2 in.) diameter high-strength steel rollers, and corresponding 102 mm (4 in.) wide by 25 mm (1 in.) thick steel plates in bearing with the top of the stub girders. As with the beam specimens, the plates in contact with the top of the stub girders were leveled utilizing Hydro-stone gypsum cement.

The column reinforcing cage consisted of Grade 420 MPa (60 ksi) #36 (#11) corner bars with Grade 420 MPa (60 ksi) #10 (#4) ties at 102 mm (4 in.) within the isolated column section, with 203 mm (8 in.) spacing throughout the beam height, as shown in Figure 4.4. The longitudinal column bars were welded to the base plates.

The flexural steel configuration followed the work of previous bent cap specimens, consisting of three cutoff locations within the shear span. The flexural steel was placed in three layers, with a 4-4-2 bar configuration, from the bottom of the cap beam. Previous test results showed the specimen with two bottom bars extending into the column provided the lowest overall strength (*Senturk and Higgins in press*). Thus, the two outer bars within the bottom layer extending into the column were selected for the repair specimens. For this scenario, the remaining two bars within the bottom layer terminated at the face of the column. The second layer of reinforcing included two outer bars terminating at the face of the column, while the two inner bars were placed at 2679.5 mm (105.5 in.) from the centerline of the bent. The top layer of flexural steel included two outer bars at 2146.5 mm (84.5 in.) from the centerline of the bent.

In addition to flexural details, the repaired bent caps reflected similar stirrup details to the previous work at OSU. In the previous study, the stirrup size and grade varied from Grade 280 MPa (40 ksi) #13 (#4) to Grade 420 MPa (60 ksi) #16 (#5) with a consistent 222 mm (8.75 in.) average spacing. Thus, to replicate the weakest specimen from the previous work, Grade 280 MPa (40 ksi) #13 (#4) stirrups at 222 mm (8.75 in.) spacing were used in the current study.

The indirect loading of the bent cap required heavily reinforced stub girders to ensure failure occurred within the shear span. As such, the stub girders consisted of Grade 420 MPa (60 ksi) 16 (#5) horizontal and #19 (#6) vertical closed ties.

4.3 MATERIALS AND REPAIR SCHEMES

The materials selected for each repair method were based on products that were readily available, representative of similar products, and pre-approved by state transportation agencies. Application of each individual repair method followed the manufacturer's recommendations and/or the advice of suppliers and approved contractors. Material tests of the repair media as well as traditional steel and concrete materials were included for each specimen.

4.3.1 Concrete

Concrete was provided by a local ready-mix supplier for both beam and bent cap specimens. The mix design was based on 1950's AASHO "Class A" concrete (*AASHO 1953*) used in previous research at OSU with a specified minimum compressive strength of 21 MPa (3000 psi) – similar to the design strength of the original in-service bridges (*Higgins, et al. 2004a*). Actual concrete compressive strengths varied across the test matrix. Tensile and compressive strengths were based on ASTM C39/C39M-05 (2005) and ASTM C617-05 (2005) completed on 152 mm (6 in.) diameter, 305 mm (12 in.) deep cylinders. Compressive concrete strength calculations for the beam specimens were completed at 7, 14, and 28 days after casting. Bent cap concrete strength was documented at a closer interval in order to complete repaired testing at a strength close to the 21 MPa (3000 psi) compressive strength – which occurred at an average of 20-25

days after casting. Tensile and compressive concrete strengths were also determined on the day of test for both precrack and failure tests. Results of the concrete compressive and tensile strengths as previously described are shown in Table 4.2.

Table 4.2: Concrete properties

Specimen #	Specimen Identification	Precrack MPa (psi)		Failure MPa (psi)	
		f_c'	ft	f_c'	ft
1	B.IT.NC.C	N/A	N/A	28.5 (4132)	3.2 (460)
2	B.IT.NC.EC	N/A	N/A	36.2 (5249)	2.8 (406)
3	B.IT.NC.ED	N/A	N/A	28.3 (4104)	2.6 (377)
4	B.IT.NC.EL	N/A	N/A	29.5 (4278)	2.7 (392)
5	B.IT.NC.EA	N/A	N/A	35.5 (5148)	2.8 (406)
6	B.IT.NC.ES	25.9 (3762)	2.7 (393)	26.4 (3823)	2.3 (339)
7	B.IT.C.ES	20.4 (2965)	1.6 (226)	20.4 (2965)	1.6 (226)
8	B.T.NC.ES	32.7 (4737)	2.3 (329)	31.8 (4614)	2.7 (388)
9	B.IT.NC.IS	24.7 (3586)	2.3 (330)	26.8 (3884)	2.0 (284)
10	B.IT.C.IS	24.4 (3545)	2.1 (303)	24.9 (3605)	1.8 (260)
11	B.T.NC.IS	27.5 (3993)	2.3 (333)	26.4 (3828)	2.5 (364)
12	B.IT.NC.CF	26.3 (3822)	2.3 (340)	27.4 (3970)	2.3 (329)
13	B.IT.NC.NS	25.6 (3718)	2.3 (329)	23.0 (3338)	2.2 (324)
14	D.T.C.CF	8.6 (1249)	1.4 (199)	15.5 (2253)	1.7 (246)
15	D.T.C.PT	22.9 (3324)	2.4 (348)	22.9 (3324)	2.4 (348)

The aggregate composition for the mix was reported by the supplier as: 97% passing the 19 mm sieve (3/4 in.), 82% passing 16 mm (5/8 in.), 57% passing 12.5 mm (1/2 in.), 33% passing 9.5 mm (3/8 in.), 21% passing 8 mm (5/16 in.), 9.3% passing 6.3 mm (1/4 in.), 3.0% passing 4.75 mm (#4), 0.6% passing 2.36 mm (#8) and 0.3% passing the 0.075 mm (#200) sieve. The sand composition of the mix was also reported as: 99.7% passing the 6.3 mm sieve (1/4 in.), 96.8% passing 2.36 mm (#8), 59.4% passing 1.18 mm (#16), 44.9% passing 0.600 mm (#30), 17.9% passing 0.300 mm (#50), 3.7% passing 0.150 mm (#100) and 1.7% passing the 0.075 mm (#200) sieve. The coarse aggregate was from Willamette River bed deposits consisting of smooth rounded basaltic rock.

4.3.2 Mild steel

All mild reinforcing steel used in the experimental program met the spacing and deformation requirements of ASTM 615/615M-05a (*ASTM International 2005*), while selection of the steel was based on an intermediate – 280 MPa (40 ksi) – grade used in the original beams. The lower grade steel posed a problem, since the steel industry has since migrated to a 420 MPa (60 ksi) standard grade bar. A solution was devised by permitting only the stirrup steel to be designated Grade 280 (40 ksi), with the remainder of the mild steel designated Grade 420 (60 ksi). A local steel producer provided a single heat of the Grade 280 (40 ksi), #13 (#4) for all of the stirrups used in the beams and bent caps.

Flexural steel consisted of Grade 420 (60 ksi) #36 (#11). The actual tensile properties of the steel bars were based on testing outlined in ASTM A370-97a (1997) utilizing a 489 kN (110 kip) capacity hydraulically controlled universal testing machine under displacement control of 0.0169 mm/sec (0.000667 in./sec). The large diameter #36 (#11) bars exceeded the capacity of the testing frame; thus they were machined down to 13 mm (0.5 in.) diameter coupons with threaded ends and tested in accordance with ASTM E8-00 (2000) Strain in the bar was measured with a class B1 extensometer with a 50 mm (2 in.) gage length. Tensile properties for beam and bent cap reinforcing steel are shown in Table 4.3.

Table 4.3: Reinforcing steel properties

Specimen #	Specimen Identification	Reinforcing Steel			
		#13 (#4) Grade 280 (40 ksi)		#36 (#11) Grade 420 (60 ksi)	
		f_y MPa (ksi)	f_u MPa (ksi)	f_y MPa (ksi)	f_u MPa (ksi)
1	B.IT.NC.C	350 (50.8)	544 (78.9)	477 (69.2)	712 (103)
2	B.IT.NC.EC	357 (51.8)	570 (82.7)	492 (71.3)	741 (108)
3	B.IT.NC.ED			484 (70.2)	728 (106)
4	B.IT.NC.EL			473 (68.6)	694 (101)
5	B.IT.NC.EA			492 (71.3)	741 (107)
6	B.IT.NC.ES	343 (49.8)	542 (78.6)	468 (67.9)	711 (103)
7	B.IT.C.ES				
8	B.T.NC.ES				
9	B.IT.NC.IS				
10	B.IT.C.IS				
11	B.T.NC.IS				
12	B.IT.NC.CF				
13	B.IT.NC.NS				
14	D.T.C.CF	343 (49.8)	542 (78.6)	458 (66.4)	706 (102)
15	D.T.C.PT				

4.4 SPECIMEN CONSTRUCTION AND INSTRUMENTATION

4.4.1 Beam specimen construction and instrumentation

All beam specimen construction and instrumentation was performed in Oregon State University's Structural Engineering Laboratory. Prior to casting, general purpose quarter bridge foil strain gages were placed at mid-height of the stirrups within the shear span and along the tensile flexural steel bars at midspan, as shown in Figures 4.7 and 4.8. In addition, strain gages were placed at the cut off locations for specimen B.IT.C.ES and B.IT.C.IS to indicate the relative increase in strain in the remaining flexural bars at the cutoff locations.



Figure 4.7: Typical strain gage locations along flexural steel



Figure 4.8: Typical strain gage locations along stirrups

Once instrumentation of individual reinforcing bars was complete, the reinforcing cage was assembled adjacent to the formwork, as denoted in Figure 4.9. Three free-standing support sections composed of tube steel were placed at third points along the reinforcing cage in order to support the reinforcing steel as it was assembled. Standard reinforcing ties were used to secure the reinforcing bars to one another. The formwork for the beam specimens consisted of two adjacent T beams such that two specimens were poured at one time.

After assembly of the first reinforcing cage, it was temporarily moved into the formwork and a second reinforcing cage was assembled with the previously mentioned support sections. The first reinforcing cage was then removed from the formwork so that a form release agent could be applied to the surfaces in order to ease removal of the final cast specimens. After application of the release agent, the reinforcing cages were placed within the formwork and concrete was placed in three equal height lifts. Due to the size of the specimens, one concrete truck per beam was used for placement. A concrete vibrator was used to ensure proper consolidation of the concrete for each individual lift.

Concrete for test cylinders was obtained midway through the placement process for each beam in order to ensure a representative sample of concrete. After placement, the top surface of each beam was troweled to a smooth surface. Approximately one hour after pouring, a saturated burlap mesh and a thin plastic sheet was placed over the length of the beams and the specimens cured for a minimum of 28 days prior to removal from the forms.



Figure 4.9: Assembly of completed reinforcing cage adjacent to formwork (IT specimen shown)

Once cured, the beam specimens were removed from the formwork and prepared for testing. External sensors were placed along the beam as indicated schematically in Figure 4.10. Mid-span displacements along both sides of the beam were recorded with 127 mm (5 in.) range string potentiometers, while support settlements at four corners were recorded with 13 mm (0.5 in.)

range displacement sensors. Support settlements were then averaged and subtracted from the mid-span displacement to reveal the true specimen deformation. Diagonal displacements were measured with 51 mm (2 in.) range string potentiometers. Load was measured through a 2450 kN (550 kip) load cell integrated with the hydraulically controlled actuator. Data was recorded on a 16 bit data acquisition system with multiple channel assignments to include strain, displacement, and load. Crack widths for the specimens were recorded by visual inspection with a hand held crack comparator.

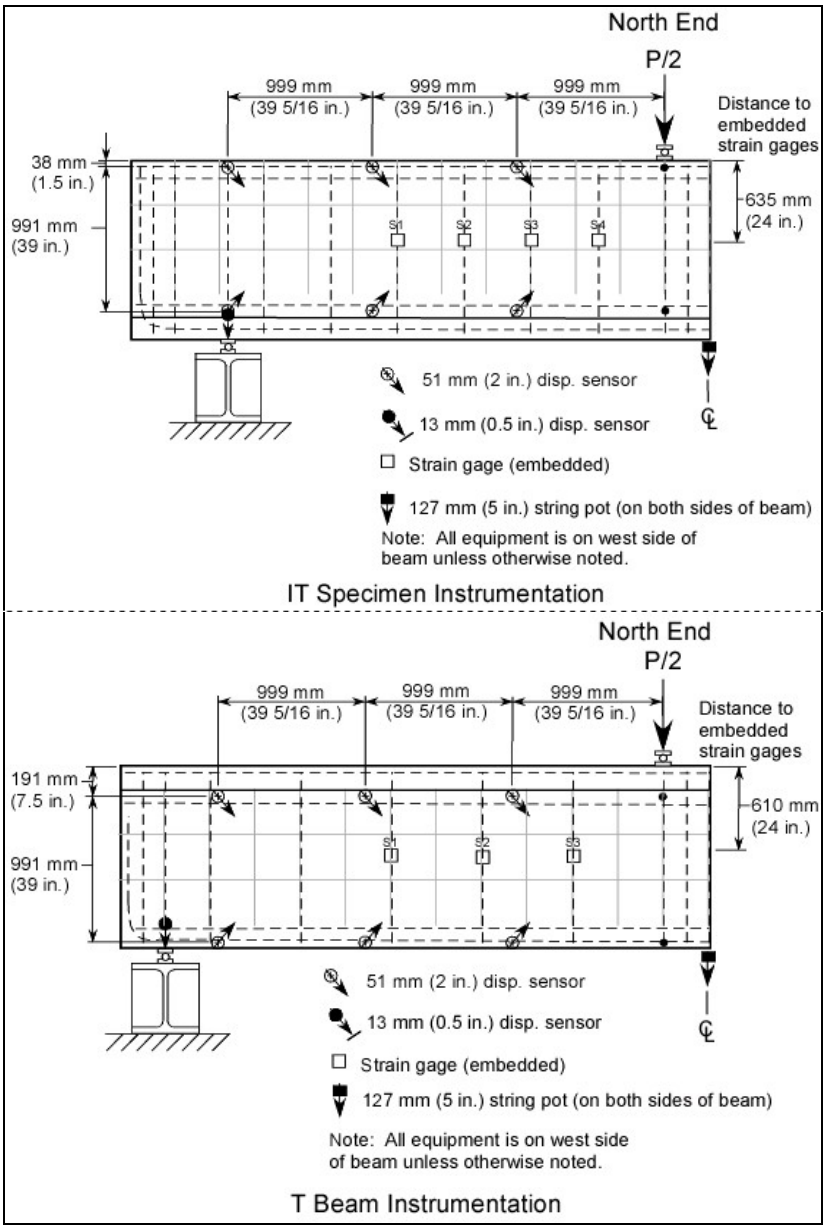


Figure 4.10: Schematic view of sensors for IT and T beams

4.4.2 Bent cap specimen construction and instrumentation

Construction of the bent cap specimen was similar to that of the beam specimen in terms of steel instrumentation and assembly. General use quarter bridge foil strain gages were attached to the stirrup and flexural steel. Based on prior tests, the location of the failure crack within the shear span was known a priori to testing; thus the stirrups were instrumented along the projected failure crack, not at mid-height as they were for the beam specimens.

Within each layer of flexural steel, one bar of each cutoff length was instrumented. For example, the first layer included two fully developed bars into the column and two bars terminating at the face of the column. In this example, one of the fully developed bars and one of the cut off bars were instrumented at midspan.

The distribution of strain for the anchorage bars into the column was of interest; thus three strain gages were attached to each anchorage bar, one at the inside face of the column, a second 152 mm (6 in.) further into the column, and a third located at the centroid of the column at a distance of 305 mm (12 in.) from the inside face.

Once the individual reinforcing bars were instrumented, assembly of the reinforcing cage and subsequent pouring began. Unlike the beam specimens, the size and relative weight of the bent cap precluded casting near the testing bay. As a result, the reinforcing cage and associated formwork were assembled within the testing bay as outlined below.

Assembly of the bent cap reinforcing steel began with the column sections, followed by compression steel, stirrups, tension steel, and stub girders. The column sections, as noted previously, were cast on 25 mm (1 in.) thick steel plates. The reinforcing steel consisting of four #36 (#11), 420 MPa (60 ksi) bars were welded to the corners of the steel plates. Closed #13 (#4), 420 MPa (60 ksi) reinforcing bars were secured with standard wire ties at 102 mm (4 in) for the isolated column section, and 203 mm (8 in.) spacing within the height of the beam.

In order to support the wet concrete and reinforcing cage during curing, 9 mm (0.375 in.) thick steel plates, supported on a combination of adjustable height inverted steel channels and tube sections, were placed at fifth points between the columns. Next, the compression steel was supported from above the testing bay by two braided steel wires, turnbuckles, and several small clevises.

The stirrups were attached to the compression steel at 222 mm (8.75 in.) spacing within the shear span with wire ties, as shown in Figure 4.11. Once in place, the tension steel was placed within the stirrups and secured with wire ties. The stub girders were then attached to the stirrup sections, as shown in Figure 4.12.



Figure 4.11: Typical bent cap stirrup assembly



Figure 4.12: Typical bent cap stub girder assembly

Formwork assembly and concrete placement followed after completion of the reinforcing cage. A custom built formwork system consisting of a combination of NDM fiberboard and common construction lumber was assembled around the reinforcing cage with assorted nuts, bolts and washers. The height of the bent prohibited pouring directly from a typical concrete truck; thus a pump truck was used to place concrete in three lifts. A concrete vibrator was used to ensure

concrete consolidation in the forms. After pouring was complete, the top surface of the concrete was troweled smooth. Approximately one hour after pouring, a saturated burlap material and thin plastic sheet were placed over the top surface of the concrete.

After curing, the formwork for the bent cap was removed and the specimen was prepared for testing. External sensors were placed along the bent as indicated schematically in Figure 4.13. Mid-span and stub girder displacements along both sides of the beam were recorded with 254 mm (10 in.) and 127 mm (5 in.) range string potentiometers respectively, while support settlements at four corners were recorded with 38 mm (1.5 in.) range displacement sensors. Support settlements were then averaged and subtracted from the mid-span and stub girder displacements to reveal the specimen deformation.

The two anchorage bars within the column were monitored for slip at the free end with a single 102 mm (4 in.) range string potentiometer mounted to the outside face of the columns. Elongation between the column sections was measured at mid-height of the isolated columns. The absolute movement of the column supported on the roller end was measured by a 102 mm (4 in.) string potentiometer. Diagonal displacements within the two shear spans were measured with 51 mm (2 in.) range string potentiometers. Load was measured through a 2450 kN (550 kip) load cell integrated with the two hydraulically controlled actuators. Data was recorded on a 16 bit data acquisition system with multiple channel assignments including strain, displacement, and load. Crack widths for the specimens were visually inspected and measured with a hand held crack comparator.

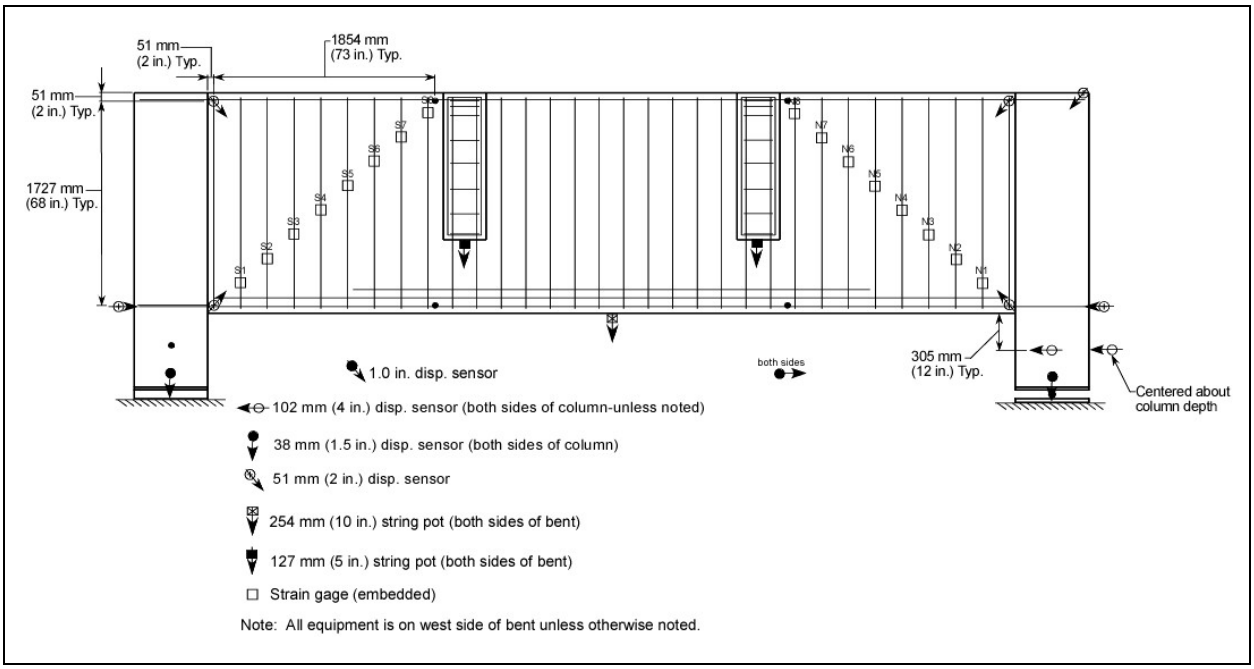


Figure 4.13: Schematic view of sensors for bent cap

4.5 TESTING PROTOCOL

4.5.1 Beam specimen testing

The testing protocol for beam specimens included incremental loading to produce initial diagonal cracking of the specimens. The maximum applied load during precracking was determined as a percentage of the ultimate capacity of the base specimen. The base beam specimen capacity was determined using the computer program Response 2000 (*Bentz 2000*). The program estimates capacity of traditionally reinforced and post-tensioned concrete sections based on a sectional analysis (all steel specified in the analysis is assumed developed at the point of interest) utilizing Modified Compression Field Theory.

Force was applied at 222 kN (50 kip) increments through a hydraulically controlled 2224 kN (500 kip) capacity actuator under force control at a quasi-static rate of 9 kN/sec. (2 kip/sec.). The initial IT beam was loaded up to 1112 kN (250 kip), representing approximately 70% of the base specimen capacity. Due to loss of internal foil strain gages at this level, the remainder of the IT and T beams were loaded up to 890 kN (200 kip). This represents 55% of the ultimate strength of the T and IT specimens respectively. At each load increment, the maximum force was reduced by 10% in order to take crack width measurements, map crack lengths, and reduce the effect of creep. After the maximum load was reached, the specimen was unloaded, the sensors were zeroed and a second test was conducted to obtain the new post-cracked baseline response of the beam.

4.5.2 Bent cap specimen testing

The testing protocol for the bent cap specimens mirrored that of the beam specimens, with a slight modification for the use of two actuators. Estimation of the base specimen capacity followed from the results of previous work at OSU for specimens with comparable concrete strength. Force was again applied at 222 kN (50 kip) increments through a hydraulically controlled 2224 kN (500 kip) capacity actuator under force control at a quasi-static rate of 9 kN/sec. (2 kip/sec.).

Initially one actuator was loaded to the first load point of 1112 kN (50 kips), then reduced by 10% in order to reduce the effects of creep while taking crack width and length measurements. Then the specimen was unloaded, and the second actuator was loaded to the first load point, measurements were taken, and load released. Next, the two actuators were loaded together, the first followed by the second, measurements were taken, and load released in the reverse order it was applied. This sequence was repeated until a combined load of 8896 kN (400 kip) was applied to the base specimen. As with the beam specimens, once the bent cap was unloaded, the sensors were zeroed and a second test was conducted to obtain the new post-cracked baseline response of the bent cap.

5.0 REPAIR METHODS

This chapter describes experimental and analytical findings for each of the repair methods considered. Each method, specific material properties, installation, test variables, and unique responses are described for each type separately in this chapter. Comprehensive details of the measurement data collected for the experiments are contained in Appendix A.

5.1 EPOXY INJECTION FOR GIRDERS

5.1.1 Material and application details

The epoxy selected was SCB Concresive 1360 produced by Chemrex. This particular resin is a two-part, ultra low-viscosity liquid epoxy. The specified material tensile strength for SCB Concresive 1360 is 55.2 MPa (8000 psi). The surface sealant used was Concresive SPL Paste, which is a two-part, 100% solids epoxy. These two materials are commonly used, are pre-approved for use by several State DOTs, and they are representative of similar epoxy materials. All injection materials were provided by local suppliers. Additional installation guidance was provided by qualified contractors to establish a repair protocol that satisfied the manufacturer's installation recommendations. The procedure that was established is summarized below.

The concrete surfaces around the diagonal cracks were cleaned with a wire brush to remove loose particles and dirt. Vacuuming was performed to assure a clean surface area. The crack perimeter was sealed, and injection ports were surface mounted every 356 mm (14 in.) or roughly equal to the width of the girder web. The surface epoxy cured for 24 hours before the injection process was initiated. Diagonal cracks were injected starting from the lowest port working up, which allowed for release of entrapped air. "Window" ports were placed on the backside of the beam to serve as a visual aid for assurance of epoxy penetration through the beam web. A specialized injection machine was used to mix the two-part liquid epoxy in the manufacturer's recommended proportions and deliver the mixture into the beam under pressure. This machine is commonly used by contractors performing this work.

Each port was injected to a maximum pressure of 690 kPa (100 psi). As liquid epoxy began to seep from the next higher tube, the lower port was capped and the injection nipple moved to the next higher position. Near the top of each diagonal crack, the injection pressure climbed more quickly to 690 kPa (100 psi), and it would take longer to dissipate, signaling that there was little available space to pump additional epoxy resin. When the maximum pressure could be maintained, the final port was capped. After injection, all specimens were allowed to cure for at least seven days. A heated plastic enclosure was placed around the specimen to ensure that temperatures were maintained above 4.5º Celsius (40º Fahrenheit). Thermocouples outfitted with data loggers were placed into a small void cast into the end of the specimens and on the exterior to record temperatures and ensure the specified curing conditions.

5.1.2 Experimental results

Five specimens were tested to investigate the effect of epoxy injection on member behavior. A simply-supported four-point loading configuration was used with an overall span length of 6604 mm (260 in.) from centerline of supports. Force was applied with a hydraulic actuator at a constant rate of 8.9 kN/sec (2.0 kips/sec) and was measured by a 2224 kN (500 kip) capacity load-cell. A spreader beam distributed the applied actuator force to 102 mm (4 in.) wide plates spaced 610 mm (24 in.) symmetrically about midspan. Loading was applied in steps with incrementally increasing load followed by unloading. Load magnitudes increased each cycle by an amount of 222 kN (50 kips). At each load peak, the load was reduced by 10% to minimize creep effects, and visible cracks were measured and marked.

Three tests were performed on each specimen with the exception of the control specimen – B.IT.NC.C – which was loaded to failure in a single test. An initial loading sequence, or precrack test, was performed to produce diagonal cracks similar to those observed in field inspections of RCDG bridges and of sufficient size for epoxy injection. A target diagonal crack range of 0.65 mm - 1.25 mm (0.025 in.- 0.05 in.) was selected based upon the prior work of Higgins et al. (*2004b*). When diagonal cracks reached suitable size, the precrack loading cycle was terminated, and a baseline test was performed to establish a reference for the specimens in the cracked condition for comparison to the post-injection response. In the final test, all specimens were loaded incrementally to failure.

To simulate the effects of different stress conditions, each specimen was subjected to a distinct loading scenario during the injection and curing phases. Specimen B.IT.NC.EC was injected and cured with no applied loads other than specimen self-weight.

Simulated superstructure dead load was applied to specimen B.IT.NC.ED before epoxy injection. A total load of 356 kN (80 kip) was applied to induce a service level dead load shear of 178 kN (40 kip). This shear magnitude is representative of an interior girder for a typical 1950's vintage 3-span continuous CRC deck-girder bridge having 15.2 m (50 ft) spans and a uniform dead load of 23.3 kN/m/girder (1.6 kip/ft/girder).

Varying live load stress was applied to specimen B.IT.NC.EL in addition to the simulated superstructure dead load. The live loading was representative of average shear magnitudes produced by ambient traffic and a fully-loaded Type 3-3 unit truck having 5 axles and a gross vehicular weight of 356 kN (80 kip) moving across a similar bridge as that for specimen B.IT.NC.ED using realistic shear distribution factors developed by Potisuk and Higgins (*2007*) from field studies. Force was applied at 0.3 Hz with an amplitude of 160 kN (36 kips) and a mean of 463 kN (104 kips). This loading represents the maximum girder shear caused by the dead load of the bridge and the truck live load with impact, as well as a minimum force resulting from hogging due to live load moving onto an adjacent span.

The fifth specimen, B.IT.NC.EA, had simulated locked in drying and thermal shrinkage strains induced by applying a uniform tension load to the specimen. The axial load was applied to a level of approximately 890 kN (200 kip) before the initial precrack transverse loading cycles began. The axial load was held at a constant magnitude of 645 kN (145 kip) during the injection

and curing phases, and then returned to 890 kN (200 kip) for the post-injection failure loading. Midspan shear-displacement responses are shown in Figure 5.1 and display the overall specimen behavior of the initial, baseline, and post-injection tests.

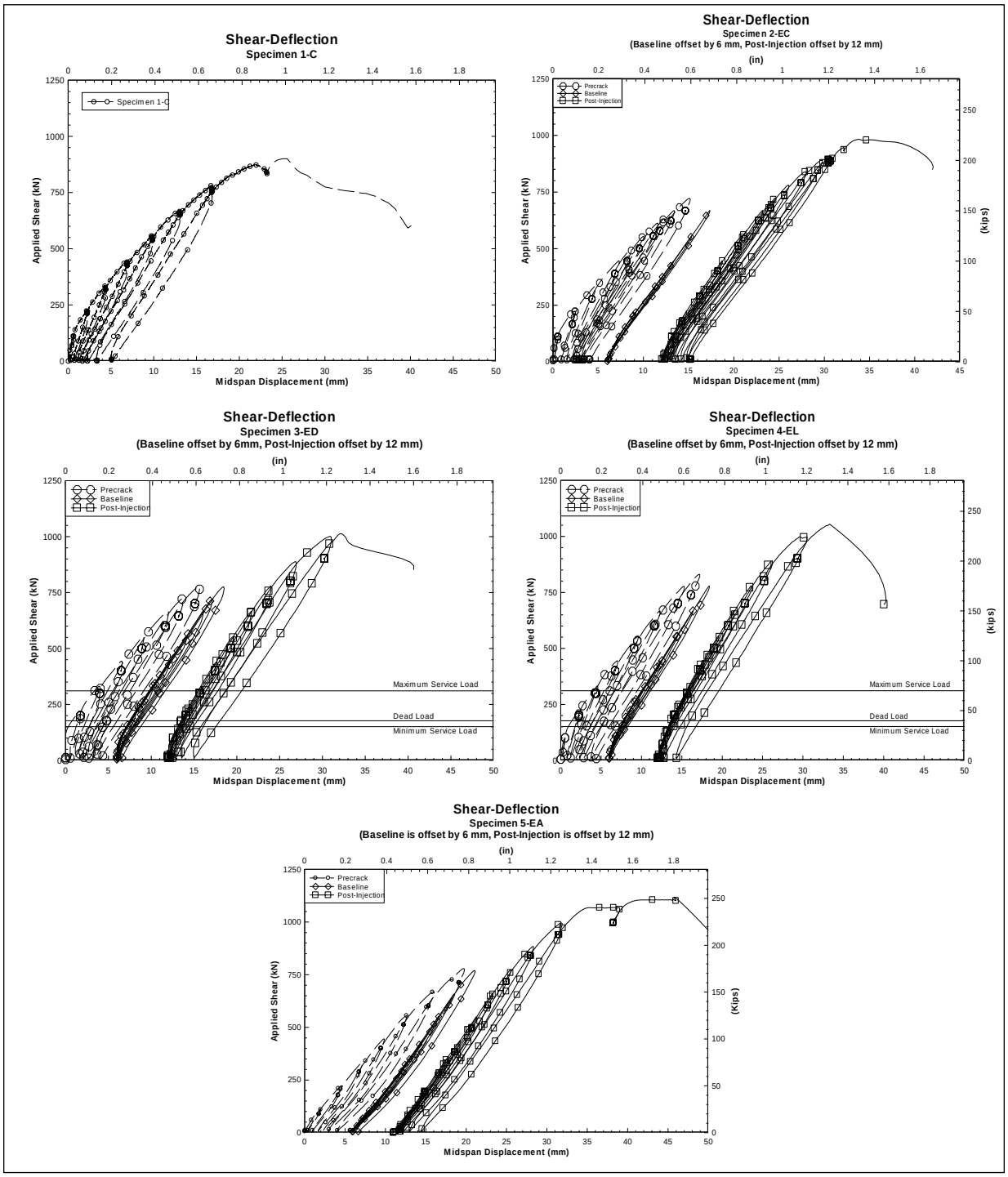


Figure 5.1: Shear-midspan displacement response

The post-injection response of each injected specimen showed decreased residual deformations and greater stiffness during the initial two or three load steps. As the applied shear magnitudes increased, the specimens began to soften due to new cracking, and residual deformations increased. This behavior was especially pronounced in specimen B.IT.NC.EL. Specimens B.IT.NC.ED and B.IT.NC.EL were similar, especially in the service load range indicated in the figures, and both had greater stiffness than specimen B.IT.NC.EC. The axially loaded specimen exhibited a unique shear-midspan deformation response unlike the other four. The curve has a slender "S" shape as the specimen stiffens and then softens during each load cycle.

Figure 5.2 displays the axial load as a function of the applied shear for specimen B.IT.NC.EA. As the applied shear magnitude increased, the specimen length increased at the level of the axial apparatus, thereby reducing the hydraulic pressure in the axial load actuators, thus reducing the applied axial tension. As the applied shear decreased, the specimen shortened along the axial loading apparatus, and the axial tension increased again. Like specimen B.IT.NC.EL, specimen B.IT.NC.EA had decreased residual deformations for many of the load cycles and did not begin to soften until near failure. Conversely, the control and precrack tests were softer, showing greater permanent deformation at each higher load step.

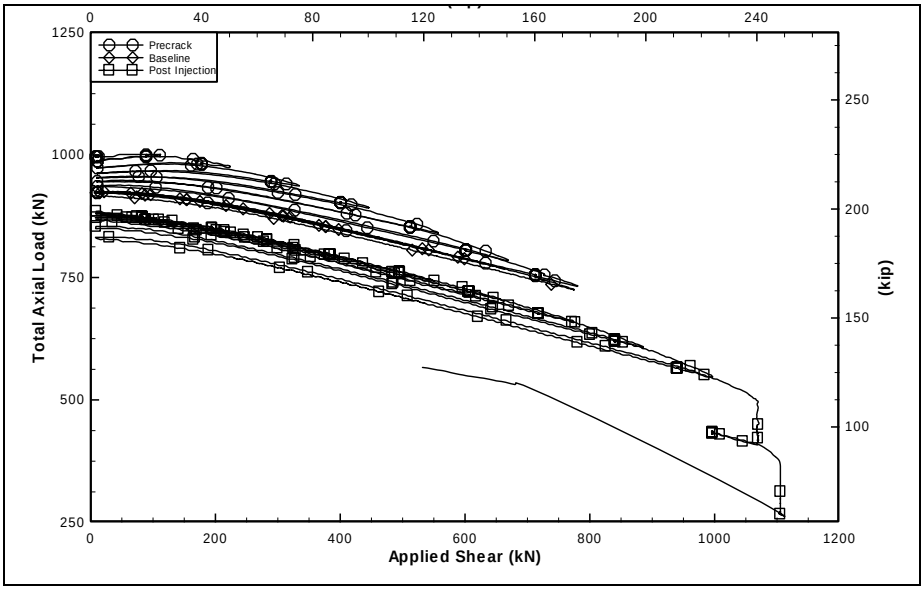


Figure 5.2: Shear-axial load variability of specimen 5-EA

Similar behavior to the shear-midspan displacement responses was evident in the post-injection diagonal displacement data shown in Figure 5.3. All of the post-injection tests for the epoxy specimens had smaller permanent deformations during the initial load steps than did the control specimen in addition to having a greater stiffness. Specimens B.IT.NC.ED and B.IT.NC.EL were stiffer than specimen B.IT.NC.EC, with specimen B.IT.NC.EL performing slightly better than B.IT.NC.ED. The largest impacts were again seen in specimen B.IT.NC.EA, which showed significantly improved stiffness and a reduced permanent deformation response. For all the specimens except B.IT.NC.EL and B.IT.NC.EA, the north and south diagonal deformations were

essentially identical, showing similar stiffness and exhibiting significant diagonal deformation at approximately the same shear magnitude. For the remaining two specimens, however, one side had a substantially larger load at the point where the diagonal deformation first changed slope. This may be a result of the uneven distribution of shear cracks and epoxy resin. For specimen B.IT.NC.EL, the side with the lower crack re-initiation load contained fewer diagonal cracks that were epoxy injected. Specimen B.IT.NC.EA had more active diagonal cracks on the side with the lower cracking shear.

The largest relative influences of epoxy injection were seen in the individual rebar strain, but these effects were highly influenced by the proximity of injected diagonal cracks to instrument locations. The orientation and location of the diagonal cracks produced during precrack and post-injection loading sequences are shown in Figure 5.4. The location of diagonal cracks that were epoxy-injected is also shown. Diagonal cracks that were injected did not reopen during post-injection tests. Instead, new cracks formed adjacent to the injected cracks and propagated at similar angles. Non-repaired cracks tended to propagate along the original paths.

Stirrups located near diagonal cracks that were injected had lower strains after injection at otherwise similar shear load. Stirrups located between diagonal cracks or far from cracks that were not injected displayed relatively little change. This behavior was observed for all injected specimens. Diagonal cracks were considered to be "near" the stirrup strain gage if the vertical distance that the crack crossed the stirrup was within the AASHTO calculated development length of the #13 (#4) stirrup. Figure 5.5 shows an example of strains measured for a stirrup located near a diagonal crack and a stirrup located at a distance greater than the development length from a diagonal crack.

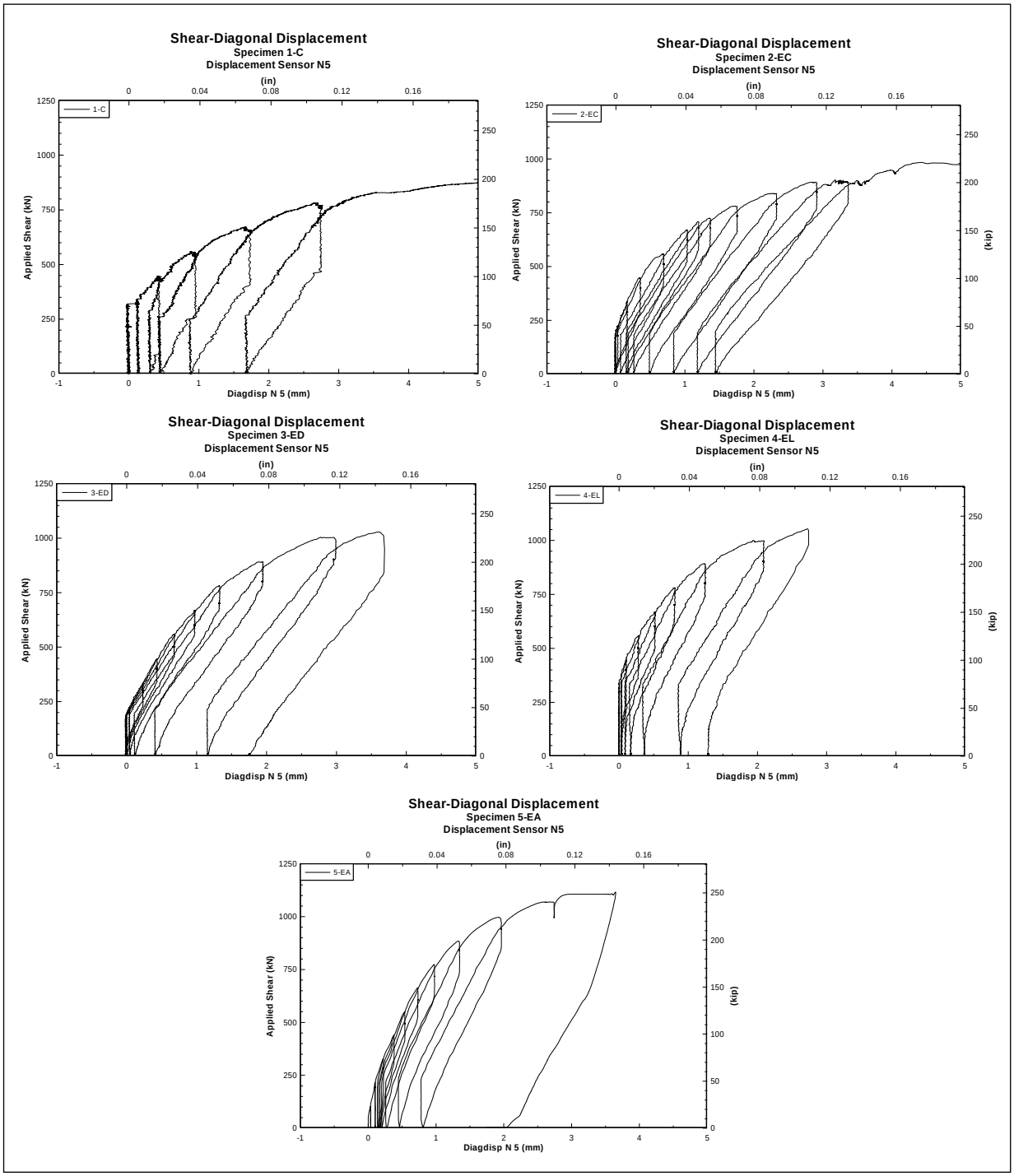


Figure 5.3: Shear-diagonal displacement response. Values were recorded near centerline of specimens on north side.

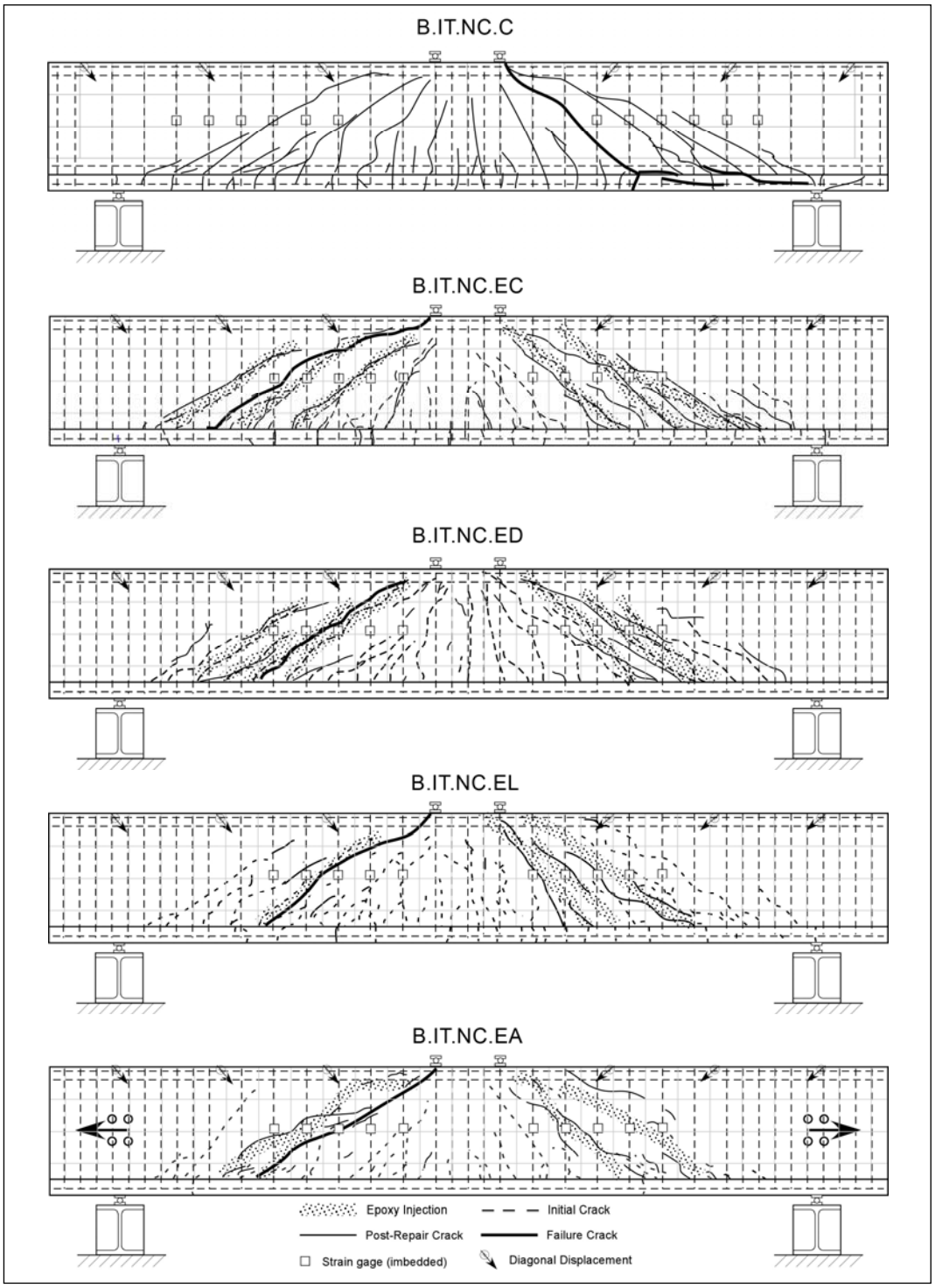
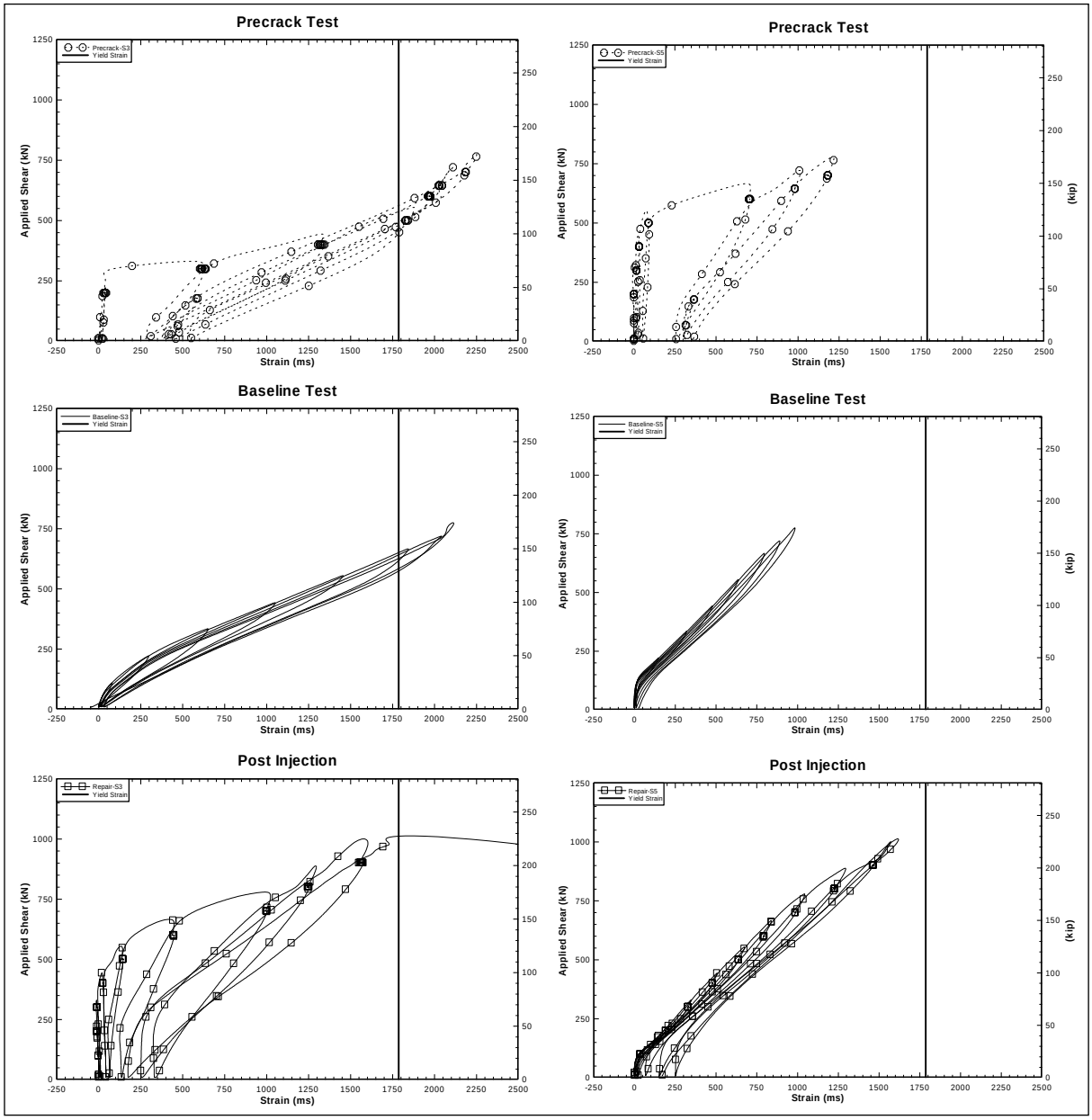


Figure 5.4: Crack pattern locations on east face of specimens. Figure includes precracking, epoxy injected cracks, post-injection cracks, and final failure crack.



(a) Near Injected Crack (b) Near Un-injected Crack

Figure 5.5: Applied shear-stirrup strain behavior for specimen 3-ED. Strain gages located near (a) injected diagonal cracks and (b) un-injected diagonal cracks.

The strain behavior depicted in Figure 5.6 shows the baseline and post-injection stirrup strains at the maximum service load level. In the figure, the baseline strains serving as the abscissa are plotted against the post injection strains operating as the ordinate. Solid symbols represent stirrup strain gages located near injected diagonal cracks as defined above, while hollow symbols represent stirrup strain gages located away from injected diagonal cracks. The dashed reference line marks the boundary between improved and un-improved behavior. Points above the line had higher strains at the same service load after injection, while the points below the line had

lower strains after injection. Most stirrup strains near injected diagonal cracks showed significantly reduced strains after injection, whereas un-injected regions were generally unaffected.

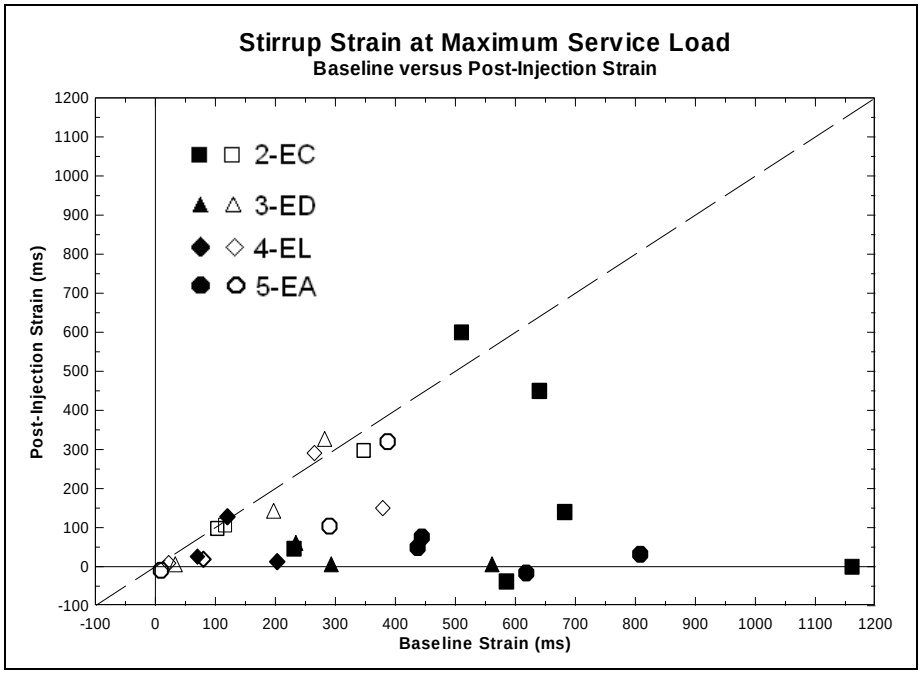


Figure 5.6: Stirrup strains at maximum service level shear (311 kN (70 kip)) before and after injection. (Solid symbol: sensor located near injected diagonal crack; hollow symbol: sensor located far from injected diagonal crack.)

The applied loads required to re-initiate diagonal cracking are portrayed in a similar fashion as seen in Figure 5.7. The load required to re-initiate diagonal cracking was determined from the applied shear magnitude at the moment the stirrup strain showed an abrupt increase. The pre- and post-injection diagonal cracking shears were compared, with the precrack diagonal cracking shear as the abscissa and the post-injection cracking shear serving as the ordinate. Injected diagonal cracks required higher applied shear than the original specimen to produce new diagonal cracking. Data above the reference line show that larger shear loads were required, while points below the line required smaller loads to propagate or re-initiate diagonal cracking. Non-injected cracks typically behaved similar to the baseline tests, where stirrup strains began increasing upon application of applied shear.

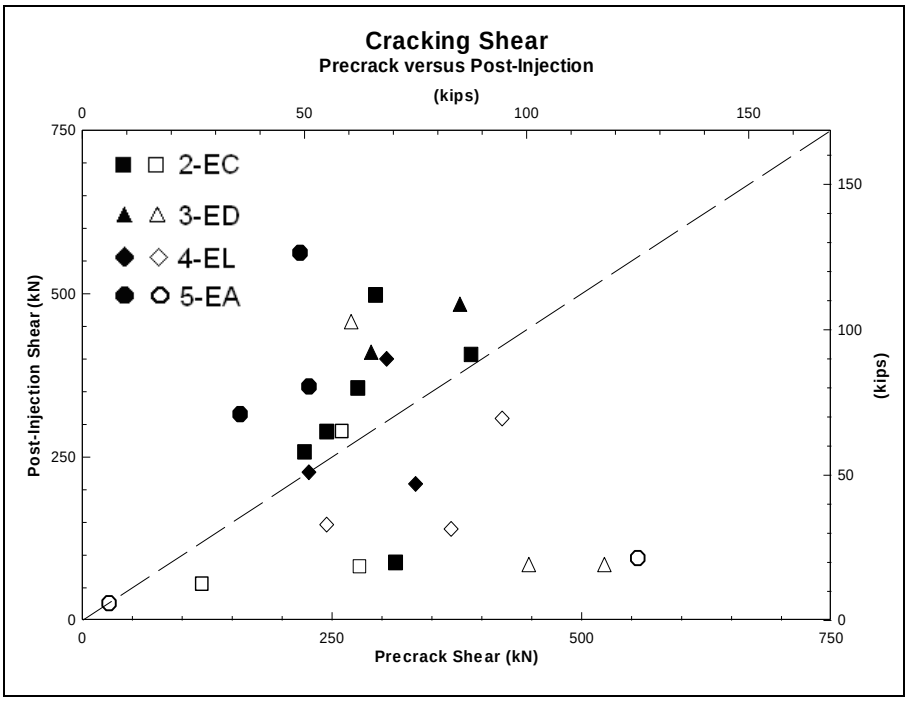


Figure 5.7: Applied shear at diagonal cracking initiation before and after injection. (Solid symbol: sensor located near injected diagonal crack; hollow symbol: sensor located far from injected diagonal crack.)

An additional test was performed on specimen B.IT.NC.EL to collect data while the specimen was curing and the cyclic service level live loading was being applied. Figure 5.8 shows the deformation range of a representative displacement sensor, while Figure 5.9 shows an example of the stirrup strain throughout the curing period. Also shown in Figure 5.9 are the internal and external temperature recordings. The curing time reported by the epoxy manufacturer is seven days at 4 ºC (40 ºF) and 2 days at 25 ºC (77 ºF). The average curing temperature for specimen B.IT.NC.EL was 10 ºC (50 ºF), which correlates to a curing time of approximately six days. The diagonal deformations for the region containing epoxy-injected diagonal cracks showed marked decrease in deformation within 12 hours of injection. Over the next three days, the deformation range decreased by nearly 75%. For a stirrup located in the same section as the example diagonal deformation, the strain range decreased by over 50% within the first 18 hours, but little additional effects were observed for the remainder of the curing process. The stirrup strain was also observed to fluctuate with the external temperature. Diagonal displacement measurements also tended to fluctuate with time, but the mean deformation did not alter significantly.

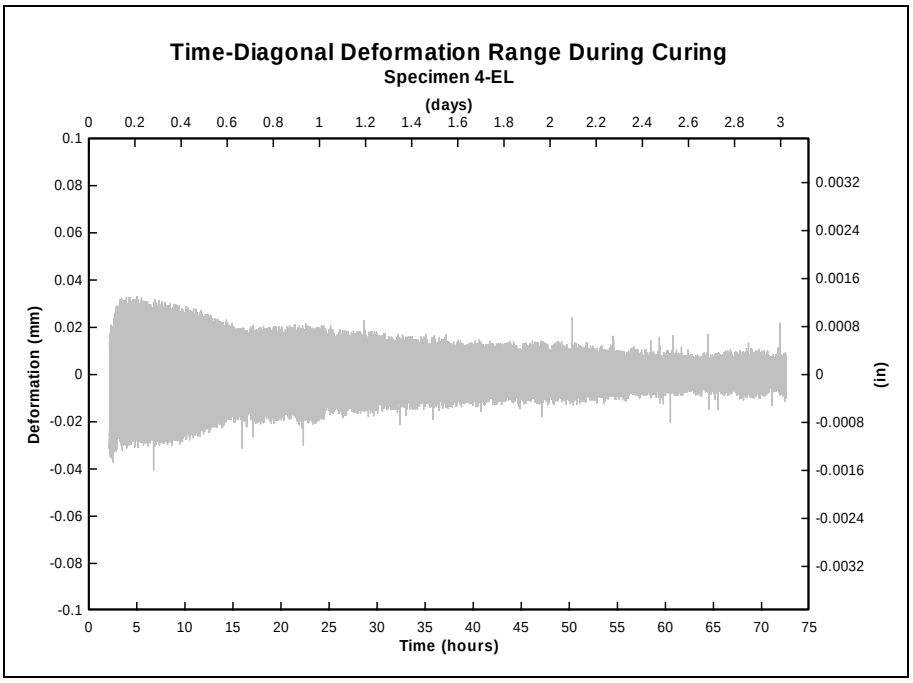


Figure 5.8: Diagonal deformation range during curing of specimen B.IT.NC.EL

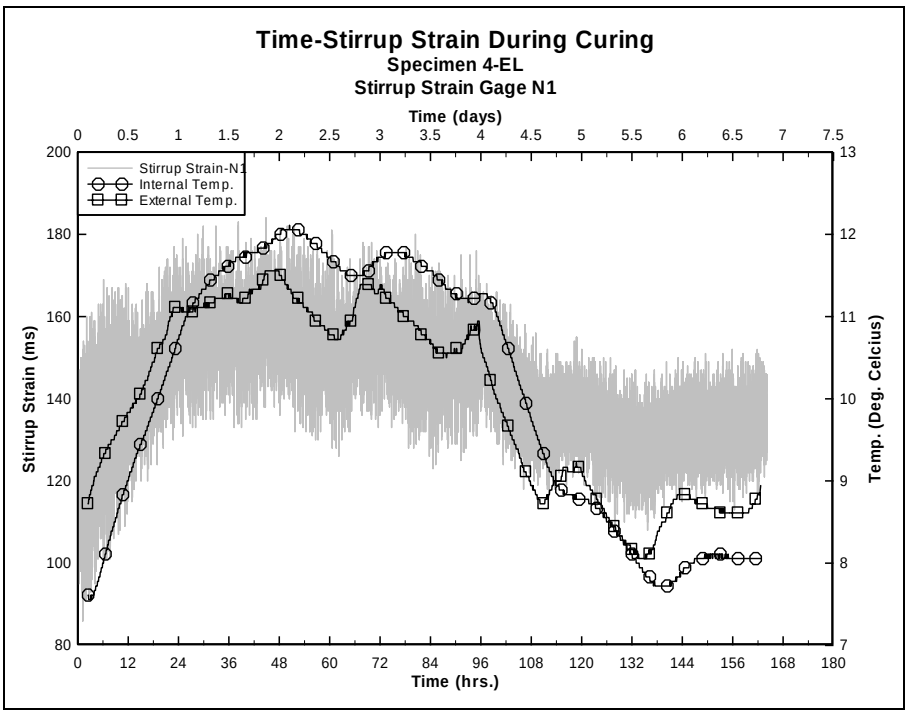


Figure 5.9: Stirrup strain during curing of specimen B.IT.NC.EL

5.1.3 Analytical methods

The material properties for concrete and steel varied from specimen to specimen, preventing direct comparisons between test specimens. In a previous study, a computer program called Response 2000 (R2K), which utilizes Modified Compression Field Theory (MCFT), was used to predict shear capacity for a series of 31 otherwise similar full-size CRC specimens (*Bentz 2000*). The program predicted capacity within 0.98 of actual with a coefficient of variation under 8% (*Higgins, et al. 2004b*). R2K was used to estimate the inherent capacities of the epoxy-injected specimens in their unaltered state (strength of specimen without injection) as well as the strength of the control specimen. The predicted shear strengths are summarized in Table 5.1.

Table 5.1: Specimen experimental summary

Specimen	V_{intial} (kN)	V_{exp} (kN)	V_{DL} (kN)	V_{app} (kN)	V_{R2K} (kN)	V_{app}/V_{R2K} (kN)	Failure Mode
B.IT.NC.C	N/A	902	16.9	919	954	0.96	Shear-Comp.
B.IT.NC.EC	723	983	20.3	1003	982	1.02	Shear-Comp.
B.IT.NC.ED	778	992	17.2	1009	967	1.04	Shear-Comp.
B.IT.NC.EL	778	1046	16.7	1063	949	1.12	Shear-Comp.
B.IT.NC.EA	778	1112	18.4	1130	943	1.20	Shear-Comp.

$V_{initial}$ = shear to produce diagonal cracking before injection.
V_{exp} = experimentally applied actuator load.
V_{DL} = specimen self weight induced shear at critical section
V_{app} = Total shear capacity of specimen
V_{R2K} = Analytically predicted shear strength using Response 2000.

On average, the epoxy-injected specimens provided slightly larger shear capacities than predicted, ranging from 1.02 to 1.20 for specimens B.IT.NC.EC and B.IT.NC.EA, respectively. The total applied shear is a combination of the experimental load applied by the actuator and the specimen dead load comprised of the self-weight associated with the failure section. All specimens exhibited shear-compression failures. The specimens with the largest improvement over predicted unaltered shear capacity were specimens B.IT.NC.EL and B.IT.NC.EA. These two specimens received the least amount of epoxy injection in comparison to the other two specimens. Several of the diagonal cracks on B.IT.NC.EL and B.IT.NC.EA were too small to inject; consequently, only three major diagonal crack systems were injected on each of these specimens. Specimens B.IT.NC.EC and B.IT.NC.ED had more numerous diagonal cracks of sufficient size to inject. Axial load was accounted for in the R2K capacity prediction of specimen B.IT.NC.EA. In summary, specimen B.IT.NC.EA exhibited significantly greater strength than predicted, and generally had superior response over similarly epoxy-injected specimens.

5.1.4 Discussion and design recommendations

The results of this study indicate that epoxy injection affected the structural behavior of CRC girders to some degree. Overall, the more substantial effects were observed for specimens B.IT.NC.ED, B.IT.NC.EL and B.IT.NC.EA. Specimen B.IT.NC.ED exhibited a slightly higher

capacity compared to the predicted baseline capacity. Specimen B.IT.NC.ED also achieved higher loads prior to re-initiation of nonlinear response as compared to the epoxy-injected control specimen, B.IT.NC.EC.

The dead load serves to prop the diagonal cracks open, allowing for deeper penetration of the epoxy into the cracks. It further allows the epoxy to only carry superimposed live loads and leaves dead load stresses locked into the rebar and concrete. This tends to delay crack re-initiation and forces new cracks to form adjacent to the previously cracked location. This was observed by the reduced stirrup steel demand at injected diagonal cracks for otherwise similar load levels and the formation of new cracks alongside or in-between epoxy injected diagonal cracks.

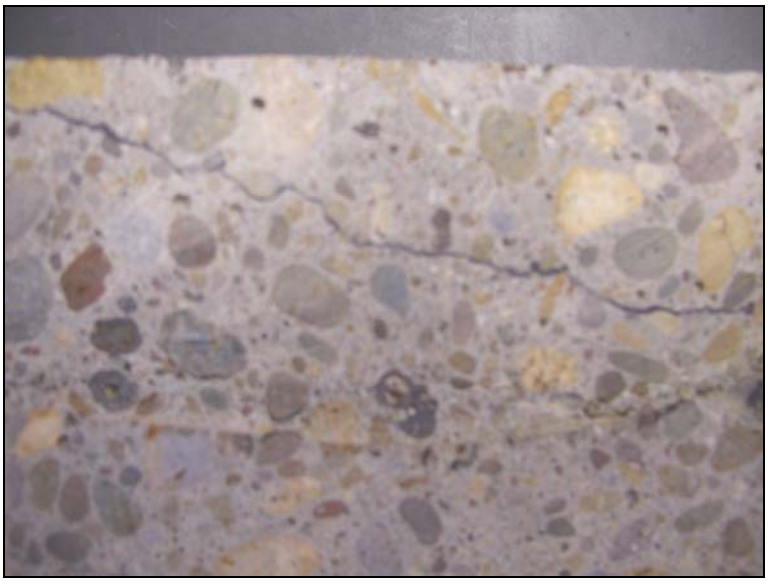
The live load magnitudes, rates, and curing conditions considered in this program for specimen B.IT.NC.EL did not reduce the effectiveness of the epoxy injection as compared to the specimen with dead load alone. The performance of both specimens was very similar. The cyclic service level live loading acted as an internal pumping mechanism that enabled the epoxy to enter and fill finer cracks than either specimen B.IT.NC.ED or specimen B.IT.NC.EC. It was observed during the injection process of specimen B.IT.NC.EL that the epoxy pump pressures built and dissipated in-phase with the actuator loading cycle. The pulsing was also observed when the surface sealant cracked and leaks developed which were then sealed with paraffin wax. The epoxy would be pushed out of the diagonal cracks as the cracks closed upon unloading.

Concrete cores measuring 102 mm (4 in.) in diameter were taken from epoxy injected diagonal cracks for both specimens B.IT.NC.ED and B.IT.NC.EL. Both cores showed epoxy was well distributed through the cracks and even filled hairline sub-cracks. The core from specimen B.IT.NC.EL had small visible pores which were evidence of bubble formations likely caused by the internal pumping action due to the working diagonal cracks. Figure 5.10 shows examples of the porous epoxy matrix observed in specimen B.IT.NC.EL compared to the solid epoxy matrix observed in specimen B.IT.NC.ED.

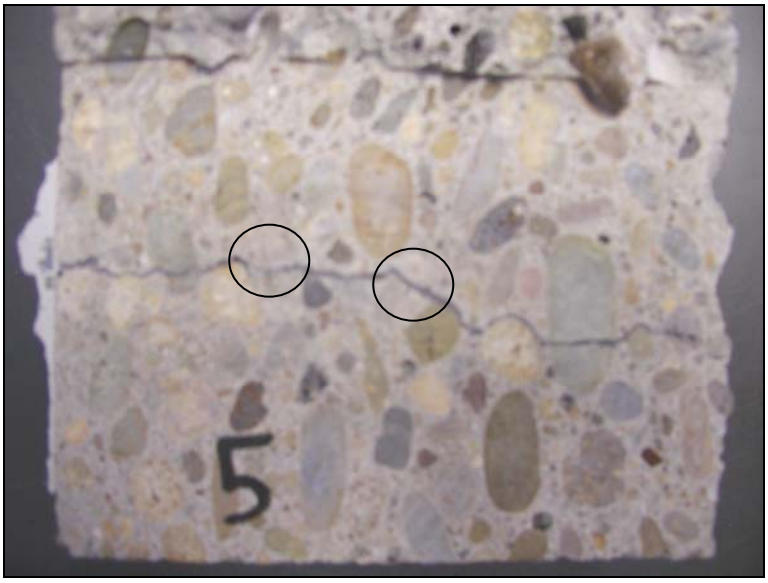
The development of fine bubbles within the epoxy were not sufficient to diminish the performance of specimen B.IT.NC.EL compared to specimen B.IT.NC.ED. It is important to note that the cyclic live loading was representative of loads moving across a typical 15.2 m (50 ft.) span continuous bridge at an approximate speed of 32 kph (20 mph). Additional research may be needed to study the effects of highway speeds and load magnitudes simultaneously applied during epoxy injection, and possible lower-range curing temperatures.

The axially loaded specimen, B.IT.NC.EA, exhibited the most dramatic change between the pre-injection and post-injection response compared to the other specimens. The specimen was injected when an externally applied axial tension was held constant at 645 kN (145 kip), the load magnitude at the end of the of the precrack test. This axial force held the diagonal and vertical cracks open, allowing for better penetration of the epoxy similar to specimens B.IT.NC.ED and B.IT.NC.EL. Additionally, as the transverse loading was applied, the axial force decreased during testing to a magnitude of 267 kN (60 kip) at failure, resulting in a tension force of 267 kN (60 kip) in the flexural steel and a net compressive force of 378 kN (85 kip) induced into the epoxy-injected section. Had the axial load not diminished with increasing transverse load, the specimen may have failed at lower load levels.

Response 2000 predicted a capacity of 853 kN (192 kip) for a similar specimen with 890 kN (200 kip) total axial tension force. Reducing the steel yield stress by an amount equivalent to the 267 kN (60 kip) axial tension and applying a 378 kN (85 kip) axial compression force on the section, Response 2000 estimates a shear capacity of 987 kN (222 kip) which is closer to the observed shear capacity. This situation of loading and curing is representative of a structure with shrinkage or differential temperature strains that are recovered after epoxy injection. The stress recovery (release of restraints at supports for example) produces a post-tensioning effect for the injected specimen, but this beneficial effect could not be relied upon in the field.



(a)



(b)

Figure 5.10: Photographs of cores taken from specimens 3-ED and 4-EL: (a) core taken from specimen 3-ED; (b) core taken from specimen 5-EL with small voids

Basunbul, et al. noticed during their experiments that the cracking loads for their epoxy-injected specimens increased in comparison to the control specimens (*Basunbul, et al. 1990*). They presented an hypothesis that the steel stresses at the location of un-injected cracks will be larger relative to the steel stress at the injected cracks upon reloading. As load is applied, unaltered cracks will have a higher propensity to grow than the injected but the higher steel stresses will help to limit the growth of the fine cracks, thus increasing the cracking load.

Based on the experimental observations, the following conclusions are presented:

- Capacity was not significantly increased by epoxy injection. The largest capacity increases were observed for specimens with continuous cyclical live load applied during injection and with externally applied axial tension (which was due principally to an unintended post-tensioning effect).

- Live loading during injection and curing of epoxy produced dynamic pressure fluctuations during the injection process and pumping of the epoxy within the diagonal cracks. Fine bubbles were identified in the epoxy matrix for cores taken after testing for the specimen with applied live loads, but these bubbles were not sufficient to diminish performance.

- Stiffness was improved and development of residual deformations was delayed by epoxy injection.

- Epoxy injection increased the load level required to reform diagonal cracks in the stem.

- Injected diagonal cracks did not reopen; instead new cracks formed adjacent to the original injected cracks.

- Epoxy injection reduced service-level stirrup strains compared to un-injected diagonal cracks. This may reduce bond fatigue thereby slowing or preventing additional crack growth.

5.2 EXTERNAL SUPPLEMENTAL STIRRUP REPAIR FOR GIRDERS

5.2.1 Material and application details

The materials used for the external stirrup steel threaded rod repair were based on a repair of a bent cap on an in-service bridge located in Salem, Oregon. The repair consisted of two C152 X 16 (C6 X 13) sections anchored by steel threaded rod meeting the requirements of ASTM A449. The superstructure of the bridge consisted of steel girders supported on bearing assemblies atop the reinforced concrete cap beam; thus there was no interference with an integral concrete diaphragm at the pier location. The aim of the current study was to assess the performance of this repair technique within the laboratory environment. Thus, ASTM A449, 13 mm (0.5 in.) diameter threaded rod was chosen to anchor the previously described channel sections on a typical beam repair specimen. The remainder of the apparatus consisted of ASTM A36 5mm (2 in.) square by 6 mm (0.25 in.) thick plate washers, ASTM F436-1 25 mm (1 in.) outer diameter (OD) round washers, and ASTM A194-2H heavy hex nuts, as shown in Figure 5.11.

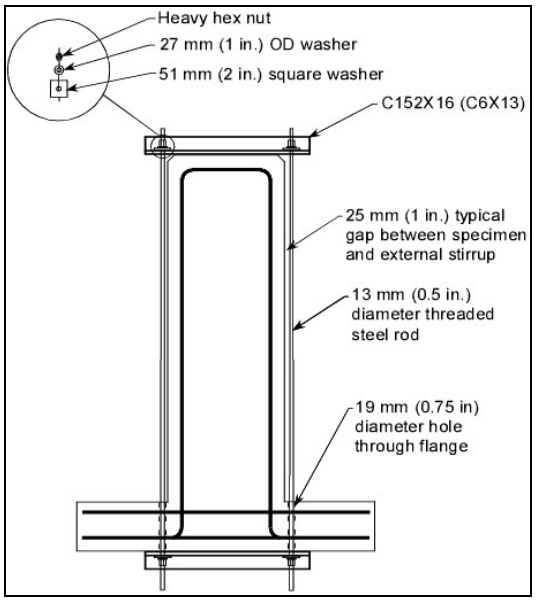


Figure 5.11: External stirrup typical section: channel repair

During the analysis phase of the repair method, the stiffness of the supporting steel sections was considered important to performance. Thus, both the channel sections and a W6X20 section were investigated. The W6X20 section, as shown in Figure 5.12, was under weak axis bending with a moment of inertia 13 times stiffer than that of the channel section. However, the initial test setup for the W section placed the steel web in local bending between the flanges, resulting in a similar performance compared to the channel section.

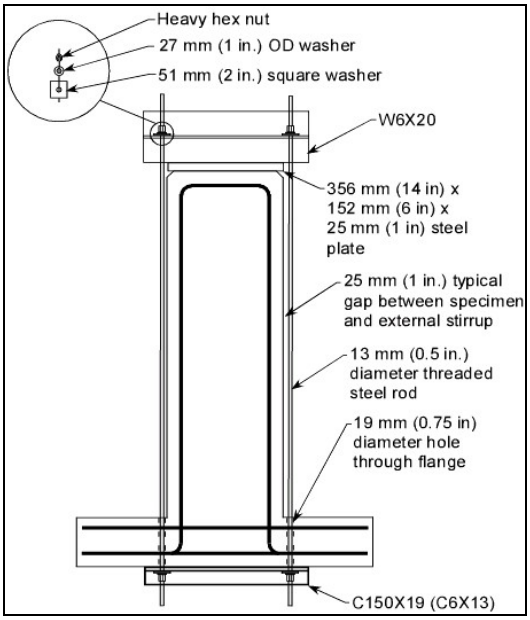


Figure 5.12: External stirrup typical section: W Beam repair

A third test setup for the external stirrup repair was then used, as shown in Figure 5.13, resulting in a significantly stiffer section. Material tests for the threaded rod were performed and the results are presented in Table 5.2.

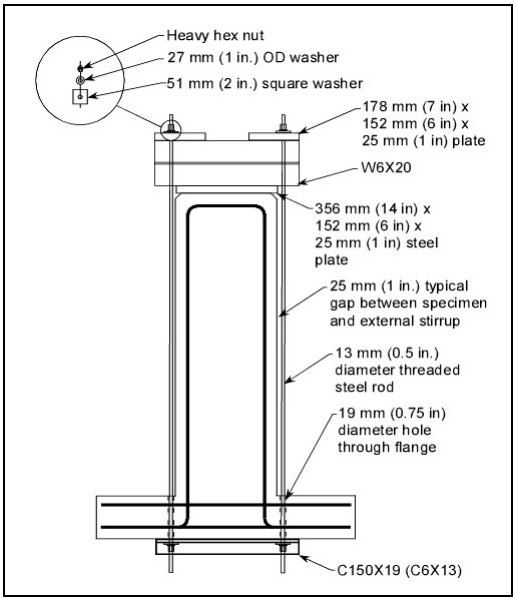


Figure 5.13: External stirrup typical section: strengthened W Beam repair

Table 5.2: External stirrup reinforcing steel properties from tensile tests

External Stirrup Steel	Yield Strength		Ultimate Strength		% Strain at Failure
	Mpa	ksi	Mpa	ksi	
	581.2	84.3	621.9	90.2	8.3

Elevation views of the repair schemes for beams B.IT.NC.ES, B.IT.C.ES, and B.T.NC.ES are shown in Figures 5.14 through 5.16 respectively.

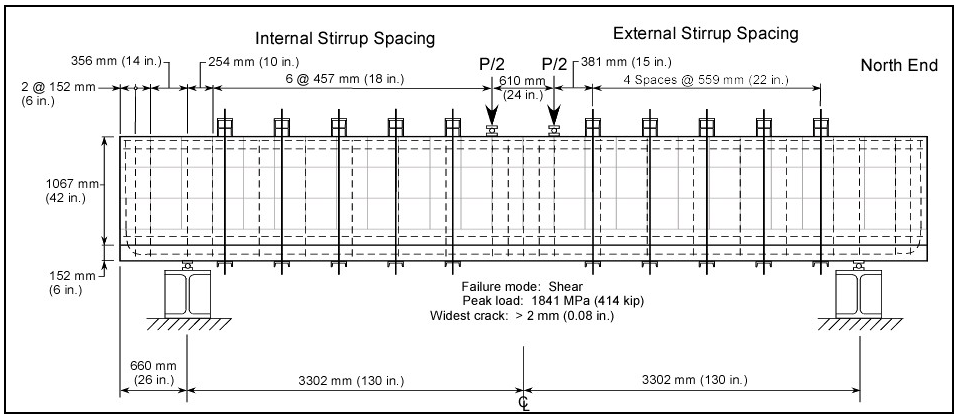


Figure 5.14: Specimen B.IT.NC.ES repair

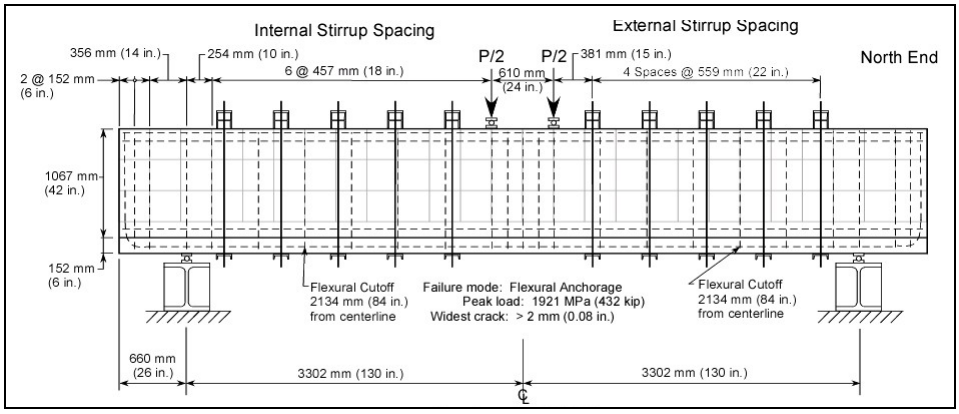


Figure 5.15: Specimen B.IT.C.ES repair

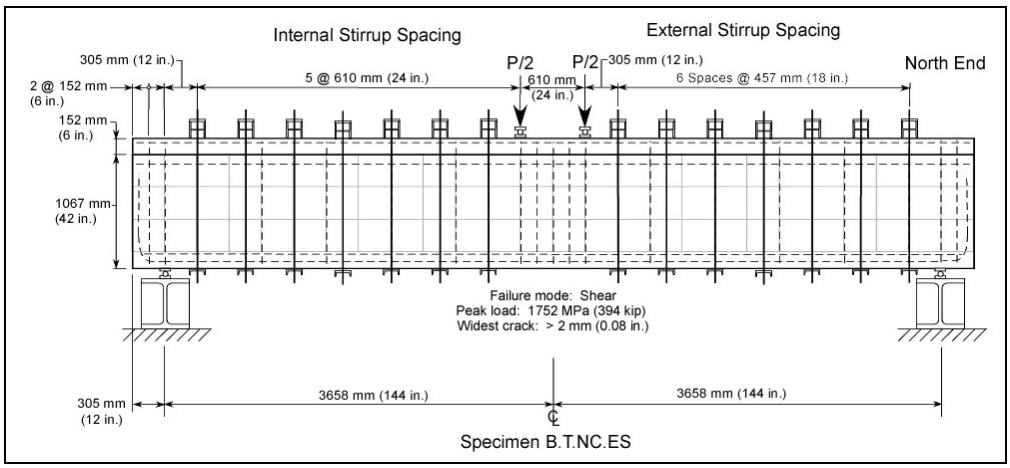


Figure 5.16: Specimen B.T.NC.ES repair

The process used for repairing the specimens with external stirrups is outlined below with reference to Figure 5.17.

- Identify external stirrup spacing along shear span.
- Locate flexural and deck steel locations on specimen with a rebar locator.
- Mark hole locations such that they fall outside the width of the web.
- Drill holes with a rotary hammer drill with caution if steel is encountered.
- Place threaded rod through holes in the flange.
- Connect reaction sections to the threaded rod and tighten to predetermined force.



Figure 5.17: External stirrup installation

5.2.2 Experimental results

5.2.2.1 Investigation on repair scheme efficiency for IT beams

The first external stirrup repair specimen, B.IT.NC.ES was investigated to optimize the repair scheme, based on varying several subsequently described parameters. The initial test specimen included application of the external stirrups at two load levels – the beam self weight or no dead load condition, and a second superimposed service condition dead load level. Comparable tests performed in the available literature negated the use of a superimposed dead load on the repair method. However, superimposed dead load force was included in the current investigation to document the effects on the clamping action related to the repair method. Crack widths due to the self weight of the beam were small in comparison to those at the first or second load step. Therefore, a superimposed shear force of 178 kN (40 kip) – representative of the weight of the deck, intermediate

diaphragms, superficial wearing surface, and traffic barrier – was applied prior to attachment of the external supplemental stirrups. This value was determined from a typical interior girder of a three span continuous deck girder bridge with 15.2 m (50 ft) spans and a uniform dead load of 23.3 kN/m (1.6 kip/ft).

In addition to the two different initial loading conditions for the external stirrups, the initial clamping force and resulting stress in each individual external supplemental stirrup leg was varied. The first loading case, denoted as the snug condition, was chosen to overcome any seating losses associated with uneven bearing surfaces and to apply strain in the threaded rods just upon application of additional shear. Each of the two threaded rods required for the repair method was instrumented with common foil quarter bridge strain gages such that the two bars were stressed equally at the start of each test. The snug condition resulted in a 200 με value corresponding to a 34 MPa (5 ksi) stress in each external stirrup leg.

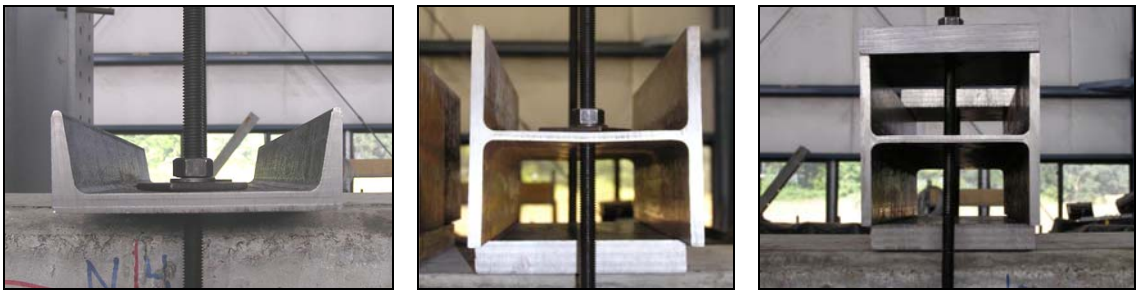
The second post-tensioned stress condition was determined based on an assumed common failure strain between the external and internal stirrups. Uniaxial tension tests on the integrally cast stirrups resulted in a yield strength of about 345 MPa (51 ksi). Similar tests on the external stirrups resulted in a yield strength of about 586 MPa (85 ksi); thus the external stirrups were post-tensioned to 207 MPa (30 ksi), corresponding to 1034 με, to provide essentially the same stress range prior to yielding between the two bars at failure, assuming compatibility among the internal cast-in-place and the supplemental external stirrups.

The first external stirrup specimen initially utilized two different steel support sections at the base of the web, as shown in Figure 5.18a and b. Recall the external stirrup repair was chosen to investigate a current repair of an in-service bridge within Oregon's bridge inventory utilizing channel sections which react about the top surface of the deck and the bottom of the web. For this loading condition, the channel section at the base of the web is placed in weak axis bending due to edge bearing at the corners of the stem. Thus, the strain in the external stirrups was dependent upon the relative flexural stiffness of the reaction section and the moment arm from the corner of the stem to the external stirrup axial stiffness.

To reduce the effect of the reaction section on the repair scheme (enable more strain to occur in the stirrup legs), a W section in weak axis bending with mounting hardware reacting against the web of the section was placed at the base of the concrete stem, providing approximately 13 times the stiffness of the channel section. Also, the external stirrups were positioned as close to the stem as possible (typically 12 mm (0.5 in.)) in order to minimize the effect of the moment arm on the steel sections.

Initial testing of the W section indicated local bending of the web, as shown in Figure 5.18b. The W section apparatus was modified, as shown in Figure 5.18c, by placing a 25 mm (1 in.) thick steel plate atop the W section. For this loading condition, the top steel plates extend from the outside of the W section toward the centerline of the beam, which in turn increases the bending stiffness of the system significantly. A testing matrix for specimen B.IT.NC.ES is shown in Table 5.3, taking into account the three steel support

sections, the two specimen initial loading conditions, and the two initial stress levels in the supplemental external stirrups prior to testing.



(a) (b) (c)

Figure 5.18: External stirrup repair: (a) channel section; (b) W Beam; (c) Strengthened W Beam

Table 5.3: External stirrup specimen B.IT.NC.ES testing matrix

Test:	Channel Section:	W Beam:	Strengthened W Beam:	Post-Tensioned	Snug Tightened	Dead Load	No Dead Load
1	X				X		X
2	X			X			X
3	X				X	X	
4	X			X		X	
5		X			X		X
6		X		X			X
7		X			X	X	
8		X		X		X	
9			X		X		X
10			X	X			X
11			X		X	X	
12			X	X		X	

Applied shear force versus midspan displacement graphs (Figure 5.19) illustrate the effects of changes in stiffness for the three steel reaction sections, taken for the case of no dead load, including snug and post-tensioned stresses in the external stirrups. The global member stiffness improved slightly for the strengthened W Beam case; the remaining repair sections did not show appreciable change. However, for slender beams the overall deformations come principally from flexural strains and thus local diagonal deformations are more descriptive of the response characteristic impacted by the repair alternatives.

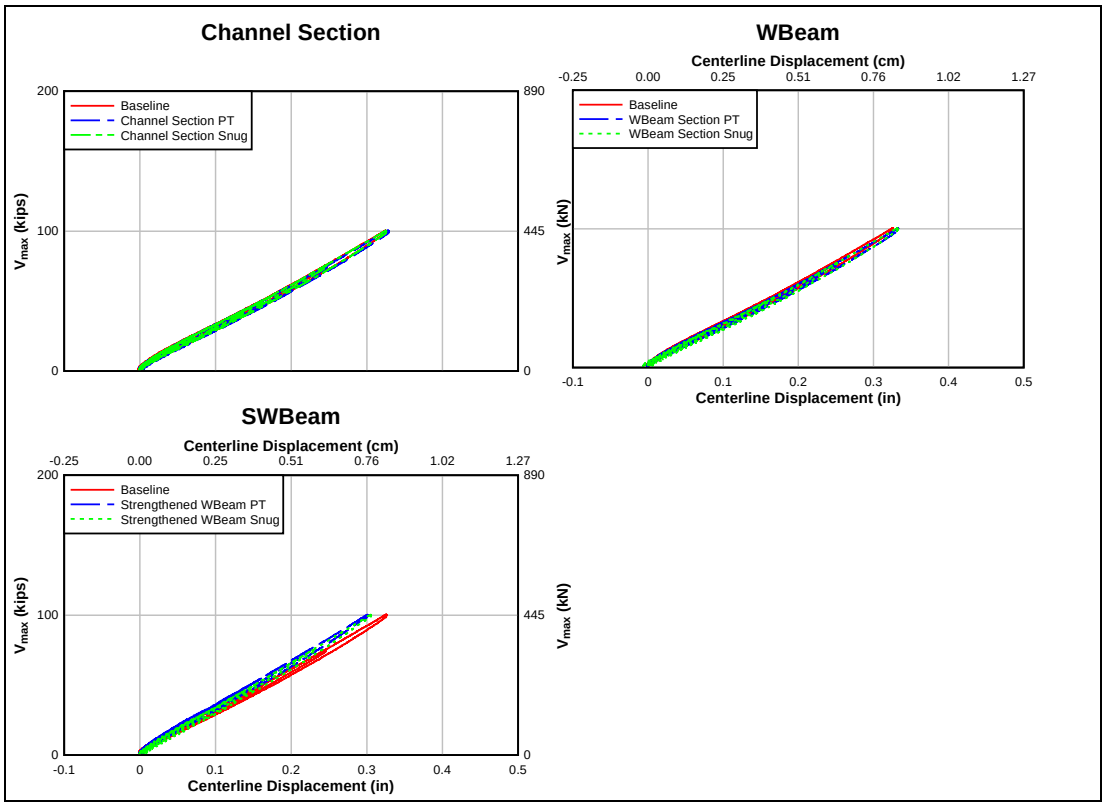


Figure 5.19: Maximum shear force versus centerline displacement

To more clearly identify the impact of the repair alternatives, the diagonal sensors along the west face of the specimen were used to measure the average vertical strain over the height of the stem. This data can then be used to investigate strain compatibility between the external stirrups and the specimen. Diagonal displacement sensors were placed within the shear span, resulting in three "panels" which measured the elongation and/or contraction of each sensor depending on its orientation with respect to a diagonal crack.

In order to define the total average vertical strain over each panel, a third direction must be measured, analogous to a strain rosette, which utilizes three strain gages at defined angles to determine principle strain values. In the case of a cracked concrete beam, the proposed failure crack indicates the orientation of principle strain in the concrete within the panel of interest. From this orientation, the average vertical strain over the panel length can be calculated using Mohr's circle for strain, following the procedure outlined below. It should be noted that Mohr's Circle for strain is similar to Mohr's Circle for stress, with the variation of the inclusive angle between the axis and the point of interest is taken as 2θ, not θ, as indicated in Figure 5.20.

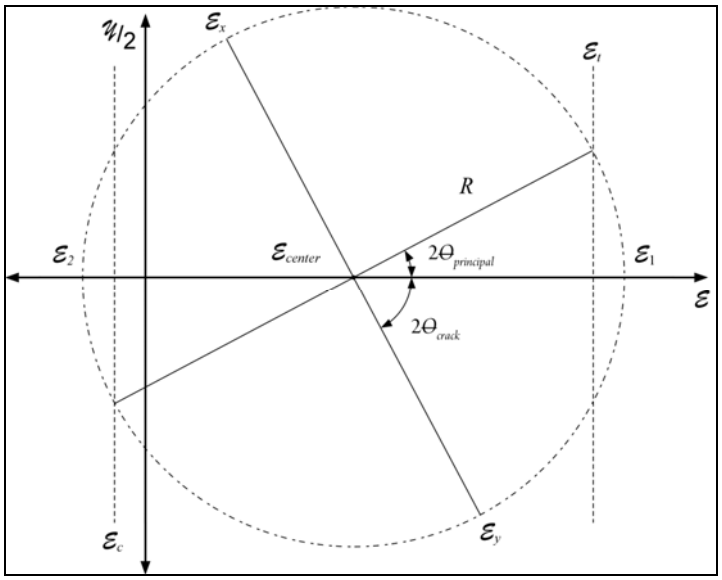


Figure 5.20: Mohr's circle for strain

The conversion of diagonal sensor data to average vertical strain in a specific panel is dependent on five known quantities, as identified in Figure 5.21 (*Dawson 2008*): diagonal tension displacement (L_t), diagonal compression displacement (L_c), diagonal displacement gage length (L_0), diagonal displacement gage orientation ($\theta_{diagonal}$), and crack angle (θ_{crack}). Variation in the orientation of the diagonal sensors was assumed to be negligible.

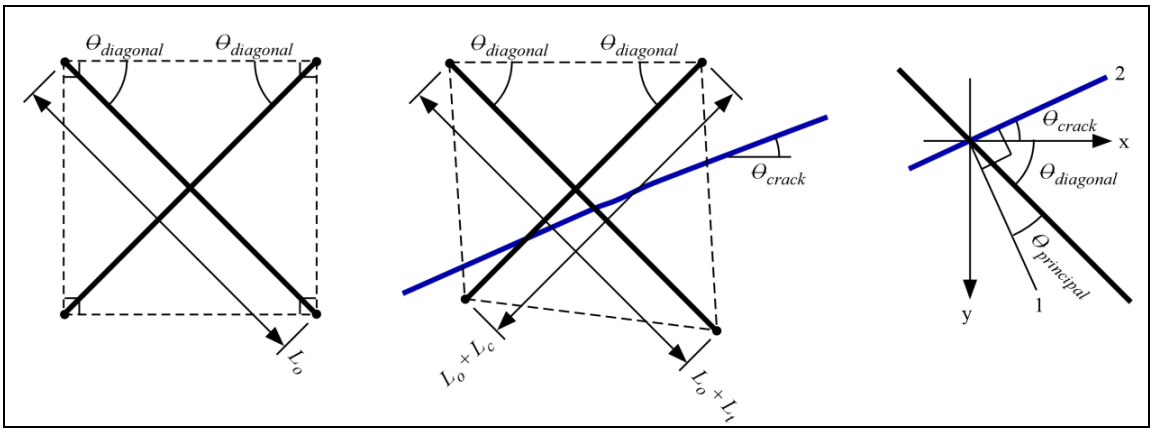


Figure 5.21: Diagonal displacement geometry

Once the quantities of interest are known, conversion to average vertical strain follows from the equations noted below, taken from Mohr's circle for strain. The diagonal

displacements were converted to strains ε_t and ε_c from Equation 5-1 and Equation 5-2 below.

$$\varepsilon_t = \frac{L_t}{L_0} \tag{5-1}$$

$$\varepsilon_c = \frac{L_c}{L_0} \tag{5-2}$$

The center of the circle is then denoted by Equation 5-3.

$$\varepsilon_{center} = \frac{\varepsilon_t + \varepsilon_c}{2} \tag{5-3}$$

Next, the orientation of the principle strain was calculated, as shown in Equation 5-4, assuming the crack angle was orthogonal to the principle strain. Recall from Figure 5.21, this value was measured with respect to the crack angle and the diagonal displacement gage orientation.

$$\theta_{principal} = 90° - \theta_{diagonal} - \theta_{crack} \tag{5-4}$$

Utilizing the angle of principal strain, the center of the circle, and the tensile strain, the radius of the circle can be found, as shown in Equation 5-5.

$$R = \frac{\varepsilon_t - \varepsilon_{center}}{\cos 2\theta_{principal}} \tag{5-5}$$

All quantities for Mohr's circle were calculated; thus the principal strains, ε_1 and ε_2, as well as the vertical and horizontal strains, ε_x and ε_y could be calculated, as shown in Equation 5-6 to Equation 5-9.

$$\varepsilon_1 = \varepsilon_{center} + R \tag{5-6}$$

$$\varepsilon_2 = \varepsilon_{center} - R \tag{5-7}$$

$$\varepsilon_x = \varepsilon_{center} - R\cos 2\theta_{crack} \tag{5-8}$$

$$\varepsilon_y = \varepsilon_{center} + R\cos 2\theta_{crack} \tag{5-9}$$

The average vertical strains were determined for panel 2S, corresponding to the center panel along the eventual failure diagonal crack. As a starting point for comparison of the three reaction sections, the change in average vertical strain due to post-tensioning with and without dead load were compared for the static condition prior to application of

additional load on the specimen. The results are shown in Figure 5.22 with the no dead load condition on the left and the dead load condition on the right for the channel, W Beam and SW beam, respectively. For the no dead load condition, each reaction section provides essentially the same reduction in average vertical strain. This is a result of the small diagonal crack widths when only the self weight of the specimen is used. For the superimposed bridge dead load condition, the more flexible channel section appears to be less capable of compressing the cracks over the depth of the stem compared to the other two methods.

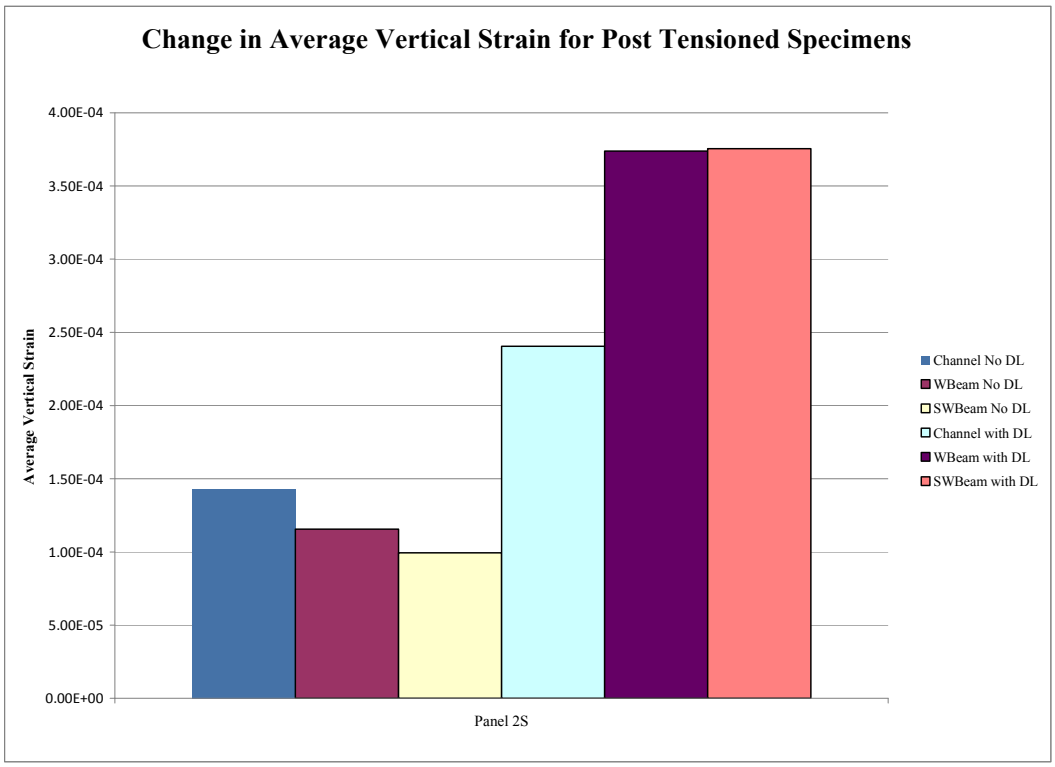


Figure 5.22: Average vertical strain comparison between different dead load and external stirrup support conditions at installation of external stirrups due to post-tensioning condition

Comparison of the average vertical strain for the no dead load snug and post-tensioned conditions throughout the service loading range is presented in Figure 5.23. A best fit curve for each repair section is shown. For the no dead load case, the channel section appears to provide a higher reduction in average vertical strain compared to the other sections. However, for the post-tensioned case, the channel section and strengthened W beam provide a slightly higher reduction than the W beam alone (due to local bending of the W section web).

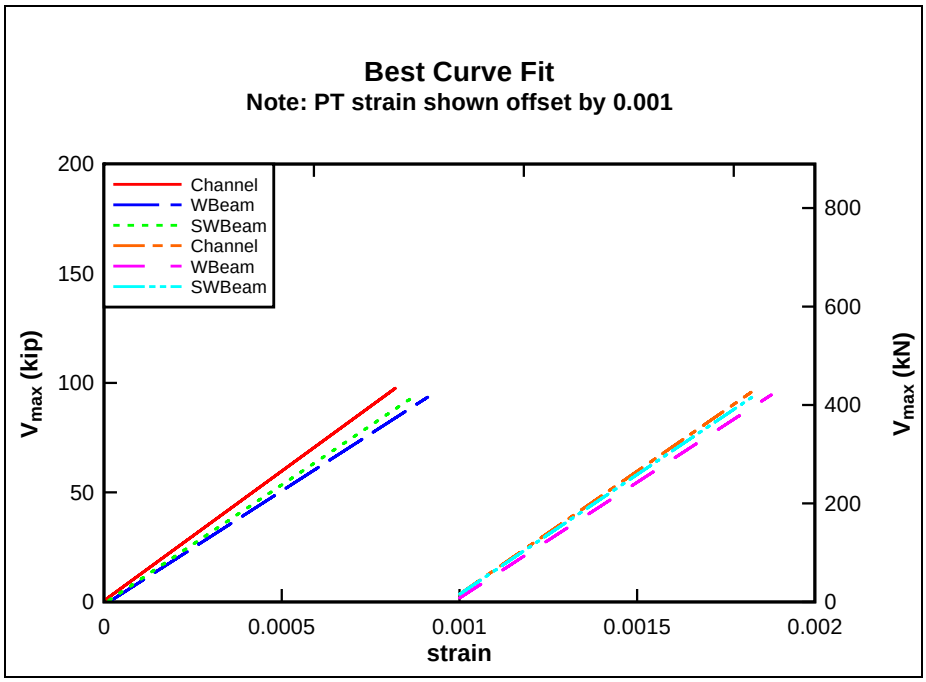


Figure 5.23: Best fit curve of shear versus average vertical strain for panel 2S: beam self weight

Turning toward local behavior, the interaction of the integrally cast stirrups and strain compatibility of the section was investigated. The static reduction in strain for the integrally cast stirrups, due to the clamping force applied by the supplemental external stirrups, was investigated for the three reaction sections. For both the self weight and the dead load case, the snug loading had a negligible effect on the internal stirrup strain, as the small initial force in the external stirrups was unable to produce a measurable reduction in strain for the internal stirrups. However, the post-tensioning case resulted in a reduction in internal stirrup stress for both the self weight and dead load cases.

In both instances, the reduction in strain was similar for each of the three reaction sections (as each pair of external stirrups was tightened to the same force, even as the deformations were different). For the self weight case, the internal stirrups were placed into compression, while the dead load case resulted in a reduction of strain but was not sufficient to place the stirrups into a compressive state.

Comparing the reduction in strain for the dead load and self weight cases resulted in a slight contradiction. For stirrups N1 and S2, the data indicated that the self weight case resulted in a higher strain reduction than the dead load case, but the opposite held true for stirrups N3 and N4, as shown in Figure 5.24. The reason for the discrepancy was from exposure of the steel stirrup legs from the surrounding concrete at stirrups N1 and S2 due to strain gage failure after the initial precrack load was applied. A rotary hammer was used to expose the stirrup steel at the location of the existing strain gage as shown in Figure 5.25, a new gage was mounted, and the baseline loading cycle was repeated. Due

to the additional exposed length of stirrup leg, larger reductions in strains occurred at the no dead load condition.

For stirrups N3 and N4, which functioned successfully throughout the series of tests, the exposed length of steel was only equal to the width of the diagonal cracks crossing the stirrup over the height of the specimen. Therefore, they were subjected to a smaller length reduction at the self weight condition, since the existing crack widths were small compared to the loaded condition. Figure 5.24 also indicates that reductions in internal stirrup strains just after post-tensioning were essentially equal across the three reaction sections.

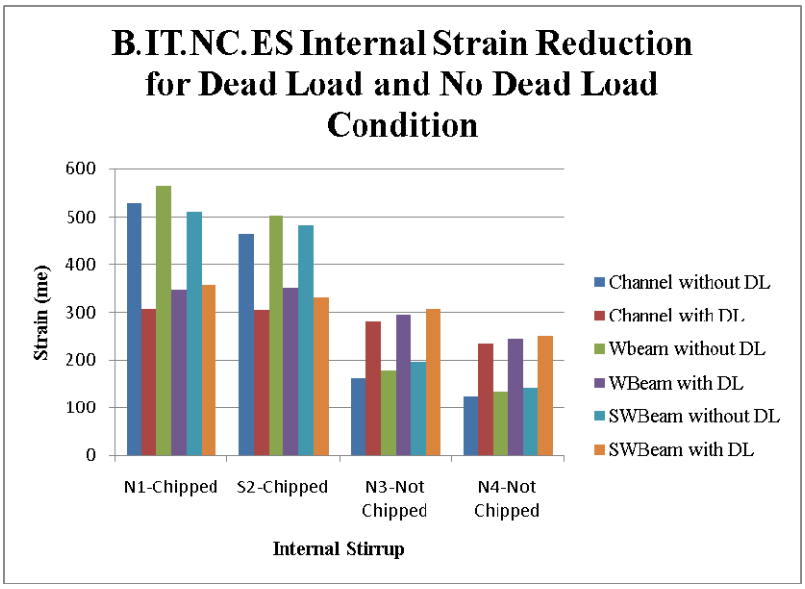


Figure 5.24: Integrally cast stirrup absolute strain reduction due to post-tensioning



Figure 5.25: Exposure of integrally cast stirrup leg to replace failed strain gage

The strain measurements for internal gage 3N are shown for the dead load snug and post-tensioned cases in Figure 5.26, in order to investigate the behavior of the integrally cast stirrups for each reaction section over the service loading range. In each case, the shape and strain range was identical, but the initial strain value varied depending on the post-tensioning force applied. The reduction in the starting internal stirrup strain was proportional to the applied post-tensioning force in the supplemental external stirrups.

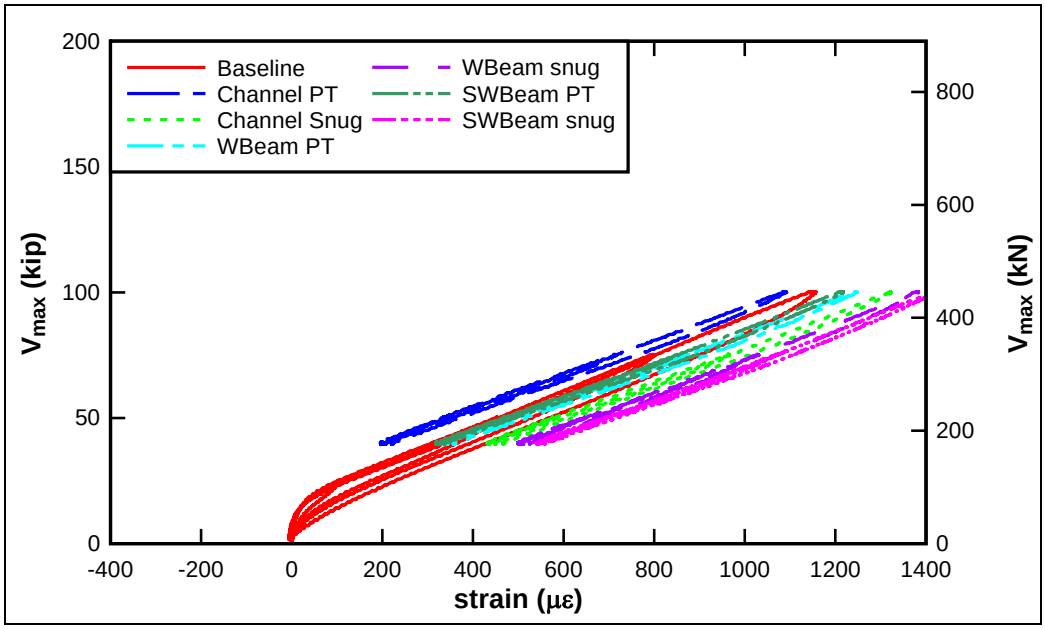


Figure 5.26: Shear force versus internal stirrup 3N strain range for three reaction sections: service loading

The investigation considered the external stirrup strain and corresponding strain compatibility with the girder average vertical strains previously described. External stirrup 3S (along the eventual failure crack) was chosen due to its location directly in the center of panel 2S, which was used to measure average vertical strains in the specimen. The strain range for this stirrup for the four loading conditions and three reaction sections is shown in Figure 5.27. The figure indicates that a stiffer reaction section results in a higher strain range for the external stirrups. For the realistic installation case of superimposed dead load for a typical bridge, the snug condition results in no advantage for the higher resistance sections. However, for the post-tensioned dead load case, it is clear that the higher strain range in the external stirrup is affected by the stiffness of the supporting reaction sections.

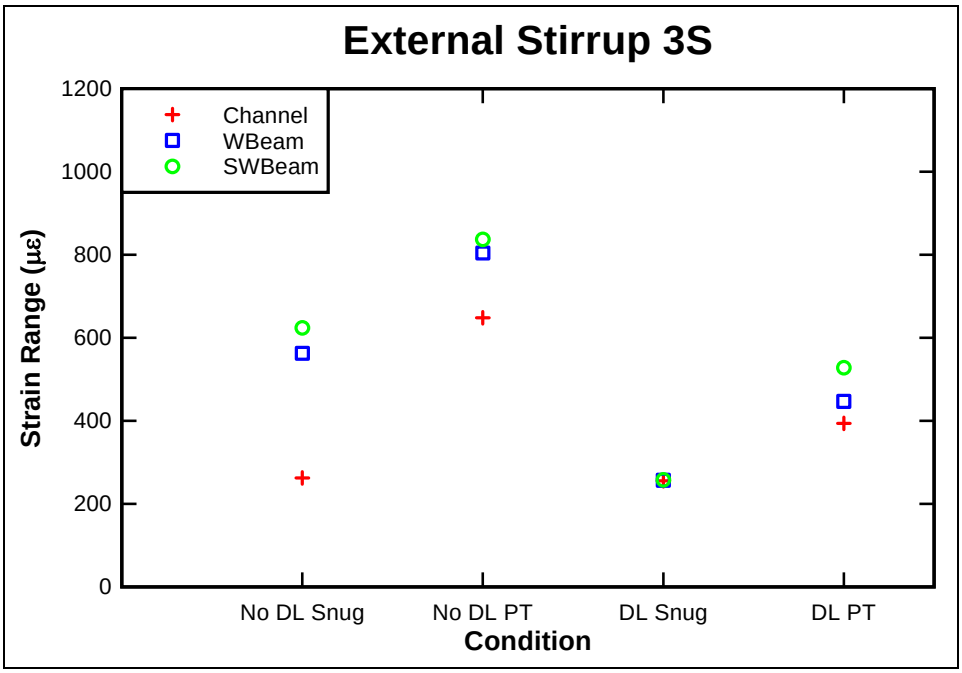


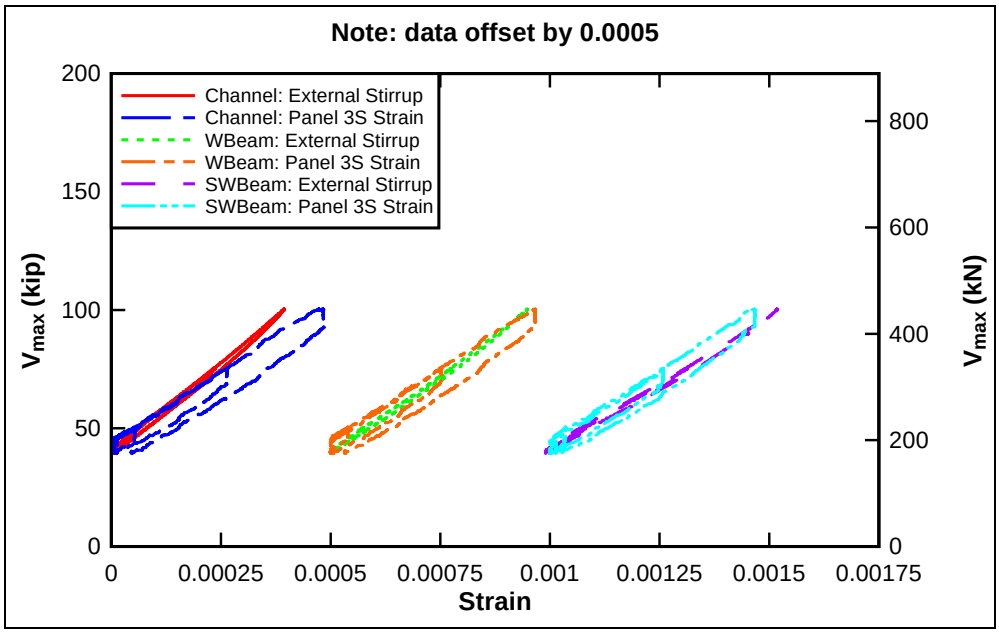
Figure 5.27: External stirrup 3S strain range for various initial conditions at service level loading

The external stirrup strain values indicate that strain compatibility of the external stirrups with the average vertical strain should be similar. For the realistic case of superimposed dead load with post-tensioning, the applied shear versus average vertical strain in panel 2S and the external stirrup 3S is shown in Figure 5.28a. By focusing on the slope of the average vertical strain and external stirrup strain values, it is clear that the efficiency increases as the stiffness of the reaction section increases. This is evident for the case of no dead load snug and post-tensioned cases shown in Figure 5.28b.

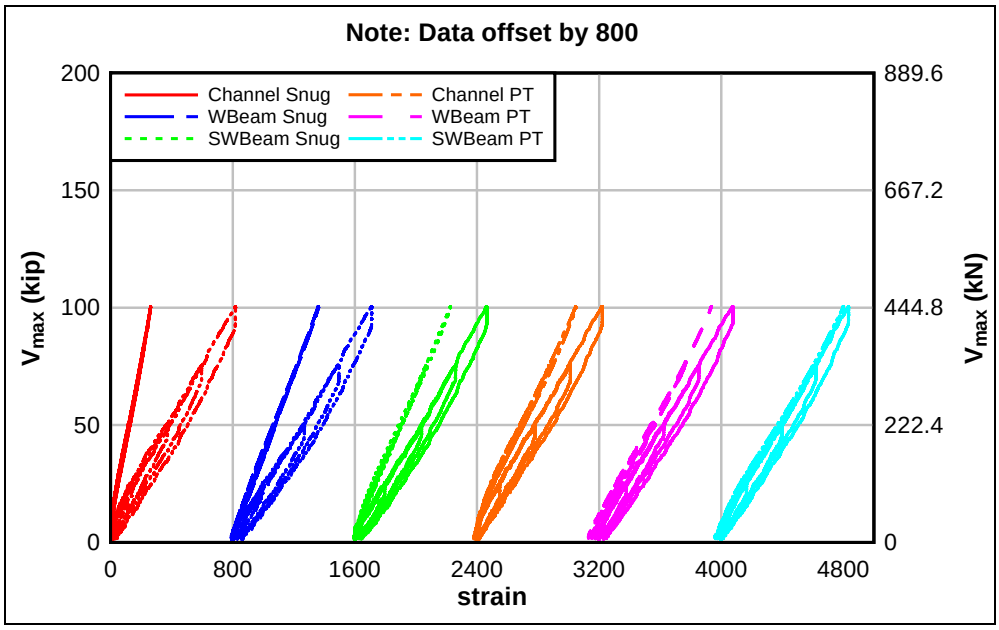
The external stirrup repair scheme can be idealized as elastic springs in series, as shown in Figure 5.29. In this figure, there are three primary springs, the first, K1, relates to the elastic properties of the external threaded rod only. The second spring, K2, relates to the reaction section at the base of the stem – which has been the focus of the current investigation – while the third spring, K3, provides any additional inefficiency to seating of the reaction sections. Nonlinear elastic response associated with the third spring are assumed to be negligible for the current investigation, since the snug loading case induced a minor stress in the stirrups thereby minimizing the effect of seating which is a principle source of nonlinear elastic response.

An indication of the efficiency of each anchorage section can be shown by focusing on K2 with respect to strain compatibility of the section. A graph of the ratio of the external stirrup strain to average vertical strain (as the values approach 100%, there is strain compatibility) versus reaction section stiffness, K2 is shown in Figure 5.30 for all but the dead load snug condition, as sensor malfunction resulted in insufficient data. The figure indicates what was shown previously for the external stirrup strain and strain

compatibility figures – the higher the flexural stiffness of the anchorage section, the higher the strain compatibility (vertical strains in the base section equal the strain in the external stirrups). The figure also indicates the snug condition is inferior to the post-tensioning for all three sections.



(a)



(b)

Figure 5.28: Shear versus external stirrup 3S and average vertical strain in panel 2S (a) with dead load, and (b) without dead load

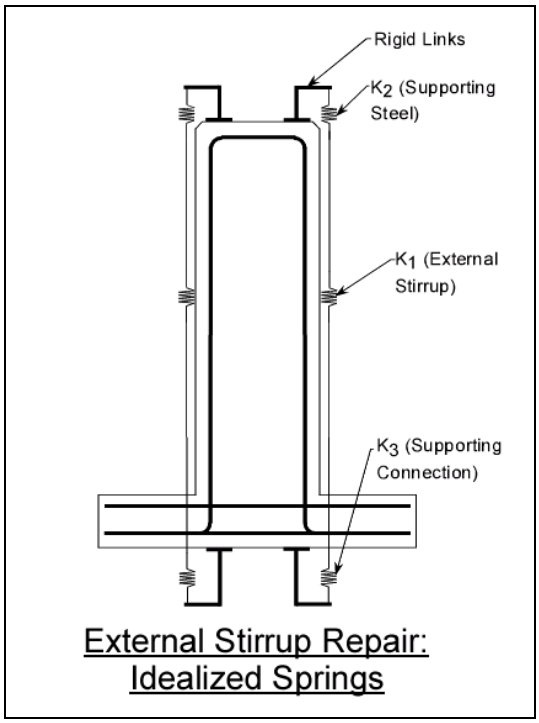


Figure 5.29: External stirrup and supports idealized as springs

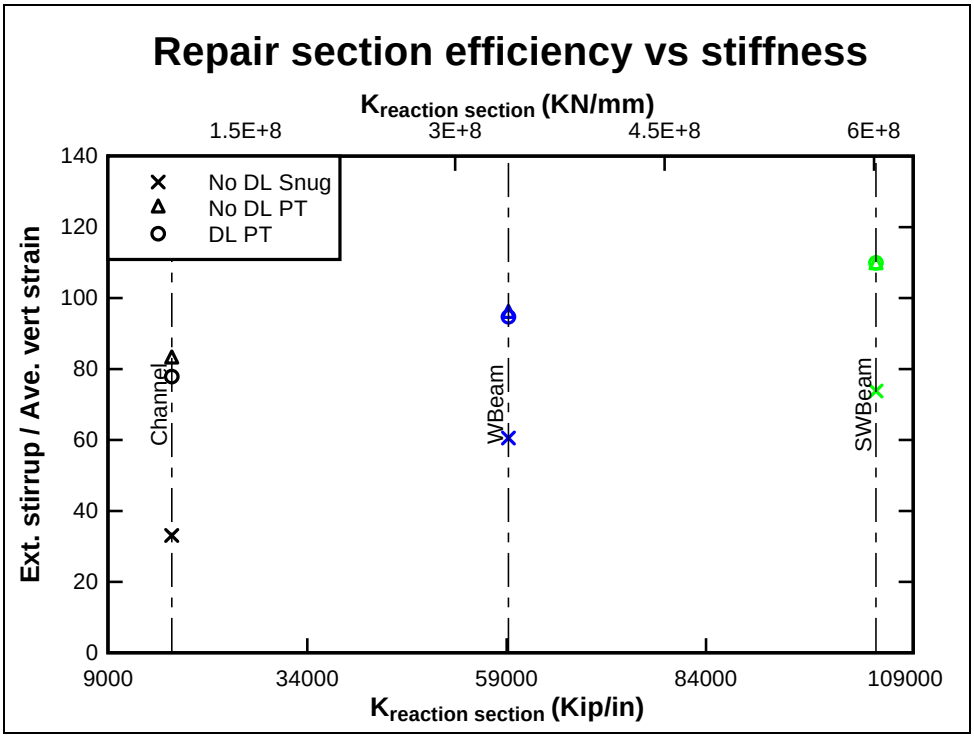


Figure 5.30: Repair section efficiency versus repair section stiffness

Returning to the remaining spring coefficients, an equivalent spring stiffness can be shown for each repair scheme, taking K3 as essentially infinitely stiff, as shown in Equation 5-10.

$$K_{equivalent} = \frac{1}{\frac{1}{k_1} + \frac{1}{k_2}} \tag{5-10}$$

The equivalent spring stiffness for each section is calculated below. For each case, the stiffness of the external threaded rod is identical; the value is shown in Equation 5-11.

$$K_{ext_stirrup} = \frac{AE}{L} \tag{5-11}$$

In the above equation, the L is the height of the section – 1219 mm (48 in.); A is the area of the external stirrup – 129 mm^2 (0.2 in^2); and E is the modulus of elasticity of the rods. For ASTM A449 threaded rod, the modulus value is 199955 MPa (29000 ksi). The stiffness contribution for the second spring comes from the weak axis bending of the anchorage section. For the channel section, the loading is as shown in Figure 5.31.

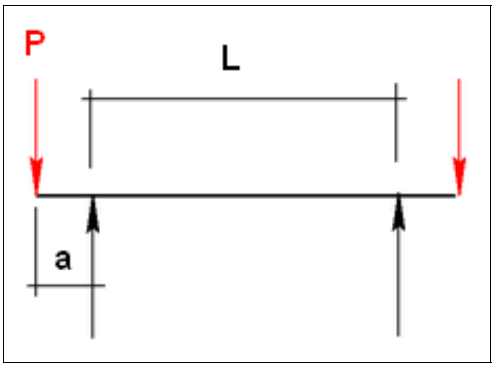


Figure 5.31: Weak axis bending of reaction section

The resulting deflection term is shown below in Equation 5-12.

$$\Delta_{flexure} = \frac{\frac{1}{3}Pa^3 + \frac{1}{2}Pa^2L}{EI_{weak_axis}} \tag{5-12}$$

where P is the applied load; a is the distance from the edge of the web to the location of the external stirrup; L is the width of the web; E is the modulus of elasticity of the section; and I is the moment of inertia about the weak axis of the channel.

The width of the web was held constant such that L was equal to 356 mm (14 in.); the distance from the edge of the web to the external stirrup was 13 mm (0.5 in.). The modulus of elasticity was taken to be 199948 MPa (29000 ksi); and the moment of inertia of the channel section was 437043 mm^4 (1.05 in^4). Comparison of the deflection estimate from Equation 5-12 with a commercially available finite element program indicated larger deformations then those from hand calculations. The finite element solution took into account the shear deformations of the section under weak axis bending, whereas the hand calculation did not. Thus, the hand calculation was modified to account for the shear deformations, as shown in Equation 5-13.

$$\Delta_{shear} = \frac{Pa}{GA_{shear}} \tag{5-13}$$

where A_{shear} is the shear area in the weak axis direction; and G is the shear modulus, defined in Equation 5-14.

$$G = \frac{E}{2(1+\nu)} \tag{5-14}$$

The total stiffness of the system is then the summation of the two equations, rearranged to indicate the stiffness term, as shown in Equation 5-15.

$$K_{weak_axis} = \frac{EI_{weak_axis}}{\frac{1}{3}a^3 + \frac{1}{2}a^2 L} + \frac{GA_{shear}}{a} \tag{5-15}$$

A similar scenario is presented for the W beam section, neglecting local web deformations, in order to estimate the stiffness term. For the strengthened W beam, the location of the top reaction plates changes the deformation of the system from bending to axial bearing (carrying the external stirrup load through the steel flanges into the girder web); thus the stiffness term is as shown in Equation 5-16.

$$K_{SWBeam} = \frac{AE}{L} \tag{5-16}$$

where A is taken as the length of the length of the section times the two flange thicknesses; and L is taken as the flange height.

From these comparisons, the stiffness term is dominated by the external stirrup, with the three reaction sections providing significantly higher values. The data does illustrate effectively that the strengthened W beam is the most efficient repair scheme for each of the loading conditions, and thus it was used for the remaining IT and T specimen external stirrup repair schemes.

To ensure that the external stirrups are effectively mobilized, the supporting steel sections should contribute only 5% to 2% of the deformation in the system (the axial deformation of the stirrups comprise 95% to 98 % of deformation).

5.2.2.2 Investigation on repair scheme efficiency for the T beam

A sequence of tests was performed on specimen B.T.NC.ES prior to the failure loading event. After a baseline loading of the external stirrup repair beam, as the failure loading sequence was applied, large midspan displacements, indicative of a flexural failure were observed and so the test was halted. Further investigation indicated that the shear force required to initiate flexural failure of the strengthened beam was lower than the anticipated shear failure load; thus the test setup was modified to decrease the length of the shear span by moving the outer bearings and reaction sections inward 457 mm (18 in.) for each shear span as shown in Figure 5.32. After this modification, a second baseline loading sequence was completed due to the changes in the moment-shear interaction due to the decreased shear span.

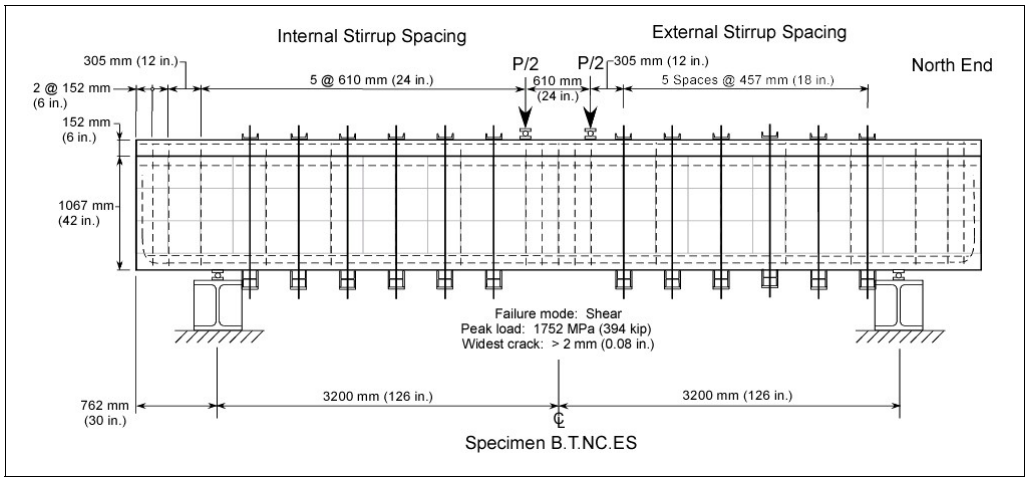


Figure 5.32: B.T.NC.ES revised test setup B

The specimen was retested, and as the theoretical failure load was achieved, the specimen did not exhibit imminent shear failure. Additional shear force would have resulted in a flexural failure; thus the specimen was unloaded a second time. A third baseline test was completed due to any accumulated damage and/or permanent deformations associated with the previous testing sequence. The contribution of the external stirrups was higher than anticipated for the given shear span; therefore a shear failure mode was only possible if the contribution from the external stirrups was reduced. Thus, every other external stirrup was removed as shown in Figure 5.33, and the remaining rods were post-tensioned for the third and final loading sequence, which resulted in shear failure of the specimen. The sequence of three tests performed on the T beam were unintended, but they provide data for two different shear span-to-depth ratios and two different external stirrup spacings.

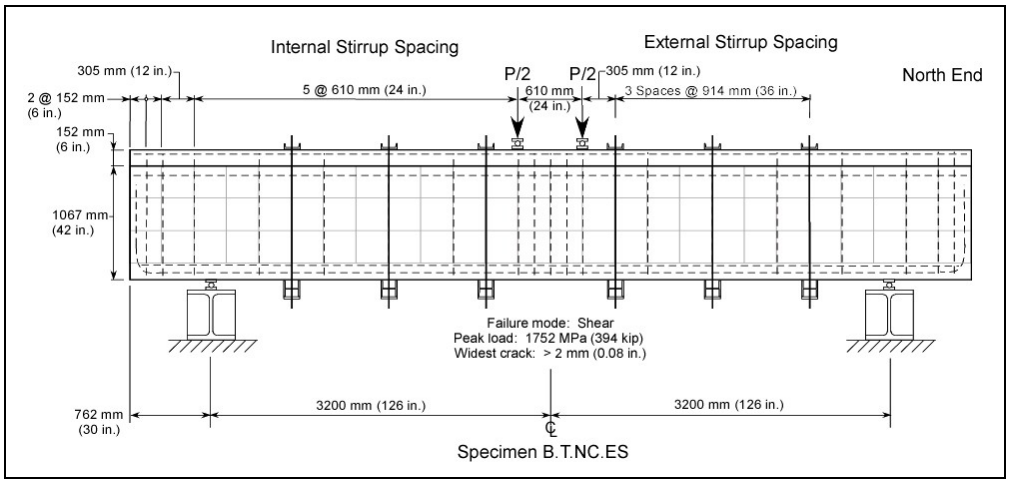


Figure 5.33: B.T.NC.ES revised test setup C

The reduction in internal stirrup strain due to post-tensioning for the external stirrup repair for the T specimen is shown in Figure 5.34. The plot includes the three tests performed on the external stirrup specimen. The graph indicates that several of the gages were placed into compression after post-tensioning (there was no superimposed bridge dead load on the girder). Figure 5.34 also illustrates that the reduction in strain for case C was less than that of case B, since the number of external stirrups was reduced by two.

A comparison of the absolute reduction in strain for the three external stirrup repair specimens is shown in Figure 5.35. The graph is interesting because the three specimens had different cracking patterns, stirrup spacing, and concrete strengths, but the reduction in strain varied consistently between 100 με to 300 με among all three specimens.

Global behavior is shown in Figure 5.36 for applied shear versus centerline displacement. The plot is noteworthy, as it displays an improvement for test A for the repaired condition as well as an overall reduction in displacement between test A and B baseline values as would be expected with a shorter shear span. Comparing the baseline and repaired conditions of tests B and C indicates that test C provides less reduction, which is proportional to the number of active external stirrups used for the final condition.

Local behavior of the integrally cast and external stirrup strain ranges is shown for the sequence of three tests in Figure 5.37 and Figure 5.38. The integrally cast strain ranges follow a similar trend to the centerline displacement. Comparison of the baseline curves for tests A and B indicate essentially the same strain range for the two cases as well as reduction in strain due to the repair. The second observation relates to the reduction in strain for tests B and C which again is related to the number of post-tensioned stirrups used in each test. External stirrup strain for each test is shown in Figure 5.38. Each curve displays an 'S' shape with a higher strain range for each subsequent test. This is consistent with the testing sequence, as test B resulted in the same shear force but different moment-shear interaction; and test C differed from test B with fewer external

stirrups, indicating the same load shared by fewer elements results in higher strain for the remaining external stirrups. Strain compatibility among the three external stirrup tests are shown in Figure 5.39 with similar shape and slope for each case.

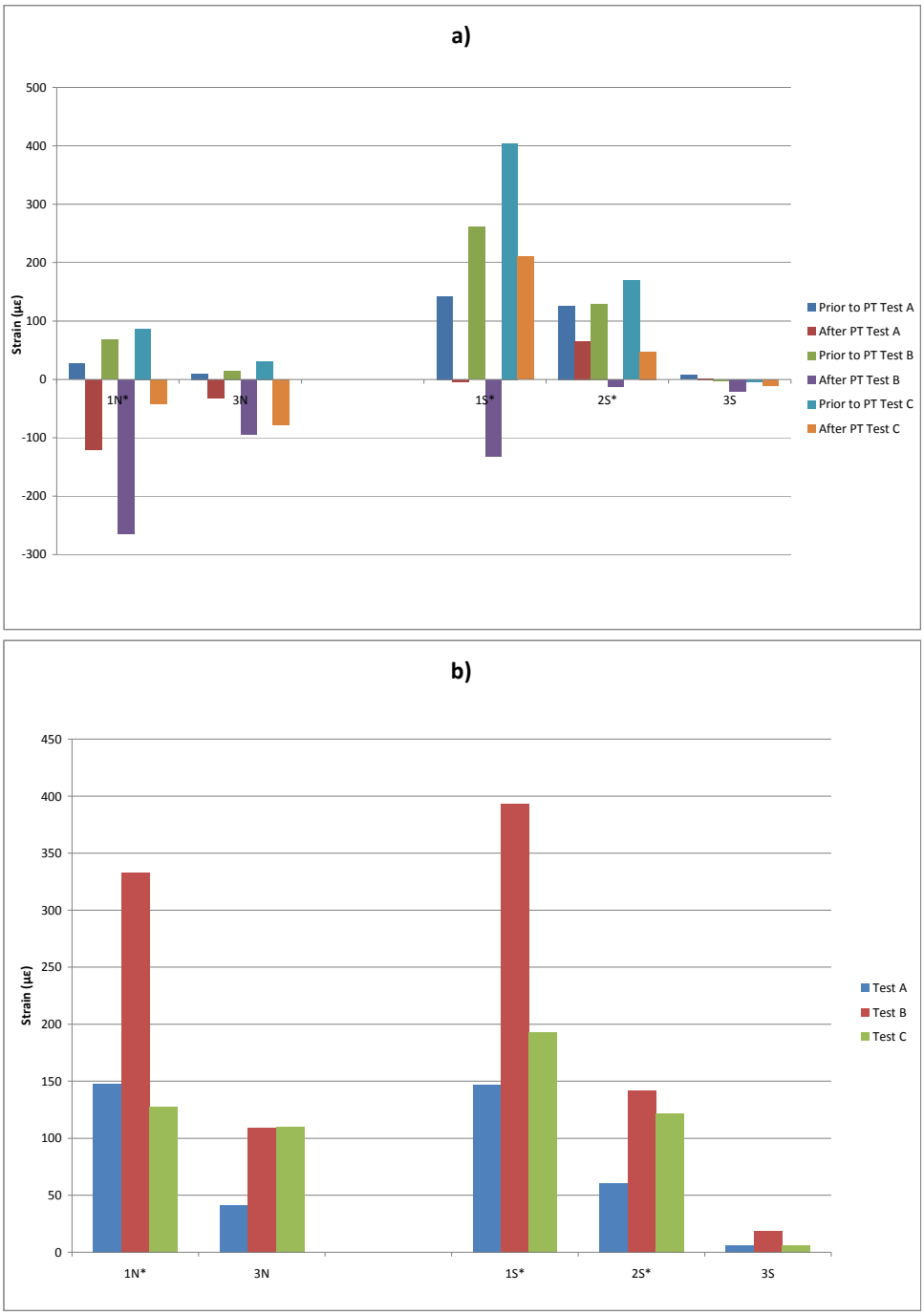


Figure 5.34: Specimen B.T.NC.ES integrally cast stirrup strain: (a) before and after post-tensioning; (b) strain reduction due to post-tensioning. Note: asterisk denotes stirrups that were instrumented by chipping into the concrete to expose the stirrup leg at the diagonal crack locations.

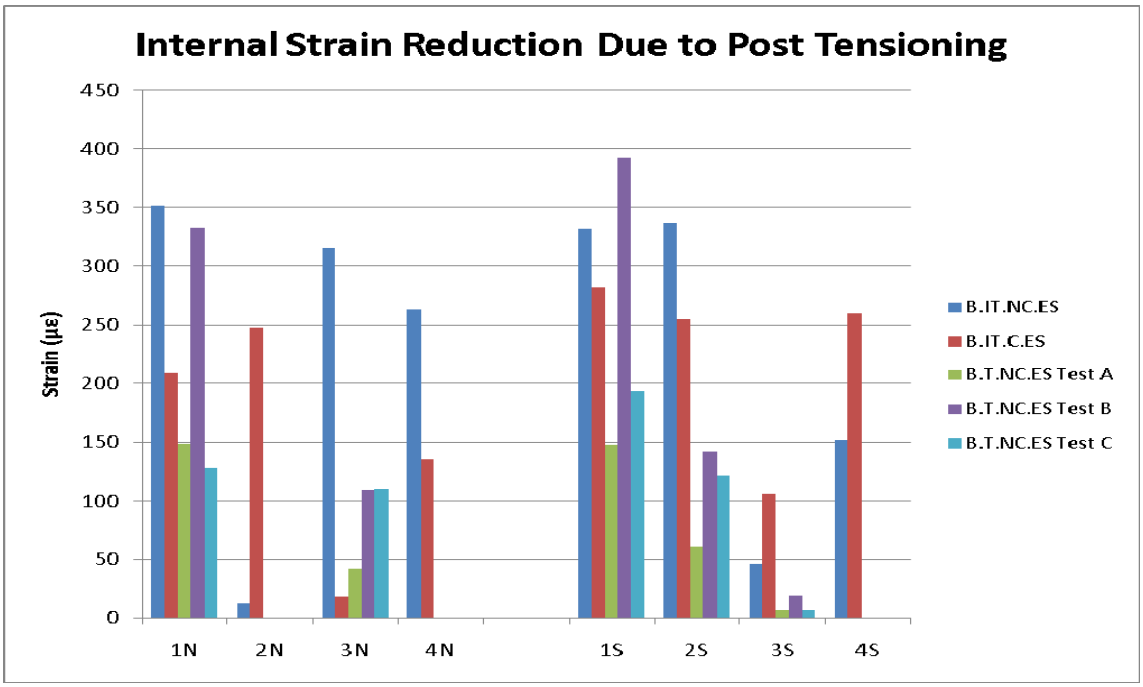


Figure 5.35: Comparison of specimens B.IT.NC.ES, B.IT.C.ES, and B.T.NC.ES integrally cast stirrup absolute strain reduction due to post-tensioning

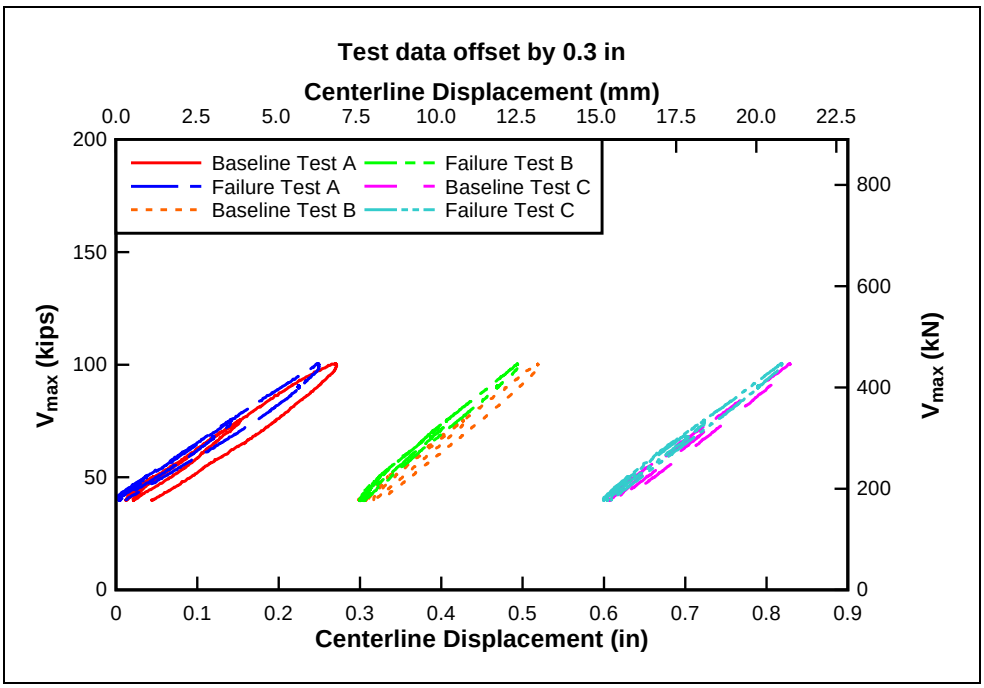


Figure 5.36: B.T.NC.ES shear force versus centerline displacement for tests A, B, and C

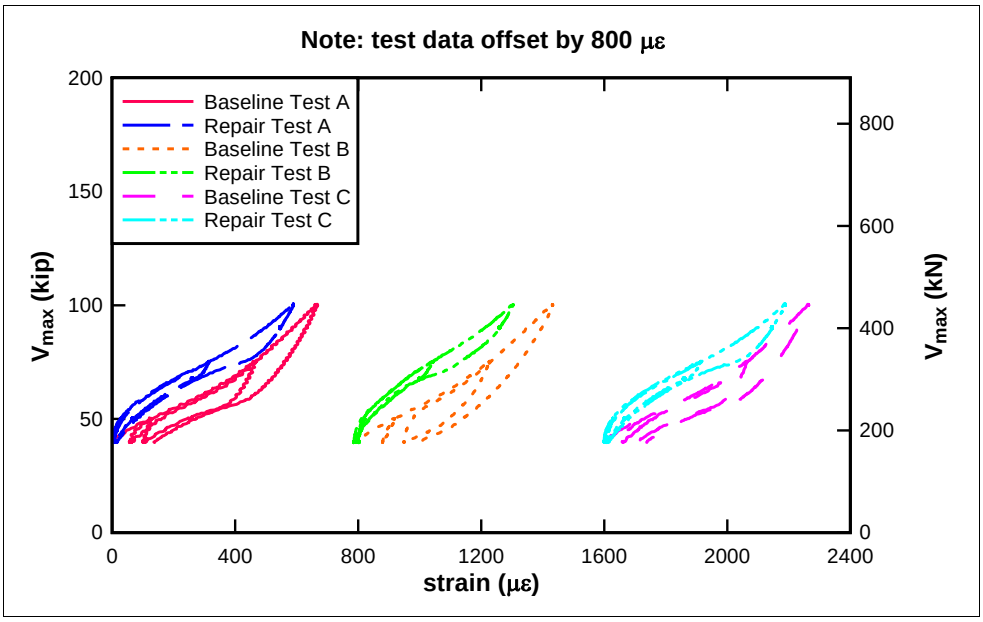


Figure 5.37: B.T.NC.ES shear versus internal stirrup 1N strain range for tests A, B, and C

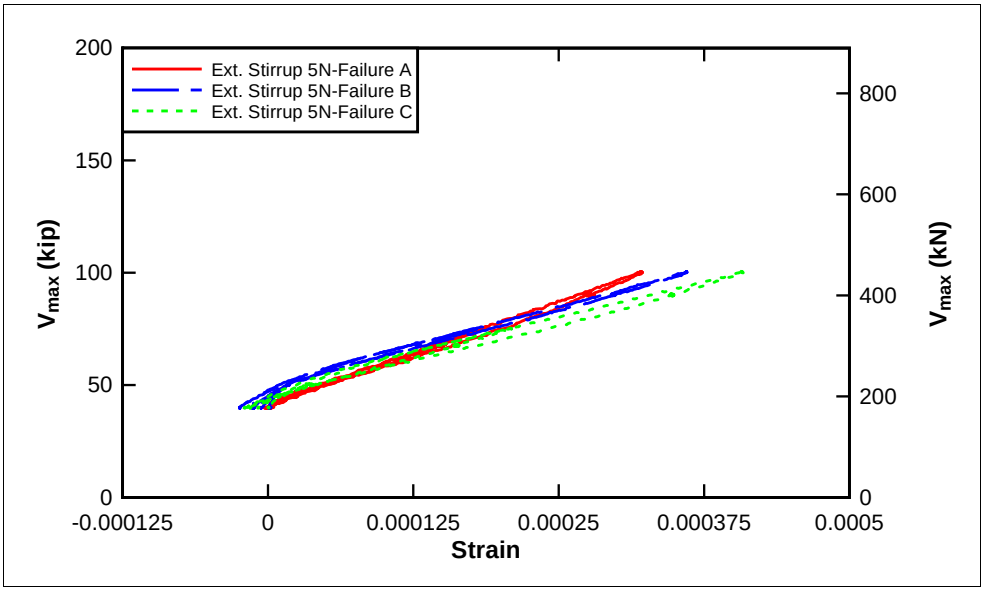


Figure 5.38: B.T.NC.ES shear versus external stirrup 5N strain for tests A, B, and C

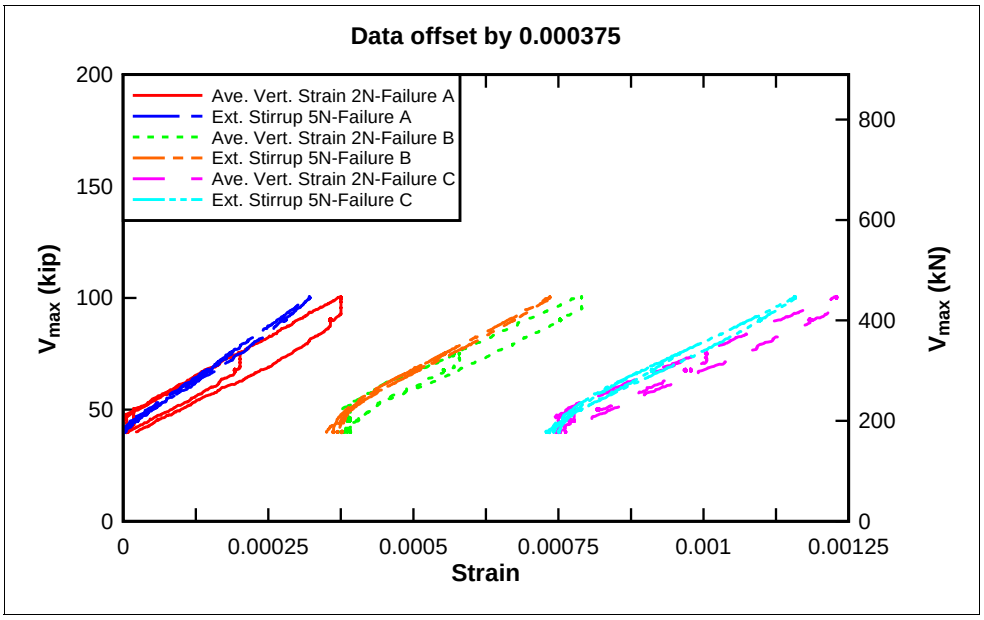


Figure 5.39: Specimen B.T.NC.ES shear versus external stirrup 5N and average vertical strain in panel 2N for tests A, B, and C, offset for clarity

5.2.2.3 Experimental results

Behavior of the external stirrup repair specimens is presented in the following section, with reference to the SPR 350 beams (*Higgins, et al. 2004b*). Shear load – midspan displacement plots for each external stirrup repair specimen – is shown in Figure 5.40. Shear load – diagonal displacement and shear load – average vertical strain plots are provided in Figures 5.41 and 5.42, respectively. Lastly, shear load – typical integrally cast stirrup strains are shown in Figure 5.43. Crack map data for all the repaired beam specimens are shown in Figure 5.44, including crack formation for each load increment. The crack map data is replicated in Figure 5.45 for all the beam specimens with the cracks identified as precrack and repair. Strain compatibility for the external stirrup repair beam B.IT.C.ES is shown in Figure 5.46 as an example of external stirrup strain and average vertical panel strain. Compatibility between the two responses is consistent throughout the loading history, even when strain is beyond the limits of the foil strain gages, denoted by the vertical line on the curve.

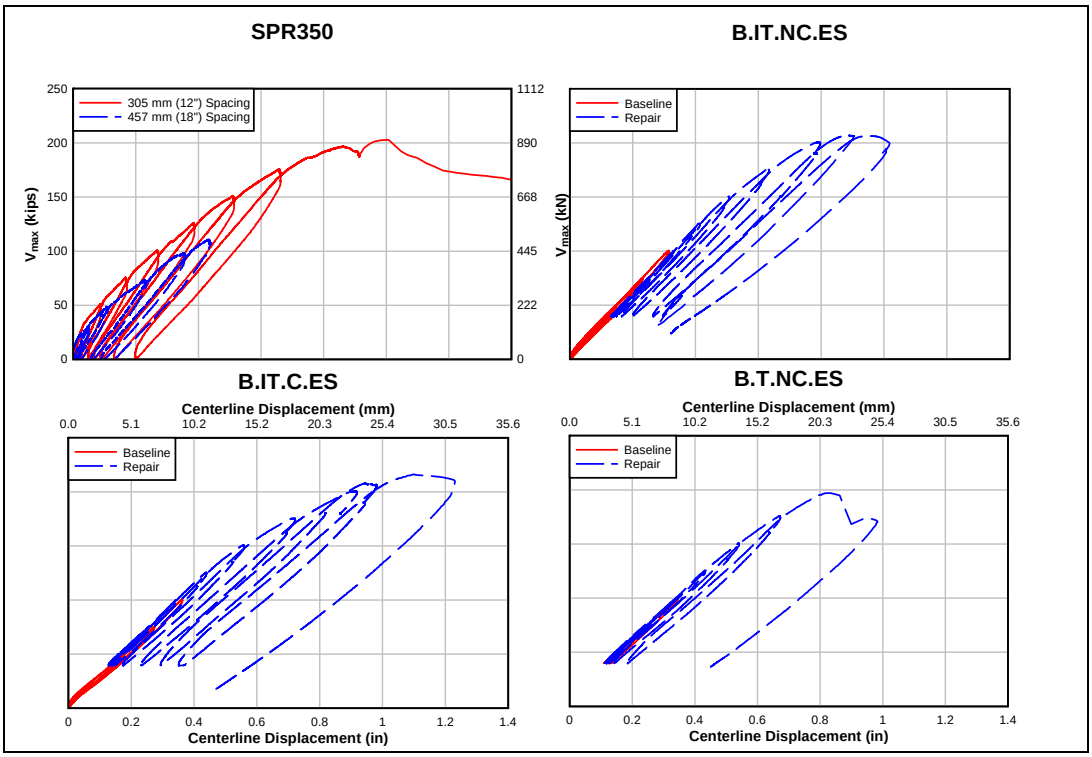


Figure 5.40: External stirrup repair specimens shear force versus centerline displacement

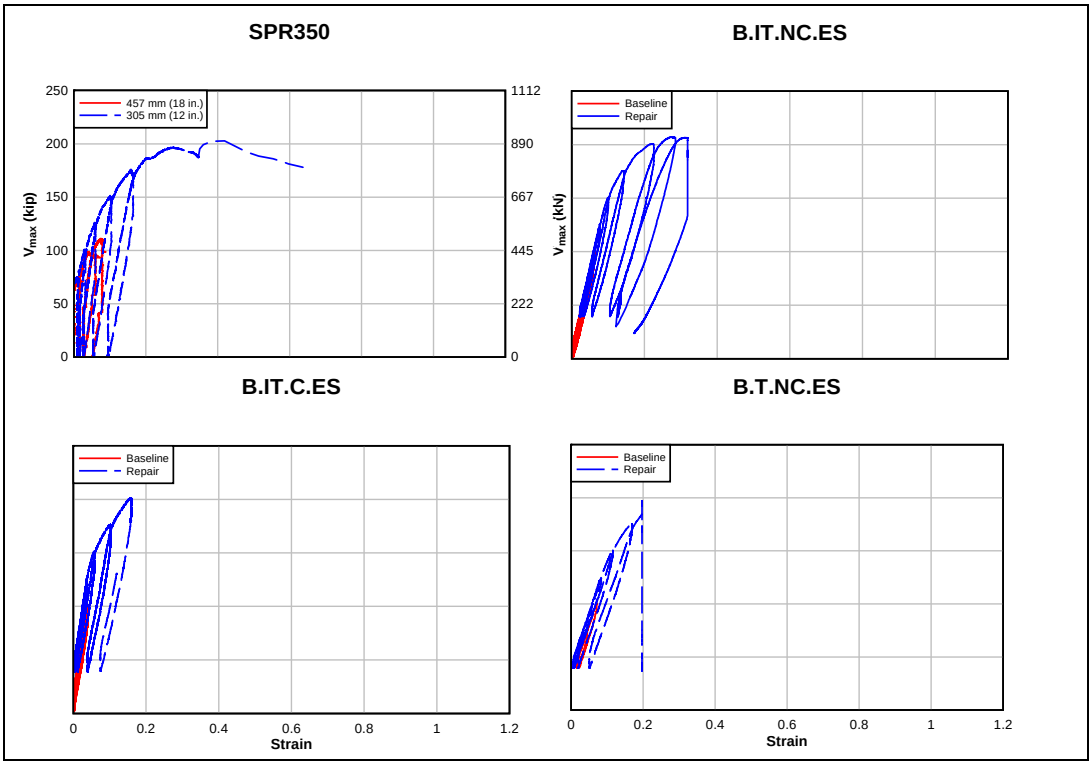


Figure 5.41: External stirrup repair specimens shear force versus diagonal displacement

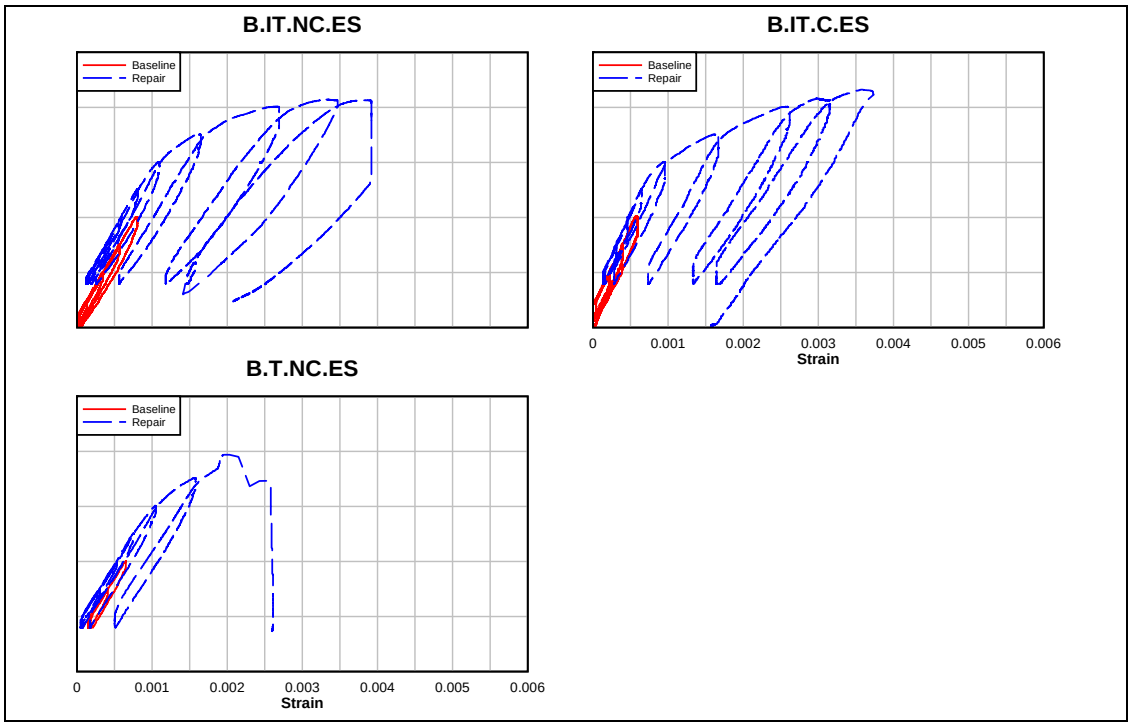


Figure 5.42: External stirrup repair specimens shear force versus average vertical strain

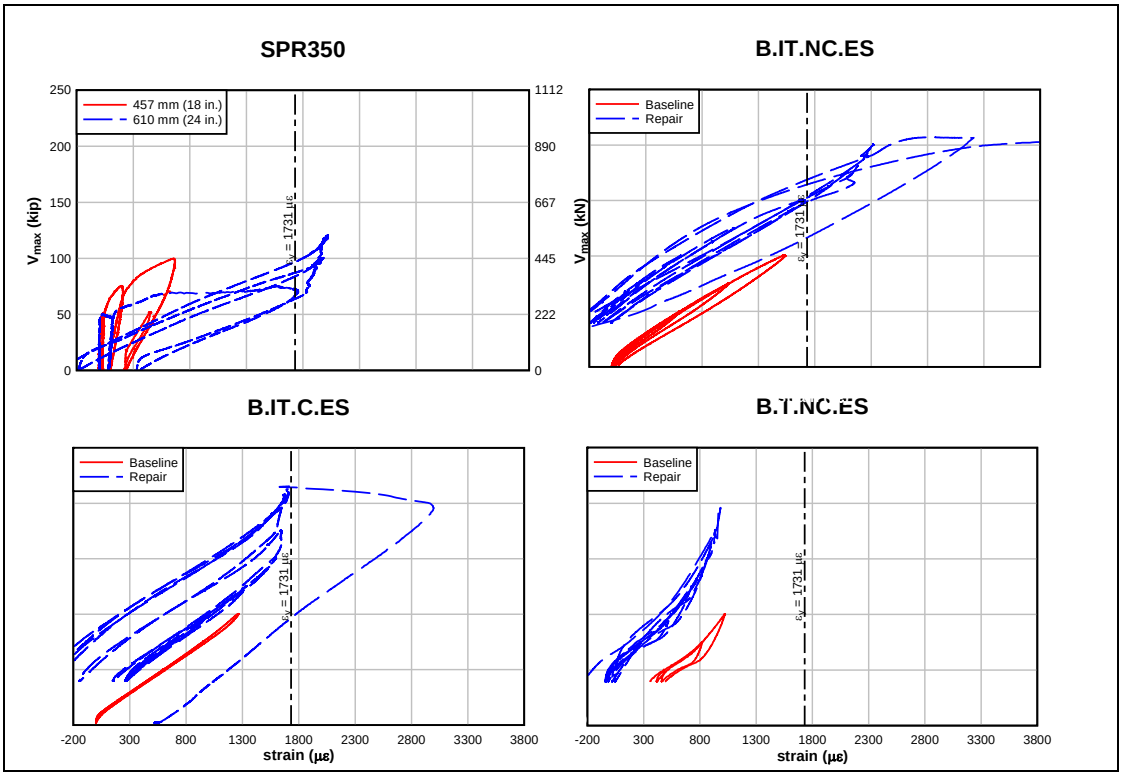


Figure 5.43: External stirrup repair specimens shear force versus typical internal stirrup strain

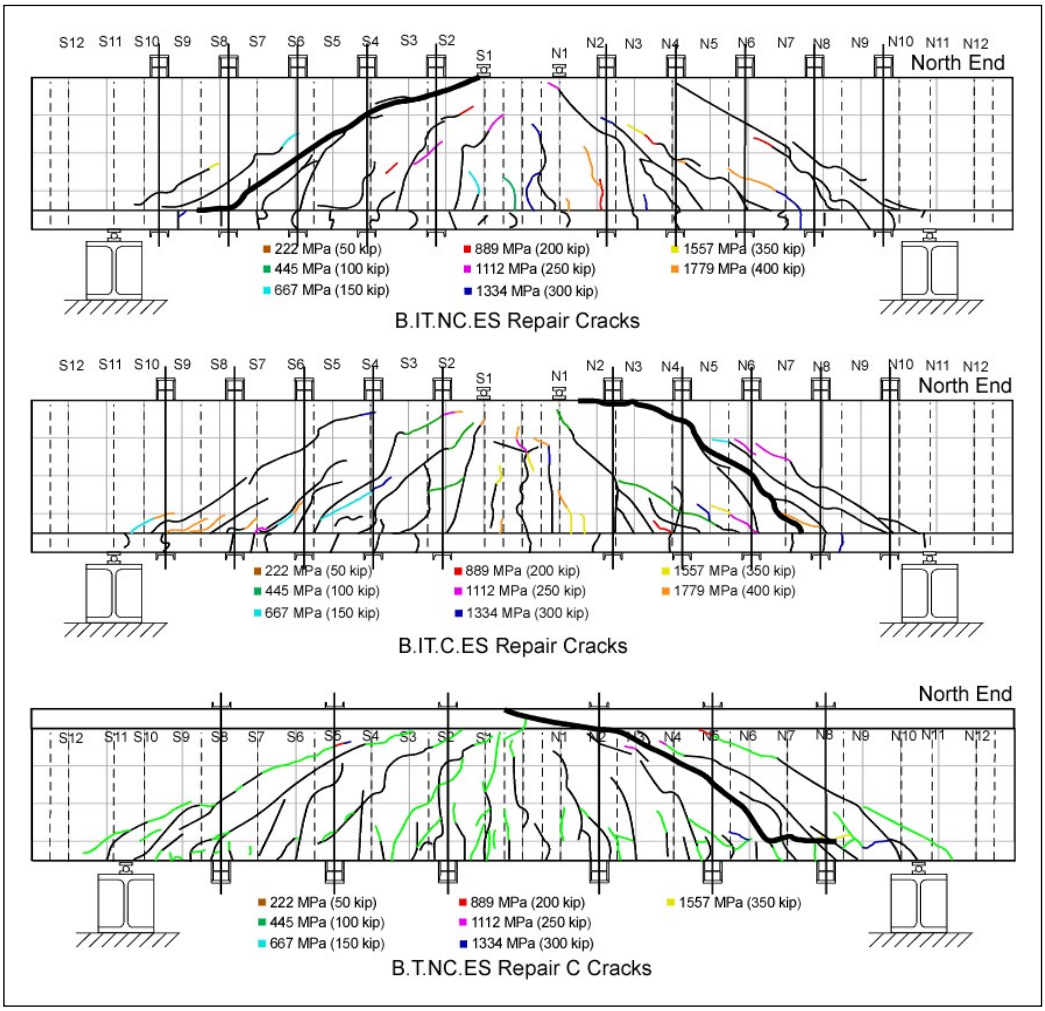


Figure 5.44: External stirrup repair specimens crack maps: individual load steps indicated

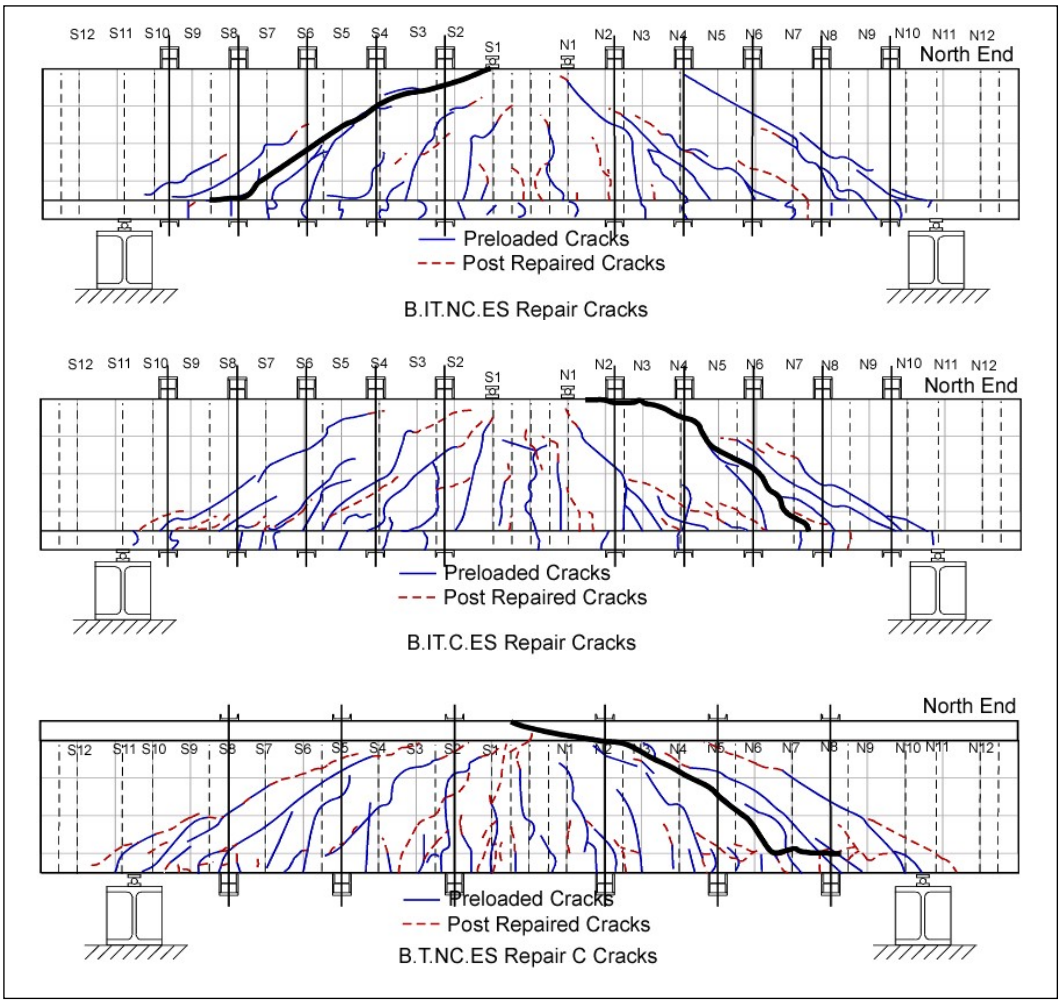


Figure 5.45: External stirrup repair specimens crack maps: precrack versus repair

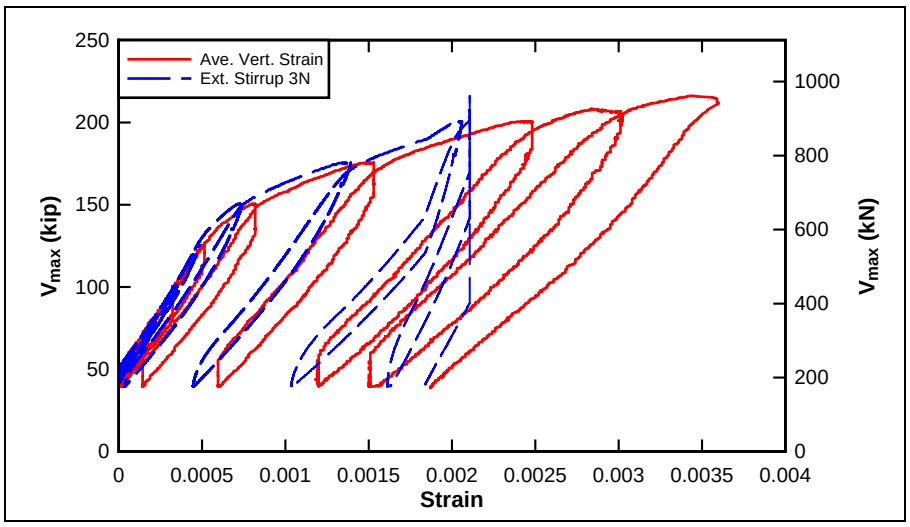


Figure 5.46: Specimen B.IT.C.ES shear force versus external stirrup and average vertical strain

5.2.3 Analytical methods

5.2.3.1 External stirrup repair: comparison with literature

Recall from Chapter 2, there were four primary investigations dealing with external strengthening of traditionally reinforced concrete beams. The first, published by Minh, et al., included one external stirrup repair specimen as one of the several repair techniques (*Minh, et al. 2001*). The specimens had realistic shear span-to-depth ratios for slender beams, but lacked integrally cast stirrups. The lone repair specimen was over-reinforced for shear, resulting in a flexural failure. The investigation provided no clear indication of the efficiency of the repair, as the exact shear contribution was not measured. Still, a plot of the interaction for this specimen is shown in Figure 5.47. Note that the shear span was cast devoid of stirrups; however, stirrups were used outside of the shear span in order to construct the specimens. The stirrups noted in this area were used for constructing the interaction graphs. As the specimen failed in flexure, the interaction curve provides little indication of the effectiveness of the method.

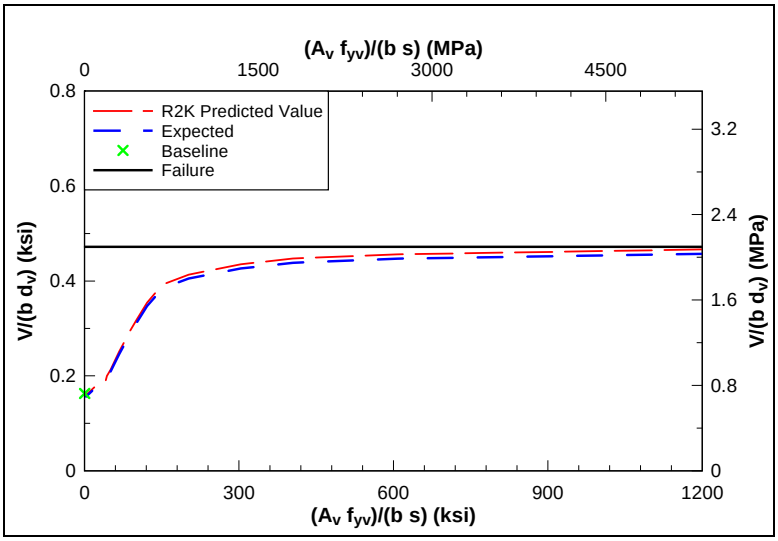


Figure 5.47: Predicted Minh, et al. shear interaction diagram using Response 2000[TM]

The second investigation, by Altin, et al., consisted of 13-half scale T specimens with varying integrally cast steel and externally applied shear reinforcement ratios (*Altin, et al. 2003*). The paper provides sufficient information for reproduction of the beam specimens in R2K; a sample of a typical beam interaction graph is shown in Figure 5.48. However, the specimens in the study were over-reinforced for shear, resulting in flexural failures in each case. Therefore, comparison of the additional shear "pressure" term is not possible in this case.

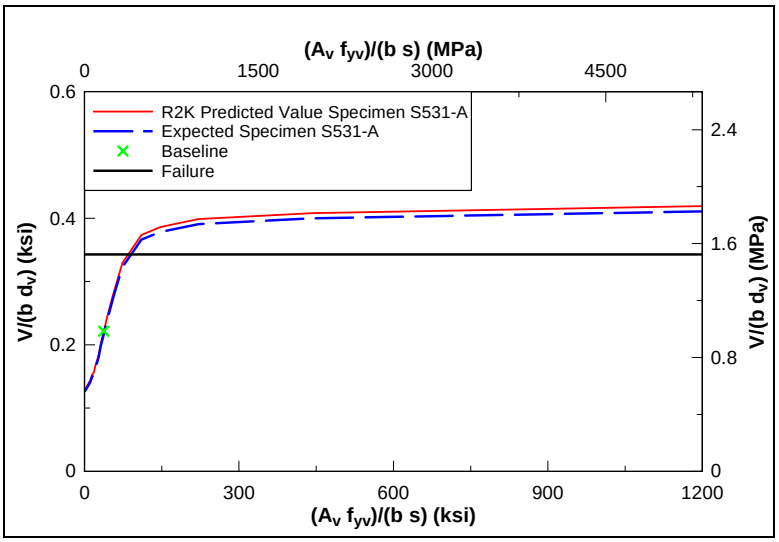


Figure 5.48: Predicted Altin, et al. shear interaction diagram using Response 2000™

The third investigation, by Kim, et al., utilized flexible high strength wire rope units in lieu of mild or high strength steel as an external stirrup repair (*Kim, et al. 2007*). The beam specimens included three shear span-to-depth ratios, covering deep and slender specimens. The orientation of the wire rope units varied from 45 to 90 degrees to the longitudinal axis of the members, as did the pre-stressing force in the wire rope units. The specimens were cast devoid of integrally cast stirrups within the shear span, loaded to failure, repaired with the wire rope units, then tested to failure a second time. Similar to the specimens constructed by Minh, et al., the integrally cast stirrups were provided outside of the shear span. However, they were not identified in the paper, which negates creation of interaction plots, as numerous combinations of steel size and grade would lead to quite different interaction plots, which may or may not be consistent with the final failure load.

The final investigation for the external stirrup repair, by Shamsai, et al., included mild steel external stirrups attached by channel sections and associated hardware (*Shamsai, et al. 2007*). However, the channel sections also included an elastomeric bearing pad and associated steel plate intended to distribute the post-tensioning force of the external stirrups equally throughout the shear span. This is not a feasible option for a full scale specimen and allows significant loss of efficiency upon loading; thus the data for this experimental program is not included here.

No consensus is reached in the literature for estimating the strength gain from external stirrups. Three of the four researchers provided extensions of the existing ACI shear capacity equation by taking the area of steel/wire rope times the yield strength. Two researchers distributed the reinforcement over a ratio of d/s, while the third investigator provided a ratio of h/s. Another point that is not agreed upon by two of the researchers is the influence of post-tensioning on the ultimate capacity of the member. Shamsai, et al. contend that the increase in post-tensioning force had no affect on the resulting shear.

Kim, et al. suggest the contrary. Based on the results of the current experiment, post-tensioning does not change the strain range for the internal stirrups; it simply changes the initial strain value. Although no direct comparison can be made for a specimen with a snug post-tensioning condition at failure, the evidence at the service load provides insight into the advantage of post-tensioning beyond the snug position to ensure efficient use of the external stirrups.

Another issue raised by Shamsai, et al. relates to the reduction in crack widths due to post-tensioning. The authors conclude that post-tensioning is sufficient to close existing cracks in concrete components. The current investigation provided evidence that, while this may be possible for small-scale specimens, crack openings are much more difficult to close under the large self weight of realistic full-sized specimens. Also, static crack width reduction is a function of the stiffness of the reaction sections used.

Another item that was investigated in the current study related to the deformation of the steel reaction section due to weak axis bending. The stiffness ratio of the reaction section to that of the entire repair setup for each of the researchers is shown in Table 5.4. The results indicate that the reaction section is sufficiently stiff with regard to the external stirrup or rod used in each case. However, the stiffness is highly dependent on the 'a' distance from the edge of the specimen to the centroid of the stiffening element. Also, the results for the OSU specimens were taken from the channel section. Data presented indicate that for the service level loading, the stiffer reaction section was superior to the channel section. Similar results would be expected at ultimate load.

Table 5.4: External stirrup reaction section efficiency

Investigator:	OSU	Altin et. al.	Kim et. al.	Mihn et. al.*
$K_{eq} / K_{ext\,stirrup}$	0.9893	0.9700	0.9923	0.9403
*Investigator did not list 'a' distance; 12 mm (0.5 in) assumed				

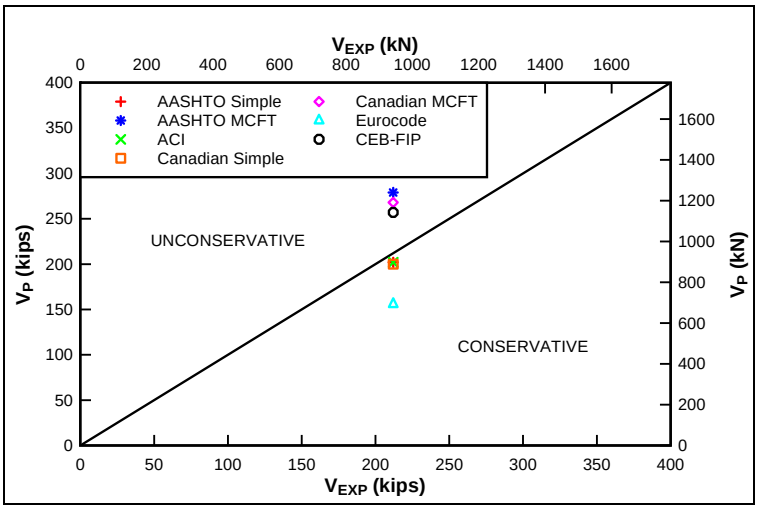
5.2.3.2 External stirrup repair: comparison with national/international codes

Comparison of the experimentally measured shear strength of the external stirrup repair specimens with those predicted by the national codes reviewed previously is shown in Table 5.5. The table provides estimates of the base specimen capacity, differentiated between steel and concrete contribution where applicable. The table also indicates the R2K predicted base specimen capacity. The additional shear contribution follows the appropriate code equations noted in Chapter 2 but utilizes the external stirrup area of steel, yield strength, and spacing. The values are taken over the entire height of the beam, not restricted to the effective depth 'd.' Also of note, the AASHTO and Canadian code provide simple and alternative methods to calculate the capacity of a specimen, based on MCFT from a series of tables of beams meeting the minimum area requirements noted in Chapter 2. The comparisons are shown graphically in Figure 5.49, including international codes.

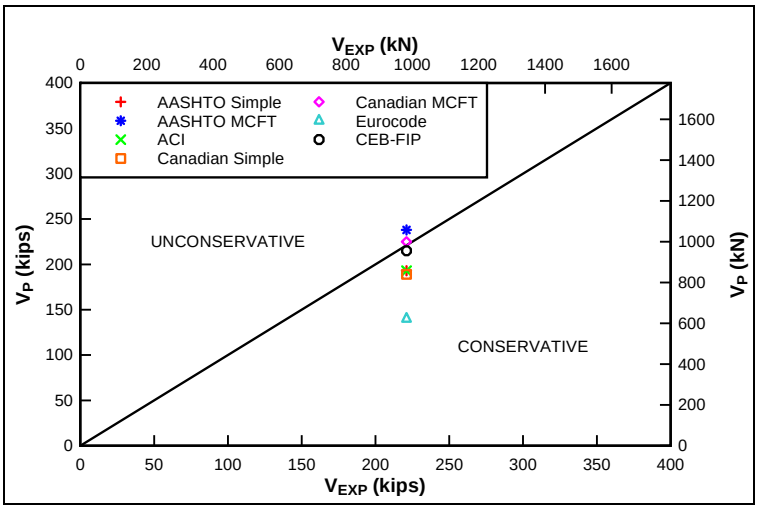
The final external stirrup repair beam exhibited fully developed flexural steel but was tested in the 'T' position. For this beam, the AASHTO requirement for minimum area of steel was not met; therefore the second table within AASHTO was used for the base strength estimate. In the repaired condition, the beam has more than minimum stirrups and the method reasonably predicted strength. The Canadian code, however, indicates that the area of steel provided is above minimum.

Table 5.5: External stirrup strength estimates based on international codes

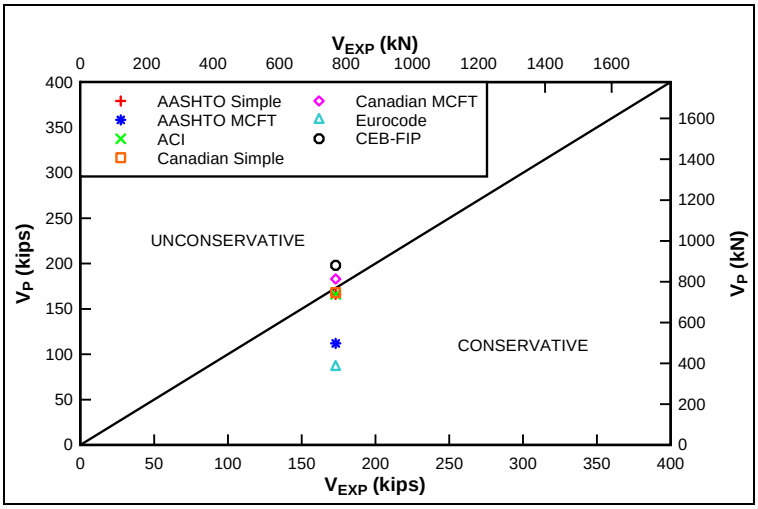
Specimen	Method	Base Capacity						Repaired Capacity		V_{exp}		V_{exp} / V_{total}
		V_c		V_s		V_{base}		V_{total}				
		kN	kip	kN	kip	kN	kip	kN	kip	kN	kip	
B.IT.NC.ES	R2K	-	-	-	-	747	168	-	-	943	212	-
	AASHTO Simple	349	78	223	50	572	129	899	202			1.05
	AASHTO MCFT	-	-	-	-	690	155	988	222			0.96
	ACI 318-05	349	78	223	50	572	129	899	202			1.05
B.IT.C.ES	R2K	-	-	-	-	676	152	-	-	983	221	-
	AASHTO Simple	307	69	223	50	530	119	857	193			1.15
	AASHTO MCFT	-	-	-	-	619	139	886	199			1.11
	ACI 318-05	307	69	223	50	530	119	857	193			1.15
B.T.NC.EIS	R2K	-	-	-	-	672	151	-	-	890	200	-
	AASHTO Simple	375	84	164	37	539	121	739	166			1.21
	AASHTO MCFT	-	-	-	-	396	89	672	181			1.10
	ACI 318-05	375	84	164	37	539	121	739	166			1.21



(a)



(b)



(c)

Figure 5.49: Code Comparison for (a) B.IT.NC.ES, (b) B.IT.C.ES, & (c) B.T.NC.ES

5.2.3.3 External stirrup repair: comparison with R2K

Comparison of the external stirrup repair with R2K was used in conjunction with the previously noted interaction plots. The difference in shear pressure from the R2K calculated unrepaired specimen capacity to the experimental failure shear was recorded for each specimen. The corresponding shear pressure term taken from the measured material properties of the external stirrup repair was then compared to the experimental results. Table 5.6 indicates the efficiency of each repair beam with respect to an equivalent internal stirrup repair by a ratio of experimental to calculated delta shear pressure.

Table 5.6: R2K shear pressure comparison for different repair methods

R2K Prediction	
Specimen:	$\Delta x_{EXP} / \Delta x_P$
B.IT.NC.ES	0.84
B.IT.C.ES	-
B.T.NC.ES	1.21
B.IT.NC.IS	1.34
B.IT.C.IS	-
B.T.NC.IS	1.01
B.IT.NC.CF	0.85
B.IT.NC.NS	0.73

For a value of 1.0, the repair was equivalent to adding integrally cast stirrups to the specimen. For a value greater than 1.0, the experimental repair performed better than the experimental data suggested. The converse, for a value less than 1.0, implies the repair was not fully effective. A comparison of the cutoff specimen is not provided, as it failed due to anchorage within the shear span. The external stirrup repair exhibited an efficiency rating of 0.84 and 1.21 for the fully developed IT and T specimens, respectively. This implies the IT repair performed below expectations, while the T beam performed better than expected.

5.2.3.4 External stirrup repair: comparison with VecTor2

All specimens in the current study were modeled with the previously mentioned VecTor2 nonlinear finite element package. A few notes about the location of elements and idealized boundary conditions are warranted prior to explanation of results. First, the analysis package provides an upper limit on the number of elements in a particular model. Therefore, the use of rectangular, quadrilateral, or triangular elements as well as the smallest mesh size resulted in the maximum number of elements the program would permit. Therefore a mesh size for the concrete elements ranging from 80 mm (3.14 in.) to 120 mm (4.72 in.) was used. Next, the program was run in SI units, with locations

rounded to the nearest 10 mm (0.39 in.), which corresponds to a maximum error of + 5 mm (+ 0.20 in.).

The truss elements representing the flexural steel reinforcing bars were extended to the limits of the specimen longitudinally, when in reality concrete cover was provided in the experimental beams. Also, the location of the repair media on some beam and/or bent cap specimens exceeded the minimum mesh size required by the program. Furthermore, the presence of the repair media resulted in concentrated mesh regions near the repair media, so that the limit on the maximum number of elements was exceeded. As such, the integrally cast stirrup and/or repair media were moved laterally a nominal distance to permit the mesh size of interest.

Support conditions were modeled as one roller and one pin, in order to provide the required number of known degrees of freedom for the models to run. Recall that the boundary conditions for the beam specimen were rollers on each end, and the bent cap was treated as fixed at one end with a roller at the adjacent end. However, the bent cap specimen at the fixed end did not provide ultimate fixity, as there was limited rotation between the steel plates. Still, the plates provided a larger degree of fixity when compared to the roller section. Senturk indicated that modeling the bent cap specimens in VecTor2 with a pin/roller combination provided a good indicator of cracking with the laboratory specimen; thus this assumption was used for the current investigation (*Senturk 2008*).

The external stirrup specimens were modeled as unbonded reinforcement within VecTor2. The meshing schemes for the external stirrups are shown in Figure 5.50. The load-deflection curves for the external stirrup beams are shown in Figure 5.51, whereas the capacity estimations are shown in Table 5.7. The load deflection curves approximated the experimental data quite well. The fully developed IT beam exhibited the uncracked response of the VecTor2 model, whereas the remaining plots accounted for the baseline loading.

The table comparisons indicate VecTor2 consistently underestimated the strength of each specimen. Therefore, modeling of unbonded steel within VecTor2 is generally acceptable and conservative. It is worth noting no reduction was taken into account within the model to account for weak axis bending of the supporting steel sections that anchor the supplemental external stirrups.

Table 5.7: External stirrup VecTor2 comparison

Specimen:	V_p (VecTor2)		V_{exp}		V_{exp} / Vp
	kN	kip	kN	kip	
B.IT.NC.ES	878	197	943	212	1.07
B.IT.C.ES	832	187	983	221	1.18
B.T.NC.ES	810	182	771	173	1.10

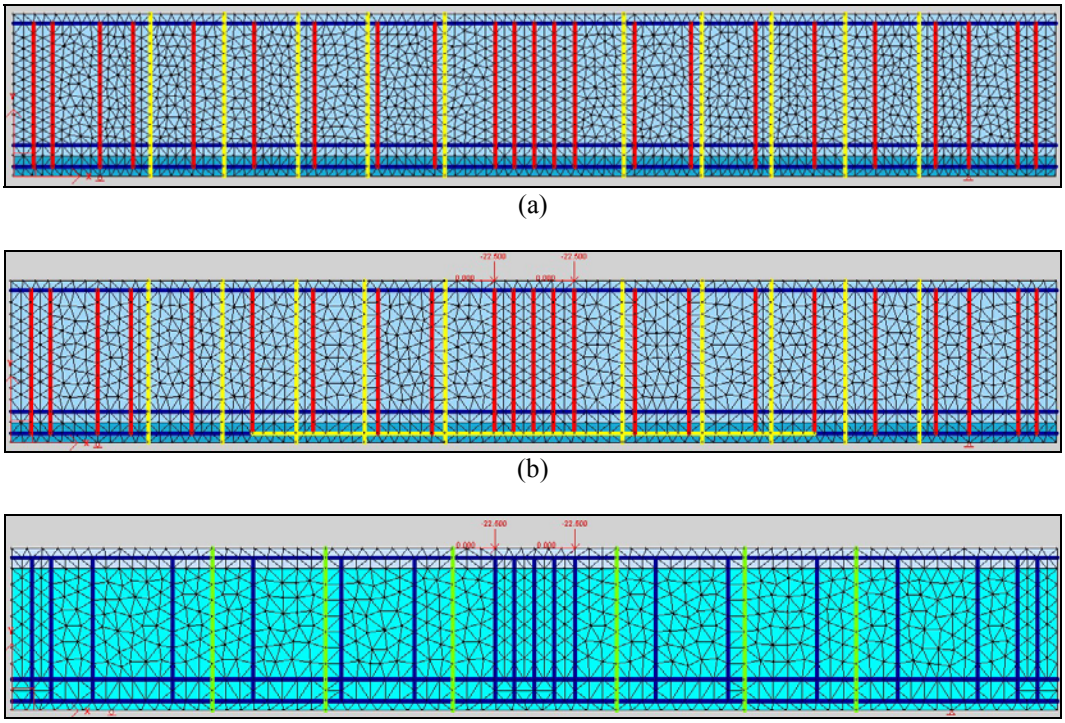
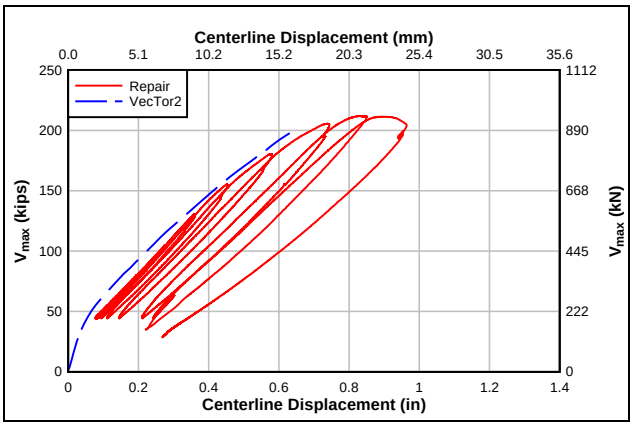
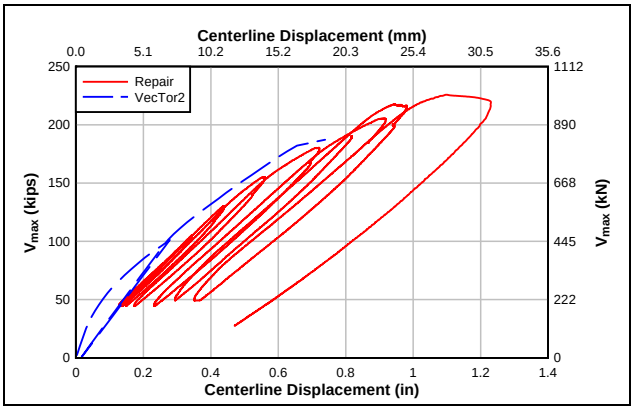


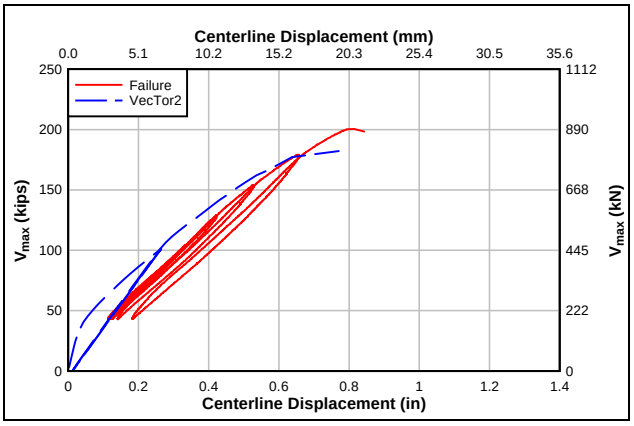
Figure 5.50: VecTor2 meshing schemes for (a) B.IT.NC.ES, (b) B.IT.C.ES, and (c) B.T.NC.ES



(a)



(b)



(c)

Figure 5.51: VecTor2 external stirrup load deflection estimates for (a) B.IT.NC.ES, (b) B.IT.C.ES, (c) B.T.NC.ES

5.2.4 Discussion and design recommendations

The design recommendations for the external stirrup repair are based on laboratory tests, previous work, and comparisons with the various international codes. For service level performance, the following design recommendations are provided:

- Selection of the appropriate steel reaction section has a direct effect on strain compatibility between the specimen and the external stirrups.

- Post-tensioning of external stirrups provides better strain compatibility over the service level loading.

- The long unbonded lengths of the external stirrups will likely result in larger diagonal crack motions than other repair methods (even with the post-tensioning effects). This point should be articulated to field inspectors of structures repaired using this method.

For strength design with supplemental external stirrups, the following design recommendations are proposed.

- The amount of post-tensioning should be chosen based on a combination of the yield strength of the external stirrups and the expected dead load strain in the internal stirrups (estimated as a fraction yield stress in the stirrup from of the service level applied shear on the section to the shear strength of the section). A projected stress range to go from the initial post-tensioning stress to yield for the external stirrups should match that available from the internal integral stirrups so that both achieve yield at failure.

- From evidence found in the literature, a higher post-tensioned force results in higher specimen capacity. The above suggested post-tensioning level, combined with stiff supporting steel sections suggested above should be adequate to achieve design strengths.

- From the available literature, the predicted shear strengths of each external stirrup specimen were quite variable. The current investigation provided a wide range of strength estimates based on either a simple 45-degree truss analogy or an approach following MCFT. AASHTO MCFT is proposed as the analysis method.

- The effectiveness of the repair is dependent on the reaction section used; however, if the external stirrup is positioned close to the web, this effect can be minimized with a typical external stirrup efficiency reduction due to weak axis bending of supporting steel sections on the order of 0.95 to 0.98.

5.3 INTERNAL SUPPLEMENTAL STIRRUP REPAIR FOR GIRDERS

5.3.1 Material and application details

Materials for the supplemental internal stirrup repair were chosen with the assistance of a contractor who successfully installed the repair method on several Oregon bridges. This approach was beneficial because it replicated the repair method both in terms of materials used and installation technique. The primary obstacle regarding the use of this method was the insertion point of the steel – either from the deck down or from the bottom of the girder up. The former method has the drawback of restricting traffic on a bridge, which may be prohibitive on a heavily traveled truck route; but it has the advantage of epoxy flowing into the hole with the assistance of gravity. The latter method is more attractive in terms of lane closures; but it may require temporary supports below the bridge to support the workers and equipment. In addition, the problem of injecting a crack against gravity poses an installation issue.

The solution proposed by the contractor was to use a high strength steel reinforcing bar with a void through the center such that epoxy could be injected through the center hole, eventually exiting through the void space between the bar and the concrete. Thus, the steel initially used for the internal stirrup repair was high strength hollow steel rod meeting the height and deformation requirements of ASTM 615/615M-05a (*ASTM International 2005*) with an outer diameter of 25 mm (1 in.) and 484 mm^2 (0.75 $in.^2$) cross sectional area. The typical section for the IT internal stirrup repair is shown in Figure 5.52.

After subsequent use in the two IT specimens, it was apparent that the large diameter, high strength bars would not be suitable for the T beam repair (i.e., possibly forcing a flexural failure). Therefore, traditional ASTM A615 deformed grade 420 (60 ksi) size #19 (#6) steel rebar was used for the T beam repair. Elevation views of the repair schemes for beams B.IT.NC.IS, B.IT.C.EI, and B.T.NC.IS are shown in Figure 5.53 through Figure 5.55, respectively.

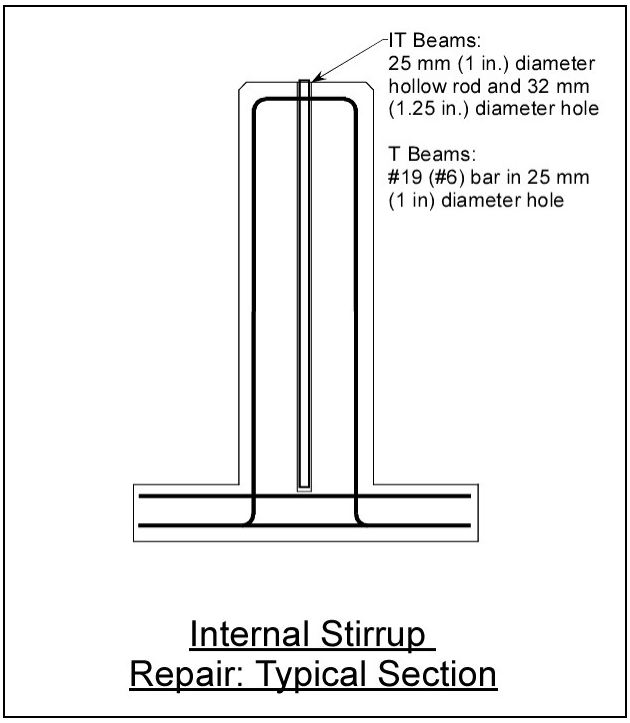


Figure 5.52: Internal stirrup typical section

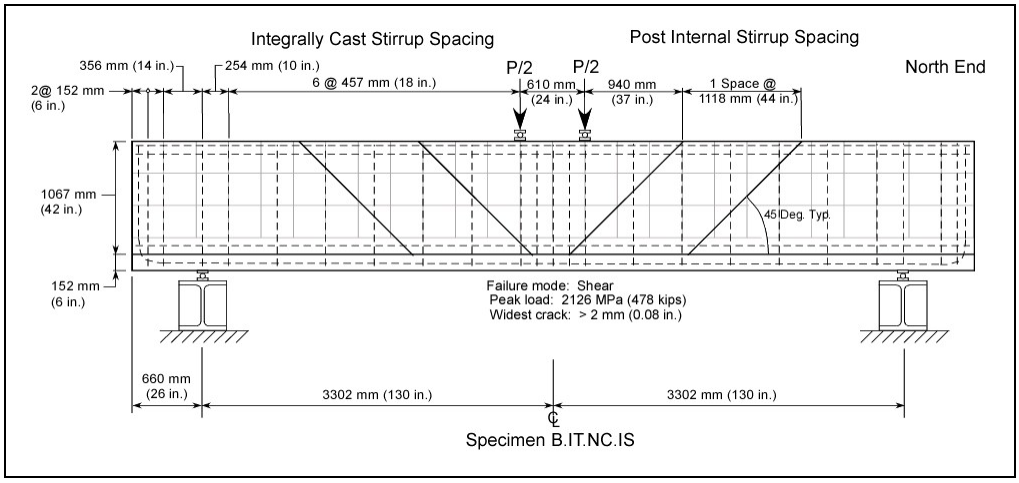


Figure 5.53: Specimen B.IT.NC.IS repair

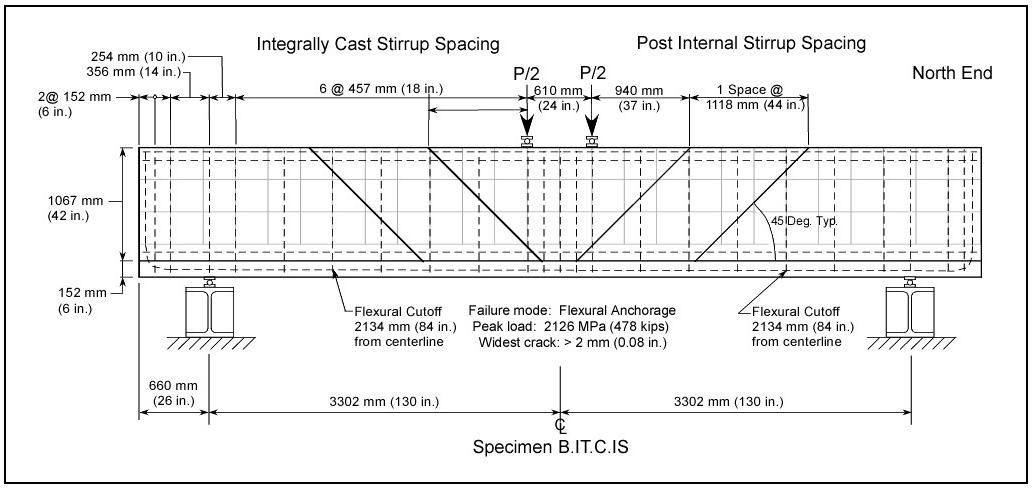


Figure 5.54: Specimen B.IT.C.IS repair

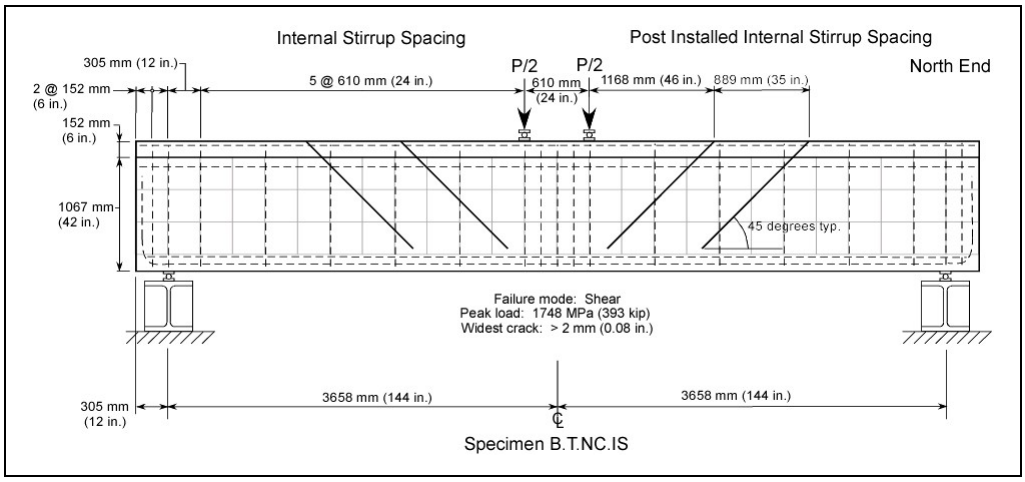


Figure 5.55: Specimen B.T.NC.IS repair

The high strength and mild steel bars were subjected to uniaxial tensile tests as well as pullout tests with the same installation epoxy to determine the pullout strength of the bars for different embedment lengths. Tension tests on the hollow bar and grade 420 (60 ksi) mild steel specimens were performed, and the results are shown in Table 5.8.

Table 5.8: Internal stirrup reinforcing steel properties

Specimen	Yield Strength		Ultimate Strength		% Strain at Failure
	Mpa	ksi	Mpa	ksi	
B.IT.NC.IS	710	103	924	134	19.3
B.IT.C.IS					
B.T.NC.IS	489	70.9	814	118	19.6

The pull-out tests were performed to indicate the embedment length required to reach yield. The process entailed coring a vertical hole within the beam, placing a premeasured amount of epoxy within the hole, placing the reinforcing bar in the hole, and anchoring it in a vertical orientation. The epoxy was allowed to cure for one week. After curing, a center hole actuator, load cell, and reaction plates were mounted concentrically with the bar. Then a mechanical splice was placed around the bar and individual screws along the splice were torqued to the splice manufacturer's specifications. The test setup is shown in Figure 5.56. Three embedment lengths were used, the largest representing the distance from a 45-degree diagonal crack to the limit of the cross section (762 mm (30 in.)). The remaining two embedment lengths – 254 mm (10 in.) and 508 mm (20 in.) – were chosen to represent typical bond lengths available at different positions along a diagonal crack.

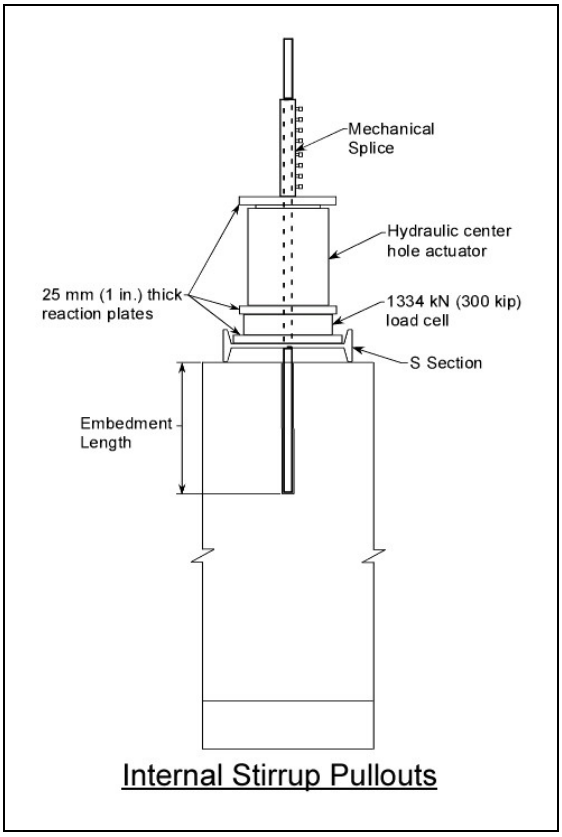


Figure 5.56: Internal stirrup pullout test setup

Results from the pullout tests provided anchorage performance estimates for the steel-epoxy-concrete system. Bar stress versus relative displacement for each of the three embedment lengths are shown Figures 5.57 and 5.58 for the high strength bar and 413 MPa (60 ksi) bar, respectively.

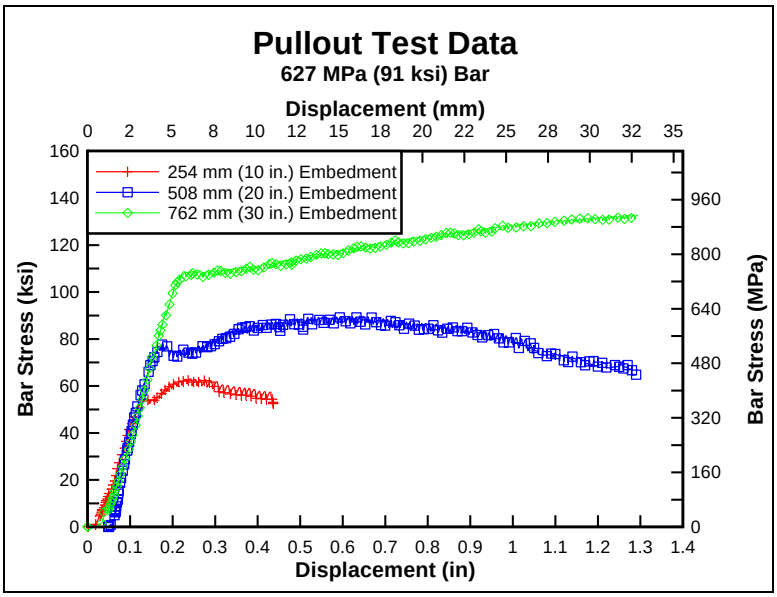


Figure 5.57: Internal stirrup 627 MPa (91 ksi): bar stress versus displacement

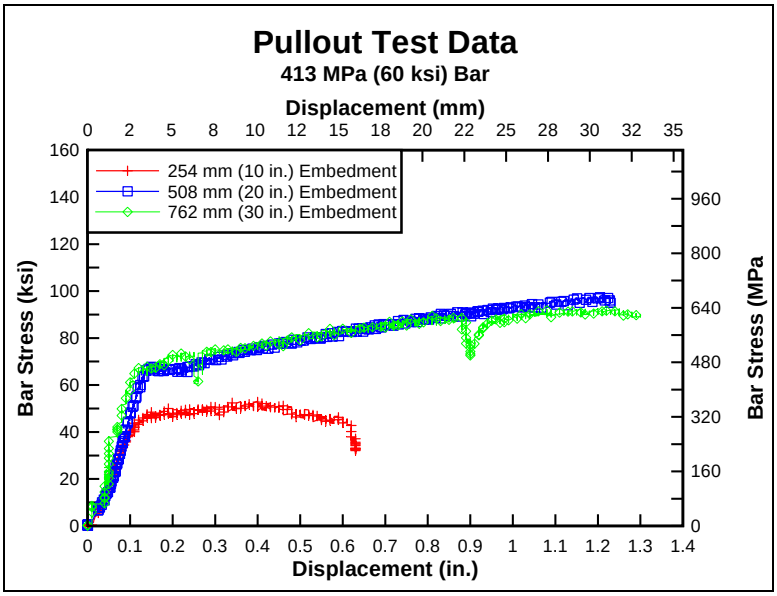


Figure 5.58: Internal stirrup 413 MPa (60 ksi): bar stress versus displacement

The shallowest embedment for the high strength rods resulted in a maximum bar stress of 374 MPa (54 ksi) prior to first slip. Slip continued until a shallow cone failure occurred prior to yield strength of the bar. The 508 mm (20 in.) embedment depth resulted in a bar stress of 528 MPa (77 ksi) prior to first slip, again failing to reach the yield strength of the internal stirrup. The final 762 mm (30 in.) embedment length achieved a bar stress of 737 MPa (107 ksi) and resulted in eventual fracture of the hollow bar after strain hardening.

For the lower strength ASTM A615 grade 60 bars, the bar diameter and yield stress were reduced; thus the 508 mm (20 in.) and 762 mm (30 in.) bars both achieved yield and strain hardening, although they were very ductile, and the test was halted prior to achieving ultimate strength. The shallowest embedment did not reach yield, with a maximum bar stress of 268 MPa (39 ksi) prior to first slip.

The results of the pull-out tests are presented in Table 5.9, although it is noted that the state of stress produced by the pull-out specimens does not represent the true state of stress within an actual girder, nor does it account for any possible beneficial dowel action that may help anchor the bars across a diagonal crack.

Table 5.9: Internal stirrup pullout tests data

	Specimen embedment depth	Max bar stress		Yield Stress	
		MPa	ksi	MPa	ksi
High strength bar	254 mm (10 in.)	434	63	828	120
	508 mm (20 in.)	618	90		
	762 mm (30 in.)	743	108		
Mild steel bar	254 mm (10 in.)	366	53	489	70.9
	508 mm (20 in.)	765	111		
	762 mm (30 in.)	638	93		

The installation process for internal stirrup repair is outlined below, with reference to Figure 5.59.

- Identify internal stirrup locations along the span of the beam.
- Locate flexural and deck reinforcing within the specimen using a rebar detector where holes must be cored.
- Mark the location of the bars and orient coring machine to avoid bars.
- Drill the holes with either a water-required concrete coring machine or a dry system with vacuum attachment.
- For traditional reinforcement:
    - Pour epoxy into hole such that it will fill the void space around the bar and concrete once the bar is inserted.
    - Insert reinforcing bar and add additional epoxy as needed until seepage is minimized.
- For center hole reinforcement:
    - Place reinforcement into hole.

- Pump epoxy through the center of the reinforcement until it fills the void space surrounding the top of the bar.
- Continue to add additional epoxy as needed until seepage has been minimized.



Figure 5.59: Internal stirrup installation

5.3.2 Experimental results

Behavior of the internal stirrup repair specimens is presented in the following section, with reference to the SPR 350 beams (*Higgins, et al. 2004b*). Shear load versus midspan displacement plots for each internal stirrup repair specimen are presented in Figure 5.60. Shear load versus diagonal displacement plots and shear load versus average vertical strain plots are shown in Figures 5.61 and 5.62, respectively. Lastly, shear load versus cast-in-place stirrup strains are shown in Figure 5.63. Crack map data for all the repaired beam specimens are shown in Figure 5.64, including crack formation for each load increment. The crack map data is replicated in Figure 5.65 for all the beam specimens with the cracks identified as precrack and repair.

A review of the integrally cast and supplemental stirrup strain data is presented in Figure 5.66 as an example for specimen B.IT. NC.IS. The integrally cast stirrups continue a similar slope from the service loading, with an increased slope at the higher load steps. This occurs as the strain in the supplemental stirrups begins to increase in both bars, which indicates the integrally cast stirrups are taking more load as the beam approaches failure.

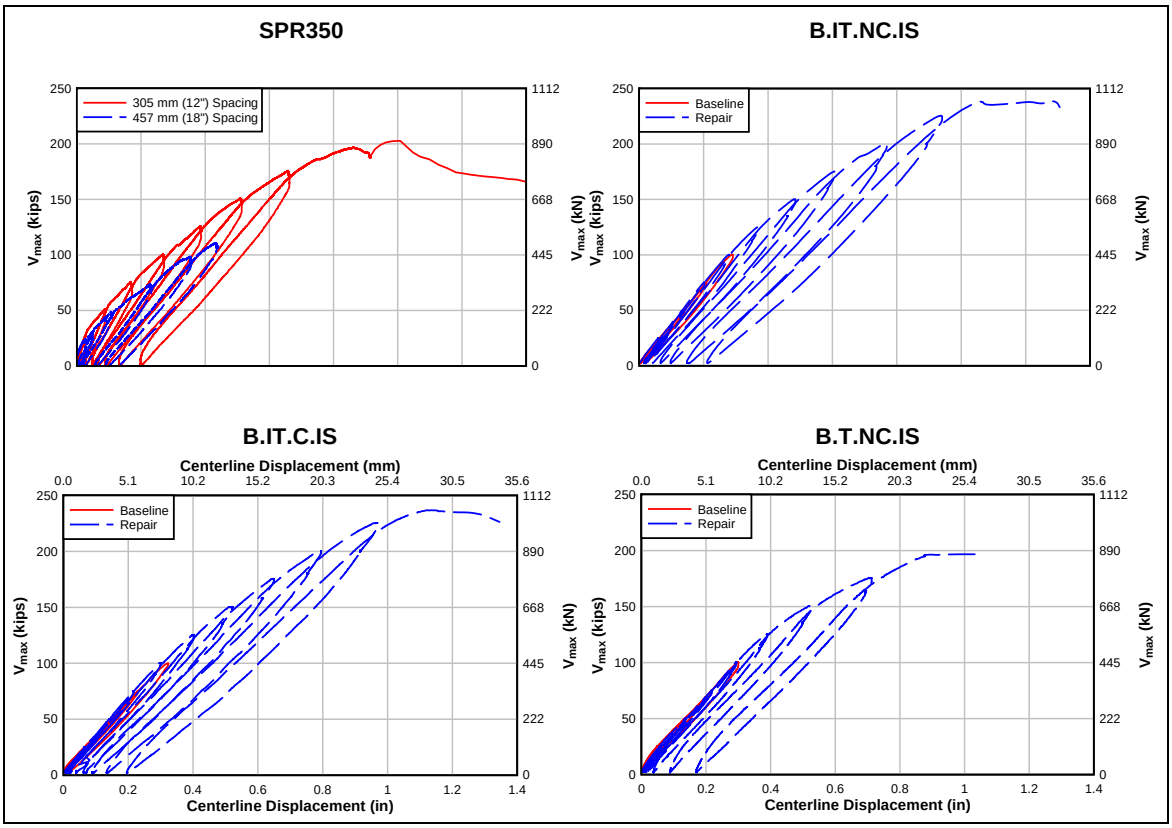


Figure 5.60: Internal stirrup repair specimens shear force versus centerline displacement

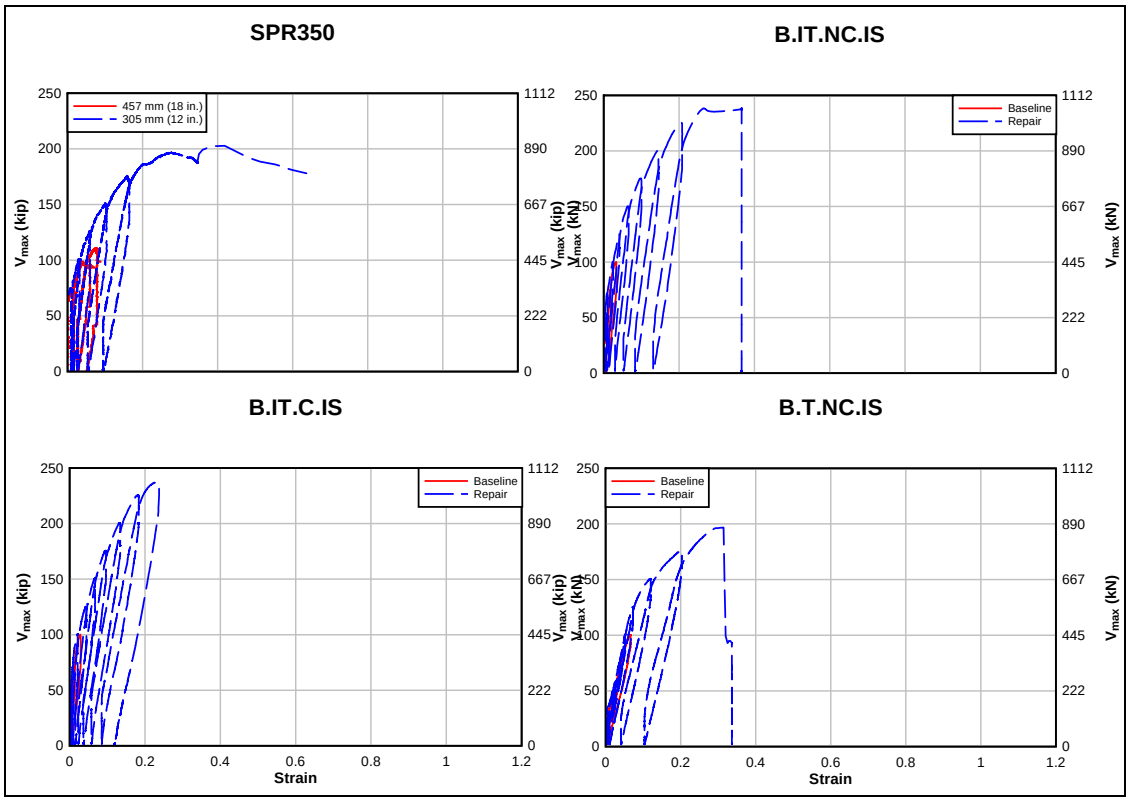


Figure 5.61: Internal stirrup repair specimens shear force versus diagonal displacement

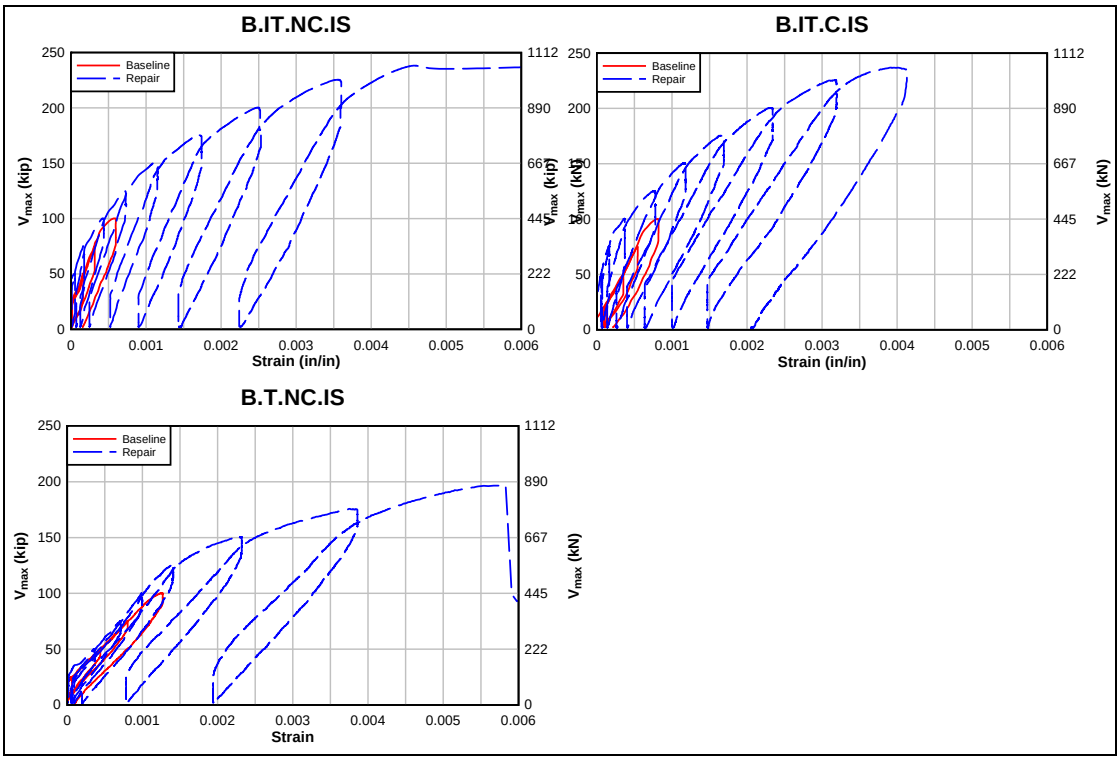


Figure 5.62: Internal stirrup repair specimens shear force versus average vertical strain

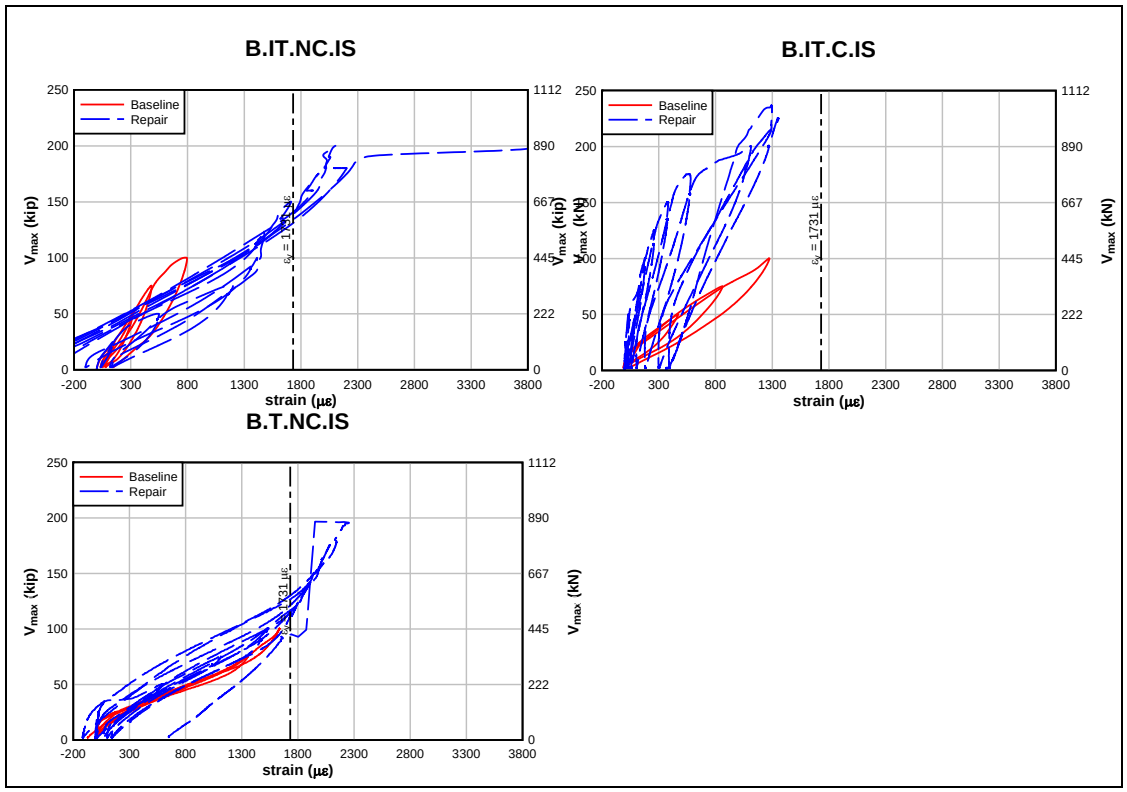


Figure 5.63: Internal stirrup repair specimens shear force versus typical internal stirrup strain

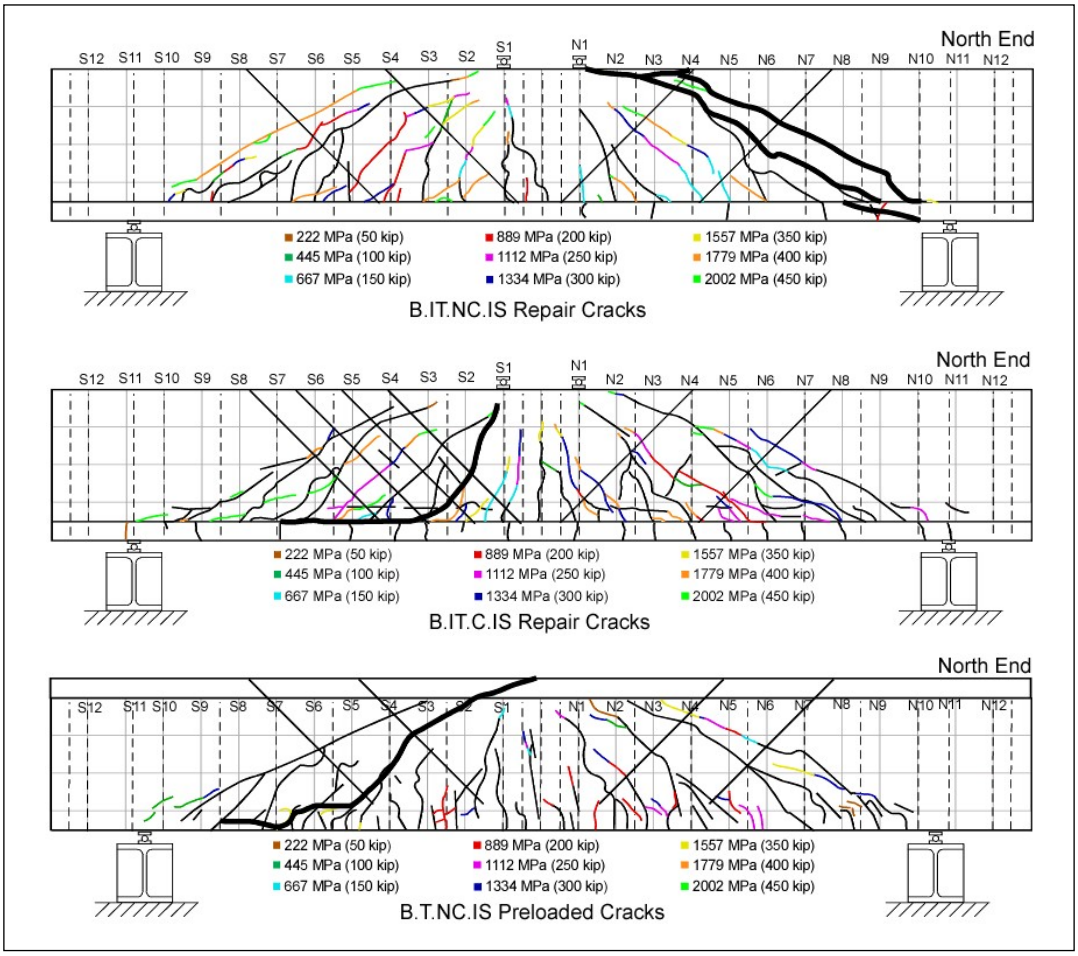


Figure 5.64: Internal supplemental stirrup repair specimens crack maps: individual load steps indicated

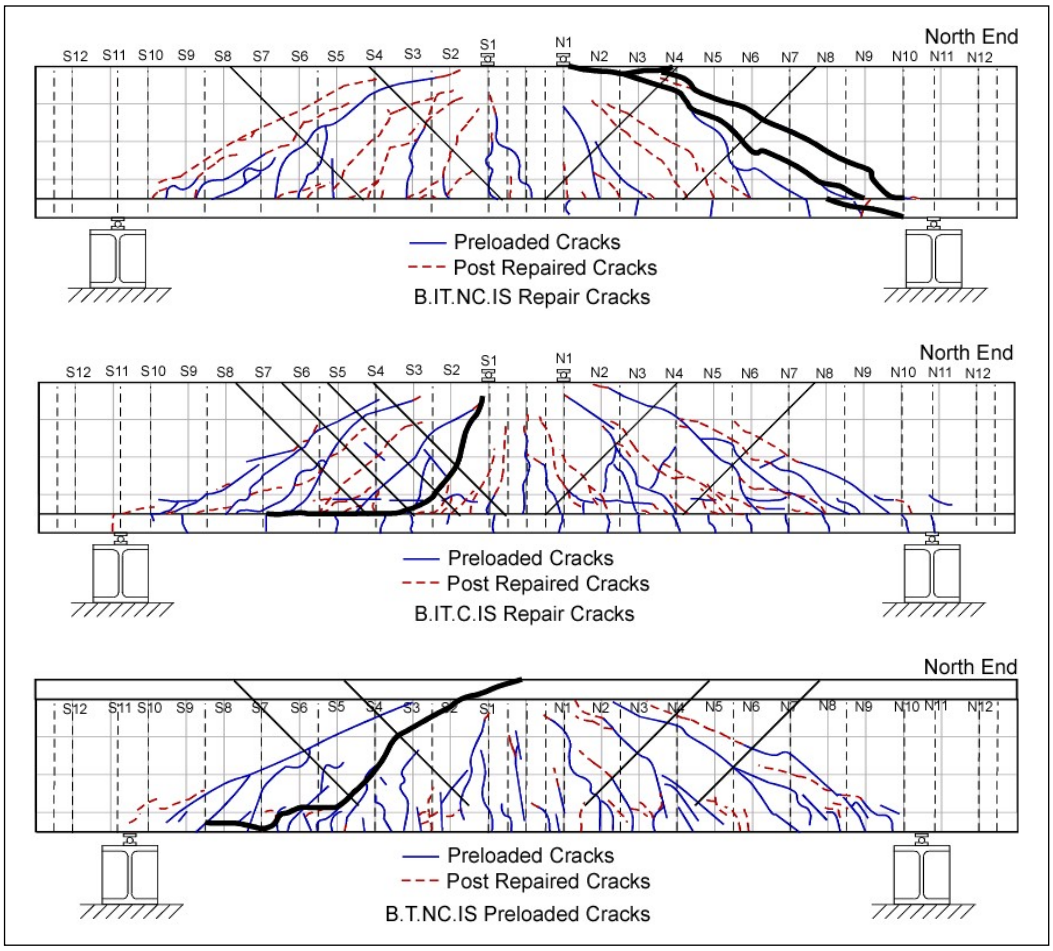


Figure 5.65: Internal supplemental stirrup repair specimens crack maps: precrack versus repair

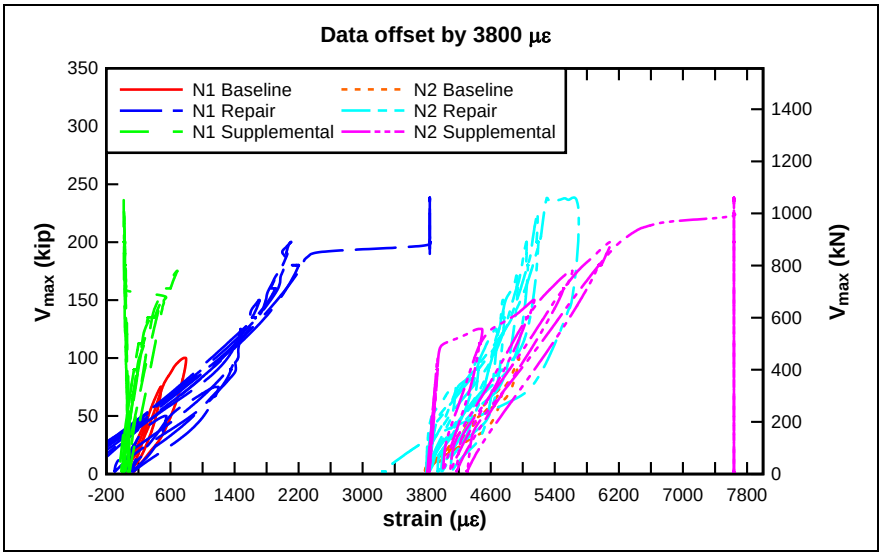
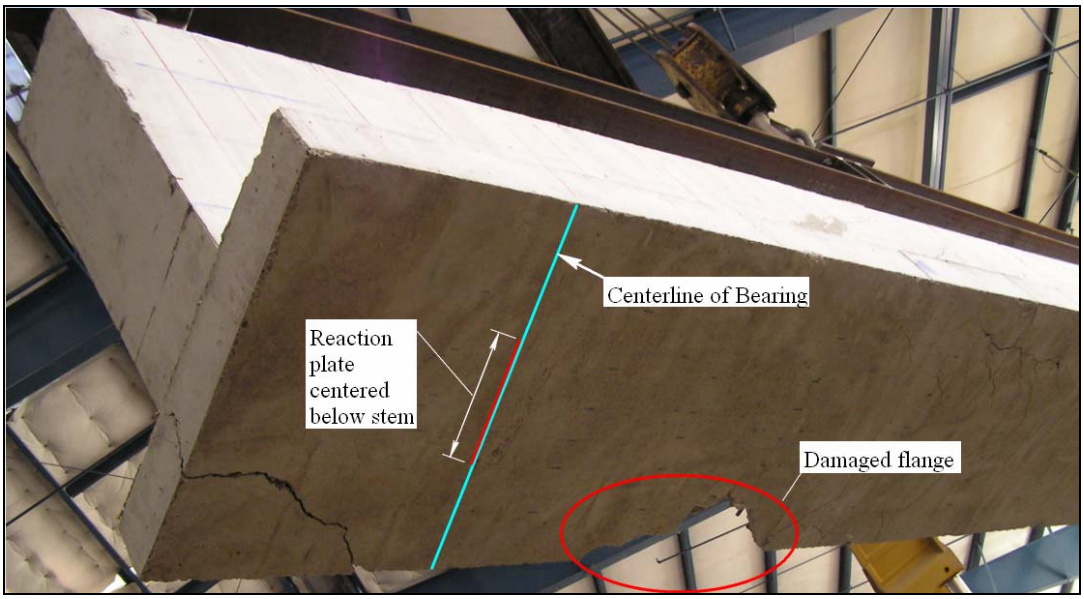


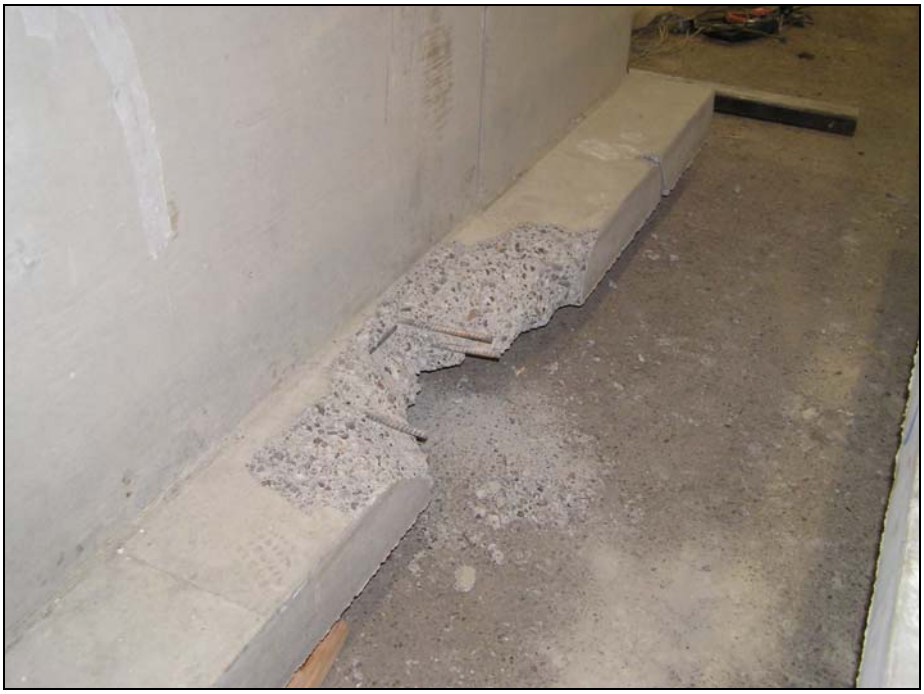
Figure 5.66: B.IT.NC.IS shear force versus internal and supplemental internal stirrup strain: strength loading

It should also be noted that one of the internal stirrup repair IT beams (B.IT.C.IS) was damaged during handling, which produced a large spall to the flange. However, the damage was contained within the outer portion of the flange at the terminal end of one of the flexural cutoff bars and did not continue through the depth of the stem, as shown in Figure 5.67. The beam was tested such that the damaged south end was loaded only through the stem. Also, the beam was repaired with four supplemental stirrup bars at the south end and only two at the north end (Figure 5.68), so as to try to force the failure on the north end of the beam where the bearing condition was identical to the previous IT beams.

The beam however failed on the south side, and therefore the pertinent strain data is presented for this condition. The failure was an anchorage failure of the flexural steel. Based on the observed failure location relative to the initial handling damage, the initial damage was not believed to have contributed to the failure mode. However, this failure mode serves as a reminder to designers to consider flexural anchorages when designing shear strengthening schemes. It is possible to encounter alternative failure modes if shear strengths are increased and higher loads permitted, based solely on the increased shear strength provided by the repair.



(a)



(b)

Figure 5.67: B.IT.C.IS flange damage: (a) top of flange and (b) side of flange

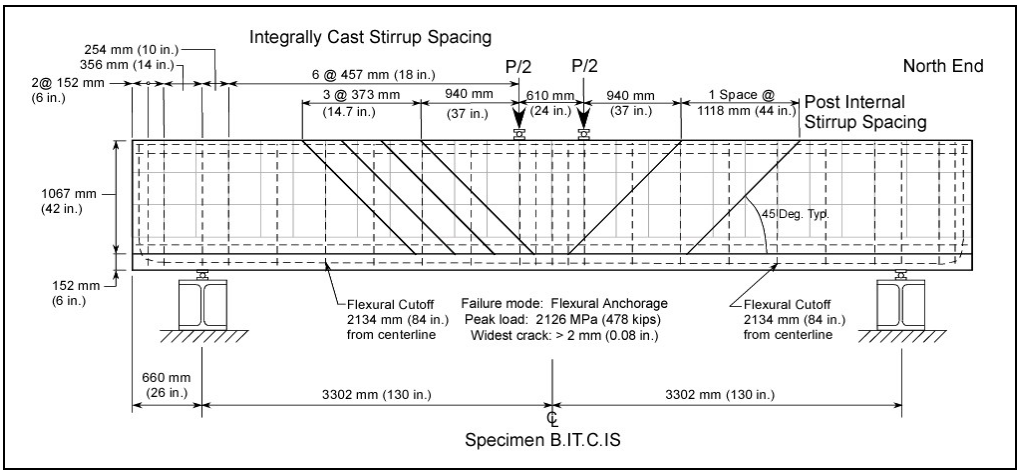


Figure 5.68: B.IT.C.IS revised repair

5.3.3 Analytical methods

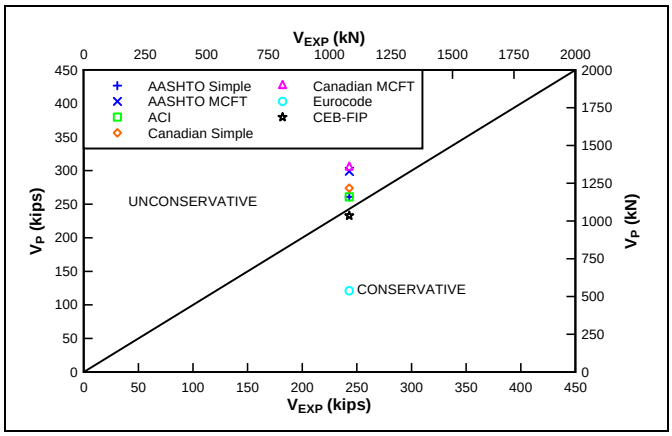
Recall from Chapter 2 that the available literature for supplemental internal stirrup repair was limited for shear repair. The major work was performed by Stratton, et al. through Kansas DOT, and the remainder of the literature review was based on the various bond models for anchorage of attachments and doweling into existing structures. The work from Kansas lacked any laboratory specimens in order to verify the expected increase in shear capacity.

5.3.3.1 Internal stirrup repair: comparison with national codes

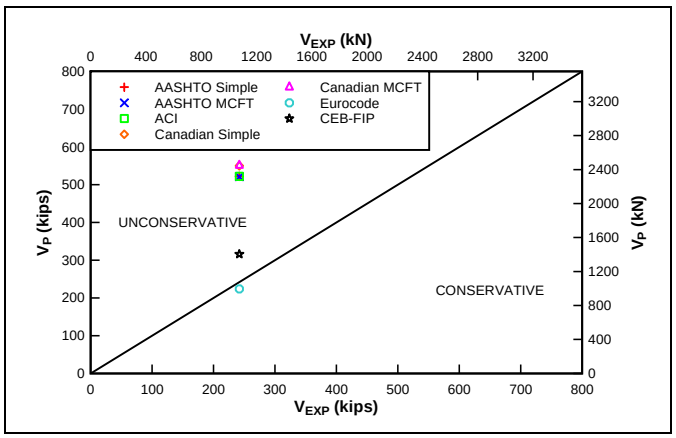
Comparison of the supplemental internal stirrup repair with the national codes is shown in Table 5.10 and graphically in Figure 5.69, including international codes. The internal steel was treated as equivalent to cast-in-place stirrups using the material tested tensile yield stress and the 45-degree installation orientation. The table is presented in similar format to the external stirrup table shown previously. The comparison of the second repair specimen is included, even though it was initially damaged and repaired with double the shear reinforcement along the south end (analysis performed on the south end conditions). This specimen failed due to anchorage, and the capacity estimates are off by as much as a factor of two, because the ACI prediction methodologies do not directly consider flexural performance on shear strength.

Table 5.10: Supplemental internal stirrup strength estimates based on national codes

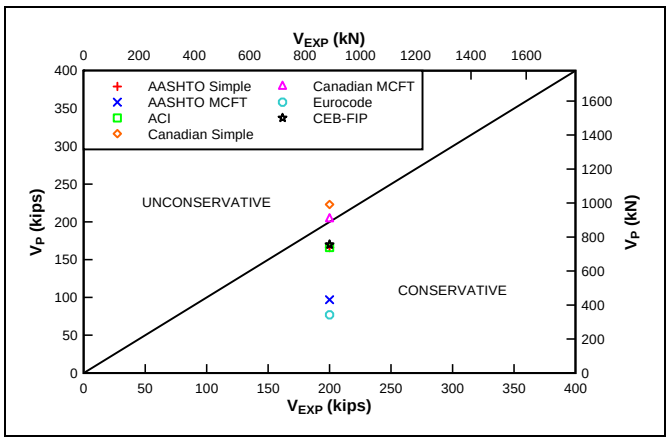
Specimen	Method	Base Capacity						Repaired Capacity		V_{exp}		V_{exp} / V_{total}
		V_c		V_s		V_{base}		V_{total}				
		kN	kip	kN	kip	kN	kip	kN	kip	kN	kip	
B.IT.NC.IS	R2K	-	-	-	-	756	170	-	-	1082	243	-
	AASHTO Simple	352	79	223	50	575	129	1163	261			0.93
	AASHTO MCFT	-	-	-	-	690	155	1214	273			0.89
	ACI 318-05	351	79	223	50	574	129	1163	261			0.93
B.IT.C.IS	R2K	-	-	-	-	730	164	-	-	1075	242	-
	AASHTO Simple	339	76	223	50	562	126	2323	522			0.46
	AASHTO MCFT	-	-	-	-	654	147	1015	228			1.06
	ACI 318-05	338	76	223	50	561	126	2322	522			0.46
B.T.NC.IS	R2K	-	-	-	-	619	139	-	-	890	200	-
	AASHTO Simple	342	77	164	37	506	114	737	166			1.20
	AASHTO MCFT	-	-	-	-	396	89	761	171			1.17
	ACI 318-05	342	77	164	37	506	114	737	166			1.20



(a)



(b)



(c)

Figure 5.69: Code Comparison for (a) B.IT.NC.IS, (b) B.IT.C.IS, and (c) B.T.NC.IS

5.3.3.2 Internal stirrup repair: comparison with R2K

Comparison of the supplemental internal stirrup repair with R2K follows that of the supplemental external stirrup specimens, as previously noted in Table 5.6. The additional shear pressure term for the IT with flexural cutoffs is not included in the table, as the specimen failed due to anchorage pullout of the flexural steel. Specimen B.IT.NC.IS exhibited an efficiency ratio greater than 1.0, indicating the repaired strength is greater than the estimated using the shear pressure coefficients. Specimen B.T.NC.IS also exhibits an efficiency ratio slightly greater than 1.0, indicating the repaired strength is equivalent to treating the supplemental stirrups as equivalent integrally cast stirrups.

5.3.3.3 Internal stirrup repair: comparison with VecTor2

The internal stirrup repair was modeled within VecTor2, utilizing perfect bond between the concrete, epoxy, and steel, as shown in Figure 5.70. The objective was to obtain an ultimate strength value. If the program over-estimated the strength, a reduction or different bond model would be considered, based on the literature review noted in Chapter 2. The results of the VecTor2 models are shown in Table 5.11. For the fully developed IT and T beams, the program provided a slightly conservative strength estimation that was within 3%-9% of the repaired strengths. These estimations are closer than the code comparisons, except for the Canadian code estimation of the T beam. The predicted strength of specimen B.IT.C.IS (which was initially damaged) was lower than the experimental strength by 26%. While this is a large margin, it is only half of the value estimated by the available codes.

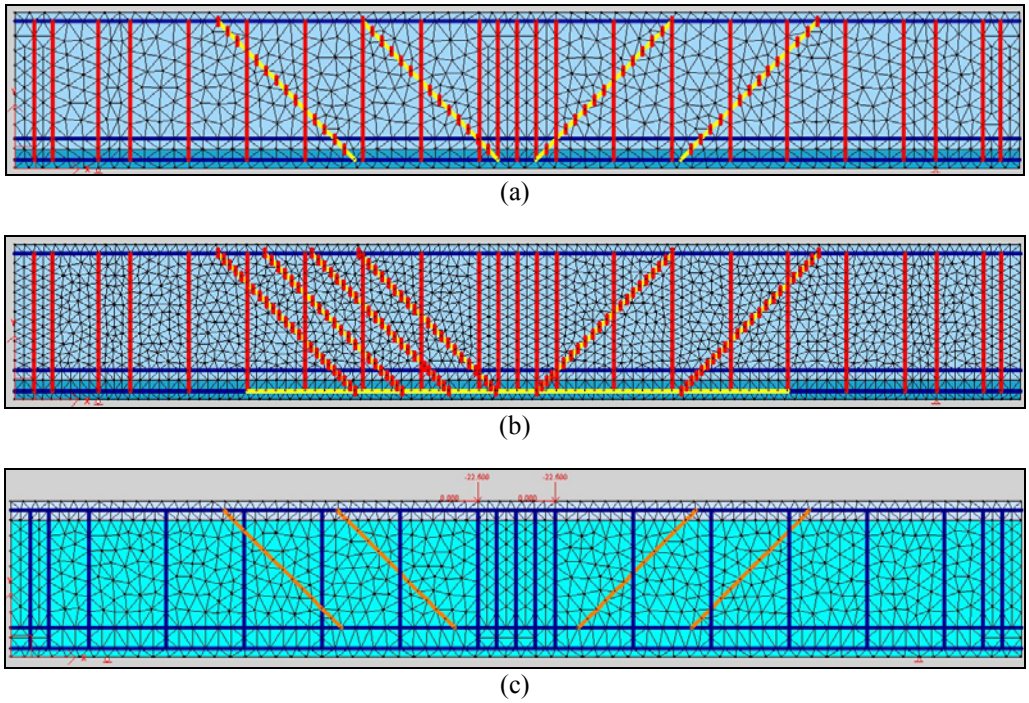
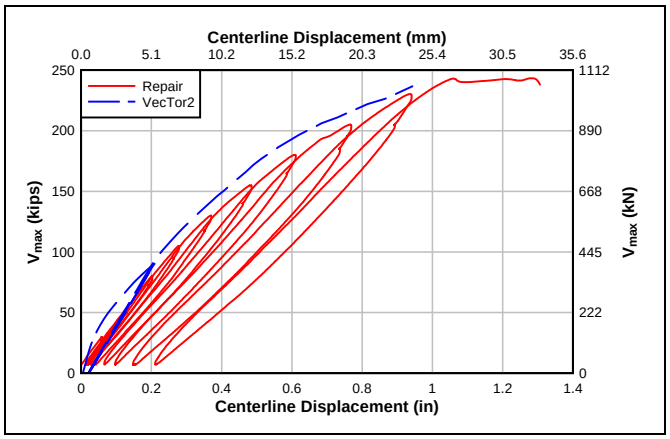


Figure 5.70: VecTor2 meshing schemes for (a) B.IT.NC.IS, (b) B.IT.C.IS, and (c) B.T.NC.IS

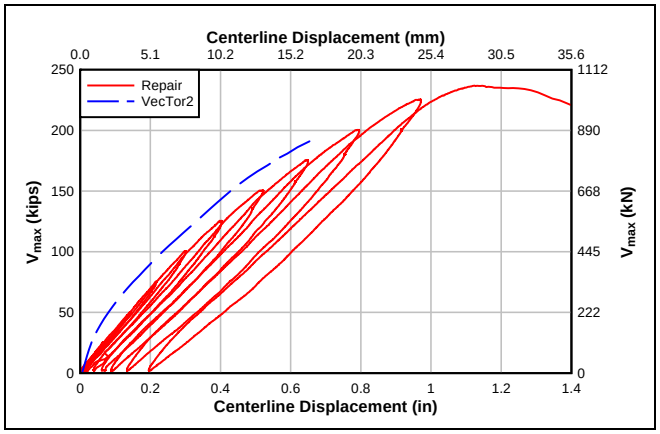
Table 5.11: Internal stirrup VecTor2 comparison

Specimen:	V_p (VecTor2)		V_{exp}		V_{exp} / Vp
	kN	kip	kN	kip	
B.IT.NC.IS	1052	237	1082	243	1.03
B.IT.C.IS	854	192	1075	242	1.26
B.T.NC.IS	817	184	890	200	1.09

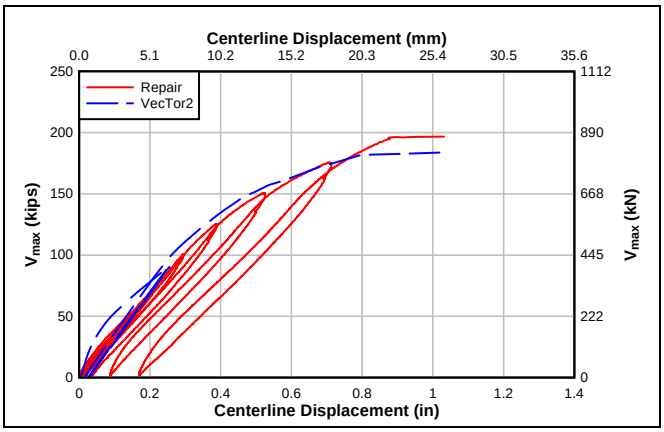
Load-displacement graphs from VecTor2 are shown in Figure 5.71. The behavior of all specimens matches the backbone curve of the experimental data well. The initial precrack loading on two of the specimens indicates the relative change in stiffness of the base specimen. The base specimen loading cycle was completed with the area of the supplemental stirrups set to a minimal value; then the analysis was run with the full supplemental area till failure. The cutoff specimen illustrates a slight offset from the experimental results.



(a)



(b)



(c)

Figure 5.71: VecTor2 internal stirrup load deflection estimate for (a) B.IT.NC.IS, (b) B.IT.C.IS, and (c) B.T.NC.IS

5.3.4 Discussion and design recommendations

As with the external stirrup repair, design recommendations are based on the experimental data and information from the literature review. For the service level performance, the following recommendations are provided:

- Quality control of supplemental internal stirrup installation is paramount for success.

- Knowledge of existing flexural steel and stirrups is required for coring purposes in order to avoid severing critical steel components.

- The exterior faces of the web should be patched at the location of the cracks, as seepage of the epoxy will eventually penetrate from the cored hole location to the exterior fiber of the beam. Alternatively, the beam could be cored after epoxy injecting diagonal cracks.

- Once a hole is created without interference with the surrounding steel, the interior concrete surface must be clean to allow proper bonding of the epoxy. Also, seepage of epoxy through the web of the section reduces the epoxy within the cored hole. Providing additional epoxy throughout the installation due to seepage ensures complete encapsulation of the steel rebar. Alternatively, epoxy injection of the cracks prior to coring would minimize seepage.

- Selection of epoxy and size/grade of steel is important in the repair. Both larger and higher strength bar with fewer holes or more common mild steel with more holes were effectively used in the current study. Relative cost and installation configuration (top down or bottom up) will provide an indication of the optimal repair combination. For a top down installation, the use of mild steel may be more economical, as specifications limit the use of higher strength steels to stresses below 80 ksi. Further, for shallower beams with less anchorage length, the lower grade steel allows development of yield over shorter bond lengths. For a bottom up installation, the use of a hollow rod though which epoxy is pumped may provide the best quality control.

For ultimate loading the following items are noteworthy:

- Post failure investigation of the internal stirrup specimens indicate a horizontal offset of the previous vertical grid lines on the specimen. Dowel action – the resistance of a reinforcing bar against forces acting perpendicular to its longitudinal axis – is likely the cause of this phenomenon. Dowel action may also increase bond efficiency and provide an additional source of shear resistance.

- Crack widths at ultimate were smaller than those of the external stirrup repair.

- Providing supplemental stirrups close to the principle strain axis of the member provides the best use of materials.

- The efficiency factors based on R2K analysis indicate the method performs better than predicted (attributed to the efficient orientation of rebar with respect to the principle tensile strains and the influence of dowel action acting on the bars).

5.4 SURFACE BONDED CFRP REPAIR FOR GIRDERS

5.4.1 Material and application details

Material used for the CFRP repair (provided by the Watson Bowman Acme Corporation (BASF)) consisted of the Wabo® MBrace CF130 unidirectional carbon fiber fabric (*Watson Bowman 2002*). In addition to the fabric, the manufacturer provided several additional products as part of the application procedure, including a low viscosity epoxy primer, high viscosity epoxy paste, and an epoxy resin (saturant) (*Watson Bowman 2002*).

A three-sided U-wrap repair scheme was selected with a wet lay up installation procedure for both the beam and bent cap specimen. For the IT beam in the current study, the three-sided U-wrap was placed such that the CFRP terminated at the stem-flange interface, which was under flexural tensile stresses, as shown in Figure 5.72. CFRP strips came from the manufacturer at 508 mm (20 in.) widths. The strips were reduced to 254 mm (10 in.) widths and placed on the beams with 51 mm (2 in.) wide gaps between strips, resulting in a 305 mm (12 in.) center-to-center spacing between strips, as shown in Figure 5.73.

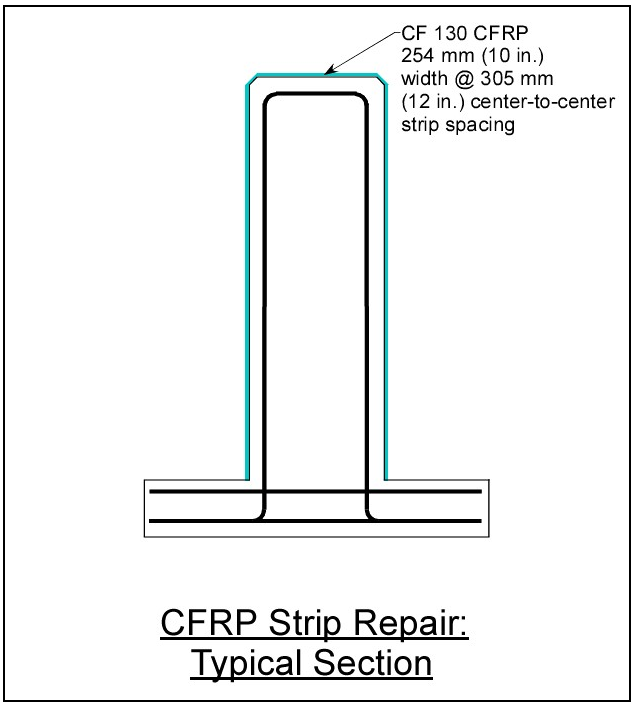


Figure 5.72: CFRP beam typical section

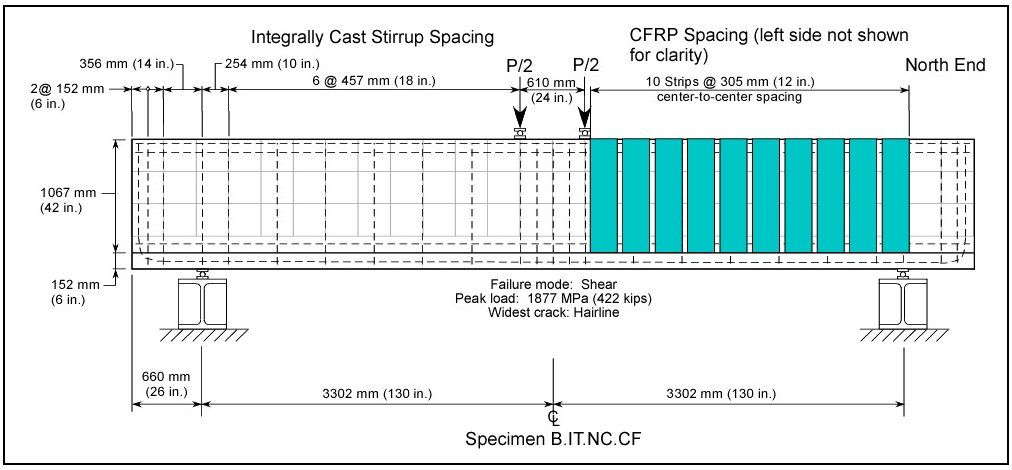


Figure 5.73: Specimen B.IT.NC.CF repair

Material testing of the CFRP system consisted of direct tensile tests of CFRP fabric embedded with saturant as well as pull-off tests to indicate the level of bond between the resin and concrete in the repaired specimen. Preparation of the CFRP tensile coupons coincided with application of the CFRP for the beam and bent cap respectively. During CFRP application, a 610 mm (24 in.) square sheet of CFRP was cut and placed on a larger perimeter non-stick Teflon plate, previously coated with saturant. Once the sheet was placed, it was impregnated with the use of a plastic putty knife, and a second coat of saturant was applied to the CFRP. A second Teflon plate was placed over the sample, and the process was repeated until several CFRP sheets were assembled. After completion of the samples, a large weight was placed atop the Teflon sheets, and the apparatus was placed adjacent to the repaired specimen, thus replicating the curing conditions of the CFRP.

The CFRP was permitted to cure for seven days, after which time the sheets were removed and prepared for testing. The 610 mm (24 in.) square sheet was reduced to an individual coupon size of 25 mm (1 in.) by 305 mm (12 in.), using a wet tile saw in order to conform to the testing requirements of ASTM D 3039/D 3039M. While great care was taken to trim the specimens to the correct size, cutting along the primary fiber direction resulted in slight variations among the individual coupons. As a result, the coupons with the best alignment of the cut edge to the fiber orientation were used for testing purposes. Fiberglass electronic boards measuring 25 mm (1 in.) wide by 57 mm (2.25 in.) long were cut and attached to the ends of the coupons with a cyanoacrylate adhesive to reduce the chance of failure at the anchorage locations. Once completed, the coupons were tested utilizing a 89 kN (20 kip) hydraulically controlled universal testing machine under displacement control of 1.25 mm/min (0.05 in./min). Strain in the CFRP was measured with a class B extensometer with a 25 mm (1 in.) gage length. Results of the CFRP coupon tests, with comparison to the manufacturer's specifications, for the beam and bent cap repair are shown in Table 5.12.

Table 5.12: CFRP tensile test data

Property:	Wabo® Design	B.IT.NC.CF		D.IT.C.CF	
		Test Mean	Test Standard Deviation	Test Mean	Test Standard Deviation
Coupon Thickness	0.6 - 1.0	1.14	0.024	1.26	0.058
mm (in.)	[0.02-0.04]	[0.045]	[0.00095]	[0.05]	[0.00227]
Tensile Strength:	625 - 1042	707.5	36.5	538.7	11.1
Mpa (ksi)	[89 - 179]	[103]	[5.3]	[78]	[1.6]
Unit Strength:	0.625	1.3	0.063	1.1	0.038
kN/mm/ply (kip/in/ply)	[3.57]	[4.62]	[0.232]	[3.89]	[0.14]
Elastic Modulus:	37.4-62.4	36.7	4.6	32.9	1.1
Gpa (ksi)	[5300-10700]	[5325]	[667]	[4775]	[155]
Rupture Strain %:	1.67	1.94	0.147	1.6	0.046
Nominal Fabric	0.165	0.165	n/a	0.165	n/a
mm (in.)	[0.0065]	[0.0065]	n/a	[0.0065]	n/a
Tensile Strength*:	3800	4897	246	4125	149
Gpa (ksi)	[550]	[710]	[35.7]	[598]	[21.5]
Elastic Modulus*:	227	254	30.3	252	13.9
Gpa (ksi)	[33000]	[36846]	[4402]	[36577]	[2015]

*Based on nominal fabric dimensions

Direct tension pull-off tests were performed after failure testing of the beam (and later bent cap) specimen in accordance with ASTM D 4541-93: Standard Test Method for Pull-off Strength of Coatings Using Portable Adhesion Tester. Three pull-off locations were chosen at random, lightly sanded, then chemically treated to provide a clean dry surface to attach a 51 mm (2 in.) square steel dolly with a high strength two-part epoxy. After curing of the epoxy, the CFRP around the dolly was removed with a circular disc grinder, thus providing an equal surface area of the CFRP to the attached dolly. Next, a 1.6 kN (3000 lb) capacity manually operated portable testing machine was attached to the dolly and the test conducted to failure. The portable machine recorded the maximum load at failure, and the process was repeated at the remaining two locations. The average bond stress of the CFRP to the concrete was calculated based on the area of the dolly. All direct pull-off tests showed failure occurred within the concrete substrate and not within the epoxy resin. Results of the direct pull-off tests are shown in Table 5.13.

Table 5.13: CFRP pull-off test results

Specimen:	B.IT.NC.CF	D.IT.C.CF
Mean	2137	3546
KPa (psi)	[310]	[514]
Standard Deviation	461	547
KPa (psi)	[67]	[79]

The CFRP strips were applied according to the manufacturer's instructions. For the beam (and later bent cap specimen), the manufacturer recommended a working time to complete application

of the CFRP system (not including epoxy injection) of approximately 12 hours; in each case, the process was completed in approximately six hours. The first step in the process was to epoxy inject cracks wider than 0.25 mm (0.010 in.). This involved the use of a wire brush to clean the cracks and adjacent surface of any loose debris. Injection ports were then mounted to one side of the specimen using a two-part 100% solids Concresive SPL epoxy paste at roughly the thickness of the specimen (355 mm (14 in.) for both the beam and bent cap repairs), as shown above in Figure 5.73. On the opposite face of the member, two or three ports were applied, equally spaced along the crack, as so called "window ports" for quality control measures to ensure full penetration through the width of the stem.

Once the surface paste cured for 24 hours, the epoxy injection began. The epoxy used was Chemrex SCB Concresive 1360, which is a two-part, ultra-low viscosity liquid epoxy with a manufacturer specified tensile strength of 55.2 MPa (8.0 ksi). A specialized injection machine was used to mix the two-part epoxy to the manufacturer's specifications (2.5 Part A to 1.0 Part B). The epoxy was injected starting at the lowest port, with care given not to exceed a pressure of 690 kPa (100 psi) while injecting the cracks. As epoxy became visible at the next highest port, the lower port was sealed and the injection nozzle moved to the next highest port. The process was repeated until the last port was encountered, at which point the dissipation of pressure within the crack slowed significantly as the void space within the crack decreased. Occasionally, a leak near a port or along a crack would form. Repairs to the crack were made with paraffin wax, which tended to seal most small to moderate sized cracks. Once complete, the epoxy was left to cure for a period of seven days. Temperature data was recorded during this time, to ensure ambient air temperature above 4.5 ºC (40 ºF) as required by the manufacturer.

The next step in the process involved application of the CFRP itself, as denoted in Figures 5.74 and 5.75. First, the paste on the outside of the beam was removed by heating the paste with a propane torch and scraping off the surface. The outer surface of the beam was ground using a diamond dressed masonry disc to expose the aggregate and then vacuum brushed to remove any dust that may have accumulated during the process. Once the surface was prepared, a two-part MBrace Primer was mixed for three minutes according to the manufacturer specifications with a hand held drill and applied to the surface using short nap paint rollers. The pot life of the primer component was 30 minutes; the product was applied prior to this threshold.

A two-part putty, each part mixed separately for three minutes, then mixed combined for three minutes – as per the manufacturer's specifications – was then applied to the surface using hand trowels, intended to fill small voids on the surface of the beam. The manufacturer permitted application of the putty while the primer coat was still wet; however, the primer was left to set up for a period of 30-45 minutes prior to mixing of the putty. The putty was also permitted to set up for 30-45 minutes prior to the next step, although the manufacturer did not place any restrictions on placing the saturant directly on the wet putty.

A two-part saturant, which included a three-minute Part A premix followed by a three-minute combined mix, was then applied with common paint rollers. Precut 25 mm (10 in.) wide CF130 carbon fiber strips were then applied to the beam using a plastic putty knife to impregnate the fibers with the saturant beneath. A second coat of saturant was applied to the CF130 carbon strips to complete the process.

The manufacturer recommended curing for seven days at an ambient air temperature of at least 4.5 ºC (40 ºF). When colder temperatures were anticipated, enclosures with space heaters were provided to raise the ambient temperature during curing above the specified minimum. Results of the ambient air temperature for specimens B.IT.NC.CF and D.IT.C.CF are included in Table 5.14 for both epoxy injection and CFRP application.



Figure 5.74: CFRP beam installation: epoxy injection



Figure 5.75: CFRP installation: ground surface (left) and primer application (right)

Table 5.14: Curing temperatures for B.IT.NC.CF and D.IT.C.CF

Specimen:	Temperature °C [°F]		
	Average	High	Low
B.IT.NC.CF	8.7	18.6	6.1
	[46.8]	[50.3]	[40.4]
D.IT.C.CF	8.2	10.2	4.7
	[47.6]	[65.4]	[43]

5.4.2 Experimental results

Behavior of the CFRP repair specimens is presented in the following section, with reference to the SPR 350 beams (*Higgins, et al. 2004b*). Shear load versus midspan displacement plots for each external stirrup repair specimen is shown in Figure 5.76. Shear load versus diagonal displacement and shear load versus average vertical strain plots are provided in Figures 5.77 and 5.78, respectively. Lastly, shear load versus typical integrally cast stirrup strains are shown in Figure 5.79. Crack map data for all the repaired beam specimens are shown in Figure 5.80, including crack formation for each load increment. The crack map data is replicated in Figure 5.81 for all the beam specimens with the cracks identified as precrack and repair.

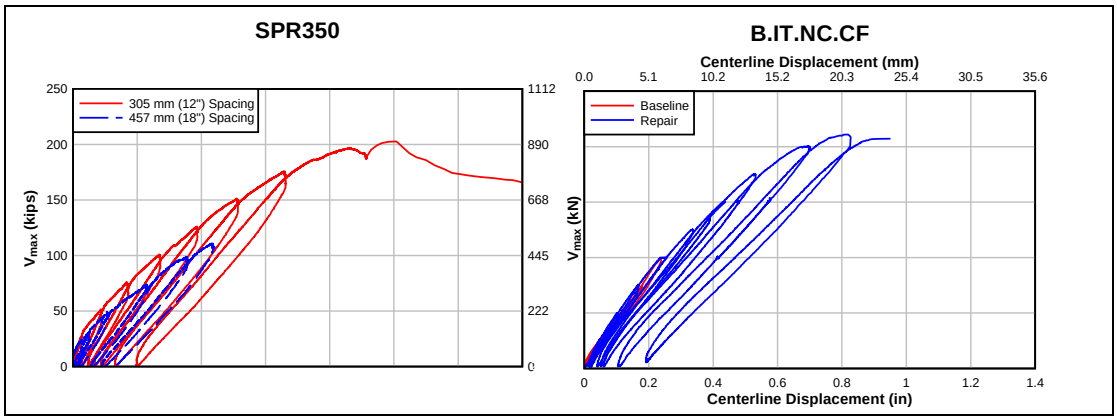


Figure 5.76: CFRP girder repair specimen shear force versus centerline displacement

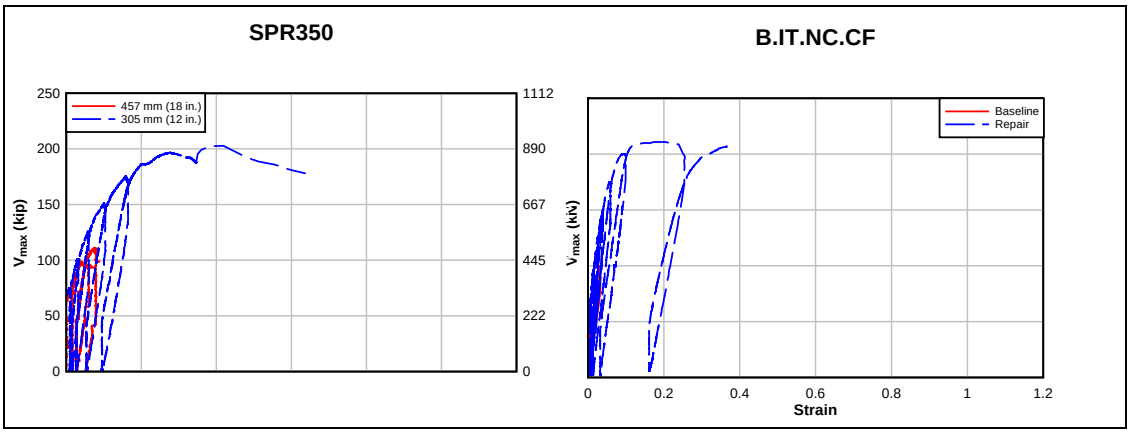


Figure 5.77: CFRP girder repair specimens shear force versus diagonal displacement

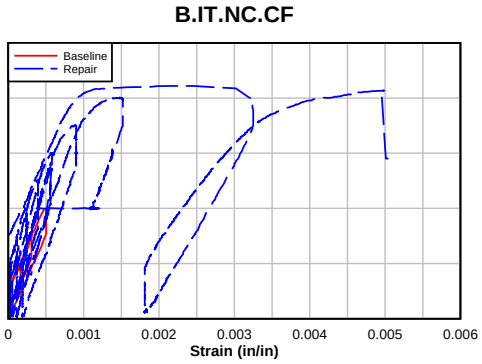


Figure 5.78: CFRP girder repair specimens shear force versus average vertical strain

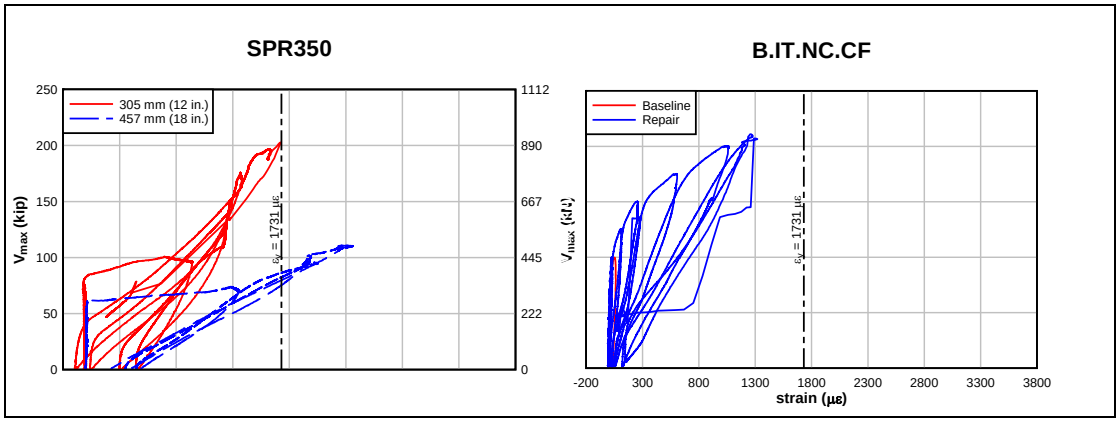


Figure 5.79: CFRP girder repair specimens shear force versus typical internal stirrup strain

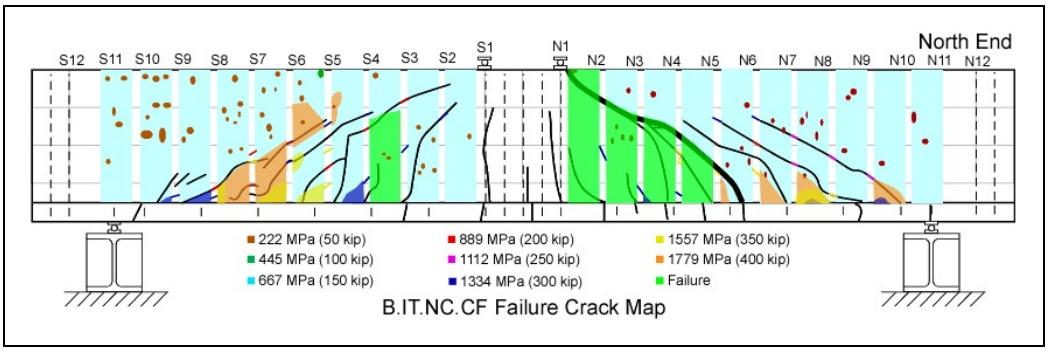


Figure 5.80: CFRP repair specimen crack map: individual load steps indicated

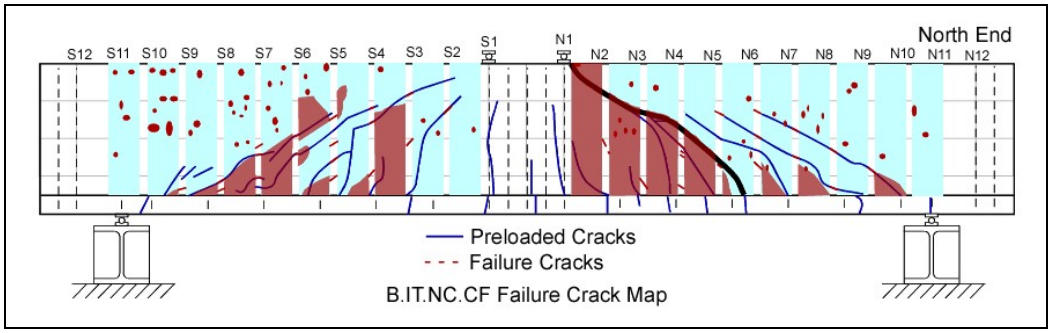


Figure 5.81: CFRP repair specimen crack map: precrack versus repair

Comparison of the carbon fiber repair specimen for the strength loading condition is shown in Figure 5.82 in terms of average vertical strain and CFRP strain. The data indeed shows a similar behavior between the CFRP and panel strain throughout the strength loading.

Local behavior of the CFRP repair during the strength loading is shown in Figure 5.83 as integrally cast stirrup and carbon fiber strain data. The stiffness of CFRP gage 3N changes at a shear force of 396 kN (89 kip), which is evident for the final load step over the service range but emerges distinctly during the following two load steps. Afterward, the stiffness changes two additional times between load steps, accompanied by ever larger permanent deformations until failure. The internal stirrup exhibits a slight decrease in stiffness before changing to a higher slope for the final load steps. The failure was due to a shear compression failure after debonding of the CFRP strips.

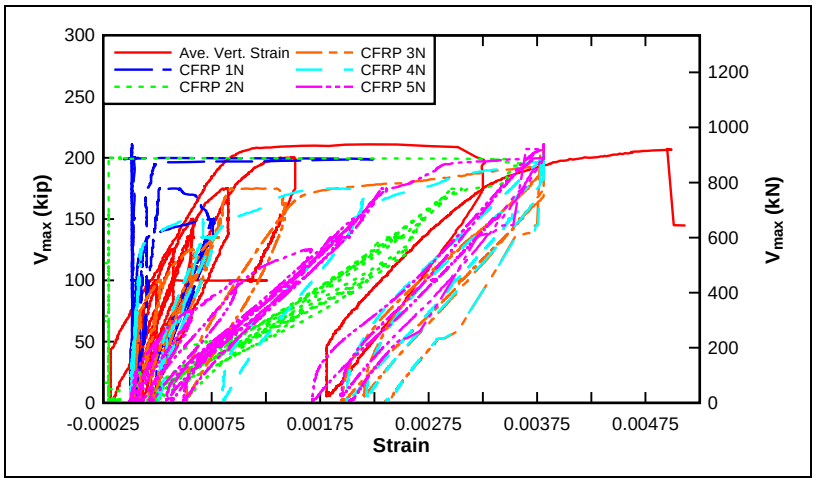


Figure 5.82: Specimen B.IT.NC.CF shear force - average vertical strain and CFRP strain

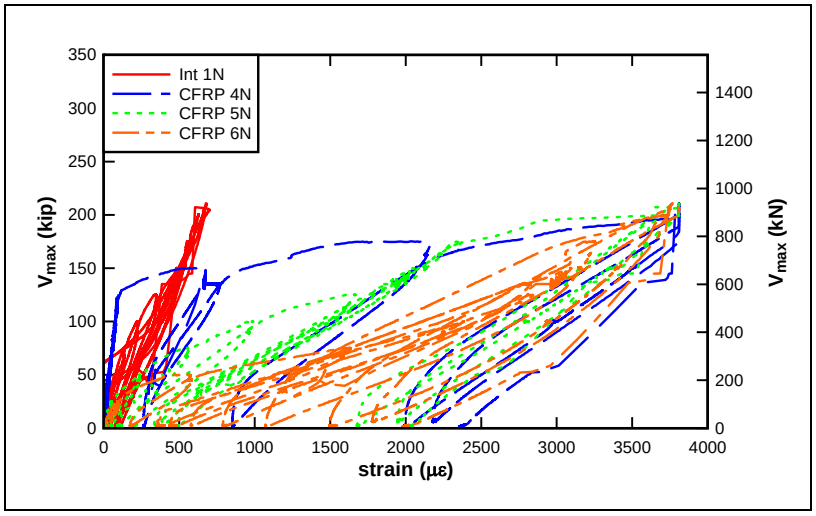


Figure 5.83: B.IT.NC.CF shear force - integral stirrup strain and CFRP strain

5.4.3 Analytical methods

5.4.3.1 CFRP stirrup repair: comparison with literature review

Using CFRP in repair for shear began to gain prominence in the mid 1990s; the evolution of the current design recommendations from ACI 440 were documented previously in Chapter 2. More comprehensive review of CFRP shear design, including environmental durability, is covered in Higgins, et al. (*2009*). The analysis method recommended is ACI 440 with supplemental check of environmental exposure and bond demands based on shear-moment interaction.

5.4.3.2 CFRP stirrup repair: comparison with international codes

The contribution from CFRP to shear is shown in Table 5.15. Recall from Chapter 2 that ACI 318 is used for design and construction of concrete members and must be used with the recommendations from ACI 440 to include strengthening guidelines for CFRP. Therefore, the strength contribution includes the base specimen capacity from R2K, adjusted for bias from the previous SPR 350 data and ACI 318. Utilizing the ACI 440 approach outlined in Chapter 2, the shear contribution from CFRP was limited by bond and thus the strain in the CFRP was limited to 0.0038 in/in. Results indicate the base specimen capacity is underestimated using ACI 318, but the composite capacity with ACI 440 results in a conservative strength estimate. On the other hand, the base specimen capacity from R2K coupled with the ACI 440 strength estimate is unconservative, by overestimating the shear contribution of the CFRP by approximately 10%. This again highlights the need to use base strength predictions with ACI 318 combined with the CFRP contribution from ACI 440.

Table 5.15: CFRP beam code comparison

Specimen:	Method:	$V_{baseline}$		ACI 440 $V_{strengthened}$		V_{s_tot}		V_{EXP}		V_{EXP}/V_{calc}
		kN	kip	kN	kip	kN	kip	kN	kip	
B.IT.NC.CF	0.98*R2K	761	171	310	70	1071	241	960	216	0.90
	ACI 318	579	130			889	200			1.08

5.4.3.3 CFRP stirrup repair: comparison with R2K

As with the previous beam analysis, a shear design curve utilizing R2K was produced for the CFRP beam with varying stirrup spacing. The results are noted previously, as shown in Table 5.4. The results indicate the repair is 85% efficient compared to the expected CFRP stress determined from ACI 440. Coincidentally, the reduction factor from ACI 440 is set to 0.85 as well.

5.4.3.4 CFRP stirrup repair: comparison with VecTor2

The CFRP specimen was modeled in VecTor2, as shown in Figure 5.84. Initially, the specimen was modeled utilizing the bond strength parameters from ACI 440, with limited success. Within VecTor2, bond elements can be modeled as link or one-dimensional contact elements. In the current study, the elements are connected with link elements. As outlined in a previous paper by Wong and Vecchio, to accurately model the behavior, two sets of nodes are assigned for each bond element; one node is assigned to the concrete and the other is assigned to the repair media (*Wong and Vecchio 2003*). The bond between the two nodes is assigned based on constitutive relationships. The link elements have no dimensions but are represented by two orthogonal springs, which are independent of each other. Movement in the two directions represent the shear and normal stresses for the bond material. Internally, selecting the bond material model for

externally applied carbon fiber strips places a significantly higher stiffness value to the normal direction, as a shear dominated failure within the epoxy-concrete substrate is most common in shear repair with CFRP. This limits the link element to displace in shear direction.

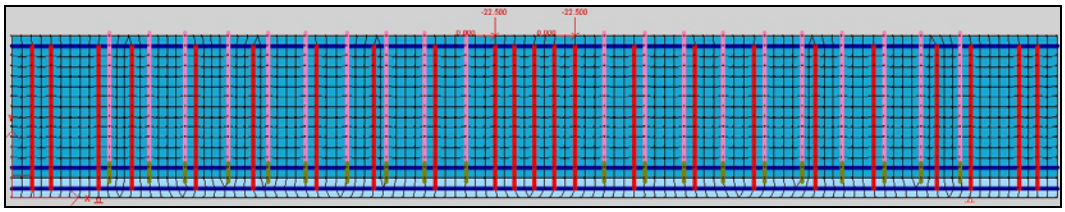


Figure 5.84: VecTor2 meshing scheme for B.IT.NC.CF

The constitutive relationship for bond-slip of CFRP strip is noted in the initial paper by Kim and Vecchio (*2008*). VecTor2 requires three unique points in order to model the bond-slip relationship accurately, as shown in Figure 5.85 (*Vecchio and Wong 2002*). The relationship utilizes a bilinear approximation of the bond-slip behavior, taking into account the compressive strength of the concrete and the carbon fiber material.

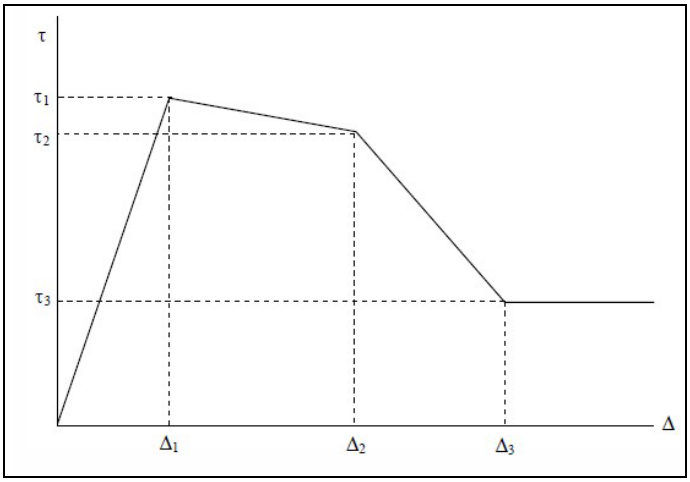


Figure 5.85: Bond-slip relationship for VecTor2 modeling of CFRP sheets

For CFRP the following equations are presented, based on the fracture energy G_f of the concrete.

$$\tau_{bFy} = \left(54 \cdot f_c^{'}\right)^{0.19} \quad \text{Kim \& Vecchio 2008} \qquad \textbf{(5-17)}$$

$$G_f = \left(\frac{\tau_{bFy}}{6.6} \right)^2 \text{ Kim \& Vecchio 2008} \quad \textbf{(5-18)}$$

$$s_{Fy} = 0.057 \cdot G_f^{0.5} \text{ Kim \& Vecchio 2008} \quad \textbf{(5-19)}$$

$$s_{Fu} = \frac{2 \cdot G_f}{\tau_{bFy}} \text{ Kim \& Vecchio 2008} \quad \textbf{(5-20)}$$

where τ_{bFY} in Equation 5-17 is the maximum bond shear stress (MPa); f_c' (MPa) is the compressive strength of the concrete; s_{FY} in Equation 5-19 is the bond slip at maximum shear stress; and s_{Fu} in Equation 5-20 is the ultimate bond slip. Utilizing these parameters, the bond stress parameters τ_1 and τ_2 were assigned the value of τ_{bFy}, and τ_3 was set to zero. The corresponding slip values Δ_1 and Δ_2 were assigned the value of s_{FY}, and Δ_3 was set to s_{Fu}.

Modeling FRP within VecTor2 requires entering the area of FRP corresponding to a particular model. It is not noted explicitly in the manual, but the two modeling papers indicate the area is based on the tributary height of the truss element. Thus, it is dependent on the mesh size. The width per vertical height of CFRP based on the mesh size was used in the current investigation. Also, modeling a U-wrapped scheme as opposed to a side-wrapped specimen presented an initial challenge in VecTor2. However, as bond failure originates at the free end, or in some cases from an existing crack toward a free end, the bottom of the U shape rarely governs the initial debonding that results in failure. As such, the lower portion of the U shape was modeled with a higher bond strength when entering the constitutive models.

Results of this modeling method are shown Table 5.16. The results are more consistent with the ACI 318 and ACI 440 combined strength, with a conservative strength estimate 15% below the experimental failure shear. The load-deformation behavior taken from VecTor2 is shown in Figure 5.86. The initial stiffness is taken as that of the uncracked beam; thus the initial slope for the VecTor2 graph would be closer to the experimental data for this case. The ultimate load is below that of the experimental data, and the load-deflection curve deviates from the experimental data for the latter load steps.

Table 5.16: CFRP beam VecTor2 comparison

Specimen:	V_p (VecTor2)		V_{exp}		V_{exp} / Vp
	kN	kip	kN	kip	
B.IT.NC.CF	834	188	960	216	1.15

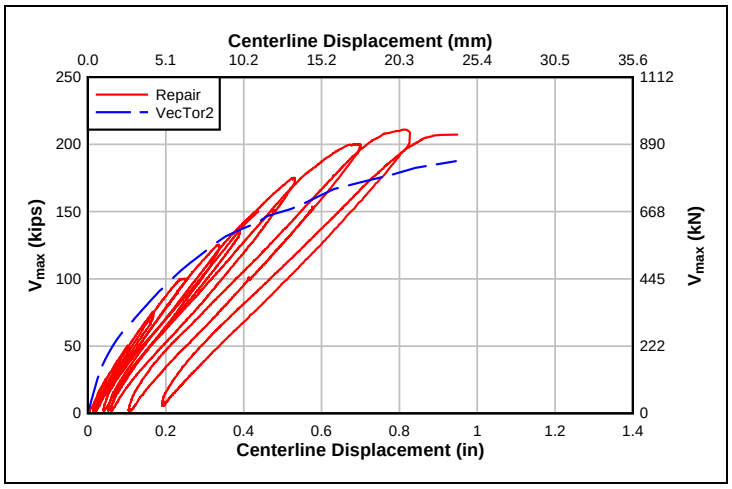


Figure 5.86: VecTor2 load-deflection response for B.IT.NC.CF

5.4.3.5 CFRP stirrup repair: design recommendations

No modifications to the existing design codes are recommended for CFRP beam repair. However, to estimate the repaired specimen capacity, ACI 318 in conjunction with ACI 440 provided a conservative strength estimate. Estimation of repaired capacity using ACI 440 and R2K is not recommended, as the base specimen capacity is overestimated, resulting in an unconservative design. VecTor2 provided a more conservative strength estimate than that of ACI 318 combined with ACI 440. Thus, using the current ACI design methods is recommended.

5.4.4 Discussion and design recommendations

No modifications to the existing ACI design approach are recommended, based on this single specimen. However, based on this and previous research to estimate the repaired specimen capacity, ACI 318 in conjunction with ACI 440 can be used (*Higgins, et al. 2004; 2009*). Readers are referred to Higgins, et al. for additional detail on environmental durability (*Higgins, et al. 2009*). Estimation of repaired capacity using ACI 440 and R2K is not recommended, as the base specimen capacity is overestimated and can result in an unconservative design. VecTor2 provided a more conservative strength estimate than that of ACI 318 and ACI 440 combined and could be used as a tool to verify designs.

5.5 NEAR SURFACE MOUNT (NSM) REPAIR FOR GIRDERS

5.5.1 Material and application details

The materials used for the NSM repair method were based on two criteria: limiting the bond thickness of the epoxy between the concrete and FRP, and maximizing the surface area of FRP relative to the concrete. Within these requirements, a rectangular saw-cut groove placed

vertically along the web of the beams precluded the use of round NSM in favor of rectangular tape. Consequently, Aslan 500 rectangular tape manufactured by Hughes Brothers was chosen as the FRP material, with a 3M DP460NS epoxy, based on the work of Shield, et al. from the literature review (*Shield, et al. 2005*). A typical section of the NSM repair is shown in Figure 5.87. Spacing of the NSM relative to the anticipated failure crack resulted in three strips per side of the beam within the shear span, as shown in Figure 5.88. This ensured the two outer strips would participate with a partial development while the center strip, located equidistant from the anticipated failure crack, would be fully developed at failure.

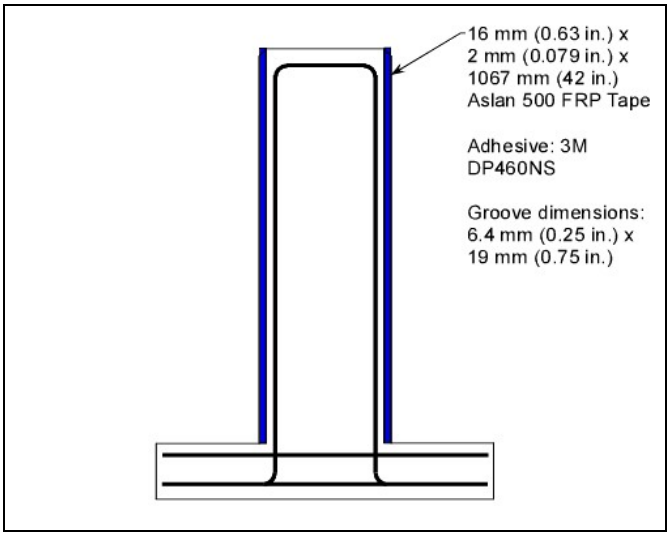


Figure 5.87: NSM FRP typical section

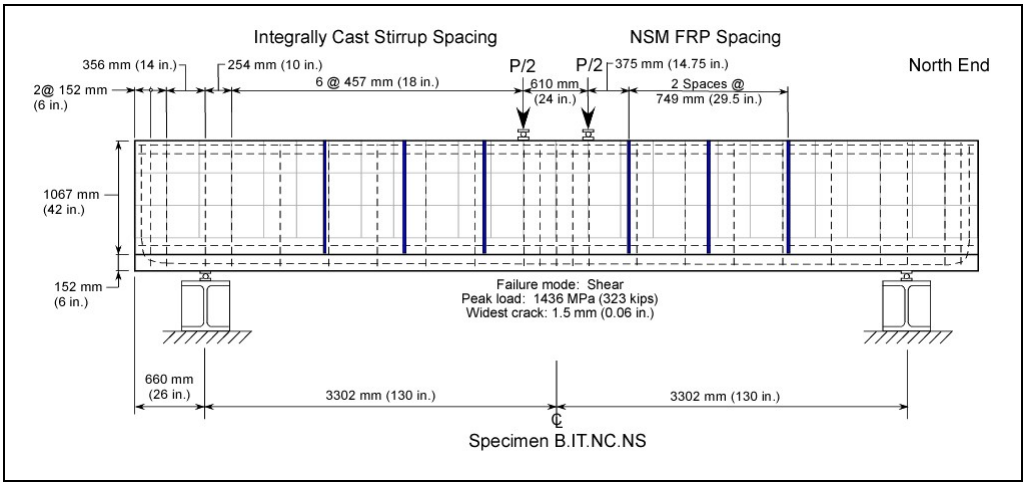


Figure 5.88: Specimen B.IT.NC.NS repair

In tensile tests on the FRP, failures typically occurred from splitting longitudinal to the specimen at or within the grip. Consequently, the tensile strength was a bit lower than that reported by the manufacturer. However, the modulus values and corresponding % strain at failure were within the range of values shown. If a gripping failure would have been prevented, it is possible that the ultimate strength values would be more in line with the manufacturer's reported values. Results of the tensile tests are shown in Table 5.17 with comparison to the manufacturer's design values. Direct pull-off tests of the epoxy were performed on the concrete, similar to that of the CFRP specimens, with failure occurring within the concrete substrate.

Table 5.17: NSM tensile test data

Property:	Hughes Bros. Reported Data	B.IT.NC.NS	
		Test Mean	Test Standard Deviation
Coupon Thickness	2	2	0.00
mm (in.)	[0.079]	[0.079]	[0.000]
Tensile Strength:	2068	1491	139
Mpa (ksi)	[300]	[216]	[16]
Elastic Modulus:	124	138.5	3.9
Gpa (ksi)	[18000]	[20082]	[568]
Rupture Strain %:	1.7	1.08	0.1

In addition to pull-off tests of the epoxy, direct tension pull-out tests were performed at depths of 51 mm (2 in.), 102 mm (4 in.), and 152 mm (6 in.) to qualitatively show the strain in the FRP at different embedment depths. Two issues made the test setup more complex than the corresponding internal stirrup pullout test. The first obstacle involved loading a single embedded NSM tape eccentrically from the center line of the beam. The second condition related to gripping of the FRP, as a mechanical splice used in the internal stirrup pull-out tests was not feasible. Therefore, a test setup was created to resolve the previously mentioned obstacles, as shown in Figure 5.89.

Loading of the FRP came from the center hole actuator used previously in the internal stirrup pull-out tests, with a reaction section modified from the external stirrup apparatus. The 51 mm (2 in.) and 102 mm (4 in.) embedment depths were located on the same end of the beam, such that reacting on the W beam induced equal stress in the two embedment depths. Gripping of the specimen was resolved by bonding two angle sections to the FRP with the same 3M DP460NS epoxy and reacting against the angle sections to induce stress in the FRP. The goal was to fail the 51 mm (2 in.) embedment first, then anchor the failed end with a threaded rod anchor. Next, the 102 mm (4 in.) side would be loaded to failure. The remaining 152 mm (6 in.) embedment was placed at another location along the beam, with the NSM located on one side and the threaded rod anchor on the opposite face.

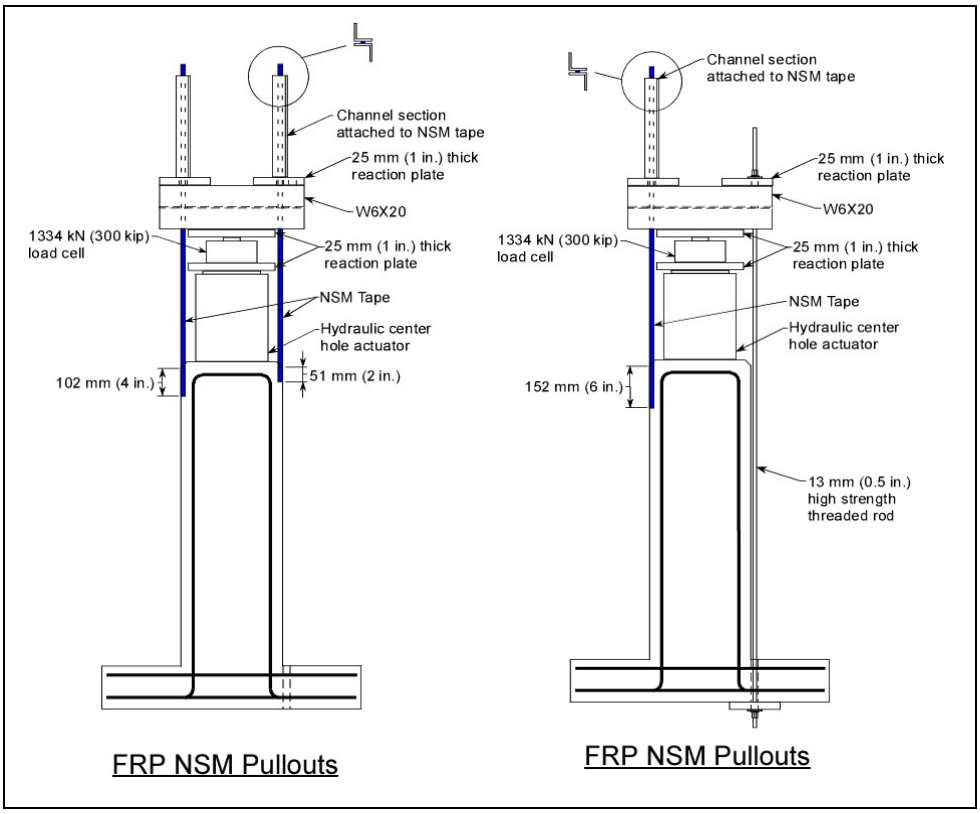


Figure 5.89: NSM pullout test setup

The goals of the initial test for the 51 mm (2 in.) and 102 mm (4 in.) embedment lengths led to unintended results. During the test, failure of the 51 mm (2 in.) embedment resulted in a rapid release of energy that sent the reaction section in a clockwise motion in the direction of the 102 mm (4 in.) embedment depth, resulting in fracture of the 102 mm (4 in.) embedment FRP. Therefore, additional testing of the 102 mm (4 in.) embedment was not possible. The strain data from the first test indicate a slight eccentricity of the load, resulting in a higher force in the 102 mm (4 in.) embedment length.

Testing of the single 152 mm (6 in.) side resulted in a similar failure mode to the previous embedment lengths. The NSM was anchored on one side of the beam and the opposite side was anchored by a threaded rod. A wedge type failure in the concrete resulted in a rapid release of energy, thereby permanently deforming the threaded rod anchor. A plot of the bar stress versus displacement is shown in Figure 5.90 for all three embedment lengths. For the 152 mm (6 in.) embedment, the sensor for recording the displacement of the NSM reached its maximum value prior to failure of the wedge; therefore the plot in Figure 5.90, which indicates a higher stress for a fixed displacement, does not fully represent the test outcome. Results of both the pull-off and pull-out tests are presented in Table 5.18.

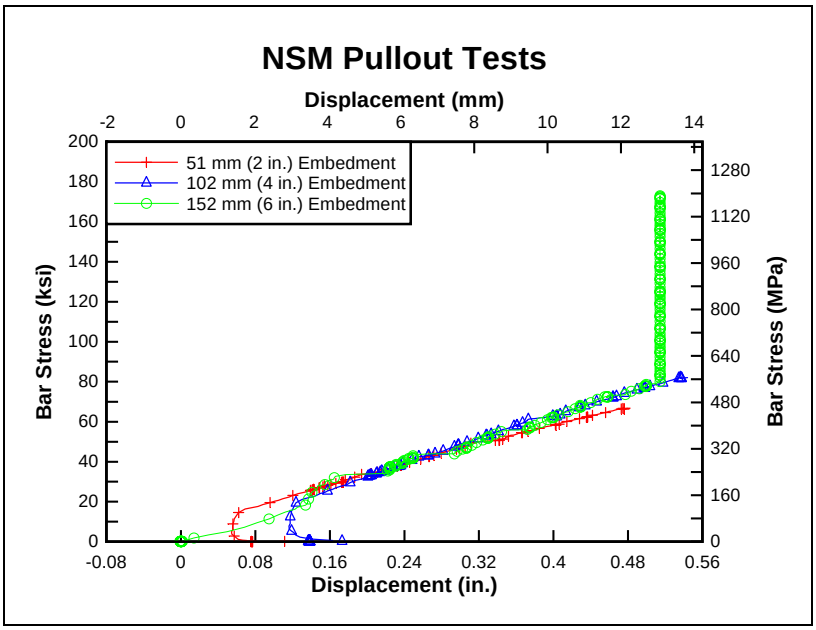


Figure 5.90: Specimen B.IT.NC.NS repair

Table 5.18: NSM pull-off and pull-out test results

Specimen:		B.IT.NC.NS	
Pulloff Tests	**Mean**	3076	
	KPa (psi)	[446]	
	Standard Deviation	264	
	KPa (psi)	[38]	
Pullout Tests	**Embedement Depth**	**Max Stress**	
	51 mm (2 in.)	462 MPa	[67 ksi]
	102 mm (4 in.)	565 MPa	[82 ksi]
	152 mm (6 in.)	1193 Mpa	[173 ksi]

The process for installation of the NSM FRP stirrup repair is outlined below, with reference to Figures 5.91 and 5.92:

- Determine spacing and location of the NSM FRP reinforcement along the span of the specimen.
- Locate the integral steel stirrups with a rebar locator such that the NSM locations do not coincide with the integral stirrups (due to variations in the concrete cover).
- Saw cut grooves in the beam at the locations for the NSM FRP.
- Remove any remaining slurry residue or debris from the grooves.

- Apply the epoxy two-thirds the depth of the hole.
- Insert the FRP rod or tape.
- If needed, apply additional epoxy to ensure complete penetration around the FRP.



Figure 5.91: NSM installation: cut grooves (left) and initial epoxy application (right)

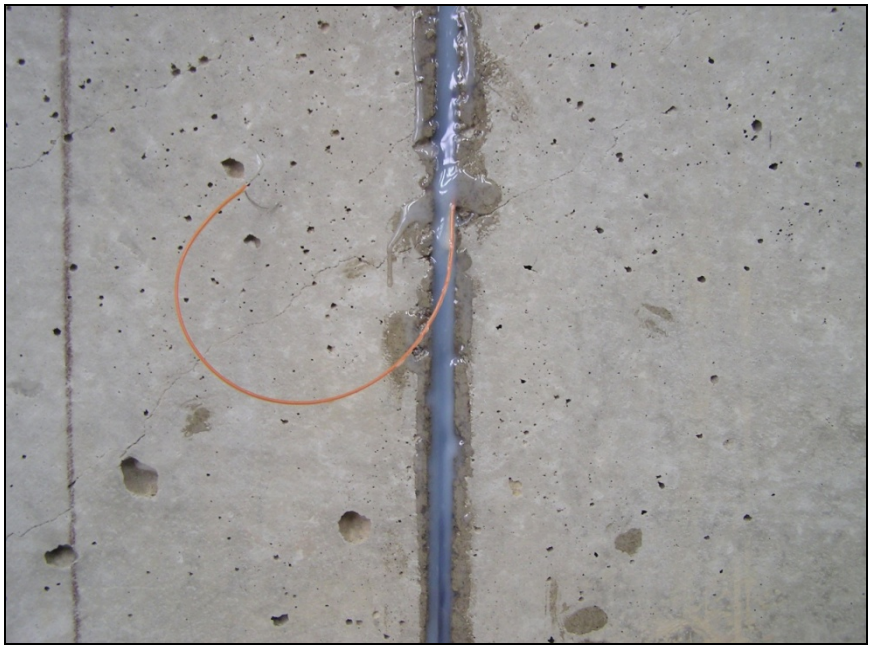


Figure 5.92: NSM installation: final product

5.5.2 Experimental results

Behavior of the NSM repair specimens is presented in the following section, with reference to the SPR 350 beams (*Higgins, et al. 2004b*). Shear load versus midspan displacement plots for each external stirrup repair specimen are presented in Figure 5.93. Shear load versus diagonal displacement and shear load versus average vertical strain plots are provided in Figure 5.94 and 5.95, respectively. Lastly, shear load versus typical integrally cast stirrup strains are shown in Figure 5.96. Crack map data for all the repaired beam specimens are shown in Figure 5.97 including crack formation for each load increment. The crack map data is replicated in Figure 5.98 for all the beam specimens with the cracks identified as precrack and repair.

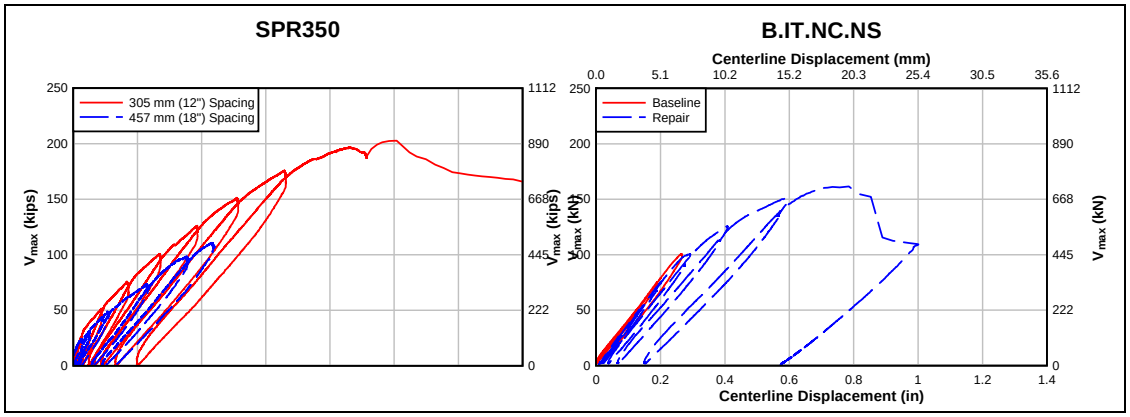


Figure 5.93: NSM repair specimen shear force versus centerline displacement

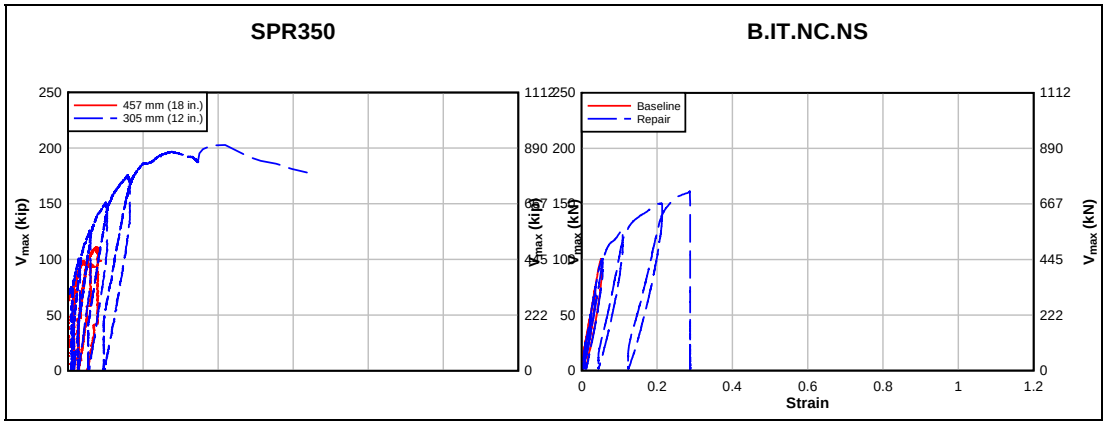


Figure 5.94: NSM repair specimen shear force versus diagonal displacement

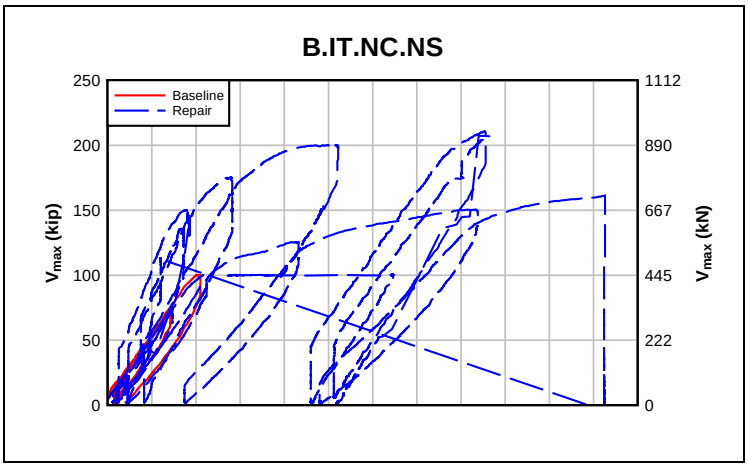


Figure 5.95: NSM repair specimen shear force versus average vertical strain

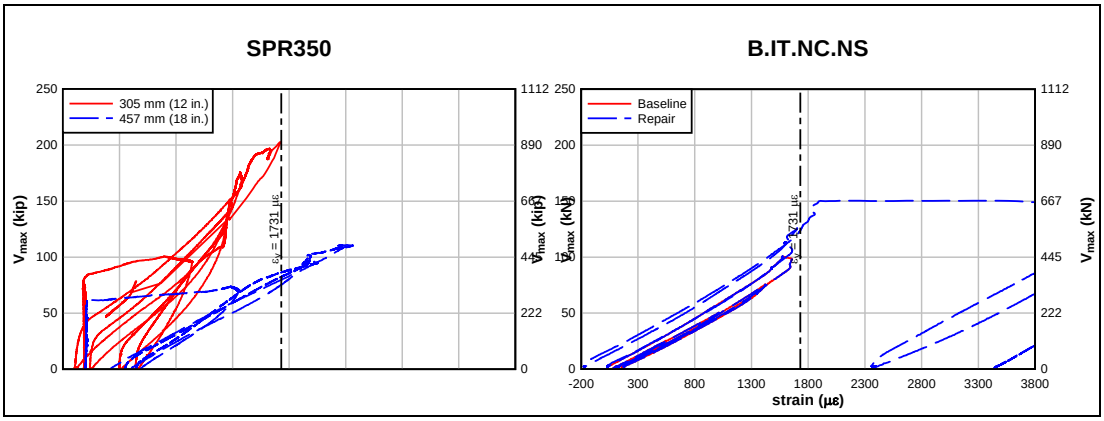


Figure 5.96: NSM repair specimen shear force versus typical internal stirrup strain

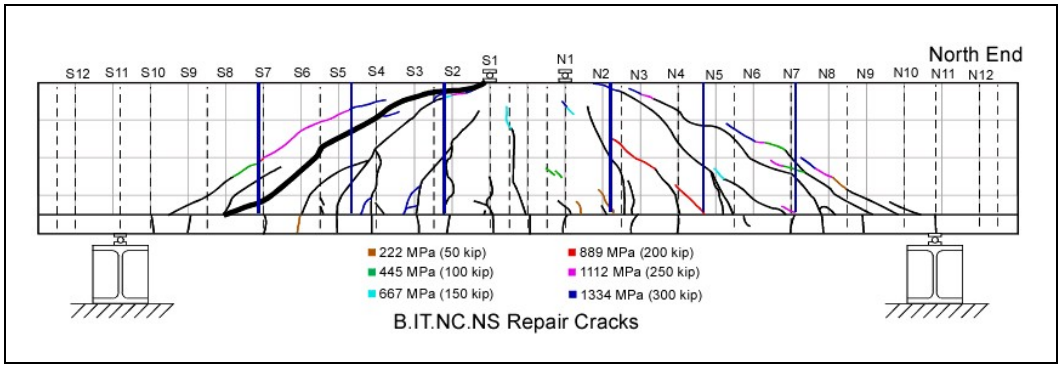


Figure 5.97: NSM specimens crack maps: individual load steps indicated

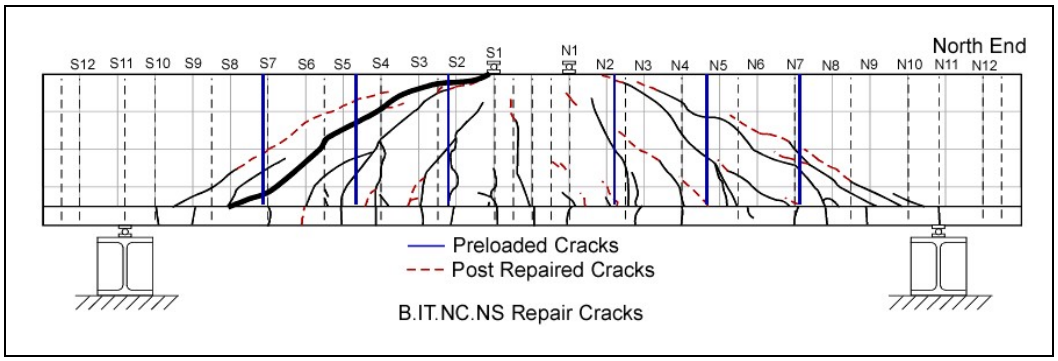


Figure 5.98: NSM repair specimens crack maps: precrack versus repair

The strength loading condition for the near surface mount beam illustrates the following: 1) strain throughout the depth of the member; 2) load sharing with integrally cast stirrups; 3) comparison of average vertical strain to carbon fiber strain; and 4) the distribution of strain within the carbon fiber at a fixed distance from a crack for the strength loading condition. The first comparison, shown in Figure 5.99 illustrates the strain data for two NSM strips at the same crack location. Figure 5.99 indicates the two curves begin to diverge from each other after the service level strains are exceeded, with a maximum deviation of approximately 1200με for the gage located on the west side of the specimen. Comparison of the integrally cast stirrup strain with that of the carbon fiber is shown in Figure 5.100. The service level range of data indicates consistent strain readings for internal stirrup 2N and the carbon fiber gages. However, as the applied shear increases, the carbon fiber begins to behave in a nonlinear fashion. At failure, only two of the NSM CFRP strips (one on each face) were effective in providing shear resistance to the section. The other strips crossed the diagonal crack at the compression zone and at the crack tip and thus could not constrain the crack. Failure was a shear-compression failure.

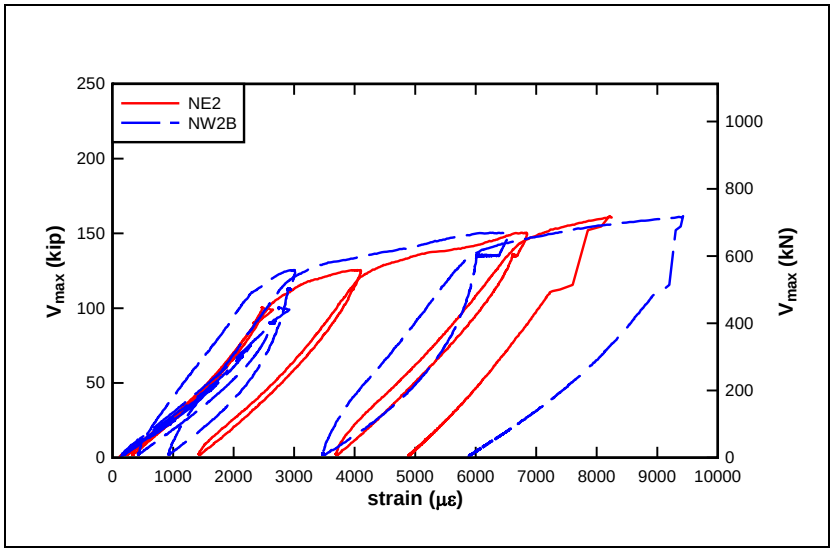


Figure 5.99: B.IT.NC.NS shear force versus NSM strain: strength loading

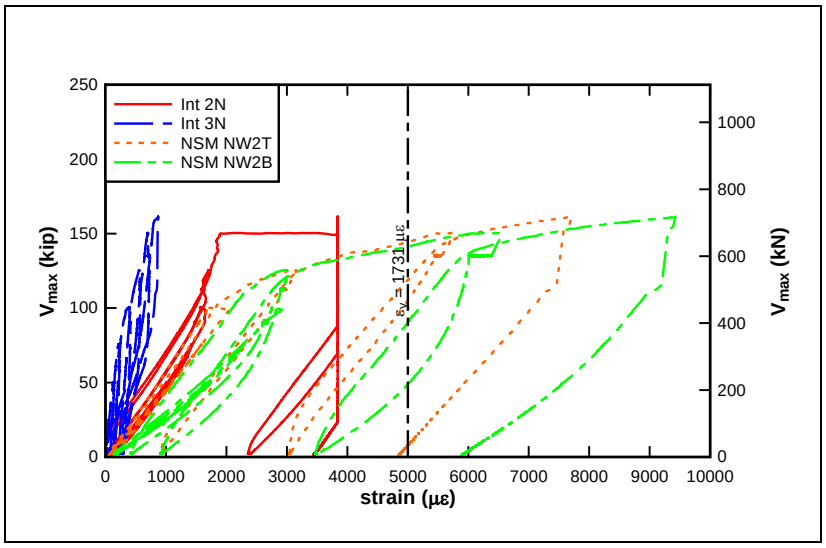


Figure 5.100: B.IT.NC.NS shear force versus NSM and integrally cast stirrup strain

5.5.3 Analytical methods

5.5.3.1 NSM stirrup repair: comparison with literature review

The bulk of the information for NSM repair has come from the available literature documented in Chapter 2. The issue related to the capacity estimates for NSM is focused on the local bond properties of the specific type of carbon fiber and epoxy. In the current investigation, the results from the work of Shield, et al., which investigated the bond properties of several epoxy products, produced a clear frontrunner with the 3M DP460NS epoxy (*Shield, et al.* 2005). The problem of relating the bond properties to the repair is outside the scope of work in the current project. However, work of De Lorenzis and that of Parretti and Nanni provide two differing values for the bond strength parameter used in design (*DeLorenzis 2004; Parretti and Nanni 2004*). As research outcomes continue to populate the literature, a better indication of the actual bond strength parameters and limits may be better established.

5.5.3.2 NSM stirrup repair: comparison with codes

The use of CFRP as a near surface mount application is a new and emerging technology. ACI 440, in conjunction with ACI 318 or R2K, similar to that of the CFRP repair specimen, was used as the primary comparison for the repair, as there is no additional guidance among the available international codes. The shear contribution from ACI 440 coupled with R2K and ACI 318 is shown in Table 5.19. As per ACI 440 guidelines, the FRP contribution to shear was dominated by bond strength and thus related to strain on the carbon fiber. The reduction in strain was based on the repair scheme – the NSM was discretely repaired on two sides as opposed to the three-sided U-wrap of the CFRP beam. The resulting increase in shear strength accounted for approximately 12 kN (3 kip) of shear. The R2K and ACI 440 strength estimate was close to the failure shear, although

the base specimen estimated by R2K was only 7 kN (1.5 kip) from the repair. The ACI 318 and ACI 440 strength estimate was very conservative, based substantially on the conservative base specimen capacity. As seen in this table, the contribution from the NSM CFPR is small in comparison to the base capacity, and future work must consider different alternative configurations (lower base strength with more NSM CFRP material) to clearly identify the supplemental shear contribution of the NSM CFRP.

Table 5.19: NSM beam code comparison

Specimen:	Method:	$V_{baseline}$		ACI 440 $V_{strengthened}$		V_{s_tot}		V_{EXP}		V_{EXP}/V_{calc}
		kN	kip	kN	kip	kN	kip	kN	kip	
B.IT.NC.NS	0.98*R2K	733	165	12	3	744	167	740	166	0.99
	ACI 318	509	115			521	117			1.42

5.5.3.3 NSM stirrup repair: comparison with R2K

Comparison of the strength gain utilizing R2K design curves was provided, similar to the previous specimens, as shown in Table 5.6. The additional shear pressure term from the baseline to failure curve resulted in a 73% efficiency rating. The result is lower than the 85% provided in the CFRP model; but again the small increase in load can result in varied results depending on the assumed intersection on the design curves.

5.5.3.4 NSM stirrup repair: comparison with VecTor2

The NSM beam was modeled with VecTor2 following the method outlined for CFRP. The meshing scheme for the NSM beam is shown in Figure 5.101. The primary difference between modeling the NSM and the CFRP was based on the effective width of NSM per unit height. The dimension for this value was taken as the three inside faces of the rectangular groove. Also, no increase in bond strength was provide at the bottom of the FRP strips, as the NSM repair scheme resulted in discrete strips, not 'U' shaped repairs.

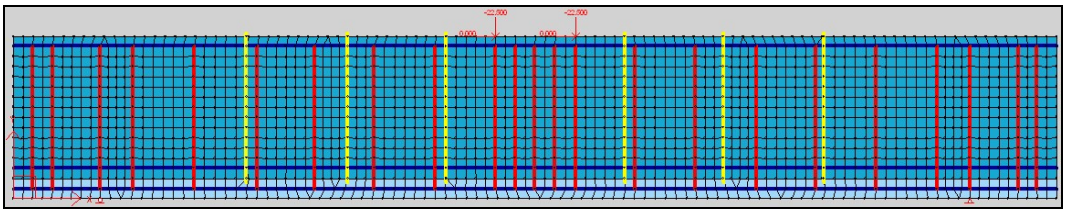


Figure 5.101: VecTor2 meshing scheme for B.IT.NC.NS

Results of the VecTor2 comparison for the NSM repair are shown in Table 5.20. The analysis resulted in a slight under-estimate of the beam strength (3%). Load-deformation response is shown in Figure 5.102. Similar to previous graphs, the initial stiffness of the VecTor2 graph is higher than the experimental data to account for lack of precracking. However, after this initial phase of the graph, the program corresponds well with the experimental data until premature softening occurs. The identical response was noted for the CFRP beam in which the VecTor2 response does not match that of the experimental data as slip becomes more prevalent, although ultimate load is comparable to the experimental work.

Table 5.20: NSM VecTor2 comparison

Specimen:	V_p (VecTor2)		V_{exp}		V_{exp} / Vp
	kN	kip	kN	kip	
B.IT.NC.NS	720	162	740	166	1.03

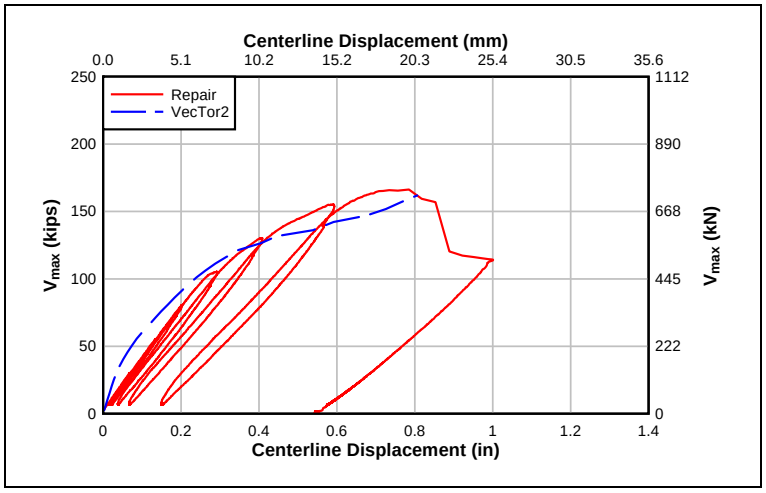


Figure 5.102: VecTor2 load-deformation response for B.IT.NC.NS

5.5.4 Discussion and design recommendations

The single specimen considered here provided a proof of concept, and more data are needed to further validate use of NSM FPR for shear strengthening. Thus no specific design recommendations are provided at this time for the NSM repair method. As of the publication of this document, additional work has been funded by the Oregon Department of Transportation to further investigate the use of NSM CFRP for shear strengthening. The limited test data available within the literature, coupled with this future work, may allow further design modifications to ACI 440 for NSM retrofits. However, at the present time, there is a lack of a consensus for use of NSM.

Based on the available test result, the observed behavior of the NSM repaired beam showed excellent crack restraint at the NSM locations. Figure 5.103 illustrates the specimen under load with cracks reducing in size in the vicinity of the NSM. Also, the epoxy used in the program bonded well to the surrounding concrete and may serve effectively for future applications. Failure photographs indicate failure occurred in the concrete section around the NSM CFRP strips.

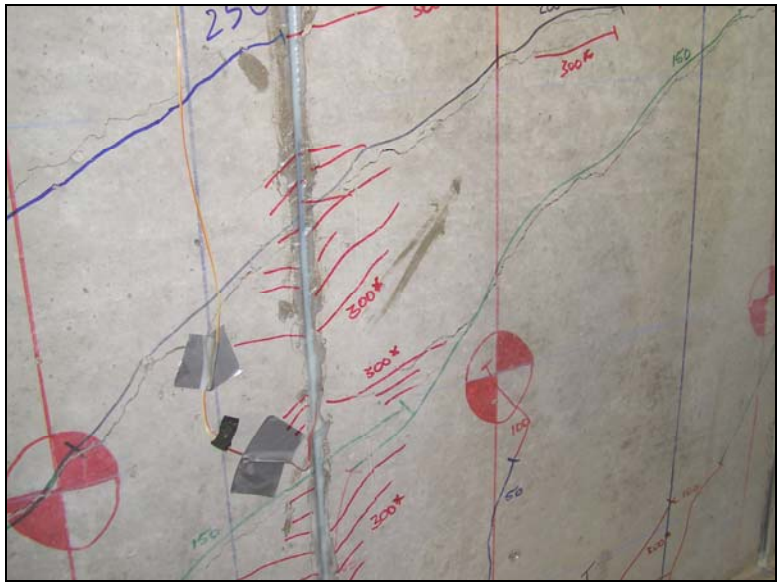


Figure 5.103: B.IT.NC.NS restraint of cracks under load

5.6 REPAIR METHODS FOR BENT CAPS: CFRP AND LONGITUDINAL POST-TENSIONING

The bent caps have behavior quite different from slender beams, and two specimens were investigated. One was repaired with surface-bonded CFRP strips and one with longitudinal post-tensioning. These are described in the subsequent sections.

5.6.1 Material and application details

Surface bonded CFRP

The material properties and the process for CFRP installation on the bent cap specimen were similar to that of the beam specimens, and the bent cap CFPR and bond component properties were reported previously in Tables 5.12 and 5.13. Installation of CFRP on the bent cap specimen is shown in Figures 5.104 through 5.106.



Figure 5.104: CFRP bent cap installation: epoxy injection



Figure 5.105: CFRP bent cap installation: primer (left) and putty (right)



Figure 5.106: CFRP bent cap installation: strip installation

Longitudinal post-tensioning

Longitudinal post-tensioning for the bent cap specimen required few materials. For an in-service repair, two reaction beams and post-tensioning rods are needed; post-tensioning of the individual bars would be accomplished by a center hole ram, typically used in the prestressed industry. For the laboratory specimen, a 3.56 MN (800 kip) hydraulic cylinder and associated 1.34 MN (300 kip) load cell were used to more readily control the post-tensioning force. The test setup for the post-tensioning of the bent cap is shown in Figures 5.107 and 5.108. The test setup included two W12X120 reaction beams mounted on temporary supports to provide the post-tensioning force at the lowest possible point on the section, but they were located above the sensors to measure relative bar slip of the anchored flexural steel. The reaction beams were post-tensioned using four 32 mm (1.25 in.) diameter 1034 MPa (150 ksi) high strength Dywidag bars; the bars were instrumented to indicate the relative force distribution from the load cell, to provide uniform load distribution in all the bars. Final installation of the post-tensioning system is shown in Figures 5.109 and 5.110. The initial post-tensioning force applied to specimen was 667 kN (150 kips).

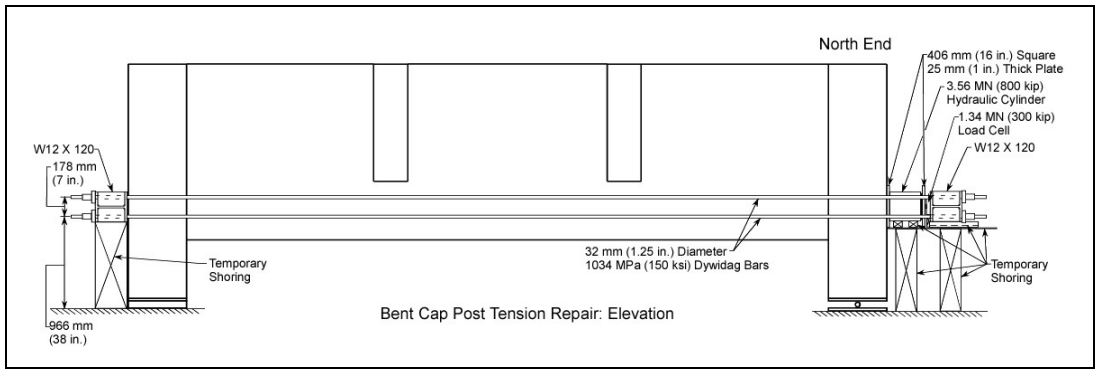


Figure 5.107: Specimen D.IT.C.PT repair elevation

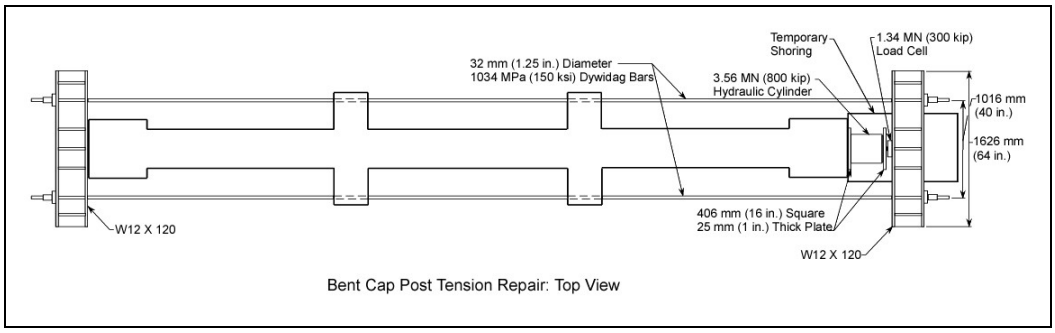


Figure 5.108: Specimen D.IT.C.PT repair top view



Figure 5.109: Post-tensioned bent cap installation



Figure 5.110: Post-tensioned bent cap installation: adjacent reaction beam

5.6.2 Experimental results

The two repaired specimens were compared with a previous specimen tested at OSU with identical geometric and similar material properties, but which was not repaired prior to failure. The bent cap specimens provided a large array of data to investigate global behavior in terms of midspan and stub girder displacement, average vertical strain data, and column lateral displacements. The specimens also provided a great deal of local behavior for the integrally cast stirrups, flexural slip of the bars embedded into the column, as well as flexural strains within the column and at midspan. In the current study, however, the focus was on data pertaining to the integrally cast stirrup strains. The results of internal strain interactions with the repair media provided a measure of effectiveness for each repair over the service and strength loading cycles.

Crack map data for the repair specimens is shown for the baseline and repair case in Figure 5.111; failure shear for each specimen is shown in Table 5.20. Global load versus displacement graphs for midspan, south and north stubs are shown in Figures 5.112 through 5.114.

The control specimen failed before the next full load step with a large displacement at failure. (Recall that each stub was loaded first individually in a half-step loading sequence, then together in a full-step sequence.) The carbon fiber specimen failed at just over 1335 kN (300 kip) due to abrupt bond failure between the CFRP and concrete, but it failed at a larger displacement than the post-tensioned specimen. Video evidence of the failure showed that debonding of one strip resulted in a domino effect for the remaining strips and eventually the specimen itself.

The post-tensioned specimen behavior with 667 kN (150 kips) of post-tensioning force indicated that failure was imminent at a shear force lower than the carbon fiber repair, as failure was about to occur at the south end. As the expected strength gain was only marginal at this stage, the specimen was unloaded and a higher post-tensioned force 1112 kN (250 kips) was applied to the specimen, which was again loaded to essentially the same load level and failure occurred. The increased post-tensioning force did not increase specimen capacity, although it did reduce over member deformation.

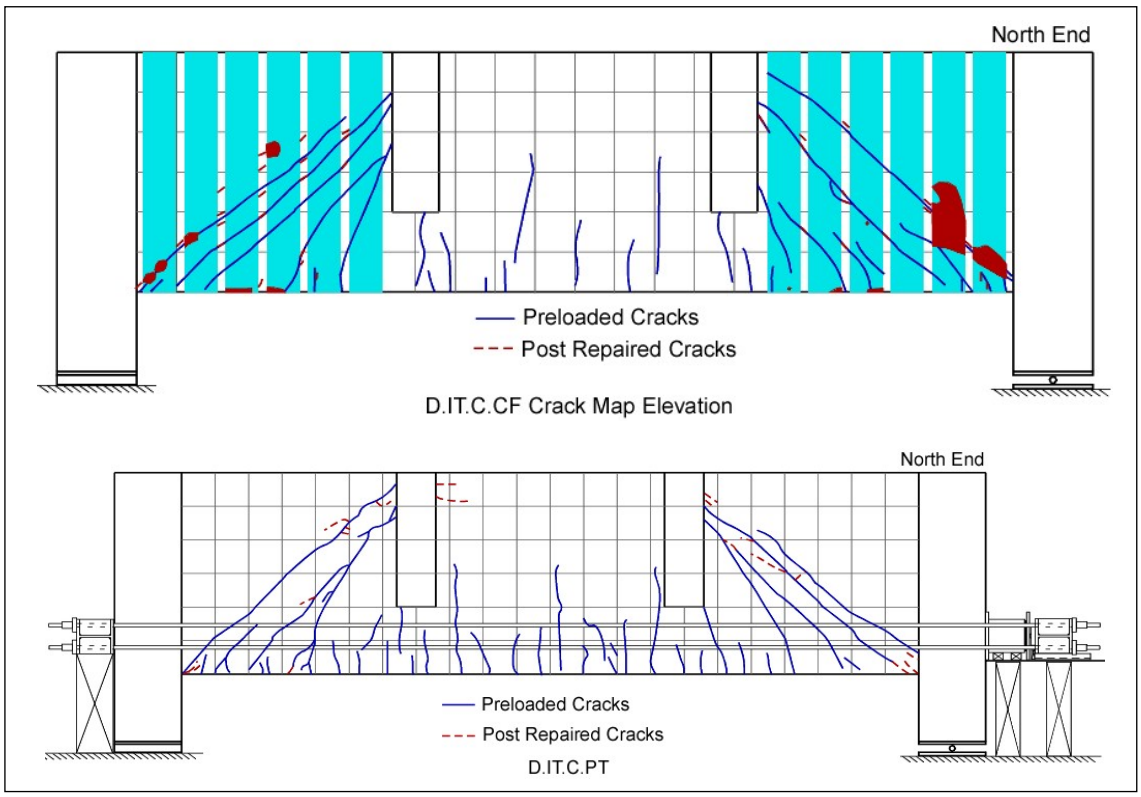


Figure 5.111: Baseline and strength loading crack maps for bent cap specimens

Table 5.20: Bent cap specimen failure shear including specimen self-weight

Specimen:	Failure Shear:	
	kN	[kips]
D.T.C.PT	1398	314
D.T.C.CF	1527	343

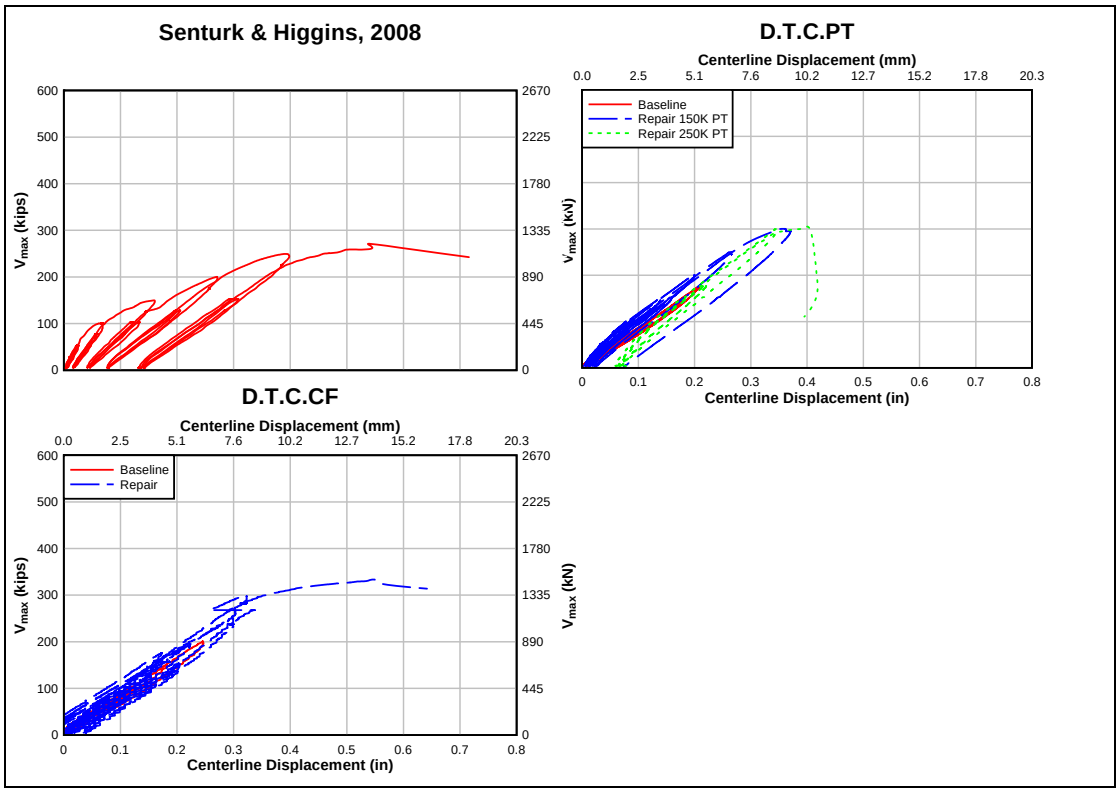


Figure 5.112: Bent cap shear force versus centerline displacement: ultimate loading condition

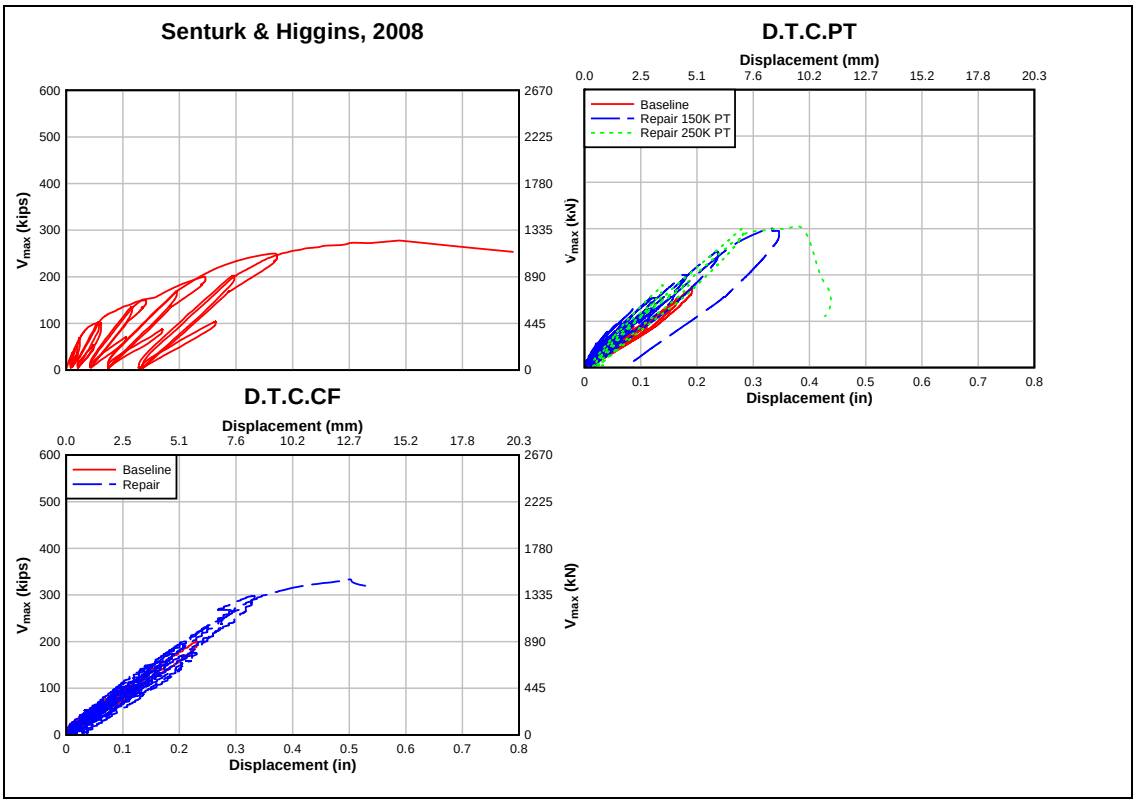


Figure 5.113: Bent cap shear force versus south stub girder displacement: ultimate loading condition

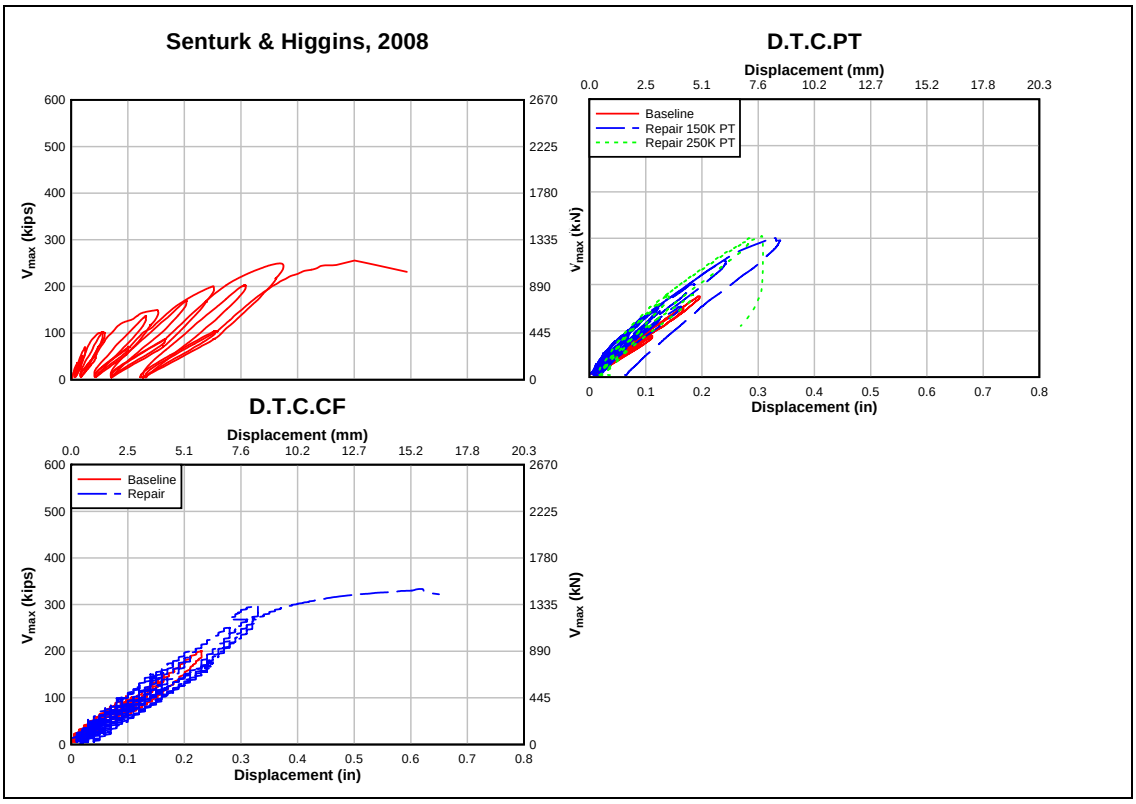


Figure 5.114: Bent cap shear force versus north stub girder displacement: ultimate loading condition

The tensile diagonal data in Figure 4.115 indicates the carbon fiber repair specimen showed lower displacement values compared to the control specimen for all but the last load step. The post-tensioned specimen exhibited a similar behavior compared to the service level loading, with gradually increasing displacement until failure.

Average vertical strain data in Figure 5.116 indicates the south end of the carbon fiber repaired bent cap progressed through the loading cycle with a near linear behavior (as the south end remained intact throughout the test). The behavior of the post-tensioned specimen along the eventual failure side shows an improvement over the baseline curve. At the higher post-tensioning cycle close to specimen failure, the horizontal line indicates significant panel elongation with no additional shear.

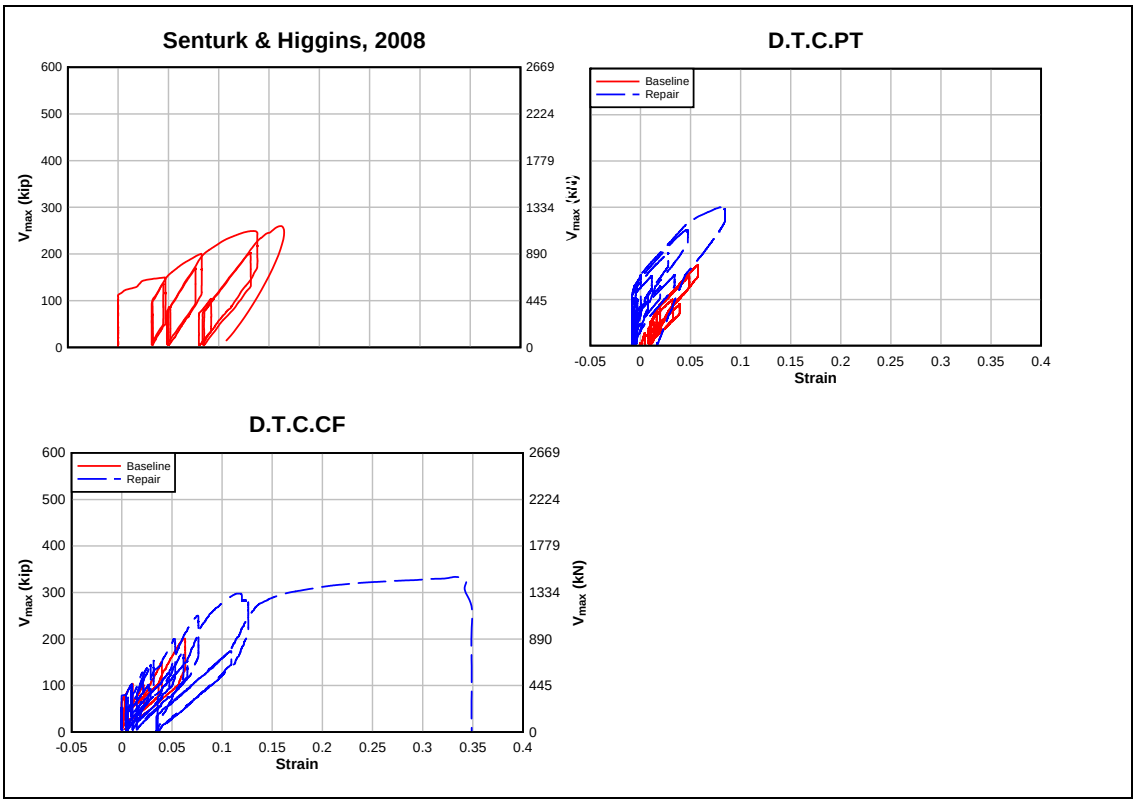


Figure 5.115: Bent cap shear force versus north tension diagonal: ultimate loading condition

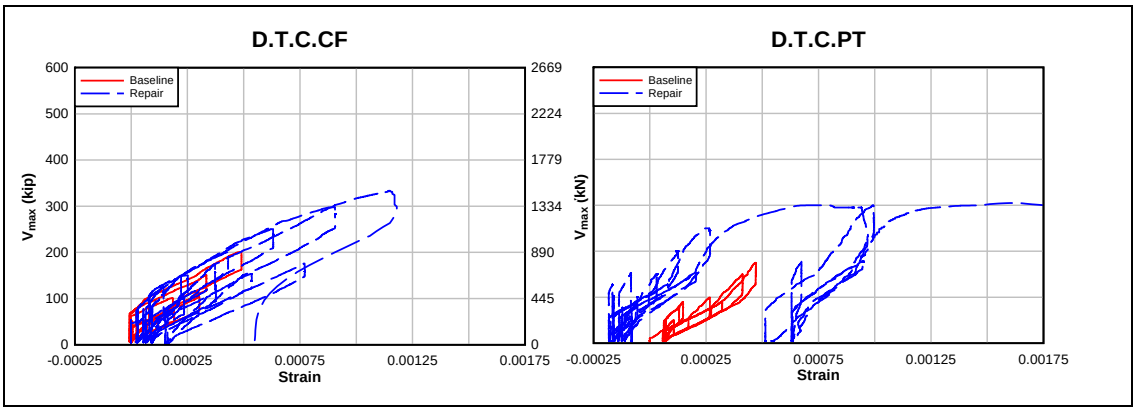


Figure 5.116: Bent cap shear force versus south average vertical strain: ultimate loading condition

Data for the south tensile diagonal is shown in Figure 5.117. The behavior of the post-tensioned specimen mirrors the initial load steps of the north end, discounting the eventual failure event with typical strain less than 0.05. The strain range is well below the other two specimens. The carbon fiber repair specimen exhibited behavior that is similar to the average vertical strain, with minor initial strain followed by a near linear behavior until failure occurred at the north end.

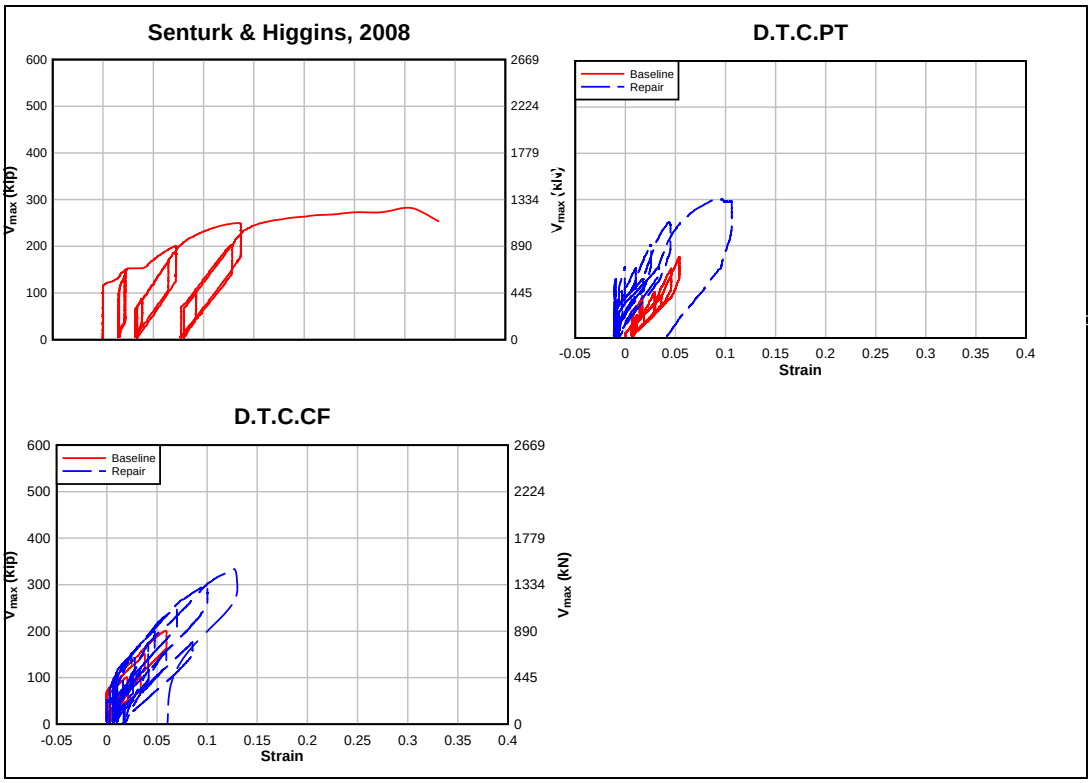


Figure 5.117: Bent cap shear force versus south tension diagonal: ultimate loading condition

Local behavior of the north and south integrally cast stirrups are shown in Figures 5.118 and 5.119, respectively. For the north end, the internal stirrup achieves yield during the service level range and continues into strain hardening as is evident in the figure for the CFRP-strengthened bent cap specimen. The post-tensioned specimen does not achieve yield at the north end. The post-tensioned specimen does achieve yield and continues into strain hardening at the south end, which is where failure occurred. The CFRP repaired bent cap also achieves yield just prior to failure. The slope of the repair curves for the two repair specimens are quite different, which indicates the CFRP repaired bent cap provides greater load sharing between the integrally cast stirrups and the carbon fiber strips.

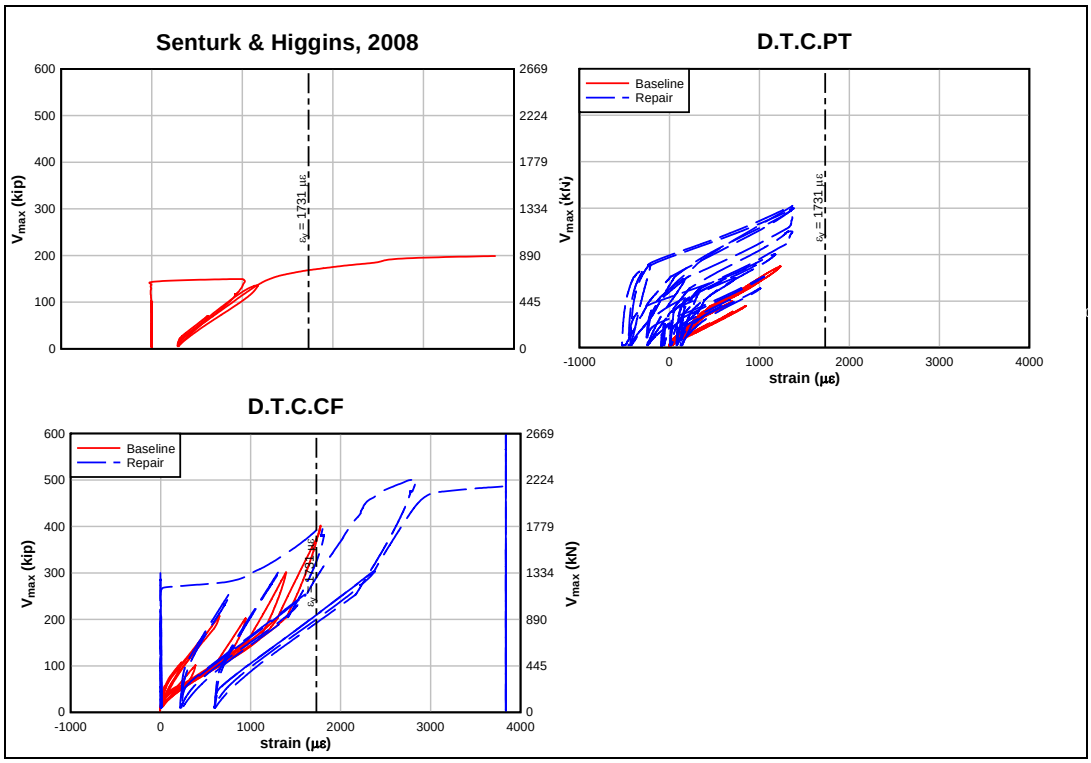


Figure 5.118: Bent cap shear force versus typical north internal stirrup: ultimate loading condition

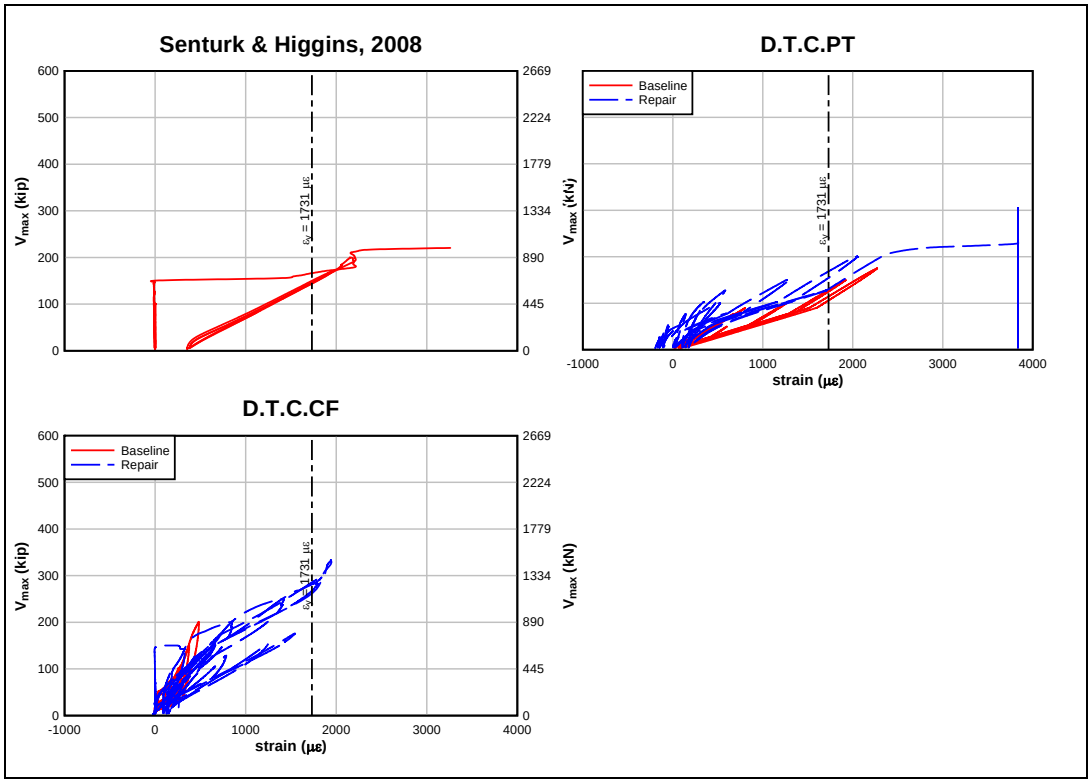


Figure 5.119: Bent cap shear force versus typical south internal stirrup: ultimate loading condition

Strain compatibility and load sharing of the carbon fiber repair specimen are shown in Figures 5.120 and 5.121. The average vertical strain values are significantly less than that experienced in the carbon fiber for the higher load steps. In the higher load steps, the carbon fiber strain is essentially twice that of the internal stirrup for the whole step values. The deep beams produce non-uniform strains that concentrate at the diagonal crack locations; thus results from slender beams that provide more uniform strain distributions may not be directly applicable to deep beam specimens.

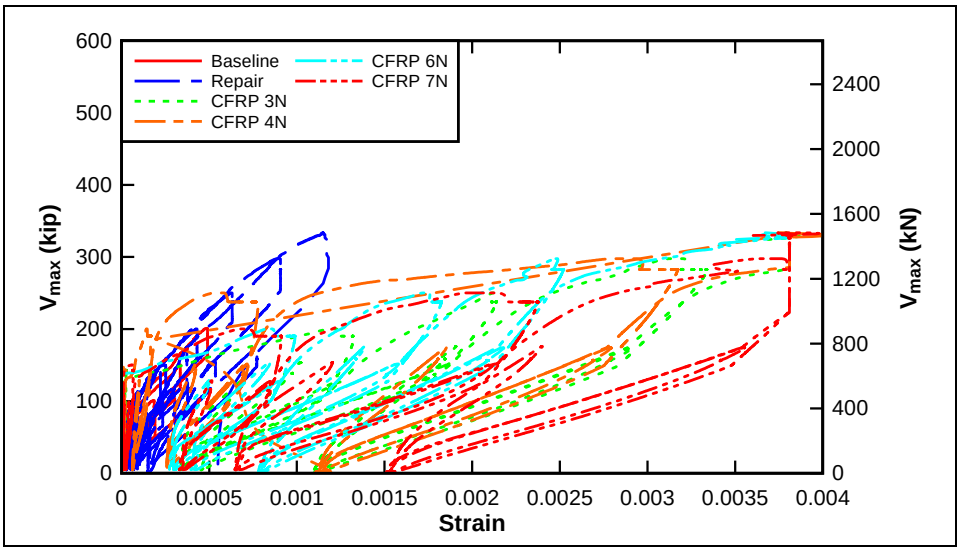


Figure 5.120: Bent cap D.T.C.CF shear force versus CFRP and average vertical strain: strength loading condition

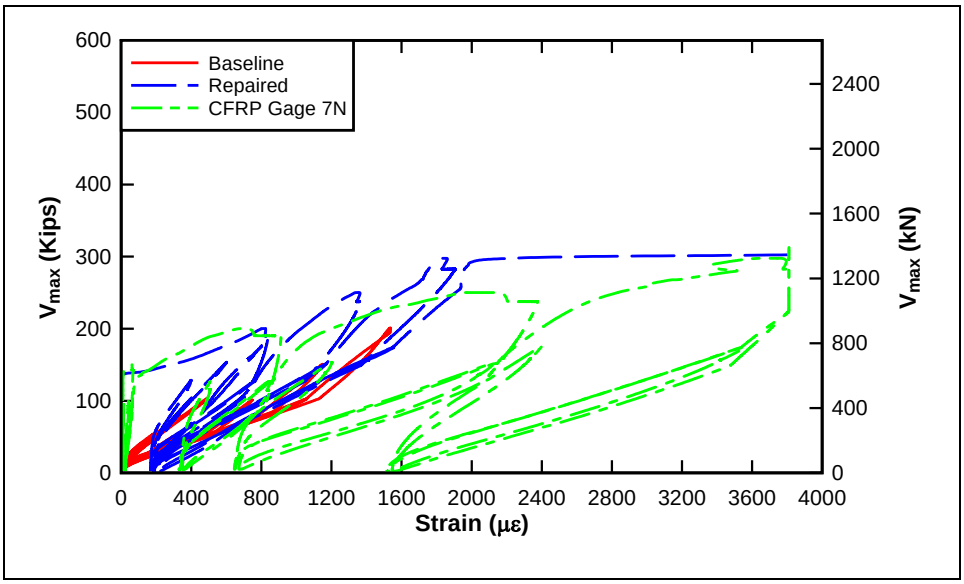


Figure 5.121: Bent cap D.T.C.CF shear force versus CFRP and integrally cast stirrup strain: strength loading condition

5.6.3 Analytical methods

5.6.3.1 Bent cap comparison: literature review

The single research paper included in Chapter 2 for post-tensioning of bent cap specimens illustrated a significant strength gain if the dominant shear crack was epoxy injected prior to post-tensioning, although no strength estimates due to post-tensioning were provided. Validation of this conclusion is not applicable to the current study, as only one bent cap specimen was included, whereas a minimum of two is needed for validation: a control specimen repaired with epoxy injection, then post-tensioned, and a second specimen post-tensioned without epoxy injection.

For the scaled specimens in the literature, the post-tensioning repair is based on several factors related to aggregate interlock across the crack. For a shallow crack angle with wide crack widths, the application of post-tensioning resulted in a reduction in strength, and the authors suggest the post-tensioning induced additional slip along the failure crack. For the current study, the crack angle was approximately 45 degrees; the degree of aggregate interlock could not be directly measured. It is worth noting that the Zararis Method assumes no aggregate interlock, and crack widths open perpendicular to the eventual failure crack (*Zararis 2003*). For an epoxy injected repair specimen, a diagonal crack will likely form at a slightly higher load adjacent to the injected crack. Thus, according to Zararis' Method, the capacity should be the same with or without epoxy injection, as the new crack provides no aggregate interlock, and the capacity is again governed by the steel crossing the crack. The two conflicting observations suggest the need for a future investigation with different crack inclinations and varying level of post-tensioning with and without epoxy injection of diagonal cracks. The current method without epoxy injection over-estimated the strength from post-tensioning and would produce unconservative results.

5.6.3.2 Bent cap modeling: ACI 440

ACI 440 was used to model the shear contribution for the bent cap repair specimen, similar to that of the CFRP repaired beam specimen. However, the base specimen capacity in this case was modeled after the Modified Zararis Method (*Higgins, et al. 2008*). Results are shown in Table 5.21. The shear capacity was limited by bond stress for the U-wrap configuration to provide an effective CFRP stress of 112 ksi. For the six strips located on each side of the bent caps, the area of CFRP was 0.78 in^2. Including the bond reduction factor ψ (0.85 for U-wrapping schemes), the ψV_f was computed as 74 kips. When used in the modified Zararis method (described in *Higgins, et al. 2008*), this contribution to member strength is reduced by half due to the equilibrium considerations (described below). Thus the predicted bend cap strength is conservative relative to the experimental result. However, the prediction of an additional shear contribution of 74 kips, if directly superimposed on a base predicted strength, would yield unconservative results.

Table 5.21: Bent cap capacity predictions

			Modified Zararis				Nominal Strut and Tie			VecTor2	
		Experimental	Base		Repaired		Base	Repaired		Repaired	
		Shear	Shear	ACI 440	Shear		Shear	Shear		Shear	
Specimen	Units	Strength	Strength	ontributio	Strength		Strength	Strength		Strength	
ID		V_{Exp}	V_{base}	ψV_f	$V_{predicted}$	$V_{exp}/V_{predicted}$	V_{base}	$V_{predicted}$	$V_{exp}/V_{predicted}$	$V_{predicted}$	$V_{exp}/V_{predicted}$
D.T.C.PT	kN	1397	1385	-	2051	0.68	1019	1027	1.36	1343	1.04
	Kips	314	311	-	461		229	231		302	
D.T.C.CF	kN	1526	1304	331	1467	1.04	836	1241	1.23	1036	1.47
	kips	343	293	74	329.7		188	279		233	

5.6.3.3 Bent cap modeling: strut-and-tie method

STM provides a general framework for discretization of a structure into regions that follow Bernoulli beam behavior and those that do not. Recall from Chapter 2 that sections with complex nonlinear stress distributions are referred to as D regions, whereas sections which conform to the Bernoulli beam behavior are denoted as B regions. Within a given structure, D and B regions may both be present, or only one may be present. For deep beams, the modeling of the D regions can be a complex task if performed by hand. Changes in the inclination of a truss or additions of more complex elements are rapidly re-evaluated by a computer.

Senturk utilized the Computer Aided Strut-and-Tie (CAST) software developed by Tjihn and Kuchma at the University of Illinois at Urbana-Champaign to evaluate the STM models used in his study. The program permits a graphical working environment for engineers to manipulate the size of the D regions, solve for internal member forces, and select the dimension of struts and reinforcement for ties. Changes to the location of nodes can be accomplished at any stage of the analysis. The program contains a capacity estimation tool, based on the ratio of the applied stress to the limits provided for the components. CAST follows the ACI 318-05 Appendix A method as well as user modifiable parameters to simulate the international code variations.

Senturk investigated three STM models for the specimens in his research. The first model was the simplest, with only two nodes and no representation of the vertical reinforcing. The second model included the effects of the vertical reinforcing, lumped as one vertical tension tie. The last model utilized a series of struts and ties in order to capture the arching affect of the specimen. Results for all three cases were conservative with respect to the laboratory specimens. The simple example provided the most conservative results, whereas the second model predicted a lower but still conservative ultimate shear load. The complex model was sensitive to minor changes in nodal geometry, resulting in quite different results for modest differences in nodal locations. Overall, each model provided a conservative design, but this approach may be cost prohibitive for evaluation of existing structures.

Senturk's work provided the basis for the STM models in the existing study using CAST. The STM leaves many possibilities for modeling the member. The primary components of the second model used by Senturk were used in the current study, as it resulted in a closer estimate of the base specimen with little sensitivity to nodal locations, and it

included transverse reinforcing. The model consisted of four nodes, as shown in Figure 5.122.

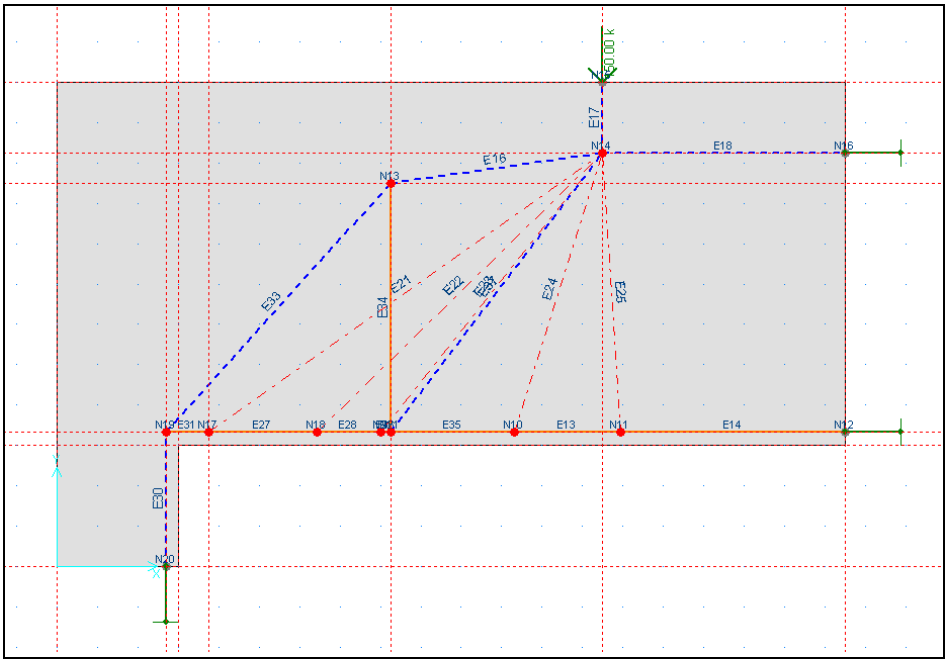


Figure 5.122: CAST STM model base specimen: member and node assignments

The procedures for constructing the STM models in CAST followed the work of Senturk and are subsequently summarized (*Senturk 2008*). The first step in creating a model in CAST is to define a series of vertical and horizontal guidelines which aid in constructing the member boundaries and the intersection of interior nodes. The use of guidelines guarantees that the nodal points between elements are coincident, and it provides for easy modification of the location of the nodes by simply moving the guidelines as opposed to manually moving each individual node. Once the guidelines are complete, the STM elements are created, material properties for concrete and steel are entered, and boundary conditions and loads are applied. Member widths are also assigned within the model.

Member and node assignments for the base STM model are shown in Figure 5.122. A common issue regarding the development of any STM relates to the effective width of the elements. The effective width of the top horizontal prismatic strut, representing the compression block, denoted as element S4, was set equal to:

$$w_c = k \cdot d \tag{5-21}$$

where d (mm or in.) is the effective depth of the section at midspan; and k is taken from classical beam theory as:

$$k = \sqrt{(\rho \cdot n)^2 + 2 \cdot \rho \cdot n} - \rho \cdot n \quad \textbf{(5-22)}$$

where n is the modular ratio between steel and concrete; and ρ is the longitudinal reinforcement ratio taken at midspan.

Next, the effective width of the vertical prismatic strut at the application of load was taken equal to the width of the stub girders that framed into the bent – 406 mm (16 in.). The final prismatic strut representing the vertical column at the base of the specimen was given a width equal to half the column width – 305 mm (12 in.) – coincident with its centerline.

Assignment of the tension ties was based on their relative location in the section. For the longitudinal steel, the effective width was taken as twice the distance bounded by the cross section and the centroid of the lowest row of steel. The effective width for the internal stirrups was taken as the total steel width for the lumped stirrups within the shear span. However, the program provides only one material property identification for steel. In other words, there was no way to differentiate the different yield strength of the flexural and transverse steel. This was resolved by reducing the lumped stirrup area to coincide with the reduction in yield strength.

As a side note, the flexural cutoffs were modeled following the ACI requirement for development length such that the node locations for the flexural bars coincided with their fully developed strength. Also, inversion of the stiffness matrix created by the program failed if an STM node attached only two elements. This condition is not explicitly described in the accompanying literature; however, it can be resolved. By attaching an additional STM member from the two-member node to a second node, without assigning the element as either a strut or tie, the program will internally assign it as a zero force member; it is used for assembly and inversion of the stiffness matrix only. These members are denoted as 'stabilizer' elements in the program documentation.

The remaining compressive strut elements were constructed assuming bottle-shaped for the ACI condition. The location of node N13, which connects the lumped stirrup tie to the two compression struts was arbitrarily placed at 1/3 the height from the top of the bent. It was positioned horizontally at the midpoint of the shear span. The effective width of the struts was taken from Senturk to be:

$$w_d = w_c \cdot \cos\theta + b_{wgirder} \sin\theta \quad \textbf{(5-23)}$$

where θ is the angle between the strut and the x-axis; w_c was previously shown; and $b_{w\ girder}$ (mm/in) is the width of the stub girders that frame into the bent.

The initial locations of the nodes were modified in order to obtain the highest strength capacity while providing the failure mode observed in the experimental program. Senturk experienced specimen failure as a result of yielding of flexural bars within the column and stirrup failure simultaneously. Modifying the model to include failure of

both elements provides the failure mechanism representative of the laboratory specimens. Senturk achieved the largest specimen capacity by increasing the inclination of the first strut from the beam-column connection. This was accomplished by moving the vertical prismatic strut representing the column member horizontally toward the shear span, which in turn increased the angle of the first compression strut and reduced the effective width of the column prismatic strut (which was bound by the exterior edge of the column). In this respect, arbitrarily moving the node to the limit of the column was not possible, as it resulted in failure of the vertical prismatic node.

Senturk also increased the capacity of the base specimen by changing the location of the upper node for the lumped stirrup tie. By decreasing the inclusive angle between the two struts at this node, the capacity increased. Thus, by adjusting the two nodes, Senturk was able to obtain the highest capacity for the given failure mode. Failure of the base STM model is shown in Figure 5.123.

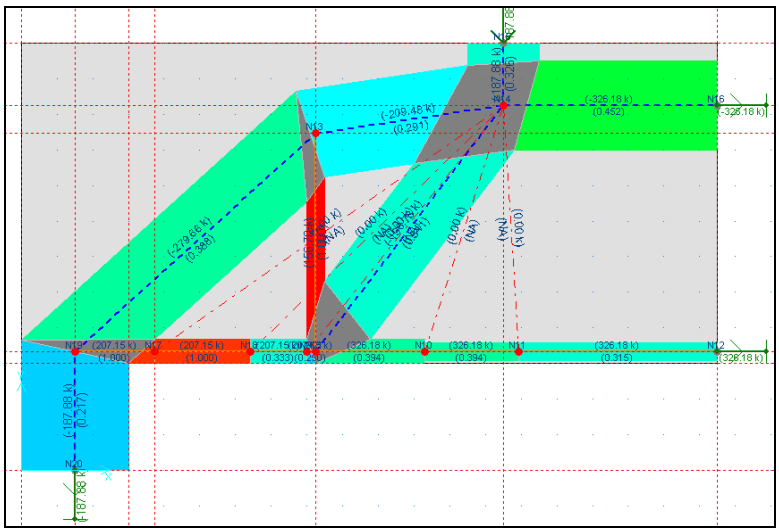


Figure 5.123: CAST STM model base specimen governing member/load

With a few exceptions, modeling of the two bent caps in the current study followed a similar trial and error method in order to reach the highest base specimen capacity. First, the strength increase for the post-tensioned specimen followed after moving the vertical column strut toward the shear span. Moving the second node upward also increased capacity, but it was limited to a height of 100 mm (4 in.) measured from the horizontal compression zone. Further vertical movement of the node would result in two parallel struts connected by a horizontal compression zone. The visualization of forces for such a model is unrealistic. For the CFRP repair specimen, the concrete strength resulted in the vertical strut placed at its vertical centroid as opposed to close to the beam-column interface. The second node was moved vertically upward in order to increase the capacity. The failure load and distribution of forces for the CFRP and post-tensioned specimens are shown in Figures 5.124 and 5.125 respectively.

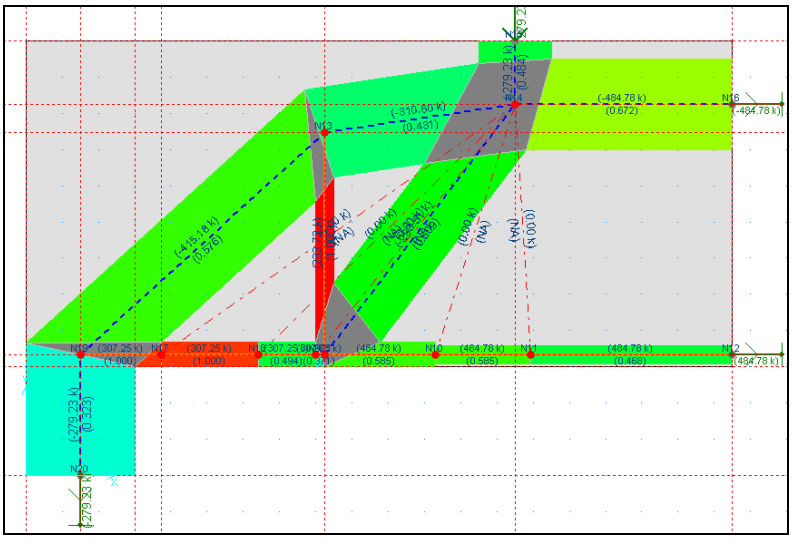


Figure 5.124: D.T.C.CF failure load – CAST STM model

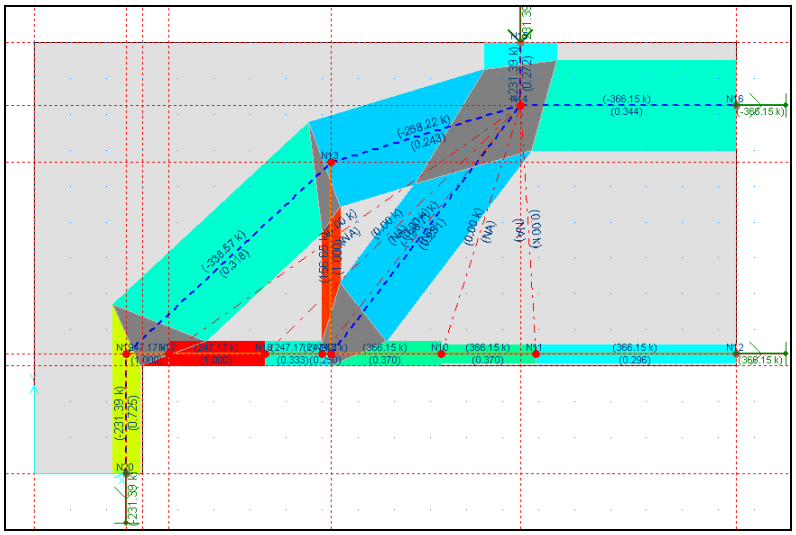


Figure 5.125: D.T.C.PT failure load – CAST STM model

Another issue to note is that the CAST program assigns strength reduction factors and over strength parameters for each strut, tie, and node. The nominal capacity of any structure can be found, but all the default reduction and over strength factors must be changed to 1.0. The program provides the option to use the over strength or reduction factors. However, if neither option is checked, the program internally does use the over strength factors if they are greater than 1. Several international codes utilize a combination of an efficiency factor used in conjunction with a strength reduction factor. In order to compare the codes on a common threshold, the final factors for shear resistance (including efficiency and strength reduction factors where appropriate) are

shown in Table 5.22. The weighted averages for each code reduction factor are show in Figure 5.126.

Table 5.22: STM strength reduction factors for various elements

Element Strength Reduction Factors							
	Code:	ACI	AASHTO	Canadian	Eurocode2	CEB-FIP1990	CEB-FIP1999
Element:	Prismatic Strut	0.638	0.595	0.6375	0.667	0.521	0.515
	Other Shape	0.478	0.595	0.6375	0.368	0.368	0.412
	Tension Tie	0.75	0.9	0.9	0.87	0.87	0.87
Node:	No Tension Ties	0.638	0.595	0.595	0.613	0.560	0.680
	1 Tension Tie	0.510	0.525	0.525	0.521	0.395	-[2]
	2 Tension Ties	0.383	0.455	0.455	0.460	0.395	-[2]

[1]Largest value shown. Can vary to as low as 0.23184

[2]For nodes with tensile forces, the code requires a check of the anchorage length or bearing capacity. Compression ties are given a value of 0.80

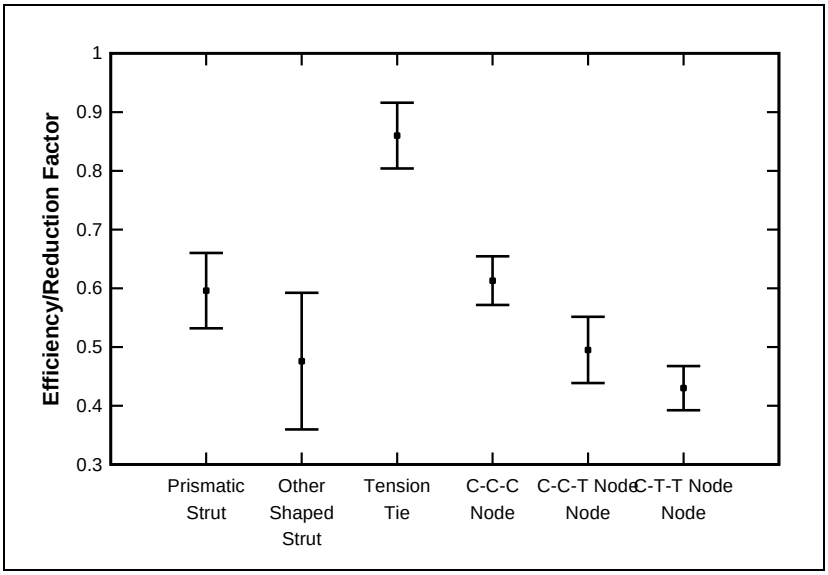


Figure 5.126: STM efficiency factors from international codes

Prior to discussion of results, the modeling of the repair types within the CAST program is described. For the post-tensioned specimen, the yield strength of the steel was increased to reflect the additional flexural capacity provided by post-tensioning. However, the internal stirrup area was also subsequently reduced to offset the increased yield strength of the longitudinal steel (only one yield strength parameter for steel is available). As such, the strength increase estimate was marginal at best.

The carbon fiber repaired specimen was modeled by increasing the area of steel to coincide with the ACI 440 contribution for shear. With a large increase in capacity for the vertical tie, the failure was still dominated by the flexural bars at the beam-column

interface, which resulted in little to no increase in strength. In reality, the repair did provide additional strength.

In order to check if the flexural bars within the column failed before or after the FRP failed in bond, the strain data was examined. Recall that the two anchorage bars embedded into each column were instrumented at three locations, each along the embedment length. The strain data indicated that only two of the strain gages (the east and west inner bars at the north end) reached yield prior to debonding of the FRP. The remaining active gages did not reach yield until after failure. Thus, increasing the capacity of the flexural bars was warranted in the CAST model. The modeling of the bars into the column do not take into account the detailing (hook, mechanical anchorage, etc). Therefore, the capacity of the bars was increased due to the clamping force provided by the applied load within the column. Koester and Higgins provided an increase in the allowable bond stress for a bar in such a configuration as shown below (*Koester and Higgins in press*).

$$\mu_{\text{mod}} = \left(0.8 + \frac{P}{800}\right) \cdot \mu_{ave} \qquad \textbf{(5-24)}$$

where P is the active confining stress in the column.

For the current investigation, the failure shear was divided by the column area to obtain the active confining pressure. The resulting increase in area for the bars permitted an increase in the shear strength due to the CFRP and provided failure in the vertical tie/flexural bars.

5.6.3.4 Bent cap modeling: Zararis Method

Previous work at OSU by Senturk (Senturk 2008) included the prediction of shear capacity based on the Zararis Method (*Zararis 2003*). Recall from Chapter 2 that this method uses a reduced compression block based on the moment equilibrium calculated on two wedge shapes (above and below the critical shear crack). Using the reduced compression block, the capacity of the section is determined by moment equilibrium of the upper wedge (that includes the concrete compression block). However, the original method over-estimated the capacity of the laboratory specimens, specifically for the horizontal compressive forces. Horizontal equilibrium was not satisfied, due to the limited longitudinal reinforcement embedded in the columns. Also, the method disregards the horizontal shear force contribution of the vertical web steel, which may be necessary to ensure horizontal force equilibrium.

The Zararis Method was modified by limiting the concrete compressive strength and by taking into account the horizontal shear contribution of the stirrups. The compressive strength was limited to $0.85*f_c'$ as a result of compression softening due to indirect loading and lack of confinement of the compression zone. The horizontal shear force contribution of the web reinforcement was taken as shown in Equation 5-25 below.

$$V_{sd} = 0.4 \cdot V_s \cdot \tan\varphi \tag{5-25}$$

For the modified analysis, the initial values of c, c_s, and P_u are computed using the original Zararis Method, but utilizing a reduced concrete strength as previously noted (where c is the depth of the compression block considering flexure alone, c_s is the reduced depth of the compression zone due to shear induced diagonal cracking, and P_u is the axial force equilibrium at capacity). Horizontal equilibrium is checked against the compression force. The first analysis case assumes the tension capacity of the available longitudinal reinforcement, denoted in Equation 5-26, is greater than or equal to the compressive force.

$$T_{\max} = A_s f_y \geq C = 0.85 \cdot f_c^{'} \cdot b \cdot c_s \tag{5-26}$$

In this case, the strength is governed by the concrete, and the original equation for shear capacity is used. If Equation 5-11 is not satisfied, applicability of a second case is checked, where the tension capacity of the longitudinal steel plus the horizontal shear force contribution from the web reinforcement is greater than the compressive force, as shown in Equation 5-27.

$$T_{\max} + V_{sd} \geq C = 0.85 \cdot f_c^{'} \cdot b \cdot c_s \tag{5-27}$$

In this case, the capacity is calculated as shown in Equation 5-28, where the horizontal shear component of the stirrups is limited to Equation 5-29.

$$V_{sd,limited} = C - T_{\max} \text{ if } T_{\max} + V_{sd} > C \tag{5-28}$$

$$V_p = \frac{T_{\max}\left(1 - 0.5 \cdot \frac{c_{s,initial}}{d}\right) + 0.5 \cdot V_s\left(\frac{a}{d}\right) + 0.5 \cdot V_{sd,limited}}{(a/d)} \tag{5-29}$$

A third case exists if the tensile stress plus horizontal shear component of the stirrups is less than the compressive force of the concrete. In this case, the strength is governed by the availability of the steel reinforcement, and the compression block is further reduced, as denoted in Equation 5-30.

$$c_{s,limited} = \frac{T_{\max} + V_{sd}}{0.85 \cdot f_c^{'} b} \tag{5-30}$$

The resulting shear strength is shown in Equation 5-31.

$$V_p = \frac{T_{\max}\left(1 - 0.5 \cdot \frac{c_{s,limited}}{d}\right) + 0.5 \cdot V_s \cdot \left(\frac{a}{d}\right) + 0.5 \cdot V_{sd}}{(a/d)} \tag{5-31}$$

Modifications for the post-tensioned specimen include a second horizontal tensile force equal to the post-tensioned force and a second lever arm. The resulting modification is shown in Equation 5-32 for the case of post-tensioning applied coincident with the longitudinal steel:

$$V_p = \frac{\left(T_{\max} + F_{PT}\right)\cdot\left(1 - 0.5\cdot\frac{c_{s,limited}}{d}\right) + 0.5\cdot V_s\cdot\left(\frac{a}{d}\right) + 0.5\cdot V_{sd}}{\left(a/d\right)} \quad \textbf{(5-32)}$$

This approach applied to the post-tensioning specimens suggested an increased shear strength, which was not observed. The possible reason for this discrepancy is that the post-tensioning force increases the compressive stresses in the reduced compression block, and for a shear-compression failure the added compression is not particularly beneficial. Conflicting findings in the literature and this research highlight the need for additional work for strengthening deep beams. For the carbon fiber repair, the base specimen capacity was determined by the Zararis Method, with the repair contribution taken from ACI 440 (divided by 2 as seen in Equation 5-31), which was governed by bond strength of the epoxy.

5.6.3.5 Bent cap modeling: VecTor2

Each of the repaired bent cap specimens was modeled in VecTor2. The post-tensioned bent cap specimen's meshing scheme is shown in Figure 5.127. For this specimen, the post-tensioning force was applied along five nodes that represent the limits of the height of the reaction section on each column section. An initial 22.5 kN (5 kip) was applied to each node, and the force was applied in several incremental steps. The post-tension force was used in a seed file for the final loading cycle. The results of the capacity estimate are shown in Table 5.21. The VecTor2 model conservatively predicted the shear force within 4% of the failure load.

The load versus midspan displacement is shown in Figure 5.128. The specimen provides close correlation with the experimental data, noting that the VecTor2 model was loaded prior to cracking moment, which would result in a more accurate slope along the initial portion of the curve.

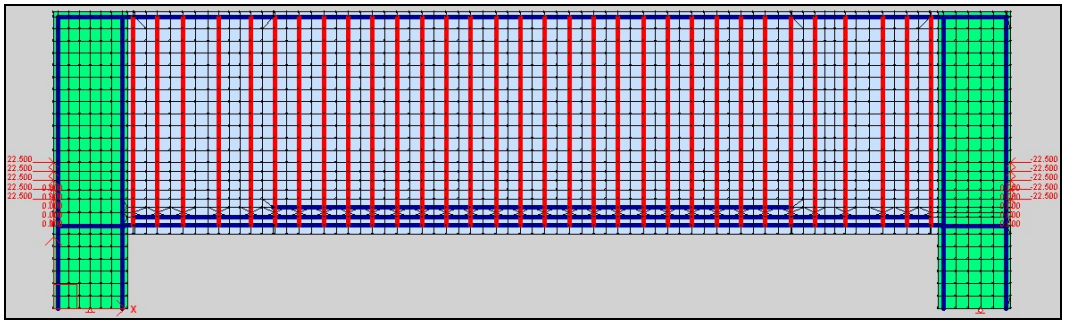


Figure 5.127: VecTor2 meshing scheme for D.T.C.PT

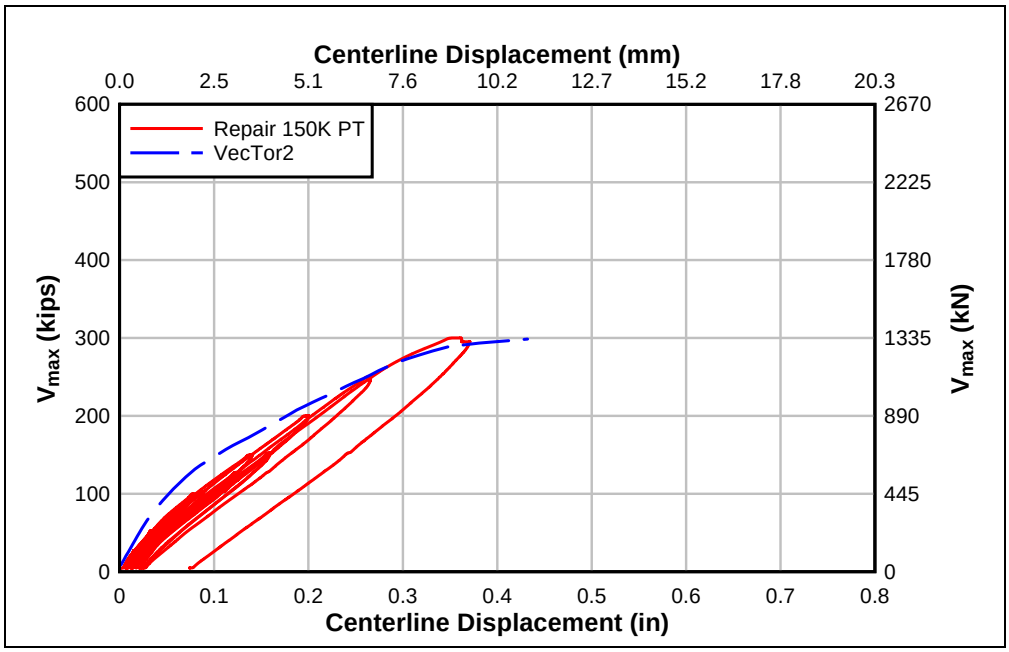


Figure 5.128: VecTor2 load-deformation response for D.T.C.PT

The CFRP repaired bent cap was also modeled in VecTor2, utilizing the bond-slip relationships previously identified for the beam specimen. The meshing scheme for the repair is shown in Figure 5.129. The strength estimate is shown in Table 5.21, which indicates no additional capacity was gained for the repair.

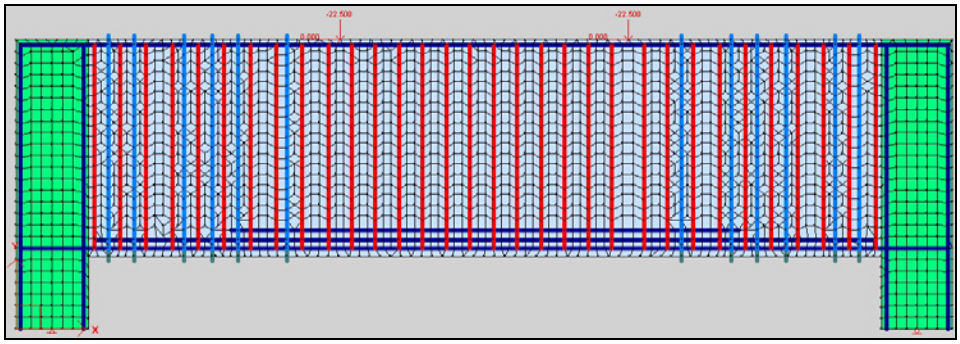


Figure 5.129: VecTor2 D.T.C.CF meshing scheme for D.T.C.CF

To better understand the behavior of the model, the midspan load-deflection curve is shown in Figure 5.130. The graph indicates a stiffness change for the cracked section with a gradual change in stiffness until failure. The constitutive models used in the literature were applied to beam specimens that have a larger a/d ratio than the existing deep beams. Therefore, the relationships may need to be modified accordingly. Also,

the premature failure may be a question of scale, as many CFRP shear beam tests are performed at reduced scales. Due to the large width of cracks and disturbed strain fields for the bent cap specimens in the current study, the bond slip relationship may not be directly applicable.

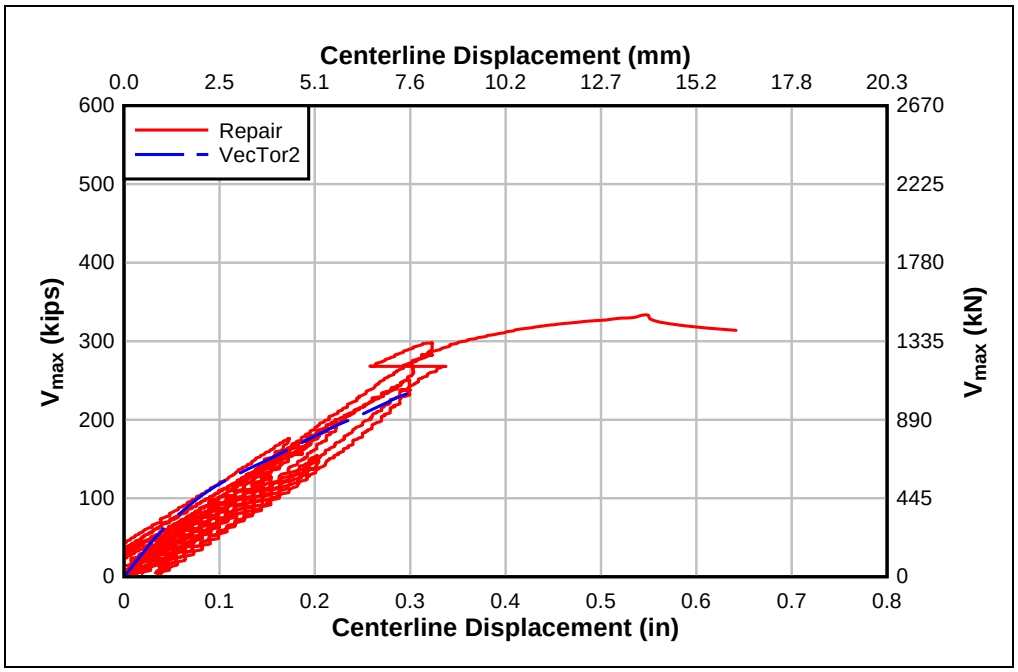


Figure 5.130: VecTor2 load-deformation response for D.T.C.CF

5.6.4 Discussion and design recommendations

Testing large scale specimens produces realistic strain conditions and removes any question of size or scale effects. However, limited resources prevent large numbers of specimens. Thus, the results of the current investigation provide an indication of two repair conditions, but they do not provide sufficient variability to provide general design recommendations. Based on the experimental and analytical results for these specimens, the following observations and recommendations are made:

- STM consistently provided a lower bound for the capacity of the repaired bent cap specimens. These may lead to excessively conservative and uneconomical results.

- If more refined estimates for the base specimen capacity are required, the Zararis Method and the Modified Zararis Method (proposed by Senturk) are recommended to compute improved shear capacity estimates, based on similar and previously tested bent cap specimens.

- ACI 440 was used to estimate the strength gain for the CFRP bent cap and, when used with the Modified Zararis Method, it provided conservative results. However, the ACI 440

predicted shear contribution alone (if using direct superposition) would just barely be conservative. The complex strain fields and concentrated cracking produced very different conditions than those of slender beams, and additional study of repair of large-size deep beams with CFRP is warranted for this material. Much of the conservatism from ACI 440 was seen to come from the base strength prediction (in the case of the slender beams) of ACI 318, which is known to be less conservative for large beams.

- The post-tensioned bent cap capacity was estimated by the Modified Zararis Method with an unconservative estimate of the repaired strength.

- The literature suggests that additional strength may be gained by epoxy injection prior to post-tensioning. However, the VecTor2 model for post-tensioning was completed such that post-tensioning was applied prior to application of vertical load. As the results are comparable to the experimental capacity of the section (not off by a factor of 2, as indicated by Aravinthan and Suntharavadivel (*2007*)), the validity of such an increase attributed to the epoxy injection alone prior to post-tensioning is uncertain. Additional study is warranted, as post-tensioning of bent caps with the proportions studied here appears to be of limited effectiveness.

5.7 LONGEVITY, RELATIVE COMPARISONS, AND SELECTION OF APPROPRIATE SHEAR STRENGTHENING METHOD

5.7.1 Longevity of repairs

Long life of repair installations depends primarily on two factors: response under repeated loading (high-cycle fatigue) and environmental durability. Based on the experimental data for the different repair materials at service levels, the anticipated life of the different steel repair materials can be estimated. The repaired member strengths can be predicted as described previously in this chapter. For predicting service life, as presented in Chapter 4, all the materials considered for girder applications exhibited strain compatibility with the cast-in-place (CIP) stirrups (true even for the external stirrups when a stiff section was used to anchor the threaded rods used as transverse reinforcing).

Based on field measured response of in-service RCDG bridges, observed in-situ stirrup strains were sufficiently low so as to provide very long life (*Higgins, et al. 2004b*). Due to strain compatibility observed experimentally between cast-in-place and repair stirrups, the supplemental transverse steel components (either rebar or threaded rod) should also have live load induced fatigue stress ranges that would be sufficiently low so that high-cycle fatigue would not limit the repaired member. Previous research on fatigue of surface bonded CFRP indicated repeated loading did not limit the life of the repairs (*Williams and Higgins 2008*). No data are available to estimate the anticipated fatigue life of NSM FRP repairs, and research is underway to assess this criterion.

Designers should estimate the live load stress range in the components to ensure that the anticipated live load stresses are below fatigue thresholds of the internal CIP and supplemental

transverse reinforcing components (internal or external steel stirurps). To estimate sharing of live load induced stresses between the internal stirrups and supplemental repair materials, the designer can assume that the diagonally cracked bridge girder carries the dead load shear (due to self-weight of components and wearing surface) with the concrete and CIP stirrups. Subsequent superimposed live load can be applied to the transverse steel (both internal CIP and supplemental). Even if the section will be epoxy injected, whereby the live load stresses will be carried by the integral composite section (the concrete and transverse reinforcing, both CIP and supplemental), upon recracking the transverse reinforcing can conservatively be considered as carrying the live load stress. Based on the experimentally observed strain compatibility between the internal CIP stirrups and the supplemental transverse reinforcing at service load levels, the live load stresses can be shared. Fatigue stresses in the transverse reinforcing should be kept below 20 ksi.

Environmental durability of the different materials was not directly considered in the present work, but recent research on surface-bonded CFRP indicates that if moisture is able to infiltrate the element at the strip termination locations, then freeze-thaw and moisture exposure can reduce the strength of girders (*Higgins, et al. 2009*). If moisture can be prevented from infiltrating into the member, no significant deterioration is observed. It is recommended that girder sections be epoxy injected to prevent moisture and possible chlorides from infiltrating the sections to protect the CIP reinforcing and any supplemental internal strengthening materials. For the external steel stirrups, these could be exposed to moisture and, in some instances, chlorides. This exposure may result in corrosion, loss of stirrup prestress, and loss of strength. The long-term durability of supplemental internal stirrups has been demonstrated for many years with field installations by the Kansas Department of Transportation as detailed in the literature review. This field experience indicates that long-term performance can be expected. Environmental durability of NSM FRP is uncertain; this will be explored in a recently funded research project.

5.7.2 Relative comparisons of repair alternatives

As detailed in this report, all the repair techniques can be used to effectively strengthen RCDG bridge girders for shear. No single technique is specifically recommended as the optimum design choice for all situations. This is because the selection can depend not only on strength and longevity, but on factors such as aesthetics, overall cost, access to bridge members, congestion of the steel in the section, traffic volume and required lane closures, availability of materials, expediency of the installation, and availability of experienced installers. Also the particular long-term environmental exposure (such as windborne or road salts) or short-term environmental conditions (time of year for installation in some locations) could impact decisions. To highlight the relative comparisons between the different methods, several possible design influencing criteria were considered. Each of the girder repair techniques was evaluated with respect to the criteria shown in Table 5.23. The criteria are described in the notes of the table.

5.7.3 Recommendation of design alternatives

While no one method may be appropriate for all given design situations, overall, the internal supplemental stirrups method appears to offer many advantages over other alternatives. This

technique is very efficient (making very efficient use of the material strength). The bonding of the supplemental steel allows good crack restraint, and the efficient angle also enables good anchorage of the bars. A key drawback is that the field installation must ensure that flexural bars or existing stirrups are not damaged during installation. Loss of flexural steel is a particular concern, as this can reduce shear strength due to shear-moment interaction. The supplemental internal stirrups cannot offer clamping force or restraint to effectively enhance flexural anchorage resistance to splitting. (This method does not provide resistance to splitting along the plane of the flexural reinforcing.) Further, hole preparation and good bonding, which cannot be directly assessed visually, are essential to successful implementation. The long-term durability of the approach has been demonstrated in the field with many years of service performance without reported issues by the Kansas Department of Transportation.

Design examples are provided for several of the repair alternatives in Appendix B.

Table 5.23: Relative comparisons between girder strengthening methods

Repair Method	1 Effective Increase Shear Strength	2 Efficiency of Matls	3 Aesthetics	4 Damage Base Strength	5 Envir. Durability	6 High-cycle Fatigue Life	7 Speed of Install.	8 Requires Lane Closures	9 Volatile Inorganic Cmpd. (VOC) Use	10 Controlled Cond.
Surface Bonded-CFRP	Yes	Yes	No	No	Good[5a]	Good[6a]	Slow	No	High	Yes
NSM-CFRP	?	?	No	Yes[4a]	?	?	Moderate	No	Moderate	Yes
External Stirrups	Yes	Yes[2a]	Yes	No	Poor	Good[6b]	Fast	Yes	None	No
Internal Stirrups	Yes	Yes[2b]	No	Yes[4b]	Good[5b]	Good	Moderate	Maybe[8a]	Low	Yes
Epoxy Injection	No	NA	No[3a]	No	Good	Good[6c]	Fast	No	Moderate	Yes

Table 5.23 Notes:

1. Effectively Increase Shear Strength: Does installation increase the shear strength of the section?
2. Efficiency of Materials: Do repairs make efficient use of the nominal material properties of the materials? 2a: If stiff support sections are used to anchor stirrups. 2b: Can easily be installed in principal diagonal tension direction to make most efficient use of material.
3. Aesthetics: Do repairs significantly alter visual appearance of bridge. 3a: Epoxy injection of diagonal cracks can leave "stripes" on the girders depending on surface coloration of girders.
4. Damage Base Strength: Can installation damage the strength of the section? 4a: Saw cutting required for installation that could cut flexural or transverse CIP reinforcing. 4b: coring required for installation that could cut flexural or transverse CIP reinforcing.
5. Environmental Durability: Is the repair expected to have long life under environmental exposures? 5a: If water can be prevented from infiltrating into the section. 5b: Proven long-term field performance in Kansas.
6. High-cycle Fatigue Life: Is the repair expected to have long life under high-cycle fatigue exposure? 6a: Experimental validation of long life under fatigue. 6b: Anticipated long life but uncertain if vibration loosens connecting components. 6c: Epoxy repairs known to exhibit recracking, but reduces stirrup stresses prior to recracking.
7. Speed of Installation: How fast is installation relative to others based on laboratory experience?
8. Requires Lane Closures: Does installation of the repair method require lane closures? 8a: Depends on whether girders are cored from underneath or on the deck.
9. Volatile Inorganic Compound Use (VOC): What relative amounts of volatile inorganic compounds does the repair use?
10. Controlled Conditions: Are controlled environmental conditions required during installation or curing (temperature or humidity)?

6.0 CONCLUSIONS

In this section, conclusions from the various repair methods are presented.

6.1 SUMMARY AND CONCLUSIONS

A research program was completed to investigate the behavior of lightly traditionally reinforced concrete girders and deep beams. The program included 15 specimens tested at full scale (13 girders and 2 bent caps), with vintage 1950's details including flexural cutoffs and widely spaced integrally cast stirrups within the shear span. Transverse steel and concrete mix design mimicked that of the original 1950's beams.

The results of the initial five repair beams for epoxy injection indicate that epoxy injection provides a means of bonding concrete across cracks and reducing steel stirrup strains, assuming the subsequent applied load is less than the maximum value previously felt by the girder. However, even strict enforcement of truck weights results in occasional overloads, which could re-crack the girder and render the repair ineffective. Further, it does not significantly increase the strength of the girders.

The remaining eight repair beams encompassed the latest emerging technologies in structural engineering for strengthening existing reinforced concrete members. External stirrups, applied to one IT beam with fully developed flexural steel, one IT beam with flexural cutoff details within the shear span, and one T beam with fully developed flexural steel, were included in the test matrix. The same three base specimens were constructed a second time, utilizing the supplemental internal stirrup repair. The remaining two beams were repaired, one with surface mounted CFRP strips in a 'U' shaped repair scheme, and one with rectangular FRP tape used in a NSM application.

All but two of the beams failed in shear after strengthening; both cutoff specimens failed due to anchorage. The bent cap specimens also failed in shear. For the beam specimens, the following general conclusions can be drawn:

- R2K can be used to develop design curves which take into account shear-moment interaction at a specific point of interest along a span.

- Using the shear 'pressure' term on the horizontal axis and the required shear stress on the vertical axis, the additional shear pressure required for the strengthening scheme is readily apparent, and the efficiency of the supplemental materials can be assessed relative to the base condition.

Results from the epoxy injection repair indicate:

- Capacity was not increased by epoxy injection. The largest capacity increases were observed for specimens with continuous cyclical live load applied during injection and with externally applied axial tension (which was due principally to an unintended post-tensioning effect).
- Live loading during injection and curing of epoxy produced dynamic pressure fluctuations during the injection process and pumping of the epoxy within the diagonal cracks. Fine bubbles were identified in the epoxy matrix of cores taken after testing for the specimen with applied live loads, but these bubbles were not sufficient to diminish performance.
- Stiffness was improved and development of residual deformations was delayed by epoxy injection.
- Epoxy injection increased the load level required to reform diagonal cracks in the stem.
- Injected diagonal cracks did not reopen; instead new cracks formed adjacent to the original injected cracks.
- Epoxy injection reduced service-level stirrup strains compared to un-injected diagonal cracks. This may reduce bond fatigue, thereby slowing or preventing additional crack growth.

Results from the supplemental external stirrup repair indicate:

- Selection of the appropriate steel reaction section has a direct effect on strain compatibility between the specimen and the external stirrups.

- Post-tensioning of external stirrups provides better strain compatibility over the service level loading.

- The long unbonded lengths of the external stirrups will likely result in larger diagonal crack motions than other repair methods (even with the post-tensioning effects). This point should be articulated to field inspectors of structures repaired using this method.

- The amount of post-tensioning should be chosen based on a combination of the yield strength of the external stirrups and the expected dead load strain in the internal stirrups (estimated as a fraction yield stress in the stirrup from the service level applied shear on the section to the shear strength of the section). A projected stress range to go from the initial post-tensioning stress to yield for the external stirrups should match that available from the internal integral stirrups so that both achieve yield at failure.

- From evidence found in the literature, a higher post-tension force results in higher specimen capacity. The above suggested post-tensioning level, combined with stiff supporting steel sections suggested above, should be adequate to achieve design strengths.

- From the available literature, the predicted shear strengths of each external stirrup specimen were quite variable. The current investigation provided a wide range of strength estimates based on either a simple 45 degree truss analogy or an approach following MCFT. AASHTO MCFT is proposed as the analysis method.

- The effectiveness of the repair is dependent on the reaction section used; however, if the external stirrup is positioned close to the web, this affect can be minimized with a typical external stirrup efficiency reduction due to weak axis bending of supporting steel sections on the order of 0.95 to 0.98.

Results from the supplemental internal stirrup repair indicate:

- Quality control of supplemental internal stirrup installation is paramount for success.

- Knowledge of existing flexural steel and stirrups is required for coring purposes in order to avoid severing critical steel components.

- The exterior faces of the web should be patched at the location of the cracks prior to inserting resin in the cored hole, as seepage of the epoxy will eventually penetrate from the cored hole location to the exterior fiber of the beam. Alternatively, the beam could be cored after epoxy injecting diagonal cracks.

- Once a hole is created without interference with the surrounding steel, the interior concrete surface must be clean to allow proper bonding of the epoxy. Also, seepage of epoxy through the web of the section reduces the epoxy within the cored hole. Providing additional epoxy throughout the installation due to seepage ensures complete encapsulation of the steel rebar. Alternatively, epoxy injection of the cracks prior to coring would minimize seepage.

- Selection of epoxy and size/grade of steel is important in the repair. Both larger and higher strength bar with fewer holes or more common mild steel with more holes have been effectively used in the current study. Relative cost and installation configuration (top down or bottom up) will provide an indication of the optimal repair combination. For a top down installation, the use of mild steel may be more economical, as specifications limit the use of higher strength steels. Further, for shallower beams with less anchorage length, the lower grade steel allows development of yield over shorter bond lengths. For a bottom up installation, the use of a hollow rod through which to pump epoxy may provide the best quality control.

- Post failure investigation of the internal stirrup specimens indicates a horizontal offset of the previous vertical grid lines on the specimen. Dowel action – the resistance of a reinforcing bar against forces acting perpendicular to its longitudinal axis – is likely the cause of this phenomenon. Dowel action may also increase bond efficiency and provide an additional source of shear resistance.

- Crack widths at ultimate were smaller than those of the external stirrup repair.

- Providing supplemental stirrups close to the principal strain axis of the member provides the best use of materials.

- The efficiency factors based on R2K analysis indicate the method performs better than predicted (attributed to the efficient orientation of rebar with respect to the principal tensile strains and the influence of dowel action on the bars).

Results from the surface bonded CFRP beam repair indicate:

No modifications to the existing ACI design approach are recommended based on this single specimen. However, based on this and previous research to estimate the repaired specimen capacity, ACI 318 in conjunction with ACI 440 can be used (*Higgins, et al. 2006; Higgins, et al. 2009*). Readers are referred to Higgins, et al. (*2009*) for additional detail on environmental durability. Estimation of repaired capacity using ACI 440 and R2K is not recommended, as this can lead to an unconservative design. VecTor2 provides a more conservative strength estimate than that of ACI 318 and ACI 440 combined and could be used as a tool to verify designs.

Results from the NSM FRP beam repair indicate:

The single specimen considered here provided a proof of concept; more data are needed to further validate use of NSM FRP for shear strengthening. Thus no specific design recommendations are provided at this time for the NSM repair method. As of the publication of this document, additional work has been funded by the Oregon Department of Transportation to further investigate the use of NSM CFRP for shear strengthening. The limited test data available within the literature coupled with this future work may allow further design modifications to ACI 440 for NSM retrofits. However, at the present time, there is a lack of consensus on the use of NSM in shear strengthening applications of large members.

Results from the bent cap repairs indicate:

- STM consistently provided a lower bound for the capacity of the repaired bent cap specimens. These may lead to excessively conservative and uneconomical results.

- If more refined estimates for the base specimen capacity are required, the Zararis Method and Modified Zararis Method (proposed by Senturk) provide improved shear capacity estimates based on similar and previously tested bent cap specimens.

- ACI 440 was used to estimate the strength gain for the CFRP bent cap and, when used with the Modified Zararis Method, it provided conservative results. However, the ACI 440 predicted shear contribution alone (if using direct superposition) would just barely be conservative. The complex strain fields and concentrated cracking produce very different conditions than those of slender beams, and additional study of repair of large-size deep beams with CFRP is warranted for this material. Much of the conservatism from ACI 440 was seen to come from the base strength prediction (in the case of the slender beams) using ACI 318, which is known to be less conservative for large beams.

- The post-tensioned bent cap capacity was estimated by the Modified Zararis Method with a modestly unconservative estimate of the repaired strength.

- The literature suggests that additional strength may be gained by epoxy injection prior to post-tensioning. However, the VecTor2 model for post-tensioning was completed such that post-tensioning was applied prior to application of vertical load. As the results are comparable to the experimental capacity of the section (not off by a factor of 2, as indicated by Aravinthan and Suntharavadivel (*2007*)), the validity of such an increase attributed to the

epoxy injection alone prior to post-tensioning is uncertain. Additional study is warranted, as post-tensioning of bent caps with the proportions studied here appears to be of limited effectiveness.

In addition to the laboratory tests, two RCDG bridges were inspected and instrumented to measure response under ambient and controlled truck loads. The Clarks Branch Bridge was strengthened with supplemental internal steel, and the Willamette River Bridge was strengthened with surface bonded CFRP strips.

Results from the field tests indicate:

- Although some concrete cracking and some loss of the protective coating was observed, the CFRP strengthened bridge exhibited similar responses to that measured 4 years previously.

- The Clarks Branch Bridge showed significant decrease in the stresses for the internal stirrups after installation of the supplemental internal stirrups.

6.2 RECOMMENDATIONS

As detailed in this report, all the repair techniques were used to effectively strengthen RCDG bridge girders for shear (except epoxy injection when applied alone). No single technique is specifically recommended as the optimum design choice for all situations. This is because the selection can depend not only on strength and longevity but on factors such as aesthetics, overall cost, access to bridge members, congestion of the steel in the section, traffic volume and required lane closures, availability of materials, expediency of the installation, and availability of experienced installers. Also the particular long-term environmental exposure (such as windborne or road salts) or short-term environmental conditions (time of year in some locations) could impact selections. For the situation where all things are equal, the internal supplemental steel stirrup method has demonstrated successful long-term service life performance, whereby the other methods do not.

6.3 FUTURE WORK CONSIDERATIONS

Additional work is needed for the NSM FRP repair in order to develop design recommendations. In addition, high-cycle fatigue performance and environmental durability need to be established. Repair of deep beams is not well known, and limited information is available in the literature or international codes. The single paper regarding the post-tensioned repair of bent caps suggests epoxy injection substantially increases the capacity. However, current findings from VecTor2 contradict this assumption, as does the Zararis Method which assumed no shear interlock along the characteristic crack. Repair of deep beams with CFRP using ACI 440 provisions, along with an appropriate base strength model, requires additional study to ensure desired performance. Further experimental data are needed to develop design methods for deep beams, as the strain conditions are significantly different than those in slender beams, upon which the code is based.

7.0 REFERENCES

AASHO. *Standard Specifications for Highway Bridges, 6th Edition*. American Association of State Highway Officials. 1953.

AASHTO. *AASHTO LRFD Bridge Design Specifications, 3rd Edition with 2005 Interims*. American Association of State Highway and Transportation Officials. 2004. 1331 p.

Abu-Tair, A. I., S. R. Rigden, and E. Burley. The Effectiveness of the Resin Injection Repair Method for Cracked RC Beams. *The Structural Engineer*. Vol. 69, No. 19. October 1991, pp. 335-341.

Altin, S., T. Tankut, O. Anil, and Y. Demirel. Response of Reinforced Concrete Beams with Clamps Applied Externally: an Experimental Study. *Engineering Structures*. No. 25. 2003. pp. 1217-1229.

American Concrete Institute (ACI). *ACI 318-05. Building Code Requirements for Structural Concrete and Commentary*. American Concrete Institute. 2005. 430 p.

American Concrete Institute (ACI). *ACI 440.1R-06. Guide for the Design and Construction of Structural Concrete Reinforced with FRP Bars*. American Concrete Institute. 2006. 44 p.

American Concrete Institute (ACI). *ACI 440.2R-02. Design and Construction of Externally Bonded FRP Systems for Strengthening Concrete Structures*. American Concrete Institute. 2002. 45 p.

Aravinthan, T. and T. G. Suntharavadivel. Effects of Existing Shear Damage on Externally Posttensioned Repair of Bent Caps. *Journal of Structural Engineering*. November 2007. pp. 1662-1669.

ASTM International. *ASTM 615/615M-05A. Standard Specification for Deformed and Plain Carbon-Steel Bars for Concrete Reinforcement*. ASTM International. 2005.

ASTM International. *ASTM A370-97a. Standard Test Methods and Definitions for Mechanical Testing of Steel Products*. ASTM International. 1997.

ASTM International. *ASTM C192/C192M-05. Standard Practice for Making and Curing Concrete Test Specimens in the Laboratory*. ASTM International. 2005.

ASTM International. *ASTM C39/C39M-05. Standard Test Method for Compressive Strength of Cylindrical Concrete Specimens*. ASTM International. 2003.

ASTM International. *ASTM C496/C496M-04el. Standard Test Method for Splitting Tensile Strength of Cylindrical Concrete Specimens*. ASTM International. 2004.

ASTM International. *ASTM C617-98. Standard Practice for Capping Cylindrical Concrete Specimens*. ASTM International. 2003.

ASTM International. *ASTM D3039/D3039M-00. Standard Test Method for Tensile Properties of Polymer Matrix Composite Materials*. ASTM International. 2001.

ASTM International. *ASTM D4541-02. Standard Test Method for Pull-off Strength of Coatings using Portable Adhesion Testers*. ASTM International. 2002.

ASTM International. *ASTM E8-00. Standard Test Methods for Tension Testing of Metallic Materials*. ASTM International. 2000.

Barros, J. A. O., and S. J. E. Dias. Near Surface Mounted CFRP Laminates for Shear Strengthening of Concrete Beams. *Cement & Concrete Composites*. No. 28. 2006. pp. 276-292.

Basunbul, I. A., A. A. Gubati, G. J. Al-Sulaimani, and M. H. Baluch. Repaired Reinforced Concrete Beams. *ACI Materials Journal*. Vol. 87, No. 4. July-August 1990. pp. 348-354.

Bentz, E.C. Sectional Analysis of Reinforced Concrete Members. PhD thesis. Department of Civil Engineering, University of Toronto. 2000. 198 p.

Chajes, M. J., T. F. Januszka, D. R. Mertz, T. A. Thomson, and W. W. Finch. Shear Strengthening of Reinforced Concrete Beams Using Externally Applied Composite Fabrics. *ACI Structural Journal*. Vol. 92, No. 3. 1995. pp. 295-303.

Chajes, M. J., W. W. Finch, T. F. Januszka, and T. A. Thomson. Bond and Force Transfer of Composite Material Plate Bonded to Concrete. *ACI Structural Journal*. Vol. 93, No. 2. 1996. pp. 208-217.

Chung, H. W. Epoxy-Repaired Reinforced Concrete Beams. *Journal of the American Concrete Institute*. Vol. 72, No. 5. May 1975. pp. 233-234.

Chung, H. W. Epoxy Repair of Bond in Reinforced Concrete Members. *Journal of the American Concrete Institute*. Vol. 78, No.1. January-February 1981. pp. 79-82.

Colak, A. Parametric Study of Factors Affecting the Pull-out Strength of Steel Rods Bonded into Precast Concrete Panels. *International Journal of Adhesion and Adhesives*. Vol. 21, No. 6. 2001. pp. 487-493.

Collins, M. P. and D. Mitchell. A Rational Approach to Shear Design – The 1986 Canadian Code Provisions. *ACI Journal*. Vol. 83, No. 6. November 1986. pp. 925-933.

Comite Euro-International du Beton (CEB). *CEB-FIP. Model Code1990: Design Code*. Comite Euro-International du Beton. 1993. 437 p.

Comite Europeen de Normalisation (CEN). *Eurocode 2: Design of Concrete Structures – Part 1-1: General Rules and Rules for Buildings*. BS EN 1992-1-1:2004. Comite Europeen de Normalisation. 2004.

Cook, R. A., J. Kunz, W. Fuchs, and R. C. Konz. Behavior and Design of Single Adhesive Anchors Under Tensile Load in Uncracked Concrete. *ACI Structural Journal*. Vol. 95, No. 1. January-February 1998. pp. 9-26.

Cruz, J. M. and J. A. O. Barros. Bond Between Near-Surface Mounted Carbon-Fiber-Reinforced Polymer Laminate Strips and Concrete. *Journal of Composites for Construction*. November/December 2004. pp. 519-527.

CSA International. *Canadian Highway Bridge Design Code (CAN/CSA-S6-00)*. Canadian Standards Association. 2000.

Dawson, M. Scale Effects on Reinforced Concrete Beams Strengthened for Shear with Discrete Externally Bonded Carbon Fiber-Reinforced Polymer U-Wraps. Masters Thesis. Oregon State University. 2008. 125 p.

De Lorenzis, L. and A. Nanni. Shear Strengthening of Reinforced Concrete Beams with Near-Surface Mounted Fiber-Reinforced Polymer Rods. *ACI Structural Journal*. Vol. 98, No. 1. 2001a. pp. 60-68.

De Lorenzis, L. and A. Nanni. Shear Strengthening of Reinforced Concrete Beams with FRP Rods. *ASCE Journal of Composites for Construction*. Vol. 5, No. 2. 2001b. pp. 114-121.

De Lorenzis, L. and A. Nanni. Bond Between Near-Surface Mounted Fiber-Reinforced Polymer Rods and Concrete in Structural Strengthening. *ACI Structural Journal*. Vol. 99, No. 2. March 2002. pp. 123-132.

De Lorenzis, L. Anchorage Length of Near-Surface Mounted Fiber-Reinforced Polymer Rods for Concrete Strengthening-Analytical Modeling. *ACI Structural Journal*. Vol. 101, No. 3. May 2004. pp. 375-386.

Dias, S. J. E. and J. A. O. Barros. Shear Strengthening of T Cross Section Reinforced Concrete Beams by Near-Surface Mounted Technique. *Journal of Composites for Construction*. May/June 2008. pp. 300-311.

FIP-Commission. *Practical Design: FIP Recommendations: Practical Design of Structural Concrete*. FIP-Commission 3. 1999. 95 p.

Hammad, B. S., R. Al Hammoud, and J.Kunz. Evaluation of Bond Strength of Bonded-in or Post-installed Reinforcement. *ACI Structural Journal*. Vol. 103, No. 2. March/April 2006. pp. 207-218.

Higgins, C., S.C. Yim, T.H. Miller, M.J. Robelo, and T. Potisuk. *Remaining Life of Reinforced Concrete Beams with Diagonal-Tension Cracks*. Report No. FHWA-OR-RD-04-12. Oregon Department of Transportation, Research Unit. 2004a.

Higgins, C., T.H. Miller, D.V. Rosowsky, S.C. Yim, T. Potisuk, T.K. Daniels, B.S. Nicholas, M.J. Robelo, A.-Y. Lee, and R. W. Forrest. *Assessment Methodology for Diagonally Cracked*

Reinforced Concrete Deck Girders. Report No. FHWA-OR-RD-05-04. Oregon Department of Transportation, Research Unit. 2004b.

Higgins, C., G. Williams, and L. Elkins. *Capabilities of Diagonally-Cracked Girders Repaired with CFRP*. Report No. FHWA-OR-RD-06-16. Oregon Department of Transportation, Research Unit. 2006.

Higgins, C., A.E. Senturk, and C.C. Koester. *Evaluation of Bent Caps in Reinforced Concrete Deck Girder Bridges*. Report No. OR-RD-09-07. Oregon Department of Transportation, Research Unit. 2008.

Higgins, C., M. Mitchell, M. Dawson, G. Sopal, and A.E. Senturk. *Environmental Durability of Reinforced Concrete Deck Girders Strengthened for Shear with Surface Bonded Carbon Fiber Reinforced Polymer*. Report No. FHWA-OR-RD-09-17. Oregon Department of Transportation, Research Unit. 2009.

Horiguchi, T. and N. Saeki. Effect of Test Methods and Quality of Concrete on Bond Strength of CFRP Sheets. *Proceedings: 3rd Symposium on Non-Metallic (FRP) Reinforcement for Concrete Structures*. Vol. 1. 1997. P. 265-270.

Kachlakev, D. and D. D. McCurry. Behavior of Full-Scale Reinforced Concrete Beams Retrofitted for Shear and Flexure with FRP Laminates. *Composites: Part B*. Vol. 31, Issue 6-7. October 2000. pp. 445-452.

Khalifa, A., W. J. Gold, A. Nanni, and M. I. Abdel Aziz. Contribution of Externally Bonded FRP to Shear Capacity of RC Flexural Members. *ASCE Journal of Composites for Construction*. Vol. 2, No. 4. 1998. pp. 195-202.

Kim, S. Y., K. H. Yang, H. Y. Byun, and A. F. Ashour. Tests of Reinforced Concrete Beams Strengthened with Wire Rope Units. *Engineering Structures*. Vol. 29, No. 10. October 2007. pp. 2711-2722.

Kim, S. Y. and F. J. Vecchio. Modeling of Shear-Critical Reinforced Concrete Structures Repaired with Fiber-Reinforced Polymer Composites. *Journal of Structural Engineering*. Vol. 134, No. 8. August 2008. pp. 1288-1299.

Koester, C. C. and C. Higgins. Testing and Evaluation of Flexural Straight-Bar Anchorages in Columns. submitted for publication to ACI Structural Journal. 2008.

Maeda, T., Y. Asano, Y. Sato, T. Ueda, and Y. Kakuta. A Study on Bond Mechanism of Carbon Fiber Sheet. *Proceedings: 3rd Symposium on Non-Metallic (FRP) Reinforcement for Concrete Structures*. Vol. 1. 1997. pp. 265-270.

Mandell, J.F., R.M. Reed, D.D. Samborsky, and Q. Pan. Fatigue Performance of Wind Turbine Blade Composite Materials. *Wind Energy – 1993*, S.M. Hock, editor, SED-Vol. 14, ASME 1993.

Miner, M. A. Cumulative Damage in Fatigue. *Journal of Applied Mechanics*. Vol. 12. Trans. ASME Vol. 67. 1945. pp. A159-A164.

Minh, H., H. Musuyoshi, B. B. Adhikary, and K. Watanabe. Experimental and FEM Study for Shear Strengthening of Reinforced Concrete Beams Using Different Techniques. *Transactions of the Japan Concrete Institute*. Vol. 23. 2001. pp. 365-370.

Norris, T., H. Saadatmanesh, and M. Ehsani. Shear and Flexural Strengthening of R/C Beams with Carbon Fiber Sheets. *Journal of Structural Engineering*. July 1997. pp. 903-911.

Parretti, R. and A. Nanni, Strengthening of RC Members Using Near-Surface Mounted FRP Composites: Design Overview. *Advances in Structural Engineering*, Vol. 7, No. 6. 2004. pp. 469-483.

Popov, E. P. and V. V. Bertero. Repaired R/C Members Under Cyclic Loading. *Earthquake Engineering and Structural Dynamics*. Vol. 4, No. 2. October-December 1975. pp. 129-144.

Potisuk, T. and C. Higgins. Field Testing and Analysis of CRC Girder Bridges. *Journal of Bridge Engineering*. ASCE. Vol. 12, No. 1. January-February 2007. pp. 53-63

Rooney, R. A. *Epoxy Resins as a Structural Repair Material*. Report No. 63-23. California Department of Transportation, Division of Research and Innovation. http://www.dot.ca.gov/hq/research/researchreports/1961-1963/63-23.pdf. January 1963. 15 p.

Sato, Y., T. Tanaka, T. Ueda, and S. Ono. Shear Behavior of RC Beams Reinforced with Carbon Fiber Sheet. *Transactions of the Japan Concrete Institute*. Vol. 18. 1996. pp. 137-142.

Senturk, A. E. Experimental and Analytical Evaluation of Conventionally Reinforced Deck-Girder Bridge Bent Caps with Vintage Details. Doctoral Thesis. July 11, 2008. Oregon State University. 376 p.

Senturk, A. E. and C. Higgins. Evaluation of RCDG Bridge Bent Caps with 1950's Vintage Details: Analytical Methods. *ACI Structural Journal*. submitted October 2008; in peer review.

Shamsai, M., H. Sezen, and A. Khaloo. Behavior of Reinforced Concrete Beams Post-Tensioned in the Critical Shear Region. *Engineering Structures*. Vol. 29, No. 7. July 2007. pp. 1465-1474.

Shield, C., C. French, and E. Milde. The Effect of Adhesive Type on the Bond of NSM Tape to Concrete. *ACI SP230: 7th International Symposium on Fiber-Reinforced Polymer (FRP) Reinforcement for Concrete Structures*. November 2005. pp. 355-372.

Stratton, F. W., R. Alexander, and W. Nolting. *Cracked Structural Concrete Repair through Epoxy Injection and Rebar Insertion*. Interim Report. Report No. FHWA-KS-RD-76-2. Kansas Department of Transportation, Bureau of Materials and Research. May 1977. 47 p.

Stratton, F. W., R. Alexander, and W.Nolting. *Cracked Structural Concrete Repair Through Epoxy Injection and Rebar Insertion*. Final Report. Report No. FHWA-KS-RD-78-3. Kansas Department of Transportation, Bureau of Materials and Research. November 1978. 56 p.

Stratton, F. W., R. Alexander, and W. Nolting. *Development and Implementation of Concrete Girder Repair by Post-Reinforcement*. Report No. FHWA-KS-82-1. Kansas Department of Transportation, Bureau of Materials and Research. May 1982. 36 p.

Tremper, B. Repair of Damaged Concrete with Epoxy Resins. *Journal of the American Concrete Institute*. Vol. 32, No. 2. August 1960. pp. 173-182.

Triantafillou, T. Shear Strengthening of Reinforced Concrete Beams Using Epoxy-Bonded FRP Composites. *ACI Structural Journal*. Vol. 95, No. 2. March-April 1998. pp. 107-115.

Triantafillou, T. and C. P. Antonopoulos. Design of Concrete Flexural Members Strengthened in Shear with FRP. *Journal of Composites for Construction*. November 2000. pp. 198-205.

Vecchio, F. J. and M. P. Collins. The Modified Compression Field Theory for Reinforced Concrete Elements Subjected to Shear. *ACI Structural Journal*. Vol. 83, No. 2. March 1986. pp. 219-231.

Vecchio, F. J. and P. Wong. *VecTor2 and Formworks Users' Manual*. Technical Report. Department of Civil Engineering, University of Toronto. 2002. 232 p.

Watson Bowman Acme Corporation. *Specification: Wabo® MBrace Composite Strengthening System with Carbon Fiber Reinforcement*. Watson Bowman Acme Corporation. March 2002.

Watson Bowman Acme Corporation. *Wabo® MBrace CF130*. Watson Bowman Acme Corporation. February 2003.

Williams, G. and C. Higgins. Fatigue of Diagonally Cracked RC Girders Repaired with CFRP. *Journal of Bridge Engineering*. Vol. 13, No. 1. January 2008. pp 24–33.

Wong, R. S. Y. and F. J. Vecchio. Towards modeling of reinforced concrete members with externally bonded fiber-reinforced polymer composites. *ACI Structures Journal*. Vol. 100, No. 1. 2003. pp. 47-55.

Zaintz, L. and J. Long. Oregon's Bridges at Breaking Point. *The Oregonian*. Sunday, February 3, 2002.

Zararis, P. D. Shear Compression Failure of Reinforced Concrete Deep Beams. *Journal of Structural Engineering*. Vol. 129, No. 4. April 2003. pp. 544-553.